An Approach to Modelling Ice Deposits Across the Solar System

Kasra Bozorgmehri-Fard

A Dissertation Submitted to the Faculty of Graduate Studies in Partial Fulfilment of the Requirements for the Degree of Doctor of Philosophy

Department of Physics and Astronomy, York University, Toronto, Ontario

November 2025

Abstract

This dissertation presents an approach to examining the exotic ices behaviour, and reconstructing non-terrestrial the glacial history (under planetary conditions other than those of Earth), including those of stratified CO_2 icesheets near Mars' south pole, through high-resolution computer simulations. Modelling ices on other planets (e.g., on Mars) is vastly different from those on Earth; hence the approach will be different for paleo-non-terrestrial glacial modelling. For this, I have augmented JPL's Ice-sheet and Sea-level System Model (ISSM) to support multi-unit ice masses, temperature-dependent material properties (beyond the already temperature-dependent rheology), and Martian environmental boundary conditions. This new codebase, the ***M***ulti-unit ***I***ce ***D***eposits ***A***nalysis and ***S***imulation (MIDAS) framework, enables the study of complex, stratified ice systems with realistic thermo-mechanical coupling under planetary conditions.

Here, I also provide two practical case studies for the application of MIDAS on Mars: the first examines the geomorphic evolution of Mt. Sharp (Aeolis Mons) in Gale Crater, where observations by the Mars Science Laboratory Curiosity rover reveal bedrock features resembling terrestrial glacial landforms. Using MIDAS, three-dimensional flow of cold-based, debris-free glaciers were modelled to examine the hypothesis that former glacial activity could have contributed to the nearby erosional features. The purpose of modelling was only to examine the potential direction of the ice flow. The modelling results show that ice accumulation and flow could have reached to shape the key landforms observed today.

The second case study focuses on the *Massive CO_2 Ice Deposits* (MCID) beneath the Martian *South Polar Layered Deposits*, where MIDAS was used to simulate the formation and thermo-mechanical evolution of the MCID's stratified CO_2–H_2O ice units over 510,000 years. The modelled results demonstrate that the inclusion of viscous and thermally conductive water-ice bounding layers could reduce internal temperatures and strain rates, and stabilize the overall set of CO_2 ice units.

Together, these studies, by integrating geomorphic interpretation with high-fidelity numerical modelling, demonstrate a process for examining the stability, flow behaviour, and climatic significance of non-terrestrial ice deposits. MIDAS, as a modelling toolset, helps advance our understanding of the glacial and atmospheric history of the planets in the solar system, and could contribute to a broader understanding of the solar system's overall evolution.

Dedication

To Nika

Acknowledgements

I would like to express my gratitude and appreciation to Professor Isaac Smith, my PhD advisor, for his unwavering patience, support and guidance throughout my research. His guidance and help insights were invaluable in directing this work.

Moreover, I am grateful to the advisory committee, Dr. Regina Lee and Dr. Joel Zylberberg for their incredible feedback. I would like to express special thanks to Dr. Nicole-Jeanne Schlegel and Dr. Mathieu Morlighem for their guidance of ISSM and support of my work. Their deep knowledge in glaciology as well as modelling helped shape this work; also, Dr. Bernard Hallet and Dr. Ronald Sletten for their contribution in the Gale Crater research and feature analysis, and providing the images and the required data sets, which offered a strong use case for the use of this research and dissertation.

The list of those who supported me through this journey is long and includes my lab mates, friends and of course my family to all of whom, I owe a debt of gratitude; specially, I am eternally grateful to Nika, with her love for “rainbow rocks,” and who believed in me and patiently remained by my side throughout this journey.

Table of Contents

List of Tables

List of Figures

Preface

My ongoing research on the MCID first appeared at the Lunar and Planetary Science Conference (LPSC) in Houston, Texas, in 2022; subsequently, its progress was presented at the "Ices in the Solar System" workshop in Montreal in January 2023, and later it was presented at the 2023 LPSC (Houston, Texas). My work on Gale Crater appeared at the 2024 LPSC (Houston, Texas), and then it was presented at the Mars Polar Ice Conference in 2024 (Whitehorse, Yukan).

The work in this dissertation is based on my published or in-review papers as follows:

- **Chapter 2:** Fard, K. B., Smith, I. B., Schlegel N. (In PREP). Multi-unit Modelling and Analysis Ice Deposits Across the Solar System Using a Modified Version of Ice-sheet and Sea-Level System Model (ISSM).
- **Chapter 3:** Fard, K. B., & Smith, I. B. (2023). Properties of water, carbon dioxide, and nitrogen ices in planetary surface environments. Icarus, 115895. *https://doi.org/10.1016/j.icarus.2023.115895*
- **Chapter 4:** Fard, K. B., Smith, I. B., Hallet, B., Sletten, R. S. (In Review). Modelling 3D Flow of Potential Glaciers on Mt. Sharp (Aeolis Mons) in Gale Crater, Mars, Icarus.
- **Chapter 5:** Fard, K. B., Smith, I. B., Schlegel N. (In Review – submitted to Journal of Geophysical Research). Modelling the Water Ice Bounding Layers in the Massive Ice CO2 Deposits, South Pole of Mars
- **Appendices:**
  - **Appendix 1, and Appendix 3:** Based on the supplementary materials from: Fard, K. B., Smith, I. B., Schlegel N. (In Review). Multi-unit Modelling and Analysis

Ice Deposits Across the Solar System Using a Modified Version of Ice-sheet and Sea-Level System Model.

- **Appendix 2**: Fard, K. B., & Smith, I. B. (2023). Properties of water, carbon dioxide, and nitrogen ices in planetary surface environments. Icarus, 115895. *https://doi.org/10.1016/j.icarus.2023.115895*

An updated, forked version of ISSM with the functionality developed by me is found on github at *https://github.com/KBF-I/MIDAS/tree/Gen-1/src*:

Fard, K. B., & Smith, I. B. (2025). MIDAS: Multi-unit Ice Deposits Analysis and Simulation (Gen-1) (Version Gen-1) [Computer software]. https://doi.org/10.5281/zenodo.17329138

1 Introduction

1.1 Dissertation Contribution Statement

My work aims to advance the scientific understanding of Martian glacial dynamics by augmenting an existing modelling tool to provide a framework to analyze the behaviour of stratified and non-stratified ice units and capture the impact of temperature-dependent material properties and boundary conditions on such models. I specifically use this tool to analyze and find support for two hypotheses in the equatorial and south polar regions of Mars.

As this framework can be used across the solar system, this can help advance our understanding of the glacial and atmospheric history of the planets in the solar system; as such, my work could contribute to a broader understanding of the solar system's overall evolution.

1.2 Background

Studying the mechanics and workings of the solar system necessitates a detailed understanding of various bodies that exist within it, along with their histories, their evolution, as well as the climatic changes they have experienced. Ice plays a key role in the climatic and geological histories of terrestrial and icy bodies alike; and much like on Earth, studying ices on other planets in the solar system provides means into understanding their histories. And, examining the evolution of planetary bodies, including their atmospheres and surfaces, provides a strong view into the workings and history of the solar system. As such, modelling the formation, flow, and ablation of icy features across the solar system becomes a valuable approach.

In terrestrial glaciology, ice masses can generally be classified as icesheets (which are large masses of ice and tend to be in contact with solid land), ice caps (similar to icesheets, but smaller in size; the differentiating factor between an ice cap and an icesheet is the area each covers with ~50,000 km^2 being the threshold), glaciers (even smaller than ice caps and constrained by non-ice-based features like mountains), and ice shelves (which are floating, and in contact with an icesheet, ice cap or glacier). Other ice-based distinct features include sea ice, lake ice, river ice, ground ice, and snow (Greve and Blatter, 2009). For the purpose of this dissertation, I will be using the terms glaciers and icesheets[1].

With the advancements in computational power, mathematical based tools to model the dynamics of terrestrial geological and icesheets have matured significantly. However, such tools remain mostly specific to terrestrial atmospheric conditions, gravity, and the single ice composition and rheology found on Earth. There is ample evidence that ice deposits on solar system bodies, other than Earth, have diverse (and often mixed) chemical compositions. Extraterrestrial glaciers, due to the low temperatures at which they formed, are likely to incorporate a wider range of compounds, particles and materials; at times, as alternating units of icy materials within the same ice mass. In short, the behaviour of ices on non-terrestrial settings is vastly different than those on Earth, and they need different approaches than terrestrial glaciology to understanding their formation, flow and evolution.

---

[1] "Icesheet" with no space, and no hyphen is the preferred form in this dissertation. However, for ISSM "ice-sheet" (the hyphenated form) was used to be aligned with the ISSM branding.

Ice deposits with chemical compositions other than water ice, and on non-terrestrial settings are generally referred to as "exotic ice" deposits. For instance, on planets such as Mars or distant icy worlds like Pluto and Triton, the glaciers are not solely composed of H_2O ice but are composed of compounds like carbon dioxide (CO_2), nitrogen (N_2), and methane (CH_4). An exotic icesheet might incorporate one or multiple of these materials in a stratified structure (e.g. on Pluto). Different types of materials have distinct physical and rheological properties, and icesheets or glaciers made up of materials other than water ice will behave differently than water-ice based ice masses. Therefore, knowledge gained from terrestrial ice studies, while conceptually useful, is insufficient for fully understanding the dynamics of stratified exotic ice deposits on other planets. It becomes important that such differences necessitates fundamentally different approaches than those used for terrestrial settings.

The rheological properties of exotic ices vary depending on environmental factors such as temperature, gravity and pressure. As a result, an ice mass may behave differently on one planetary body than another. To more accurately model behaviour of glaciers, considerations around other material properties (e.g., density, thermal conductivity, which are also sensitive to temperature) also play important roles. Because exotic ices are typically exposed to very low (and wide range of) temperatures, it becomes essential to account for the impact of temperature on these properties. This is another challenging factor in extraterrestrial glacial modelling where using fixed values for physical parameters tends to be an oversimplification.

The compositional and physical diversity increases the number factors that need to be taken into account in determining the rheological properties across an ice mass. The rheological properties govern the dynamics of an ice mass (i.e., they determine and affect the spatial distribution and deformation history of that mass). When that ice mass is stratified, with multiple “layered ice units,” each with their own distinct rheological properties, predicting the associated flow rate, internal stress and strain and temperature distribution within the ice mass resulting flow dynamics will require paying attention to various factors: the sensitivity of the deformation of the material to the slope, temperature and the stress; and the behaviour of the material present in the stratified ice unit might be opposite when they are exposed to the same topographical and thermal conditions. To explain this complexity further, consider water ice that has relatively high viscosity under terrestrial conditions. The viscosity of H_2O ice is stronger at Mars temperatures; therefore, it flows over geologic timescales in glaciers and icesheets. On the other hand, CO_2 ice is substantially weaker, with a lower viscosity that allows it to deform more easily under stress, leading to faster glacial flow on Mars (Cross et al., 2020). Even more extreme, nitrogen ice is exceptionally soft, with a viscosity that is orders of magnitude lower than that of H_2O and CO_2 ices, which enables convective overturn and comparatively more rapid glacial movement at cryogenic temperatures (McKinnon et al., 2016). Now, glaciers that have alternating layers of CO_2 and H_2O will behave differently than a glacier that is solely composed of only one of them. This is one of the complexities that present itself while analyzing exotic icesheets and will be much of the focus of this dissertation.

As mentioned, there is much evidence on the existence of exotic ices across the solar system. Many planetary bodies, including Pluto, Triton, Europa, and Enceladus serve as compelling examples of icy planetary bodies with diverse ice compositions, and therefore different flow dynamics. Each of these bodies possesses specific and rather unique ice dynamics challenges that require models capable of handling varying ice compositions, temperatures, and planetary gravities:

- Pluto's icesheet consists primarily of nitrogen ice, with significant deposits of methane and carbon monoxide ices (Moore et al., 2016). Frozen nitrogen exhibits a low-viscosity flow. 2015 observations by New Horizons suggest that icesheets in Sputnik Planitia on Pluto behave similar to those on Earth. However, the large-scale convective overturn caused by the low yield strength of frozen N_2 (McKinnon et al., 2016) is a complicating factor in modelling.
- Europa and Enceladus, two of Jupiter and Saturn's icy moons, have icy shells, with probably global subsurface oceans underneath, driven by the tidal heating effects of their host planets (Nimmo & Pappalardo, 2016). Enceladus possibly experiences active cryovolcanism, ejecting water ice plumes from subsurface reservoirs, which complicates modeling efforts (Porco et al., 2006).

Closer to home, analyzing terrestrial icesheets could also be considered equally challenging and complex. For example, layers of dust, or low-density snow and firn (i.e., uncompact snow), or any form of debris, accumulated on top of a glacier will result in discontinuities of rheology of the mass.

Mars has been the subject of much study and scrutiny. One reason is that Mars could act as a laboratory, offering cold and dry environmental conditions that could be experience on many other solar planets. The proximity of Mars enables us to test hypothesis on Mars and learn more about similar planetary environments. One venue to studying the history and evolution of the planet, therefore, will be to study and learn more about the history of the existing glaciers on Mars, as well as investigating the potential for existence of ice in recent past in other areas. A suite of surface features is consistent with, or suggest, past ice accumulation: They include the South and North Polar Layered Deposits (Smith et al., 2022 and references within); Viscous

Flow Features (Levy et al., 2014); the Latitude-Dependent Mantle (e.g., Kreslavsky and Head, 2002; Head et al., 2003; Dickson et al., 2015); and Tropical Mountain Glaciers (e.g., Shean et al., 2005; Head and Weiss 2014) which are viewed as low-latitude viscous flow features. The polar layered deposits consist of alternating layers of ice and dust in the north and the south (Byrne et al., 2009; Smith et al., 2022). The latitude-dependent mantle comprises ice deposits upwards of tens of meters thick, with a high dust content; these probably formed during recent ice ages (Kreslavsky and Head, 2002; Head et al., 2003; Milkovich and Head, 2005; Smith et al., 2016). Viscous flow features number in the tens of thousands and are primarily found between 30° and 60° in both hemispheres (Levy et al., 2014). Investigations of the spatial distribution, thickness, and dynamics of ice masses across different Martian latitudes can contribute to the understanding of the planet's climatic and geological evolution (Smith et al., 2020).

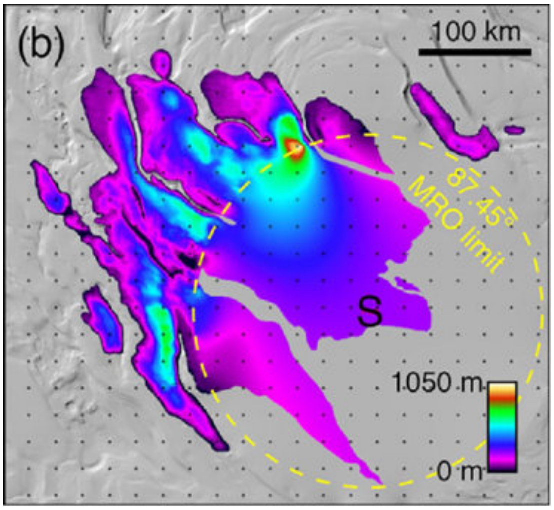

Figure 1.1 – Thickness of CO2 glaciers as mapped in 3D radar (Putzig et al., 2018)

The identified circle corresponds to the area that where no direct data is available, and the data has been interpolated using the captured data from the outside of the circle. Letter S points to the South Pole.

Martian climatic cycles share similarities with the Milankovitch Cycles of Earth (i.e., cyclical variations in orbital parameters, described and named after Milankovitch). Both planets experience regular changes in their orbital parameters such as obliquity (i.e., the tilt of the axis in relation to its orbit) and the eccentricity (i.e., the orbital deviation from being circular) (Laskar et al., 2004). Outside of the similarities, the Martian orbital parameters experience larger variations. For instance, theoretical and numerical analysis (through simulations) done by Laskar et al., (2004) on the Martian orbital parameters provides series of possible historical variations of these parameters. These results show that over the past 10 million years, the Martian obliquity (i.e., the tilt of the planet), has seen a dramatic variation, from 14 to 48 degrees (Laskar et al., 2004) (while the Earth's obliquity potentially varied from 22 to 24.5 degrees). Similarly, the eccentricity of Earth's orbit around the sun has varied from 0 to 0.06, in contrast to that of Mars, which has spanned from 0 to 0.12 (Laskar et al., 2004). Laskar et al. (2004) calculated these variations for tens of millions of years, and later work examined the impacts of the obliquity and eccentricity variations on the recent Martian climate (e.g., Levrard et al., 2007; Madeleine et al., 2009; Emmett et al., 2020), including insolation, atmospheric circulation, and thus the deposition of ice across Mars (Buhler et al., 2019; 2021; 2023). These parameters will be further discussed in section 1.4.

Recent observations by the Mars Reconnaissance Orbiter have revealed massive carbon dioxide (CO_2) ice deposits (MCID) near Mars' south pole (Figure 1.1). These deposits, reaching up to 1 km thick and totalling volumes of approximately 16,500 km^3 (Phillips et al., 2010, Bierson et al., 2016), and Putzig et al., 2018). The mass of these nearly pure CO_2 deposits is close to the Mars' current atmospheric mass (the Martian atmosphere is mainly composed of CO_2), so they serve as the primary reservoir of the most volatile compound on Mars. These deposits exhibit primary and secondary features typical of Earth’s glaciers, providing strong evidence of existing CO_2 glaciers on Mars (Smith et al., 2022).

There are other areas on Mars where with observable ice deposits, there are also paraglacial terrains, in which the ice is now gone but geomorphic and chemical evidence of their former presence remains. One such areas is Gale Crater near the equatorial region of Mars, explored by the Mars Science Lab (MSL) and the Curiosity Rover. Some studies show that the present-day features could have been the result of periglacial or glacial activities. By determining the potential processes that caused the observed features today, we can explain the manner through which many enigmatic geological features have formed; and therefore, uncover more about the Martian history and the planets evolution.

Continuing in this introduction, I will be exploring the MCID and Gale Crater as two potential areas where learning more about their glaciological history could help with answering series of outstanding questions on the history and evolution of Mars. The use of modelling can be a great way to understand these scenarios and provide interpretations that could explain some of the mysterious features that are observable today.

1.3 Massive CO$_2$ Ice Deposits (MCID) and Climate Cycles

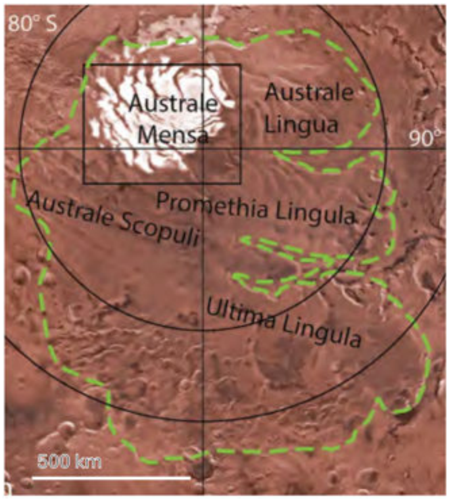

Figure 1.2 – A mosaic image from the south pole of Mars (Viking)

The bright white area is the SPRC (CO$_2$ ice). SPLD is denoted by the green dashed line and is covered by red dust during warmer seasons. The black box correlates with Figure 1.3A. Source Smith et al., 2022

CO$_2$ is a compound that is present on Mars in different shapes and forms and in various locations, from gas form in the atmosphere (the Martian atmosphere is made up of 96% CO$_2$ (Trainer et al., 2019)), to frozen forms (e.g., in and around the south pole of Mars (Kieffer, 1979)). Near the south pole of Mars, there is a frozen feature that can be observed from Earth. This is called the South Polar Residual Cap (SPRC) that is about a few meters thick and exists all year long. As it will be detailed below, primarily from spectroscopic observations, especially those made by instruments aboard Martian orbiters like Mars Global Surveyor (MGS) and MARS Reconnaissance Orbiter (MRO), it was determined that SPRC is mainly made up of

CO_2, but it also H_2O ice in its structure (Fishbaugh and Head III 2001; Brown et al. 2010) (Figure 1.2). The seasonal CO_2 ice caps form and dissipate annually on top of SPRC.

SPRC covers majority of the South Polar Layered Deposits (SPLD) (Byrne and Ingersoll, 2003), which are massive ice features and originally thought to be solely comprised of CO_2 (Figure 1.2). However, early studies on the rheology of CO_2 ice (Clark and Mullins, 1976; Durham et al., 1999; Nye et al., 2000) showed that CO_2 would not be stable enough, and as glaciers, CO_2 ice would flow rather fast (due to its low viscosity) in spite of the Martian gravitational force, and the low temperature of its south pole. The crater counting technique puts the age of SPLD in tens of millions of years, a period that glaciers made up of only CO_2 would not have survived (Herkenhoff and Plaut, 2000). This demonstrated the possibility that potentially large and thick "layer" of water ice should be in place under a layer of CO_2 ice to help with stabilizing SPLD to the shape we observe today (Byrne and Ingersoll, 2003).

In 2011, data from the Shallow Radar (SHARAD) instrument aboard NASA's Mars Reconnaissance Orbiter revealed the Massive CO_2 Ice Deposits (MCID) beneath the SPRC. (Phillips et al., 2011). Geophysical analysis and layer geometry helped confirm the composition and thicknesses of these deposits (the dielectric properties and speed of light within these deposits are consistent with CO_2 ice, and demonstrating the thickness, in some locations, reaches up to 1000 m) (Figure 1.3A). These identified deposits are primarily located in depressions. Many of these deposits are isolated and not connected. They are mostly under a layer of water-ice (with dust) and then the SPRC. The SPRC, due to its composition, helps to maintain the temperature of these CO_2 dominated deposits at about 150 K (Bierson et al., 2016; Buhler et al., 2019). The low temperature and the existence of the water-ice layer on their top have helped with protecting CO_2 deposits from sublimation for over 100,000 years (Bierson et al., 2016; Buhler et al., 2019).

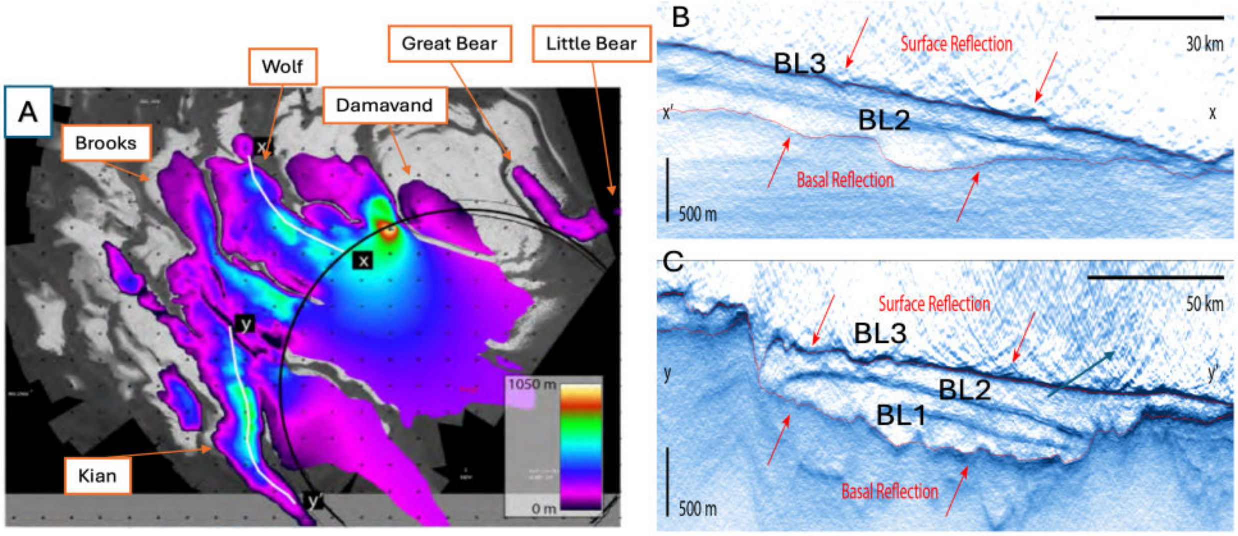

Figure 1.3 – *Massive CO_2 Ice Deposits in the south polar region of Mars.*

(A) CO_2 ice thickness over a Context Imager summer mosaic (Thomas et al., 2009). CO_2 ice thickness is mapped up to the southern latitude limit of the Mars Reconnaissance Orbiter (black circle), beyond which the ice is extrapolated to boundaries from geologic mapping. Named glaciers are marked with their names. (B) and (C) Radar profiles from a 3D radar data set (Foss et al., 2017; Putzig et al., 2018). H_2O bounding layers marked with BL1, BL2, BL3 (Alwarda & Smith, 2021). Panels modified from Smith et al., 2022.

Based on 1D modeling of CO_2 deposition, Buhler 2019 posited that the MCID must have begun forming ~600,000 years before present. The total mass of the MCID has been estimated by Putzig et al. (2018) to be approximately 2.68×10^{16} kg (Buhler & Piqueux, 2021); compare against the Martian atmospheric mass of 2.75×10^{16} kg used for calculations by Buhler and Piqueux (2021) (Haberle et al., 2008; Guo et al., 2010). According to the European Space

Agency (ESA), 95.32% of the Martian atmosphere is carbon dioxide; this makes MCID more massive than the CO_2 existing in the current Martian atmosphere.

Bierson et al. (2016) investigated the reflective properties of various areas within the MCID units, revealing the presence of multiple ice units composed of distinct material types (i.e., alternating units of CO_2 and H_2O ice arranged from top to bottom), the water ice layers acting as "bounding layers." These are not just layers at the base and the surface, but there are also layers in the middle of MCID units. The bounding layers for two distinct areas are shown in Figure 1.3 B and C. Alwarda and Smith (2021) subsequently provided the first detailed mapping of the bounding layers (BLs), showing that their thicknesses would vary between 20 to 70 meters. Bierson et al. (2016), since water ice layers protect the CO_2 deposits from sublimation after their formation, proposed that the stratification within the MCID unit could be attributed to the climatic changes on Mars, suggesting a direct influence of these changes on the formation and subsequent layering within the unit.

The dynamics of layer formation and alteration in the MCID (including its water ice bounding layers) could be interpreted as evidence for the direct correlation between the formation of MCID and the Martian obliquity cycles (i.e., the temporal variation of the title of the planet's axis). Figure 1.5 shows this possible relationship. During lower obliquity, the colder summertime temperature would result in the deposition of CO_2 from the atmosphere (Figure 1.4). The deposition of the H_2O particles could have happened through a scavenging process during the CO_2 deposition (Alsaeed, and Hayne, 2022).

1.4 Martian Obliquity

The temperature of the polar CO_2 cap on Mars is in equilibrium with that of the atmosphere. This makes the Martian atmosphere sensitive to the changes of the polar temperature which are governed by the insolation (i.e., the amount of sunlight received on a unit surface area), and albedo. The distribution of solar insolation on Mars is governed primarily by variations in its orbital parameters, which are eccentricity (how stretched the planet's orbit around the sun is), precession (the wobble of the planet's tilted axis), and obliquity (the title of the planet's axis) (Laskar et al., 2004). For Earth the variations in the obliquity cycle are stabilised by the Moon. Earth's large Moon gravitationally acts as an external torque which reduces the variations of the Earth's axial tilt; this results in damping the potential chaotic variations of the obliquity and as such keeps the obliquity changes of Earth relatively small compared with what they would have been without the stabilising effect of the Moon.

The Martian obliquity is generally affected by various factors. The level of impact of these factors on Mar's obliquity varies, however. The main impact on the Martian obliquity is that Mars lacks a large satellite like the Moon. Therefore, it does not benefit from the stabilizing influence of the Moon, and as such the Martian obliquity becomes free to experience much higher variation and be impacted by other factors that increase the chaotic nature of the Martian obliquity. This results in the planet undergoing large, chaotic variations in the Martian obliquity oscillations.

Below the factors which impact the obliquity of Mars have been divided into two groups based on their level of impact:

1) Main sources of effects: Solar gravitational torques and precession physics: Obliquity and precession follow the rigid-body equations defined by Kinoshita (1977), and these equations were later updated to be used for planets by Néron de Surgy & Laskar (1997) (Laskar et al., 2004).

In terms of precession physics, the Martian precession constant (α) depends on the planet's rotation rate, its dynamical ellipticity, and orbital distance (See Eq. 3 in Laskar et al., 2004). Also, the Martian spin axis is close to several spin–orbit resonances; this closeness amplifies the oscillations that the Martian obliquity experiences (Ward, 1973, 1974; Laskar & Robutel, 1993).

2) Negligible dissipative effects: Laskar et al. (2004) also evaluated other sources of impact, all with negligible effects. The top three, however, are:

a) tidal dissipation (following Néron de Surgy & Laskar, 1997; Correia et al., 2003),

b) core–mantle friction (Rochester, 1976; Pais et al., 1999), and

c) climate friction (Rubincam, 1990, 1993; Bills, 1999).

All of these were found to be too weak to significantly impact long-term obliquity relative to gravitational torques (Laskar et al., 2004).

To model the historical oscillations in the Martian obliquity, Laskar et al. (2004) chose a two-tiered approach, because the Martian obliquity proved to become more chaotic as the analysis went back in time:

(1) 0–20 Myr: Deterministic numerical integration

For this period, Laskar et al, (2004) performed direct numerical integration of the full Solar System using:

- a 9-planet gravitational model with general relativity (Laskar et al, cite Saha & Tremaine, 1994),
- Precession constants that were derived from Pathfinder and Mars Global Surveyor collected data (Laskar et al, cite Folkner et al., 1997; Yoder et al., 2003),
- a 1.82625-day timestep, and
- to reduce potential errors the initial conditions were compared to those of JPL DE406 numerical results (Laskar et al, cite Standish, 1998).

The approach showed that the Martian obliquity maxima and minima could have been between ~15° and ~35°, with a ~120 kyr cycle (Laskar et al., 2004 and references therein).

(2) Beyond 20 Myr: Statistical ensemble modelling

Beyond 20 Myr, the precision level showed degradation with small uncertainties causing exponential divergence, so the team leveraged statistical ensemble. They generated over 200,000 obliquity solutions to show that the probability of exceeding 60° for the Martian obliquity could be 63%, and 89% in the past 1 and 3 Gyr respectively (Laskar et al., 2004).

1.4.1 Martian Obliquity's Impact on Ice Deposition

As the deposition and sublimation of ices on Mars is directly influenced by the insolation values, understanding the magnitude and timing of Martian obliquity cycle variations becomes important. Laskar et al. (2004) discuss that low obliquity (<25°) shortens summertime and also reduces polar insolation (magnitude, not duration) year around, which increases CO_2 deposition and causing atmospheric collapse in the polar regions (Toon et al., 1980; Buhler et al., 2020). High obliquity (>40°) makes summertime longer and increases summer insolation which results in sublimation of CO_2 and H_2O in the polar regions. This change redistributes ices to the Martian atmosphere. Carbon dioxide ice may have a seasonal or diurnal cycle of deposition during these periods, but no substantial deposits are expected to form. For H_2O, molecules travel towards mid latitude regions, where, due to the lower level of insolation in winter, they could have potentially condensed on top of high-altitude areas (e.g., over Mt. Sharp in Gale Crater) (various sources, see Laskar et al., 2004 and the references therein).

During periods of higher obliquity, CO_2 layers may completely sublimate. When this occurs, the water ice particles within the CO_2 ice units could be left behind as a lag deposit, as the original CO_2 ice contained a small fraction of less volatile H_2O (under typical Martian surface pressures of about 600 Pa, CO_2 sublimates at temperatures around 148 K (Piqueux et al., 2015); a temperature less than water-ice sublimation temperature for that pressure). Should this occur, the water ice layers situated immediately above and below the vanished CO_2 layer would merge. Then, the cycle repeats itself: there is CO_2 (with H_2O particles) deposition, followed by CO_2 sublimation and the formation of the H_2O bounding layer (Figure 1.4). This process shows the dependency between Martian climate dynamics and the cryospheric structure (i.e., the frozen part of the climate system) and highlights the impact of obliquity in shaping the Martian subsurface. As a result of this process, multiple bounding layers in MCID likely indicate multiple periods of atmospheric collapse (Figure 1.4) in Mars' past (Manning et al., 2019; Buhler et al., 2019).

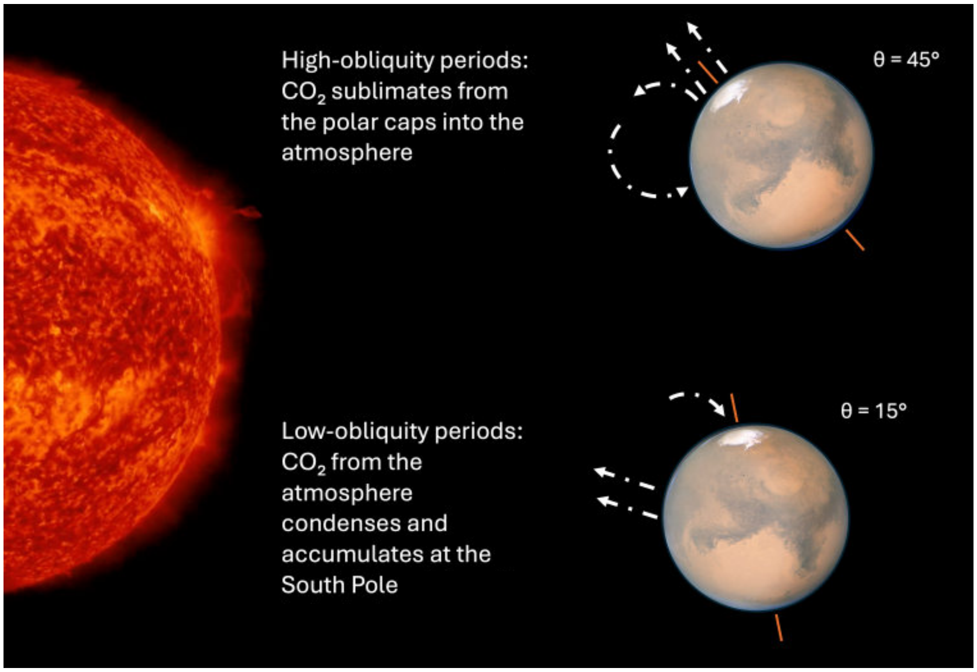

Figure 1.4 – The impact of the Martian obliquity changes to the transfer of the CO_2 *to the surface and back to the atmosphere.*

During low obliquity periods when the temperature goes down, CO_2 *transfers to the surface, an event that is generally referred to as atmospheric collapse. During the higher level of obliquity, warmer surface temperature causes* CO_2 *to sublimate and transfer back to the atmosphere. Due to the Martian surface pressure and the temperature variations,* CO_2 *cannot exist in liquid form and transfers directly back to the atmosphere (Piqueux, et al., 2015). Note that the Martian obliquity could go as high as 40 degrees, which in comparison to Earth's obliquity demonstrates a much higher variation.*

Buhler et al., (2020; 2001; 2023), through their models demonstrated the correlation between the theorical modelling used by Laskar et al. (2004) in determining the changes to the Martian orbital parameters and the timing of the formation of the MCID and its BLs (Figure 1.5).

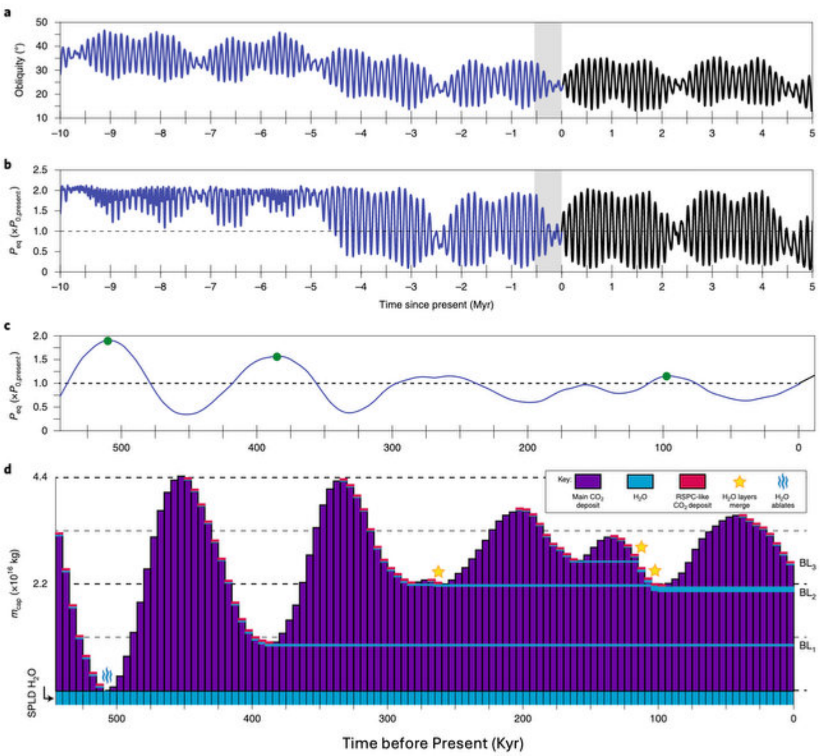

Figure 1.5 – The MCID formation and the Martian obliquity cycle

MCID formation began forming approximately half a million years ago. (a) The Martian obliquity from the past ~ 10 myrs has been mapped against (b) the Calculated equilibrium CO2 pressure in this timeframe. (c) a zoomed-in view of the pressure for the past 600 kyrs. (d) demonstrates the cycles of CO2 deposition and ablation. These cycles match the pressure change cycles. As CO2 ablates H2O particles within the CO2 unit stay back and form a water ice layer that will act as the bounding layer inhibiting the flow of CO2 ice (Buhler et al., 2020).

1.5 Massive CO_2 Ice Deposits - Background

The studies up to 2022 provided mathematical information about the MCID structure and attempted to explain the deposition of CO_2 and H_2O ice. In other words, they were focused on modelling and explaining the formation of MCID. These studies, however, relied on uniform atmospheric deposition (without the role of the glacial flow). Therefore, they were unable to explain the distribution and the shape of the structures as they are observed today. A study in 2022 done by Smith et al., used feature analysis and numerical modelling and explained the flow, distribution of CO_2 ice and the manner through which MCID ended up surviving the warm periods when the obliquity has been high in the past half a million years (Smith et al., 2022). This study showed that without glacial flow the thickness or the volumetric distribution of the CO_2 ice in MCID could not be well explained (Smith et al., 2022). One important input into this study was a more accurate understanding of the CO_2 ice rheology under Martian conditions.

1.6 Rheology of CO_2

Previous laboratory work to determine the rheology of CO_2 ice used dry ice under terrestrial conditions and made series of simplifying assumptions (no impurities, and no varying grain size) (Clark and Mullin, 1976; Durham et al., 1999). Later, Cross et al. (2020) performed much detailed laboratory tests and analysis and identified the details of the flow law, including the appropriate activation energy. Figure 1.6 is a table directly from Cross et al., 2020 which shows the results from this study in comparison with the previous studies. For detail information around the flow law parameters please see Appendix 2 (where the Arrhenius law is discussed) and Section 3.4.2 (where CO_2 flow law parameters are discussed). Cross et al. (2020) provided a better understanding of how CO_2 ice would behave under the Martian conditions, especially down the slopes, and enabled the later study of Smith et al. (2022) on the MCID, as well as the work done in this dissertation.

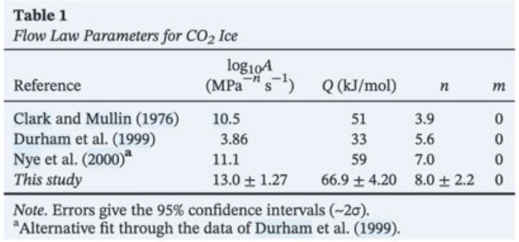

Table 1
Flow Law Parameters for CO_2 Ice

Reference	$\log_{10}A$ (MPa^{-n} s^{-1})	Q (kJ/mol)	n	m
Clark and Mullin (1976)	10.5	51	3.9	0
Durham et al. (1999)	3.86	33	5.6	0
Nye et al. (2000)[a]	11.1	59	7.0	0
This study	13.0 ± 1.27	66.9 ± 4.20	8.0 ± 2.2	0

Note. Errors give the 95% confidence intervals (~2σ).
[a] Alternative fit through the data of Durham et al. (1999).

Figure 1.6 – Flow law parameters for various studies.

"This study" refers to the work done by Cross et al., in 2020. This table is directly brought here from that work.

For their study, Smith et al. (2022) expanded an existing ice modelling tool, and incorporated the rheology of CO_2 under the Martian conditions, as defined by Cross et al. (2020). I will be explaining more about the modelling approach that they took in Chapter 5. Their study set out to address the open questions that the previous studied did not address, mainly:

1. Why are the CO_2 layers thicker within depressions (Bierson et al., 2016)?
2. How can one explain he current volumetric, thickness and mass distribution of CO_2 ice in the MCID?

Smith et al. (2022) demonstrated that deposited CO_2 ice will flow downslope into the valleys, where the ice is currently the thickest. This higher level of thickness, then, becomes the key factor for the deposit to survive the periods of high obliquity, high sublimation. Because here CO_2 ice would contain more mass than the expected ablation. On the other hand, CO_2 ice deposits at higher elevations (which are thinner) do not survive the ablation.

These all demonstrate the value of studying and understanding the formation, evolution, and dynamics experienced by the MCID. While Smith et al. (2022) demonstrated that the CO_2 ice units must have flowed down the slopes into the basins to survive the periods of high obliquity, and therefore addressed open questions, their work made one major simplifying assumption: it ignored the presence of water ice bounding layers.

Just as tree rings can help us determine the age of a tree, and by extension, the history of the environment and ecosystem and conditions under which it has grown, the bounding layers within the MCID offer chronological markers. Understanding these markers better and in more detail, including the timing of their formation, would provide a more accurate view into the timing and the conditions of the Martian atmospheric collapses. This, in turn, would offer a more accurate view into the Martian orbital variations and, consequently, the Martian climatic and geological evolution. Therefore, the omission of BLs in the 2022 study became the impetus for my work, motivating an approach for modelling stratified icesheets through this dissertation.

1.7 Gale Crater

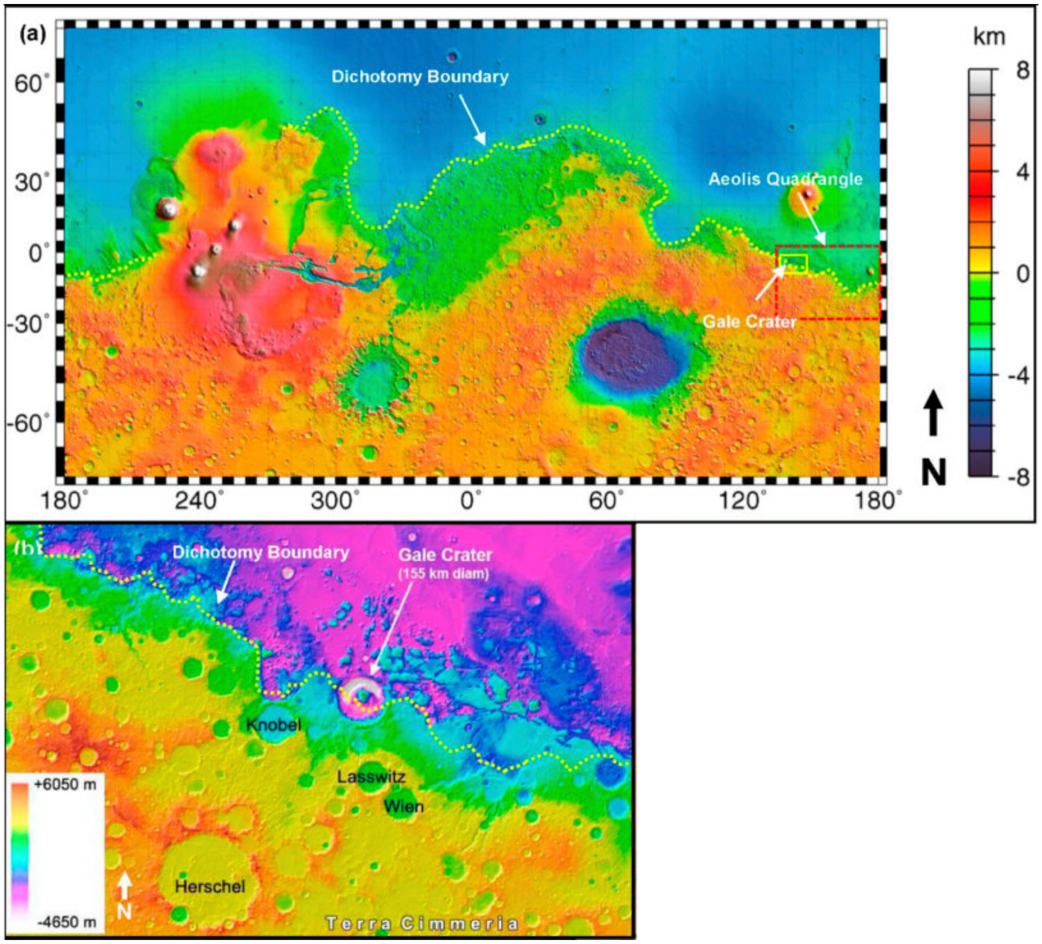

Figure 1.7 – Location of Gale Crater on Mars

This images from Williams et al., (2022) show Gale Crater is on the Martian dichotomy boundary. This boundary divides the planet into two hemispheres: the northern hemisphere that is generally smooth, flat, and contains younger geological features (as the age is estimated by counting the number of craters, this mean areas with less impact craters); and the southern hemisphere what is more heavily impacted by craters, indicating older regions.

(a) Mars 463 m/pixel context map – this is from Mars Global Surveyor Mars Orbiter Laser Altimeter (MGS MOLA). (b) inset (yellow box). This shows the crater location in respect to the dichotomy

boundary. Mt. Sharp is in the middle of the crater. Credit: NASA/JPL-Caltech/ESA/DLR/FU Berlin; Williams, J.M.

The ~155 km- diameter crater is located at 5.4°S 137.8°E, near the equator (Figure 1.7) and on the dichotomy boundary of Mars (Figure 1.7 shows and explains this boundary). Gediz Vallis is part of this crater that has been explored in detail by the Mars Science Laboratory (MSL) Curiosity rover (Figure 1.8B). The age of the crater is estimated to be 3.6 to 3.8 billion years, placing its formation during the Late Noachian to Early Hesperian period. Gale Crater features a central mound that rises roughly 5 km above the crater floor: Aeolis Mons, also known as Mt. Sharp. The sedimentary origin of Mt. Sharp remains a mystery. Published ideas about the formation of Mt. Sharp includes aeolian activity, volcanism, lacustrine deposition, and spring-related processes (e.g., Kite et al, 2013; Fairén et al., 2014; Williams et al., 2022 and references therein). There is a suite of surface features located within Gale Crater on Mars that suggest past ice accumulation, even though there is no ice existing within the crater today. Evidence of aqueous activity and former lakes is abundant and extensive in the crater. Previous studies suggest at least three distinct lake stands could have occurred after the formation of Mt. Sharp. Each of these would have existed for over 1,000 years (Palucis et al., 2016). These lakes would have been initially sourced by regional fluvial systems, from locations such as Farah Vallis (northeast of Mt. Sharp), and later by more localized hydrological inputs. Moreover, the Peace Vallis fan system (northwest of Mt. Sharp) may have been produced by sustained fluvial activity, and potentially from snowmelt, which would have transported sediments that formed the deposits observed at the Curiosity landing site (Palucis et al., 2014). There is also evidence of significant chemical alteration (Mangold et al., 2019), which includes the dissolution of minerals and formation of new minerals, due to aqueous interactions (Milliken et al., 2010;

Caravaca, et al., 2021; Chan and Netoff, 2017). This implies minerals would have interacted with liquid water over prolonged periods. Hughes et al. (2022) argue that canyon floors could reflect fluvial activity, landslides, and debris flows; by relying on the location, distribution, and the way the debris is sorted on the canyon floors. The floor of Gale Crater (known as Aeolis Palus) also reflects past water activity through fluvial and deltaic sandstones and conglomerates (Stack et al., 2019; Williams et al., 2022). Moreover, some recent published studies have also suggested that massive, buried ice could currently be present on the East side of Gale Crater (Fastook and Head, 2024; and Watters et al., 2024).

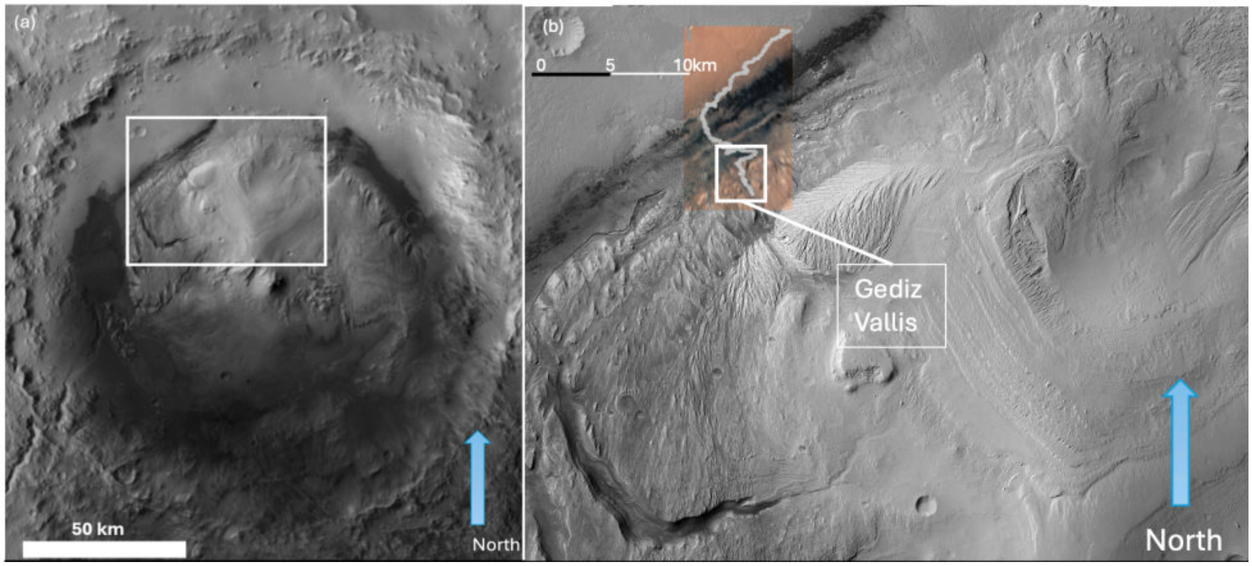

Figure 1.8 – Gale Crater Geographic Setting

(a) Gale Crater with rectangle showing focus area for this study. (Source: Context Camera Mosaic) (b) The region of interest for my work in this dissertation: Gediz Vallis. The path of Curiosity (up to sol 4042) is marked; it ascends into Gediz Vallis (Source: https://science.nasa.gov/mission/msl-curiosity/location-map/).

As mentioned in section 1.4, Laskar et al. (2004) reported probabilities of ~60% and ~90% for Martian obliquity exceeding 60° over the past 1 and 3 Gyr, respectively. These are periods that are more recent than the formation of Gale Crater and likely correspond to times when liquid water could have been stable at the surface. Such obliquity variations could have permitted periodic ice accumulation at low latitudes (Madeleine et al., 2009), particularly on high mountains such as Mt. Sharp (Forget et al., 2006). In their study, Madeleine et al. (2009) simulated ice accumulation across the northern hemisphere at an obliquity of 35°, finding rates exceeding 1 mm/yr within Gale Crater. As previously mentioned, Laskar et al. (2004) showed that this obliquity has occurred within the past 4 Myr, raising the possibility that ice accumulated on Mt. Sharp during the geologically recent past.

Considering the age of Gale Crater, as well as the long-term variability in orbital parameters, accumulation of considerable ice deposits would have been likely in several points in the past. Given the current orbital values, ice is currently unstable on the surface of Mars except for in polar regions; however, Mellon and Sizemore (2022) suggest that: […ground ice] "*would have been stable at all the landing sites for extended periods of tens of Kyr when the obliquity exceeded about 29º–33°*." Those values were quite common until 5 Myr ago, and some ice could have persisted for the duration of half of an obliquity cycle, perhaps more than once during the most recent 5 Myr. These arguments support the notion that Gale Crater would have experienced major environmental changes and possibly was mantled with thick, flowing ice as recently as early as 5 Myr ago, when the average obliquity was higher. Le Deit et al. (2013), following studies conducted by Anderson and Bell (2010), proposed a glacial hypothesis for the evolution of lobate features on the flank of Mt. Sharp. This hypothesis suggests that ice accumulation occurred on Mt. Sharp and that the associated glacial and periglacial processes led to diverse landforms. This has motivated various studies to investigate the potential existence of ice in the crater (Fairén et al., 2014; Williams et al., 2022). Fairén et al. (2014) use high-resolution images from orbit to describe potential glacial, periglacial, and fluvial (including glacio-fluvial) landforms within the crater, as well as the potential existence of past ground ice and ice-related lakes high up on Mt. Sharp. Williams et al. (2022) presented the first ice flow modelling results to help describe rock glacier-like features on the northeastern slopes of Mt. Sharp. They modelled the shape of these forms to constrain their potential formation times and flow rates.

The hypothesis that water-based glaciation specifically contributed to the formation and/or preservation of Gediz Vallis, and other Valles and features around Mt. Sharp in Gale Crater can be tested using advanced modelling as long as the modelling approach can be used on the Martian settings and is capable of ensuring the material properties are temperature sensitive. The modelling will need to be supported by the observable features (especially those captured by the Curiosity Rover).

1.8 Icesheet Modelling

As planetary studies continue, one practical way to learn about different processes occurring on a planet is to leverage modelling. To highlight the value of icesheet modelling, we can look at an excerpt from the first chapter of *The Physics of Glaciers* by on terrestrial glaciology, where Cuffey and Patterson (2010) highlight the challenges in management and conducting terrestrial glaciological studies:

"*…Understanding of glaciers has improved dramatically over the past half-century or so… [with an] abundance of information now available to evaluate theoretical models. Yet the deep inadequacies of the science should be kept in mind. Observation of the glacier bed remains a very difficult task. Interpretations of such data are usually tenuous… Drilling boreholes in ice sheets is expensive and time-consuming; it is rarely done for dynamics studies... Keeping track of year-to-year variations in melt and snowfall […] requires a consistent commitment of resources… Geological reconstructions of past ice incursions provide the best hope for validating numerical models…*"

Adding the exotic aspects of ice sheets on non-terrestrial settings, as it is the scope of this dissertation, further increases the difficulties faced by scientists, because there are even fewer opportunities for direct ground observation; and the vast distances introduce substantial cost and logistical challenges, for ground, or orbital observations, and for tracking temporal variations. For example, drilling boreholes into the ice shells of Europa remains a technological goal for the future rather than a present-day capability. These challenges even further promote the use of modelling for studying ices on other planets.

The Jet Propulsion Laboratory (JPL) at NASA has developed a software application to model the flow of ice masses and their thermal characteristics on terrestrial settings (Larour et al., 2012). This open-source software is called the Ice-Sheet and Sea-Level System Model (ISSM). For my work and past work (Smith et al., 2022), this software was extended to model ice accumulation, flow, and associated thermal properties, for non-terrestrial settings, including the capability to simulate flowing carbon dioxide ice (Smith et al., 2022) and to incorporate temperature dependent material properties as catalogued by Fard and Smith (2023). ISSM uses the finite element method (FEM) to solve for stress and temperature distributions within ice masses in three dimensions (Larour et al., 2012). The FEM approach requires subdividing a large solid block of material into smaller, manageable "elements" connected at "nodes," and forming a "mesh" over a "domain." Then, the governing differential equations (i.e., stress balance equations) are setup and solved numerically for every node in the model. ISSM solves these equations natively in a Full Stokes (FS) mode. This is the most computationally intensive approach. Alternatively, ISSM can reduce the complexity by using various approximations in solving the equations. The Blatter-Pattyn approximation (BP) (Blatter,1995; Pattyn, 2003), also known as the BP-Higher Order (where HO is referred to in this dissertation, it means the BP Higher Order approximation, as the BP approach is the only type of Higher Order approximation being used here), much like FS, is a 3-dimensional approach to modelling icesheets. To simplify the FS approach, HO assumes that the velocity in the vertical direction is much smaller than the velocities in the x-y plane, so that it can be ignored during the calculations without a major impact on the model results. HO is computationally intensive, but less so than FS. The complexities and horizontal scales involved in the three regions of interest motivate the use of a high-resolution mesh and a HO approach to solve the differential equations in the ISSM model.

The main ISSM website (https://issm.jpl.nasa.gov) covers details of how to use ISSM, and its toolset. A detailed set of tutorials as well as the available support is also highlighted on the website. ISSM is supported by series of well-written publications. A comprehensive list of these can be found here: https://issm.jpl.nasa.gov/publications/. The ISSM class model is accessible through *https://issm.ess.uci.edu/doxygen/chtml/index.html*. This section summarizes part of the ISSM capabilities (see Larour et al., 2012; Seroussi et al., 2019; Larour et al., 2012; *ISSM Documentation*, and the references therein)

Note that the purpose of this dissertation is not to compare the capabilities currently offered by ISSM with those of other glaciological modelling tools that are in existence at the time of this writing. Many of the features introduced above might also be offered by other commercial or open-source products, and the purpose of this section is not differentiate ISSM, promote it, or position its capabilities such that it might be misconstrued that such features might solely be offered by ISSM.

1.8.1 Thermal Balance

ISSM includes a three-dimensional thermodynamic model. Such model solves the advection-diffusion equation based on the internal temperature of a block of ice. In such models, heat is transferred by internal conduction through the block, and then by advection during the flow and movement of the ice. For the model, the thermal boundary conditions are applied at both the surface and base. The surface temperature can be set to a value that generally represents the mean annual air temperature; at the bed, however, the geothermal heat flux determines the boundary values. If there is sliding at the base of the block of ice, the heat caused by the friction will be added to the heat at the bed. This way ISSM captures the thermal profile of a block of an ice, including warming from internal strain and geothermal input from below as these impact the ice viscosity and flow dynamics through thermomechanical coupling.

1.8.2 Mass Balance

ISSM, like many other available tools, uses the conservation of mass law to maintain the growth or shrinkage of ice mass during a modelling period. The conservation of mass connects the ice-thickness evolution to ice flow divergence and external mass balance forcing. ISSM uses "surface mass balance, or SMB" as a means of imposing the net accumulation (or ablation) on surface of a block of ice. Positive SMB represents accumulation; negative values represent ablation on the ice surface. This way, ISSM accounts for the gains or losses of ice mass in the model geometry, before proceeding to solving the model for that time period.

1.8.3 Numerical Methods

As mentioned ISSM uses the finite-element method to model thermomechanical ice flow. ISSM can use a variety of approaches to solve the stress balance in 3D using the Full Stokes (FS) equations for glacier flow. FS is the most accurate and yet computationally intensive approach.

The Full Stokes set of equations include various parameters including the gravitational, centrifugal and the Coriolis forces that act on an icesheet. The first two forces can be considered related as the gravitational force ($\vec{f}$) can be defined as density times the gravitational constant or:

$$\vec{f} = \rho\vec{g} \qquad eq.\ 1.1$$

The Coriolis force is a function of the ice flow velocity ($\vec{v}$) and the planet's angular velocity ($\vec{\omega}$). As the ratio of the Coriolis force to pressure gradient on Earth can be shown to be negligible, the Coriolis term can be ignored as a force acting on the icesheet (Greve and Blatter, 2009). This is an assumption in ISSM, that is carried over into MIDAS.

Using Full Stokes, ISSM solves for the icesheet stress balance with the associated differential equations and provides the velocities in three directions (i.e., x, y and z), as well as the pressure. ISSM also offers other approaches to solve models which leverage different levels of approximation. The higher-order (HO) 3D model (also known as the Blatter-Pattyn first-order approximation) keeps longitudinal and vertical shear stress components while assuming nearly hydrostatic vertical stress equilibrium (Blatter, 1995; Pattyn, 2003). The HO approach provides a good compromise, capturing much of the 3D stress state of the ice at lower cost than FS. For even greater efficiency, ISSM offers the 2D Shelfy-Stream Approximation (SSA). SSA assumes horizontal velocity does not vary with depth (Morland, 1987; MacAyeal, 1989). This assumption while reduces the accuracy of the results in comparison to HO or FS methods, greatly improves the efficiency of the calculations. As SSA treats the ice as a single "shelfy-stream" layer, it becomes a rather appropriate method for solving models that include floating ice shelves or fast-sliding ice streams where flow is dominated by basal motion.

ISSM also offers Shallow Ice Approximation (SIA) method to solve the stress balance model. As Full Stokes equation is very resource intensive, each method (HO, SSA and SIA) increases the approximation level and as such, computationally, is less resource intensive. For the use of MIDAS libraries, while all approaches can be used, HO is recommended as it captures the 3D stress, it is not as computationally expensive as FS, and also that, it is considered more accurate than SSA and SIA approaches. There is substantial body of literature covering the mechanics of glaciers. For the sake of completeness, a summary of the relevant mathematics, including further reviews of the four approximation methods above, has been collected in Appendix 1.

1.8.4 Different Stress Balance Formulations

Accurately modelling the evolution of Martian ice deposits requires an approach that captures the full three-dimensional stress and temperature structure of the system for various reasons:

The Massive CO_2 Ice Deposits (MCID) are not vertically uniform. The alternating units of CO_2 and H_2O ice have vastly different sensitivity to stress, and as such they have different viscosities. They also possess different activation energies and thermal conductivities. These stratified layers interact mechanically and thermally and influence internal shear, vertical heat transport, and basin-scale deformation. Moreover, the thicknesses of these units vary from one location to the other, therefore, the impact of all nodes will have to be considered. The

Higher-Order (HO) formulation retains both vertical shear stresses and depth-integrated longitudinal and transverse stress gradients. This level of fidelity is required to assess how CO_2 flows into basins, how bounding layers inhibit the flow, and therefore how the deposits evolve under orbitally controlled accumulation and ablation cycles.

The Shallow Ice Approximation (SIA) collapses the stress balance into a shear-dominated, two-dimensional framework. SIA assumes homogeneous rheology, negligible horizontal stress transmission, and flow guided only by local surface slope. In a stratified system such as the MCID, this simplification inherently merges all layers into a single effective material. This will eliminate the rheological contrasts that define the system's behaviour. It stands to reason that in 2-D, SIA would misrepresent stability, and lateral fluxes. Moreover, the locality that is inherent in SIA does not allow for the integration required across the ice unit that MCID requires. These contrasts will be further explored in sections 4.6.1 and 5.2.4.

1.9 Objectives

As mentioned earlier, the motivation for this dissertation stemmed from the continuation of the work done by Smith et al. (2022) in modelling and understanding the glaciological behaviour of the MCID (see section 1.3). Complexities inherent in the MCID structure calls for the use of three-dimensional models to capture the details of the topographical features and analyze the stress, strain and velocity of the flow in at least two directions, and on various virtual plans, stacked on top of each other (Figure 1.9). Smith et al. used ISSM with the topography and basal characteristics of the CO_2 deposits (from Putzig et al., 2018) and ran their models for 600,000 years without the inclusion of the water ice bounding layers. As MCID is stratified, the ice deposits need to be handled more properly to provide an accurate characterization of the MCID over hundreds of thousands of years.

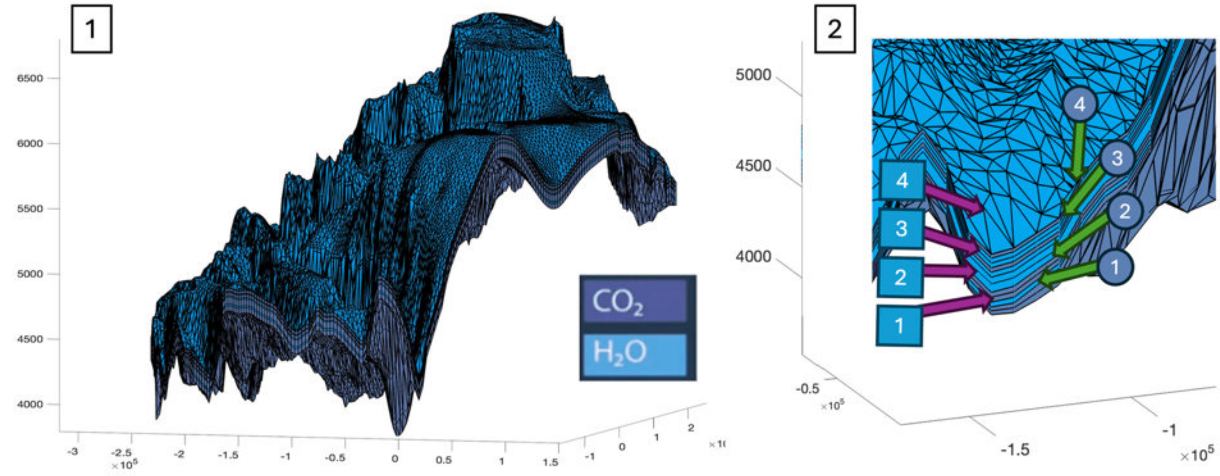

Figure 1.9 – Multi-unit ice gridded mesh in MIDAS

(1) ISSM's upgrade to support multi-unit, multi-ice 3D models of ice deposits. At present, the CO_2 *ice cap in the south pole of Mars can be modelled with alternating layers of* H_2O *ice and* CO_2 *ice. This figure demonstrates the gridded mesh of the south pole of Mars as set up in MIDAS, with alternating layers of water and CO2 ices. (2) A zoomed-in view to demonstrate the multiple units of ice managed by MIDAS. As a result of alternating units of ice, determining the rheological law governing the entire model will be a complex undertaking; however, finite elements method allows parameter values for each grid of mesh to vary. They are determined and applied for each grid cell locally before the stress, deformation and velocity of the entire domain is solved.*

This dissertation focuses on providing a new tool and approach of modelling ice growth and presents the development and application of changes to ISSM, so there will be fewer simplifying assumptions to be made during modelling of an icesheet made up of exotic compounds and located on other planetary bodies. This approach is called the Multi-unit Ice Deposits Analysis and Simulation (MIDAS).

1.9.1 What Does MIDAS Do?

MIDAS augments ISSM with the capability to:

(1) Simulate icesheets composed of multiple materials (with different rheological properties), including N_2, CO_2 and H_2O,

(2) Function under conditions from other planets such as Mars and Pluto, and

(3) Apply temperature-sensitive properties such as density, thermal conductivity, and latent heat of fusion on non-terrestrial settings.

ISSM, out of the box, assumes static ice properties, significantly limiting its predictive accuracy for planetary conditions where temperature gradients are often substantial. (ISSM always treated rheological laws as temperature dependent) MIDAS addresses this limitation by using material properties based on local (temperatures within each mesh cell) temperatures and will re-calculate those throughout the icesheet, to offer a much more realistic model of internal stress and flow. The equations used are detailed in 'Properties of water, carbon dioxide, and nitrogen ices in planetary surface environments' (Fard & Smith, 2023).

As offered by ISSM, MIDAS, too, uses a range of methodologies to solve icesheet models, including Full Stokes (FS), Higher Order (HO), Shallow Shelf Approximation (SSA), or a combination of them across specified sections of a gridded mesh, to solve differential equations.

Once MIDAS was operational, and had been fully tested, I used it on different separate scenarios:

(1) Focusing on three locations in Gale Crater (homogeneous water ice-based glaciers on Mars with temperature sensitive material properties, using adaptive grided mesh, under two ice accumulation scenarios). Gale Crater presents an opportunity to examine the possibility of past

ice. For Gale Crater, my focus has been on Gediz Vallis, where the Curiosity has offered (and continues to offer) a wealth of knowledge directly from the ground. While current surface observations by the Curiosity rover have not directly detected subsurface ice, the morphologies, slope distributions, and spatial arrangements of these features resemble remnants from glacial observed in mid-latitude terrestrial regions. Given its proximity to Mars' equator, modelling potential ice formation and flow in Gale Crater can enhance our understanding of Mars' water cycle over time, focusing on areas like Gediz Vallis and the eastern side of Mount Sharp (see next Chapter for further information). This case study is not a multi-unit ice analysis. However, it leverages the use of MIDAS on Mars with temperature sensitive material properties.

(2) Partial MCID for its entire age, which used MIDAS's full functionality. In this dissertation, using MIDAS, I have modelled the formation of the bounding layers with sublimation for the first time and incorporated the variable material properties in the development of parts of the MCID. Results from these simulations demonstrate how the bounding layers formed, and how these layers inhibited the flow. In the future the expansion of these simulations to the north polar layered deposits (NPLD), which is also composed of stratified ice and dusty layers, will further scientific insight into the climatic variations of the planet.

1.10 Contributions of this Dissertation

My research presented in this dissertation aims to continue the journey in reducing the knowledge gaps in, and advancing scientific understanding of Martian glaciology. My main objective is to help with reconstructing the past history of Mars.

Martian water and CO_2 cycles are of paramount importance to understanding past, present and forecasting the future climate, atmospheric pressure evolution, potential habitability, and long-term surface processes. Here, for the first time, I present a 3-D, simulation framework that can be used to evaluate the formation, and flow dynamics of CO_2-dominated ice. Prior studies of the Martian CO_2 Ice Deposits (MCID) and mid-latitude glaciation relied mainly one- or two- dimensional thermal models, or qualitative comparisons between landforms and expected ice-flow patterns. As presented in this dissertation my research supports:

1. Quantifying the Thermo-dynamical Role of H_2O Bounding Layers within the MCID

One contribution of my work is the demonstration that water-ice bounding layers in the MCIDs control the stability of CO_2 glaciers. My simulations, presented in this dissertation, show H_2O layers:

- increase the overall viscosity and stiffness of MCID glaciers.
- reduce basal temperatures by enhancing vertical thermal conduction.
- reduce the basal shear strain and slow the overall flow of the glaciers.
- support the retention of CO_2 even during high-obliquity periods.

These results expand on the previous understanding of the MCID structure, and why the MCID has survived multiple obliquity cycles and why observed SHARAD radargrams is consistent with long-term stability (Smith et al., 2022).

2. First-Order Test of Glacial Flow at Gale Crater

The simulations of the Gediz Vallis system provide the first 3-D numerical modelling (using Higher Order stress balance formulation) and examine the proposed glacial hypothesis at Gale Crater: if ice existed on Mt. Sharp, would its flow directions have been aligned with the features observed in Gediz Vallis and be a participant in the processes forming the valley? The results presented in this dissertation show that, when modelled:

- Ice formed on Mt. Sharp flows downslope into Gediz Vallis, and follows patterns that are consistent with mapped landforms.
- Flow directions of modelled ice are aligned with the observed features.

The modelling results, therefore, support the glacial hypothesis.

1.11 Dissertation Structure

Following the introduction, chapter 2 (next chapter) introduces the changes and the mechanics of MIDAS. In this chapter, first, I will provide foundational knowledge on ISSM, before providing a detailed review of the methodology behind the MIDAS framework, its implementation within ISSM, and the improvements it introduces over existing modules and libraries. The interested reader can find a high-level view of the glacial mathematics in the appendices: Appendix 1.

Chapter 3 will discuss the temperature sensitive equations for the material physical properties, and how I have arrived at the equations. The interested reader can find the definition of these properties in the appendices: Appendix 2.

Starting from chapter 4, I will present scientific case studies for which I have used MIDAS to investigate specific scientific questions related to Martian climate history and glacial dynamics. These two case studies have been selected specifically with the aim to contribute to the ongoing modelling efforts and examining existing theories. These are the practical application of MIDAS in two distinct Martian regions.

Chapter 4 provides an analysis of potential glaciers within in Gediz Vallis - Gale Crater. I have compared the modelling results against newly captured evidence from Vallis. This case study sets the context for the next case study where the multi-unit capabilities of MIDAS is employed.

Chapter 5 demonstrates the use of MIDAS in the modelling of partial MCID. After detailed analysis of the results, I will discuss what we learn from this modelling, as this is the first time that MCID with the water ice bounding layers are being modelled. Appendix 3 provides some background data to support this chapter further.

Finally, chapter 6 concludes the dissertation by summarizing key findings, reflecting on methodological advancements, and outlining future research avenues. This chapter will discuss how MIDAS can be further improved and also be applied to other use cases.

Beyond Chapter 6, this dissertation includes three appendices. As mentioned earlier, Appendix 1 provides a brief overview of the mathematics underlying glacial dynamics. It begins with general and foundational concepts before outlining the required formulations. While these materials are available through various sources, they are presented here for completeness.

Appendix 2 provides foundational definitions of key terms and properties used throughout this dissertation. Its purpose is to assist the reader in locating the necessary definitions as they appear in the text.

Finally, Appendix 3 provides further supporting materials and tables for Chapter 5.

Overall, this dissertation aims to provide tools that can help advance the understanding of ice dynamics and climatic evolution on planetary bodies, offering insights into planetary processes that can inform future exploration and improve our ability to interpret past, present, and future planetary environments.

2 3D Icesheet Modelling

2.1 ISSM/MIDAS Upgrade Summary

2.1.1 Contributions of this Work

Here, I present a summary of the changes I made to ISSM, to augment the tool and provide a modelling toolset and framework for modelling exotic ices. These include (1) temperature dependent material properties (other than the flow laws that are already temperature dependent in ISSM), (2) flow laws for N_2 and CO_2 ices, and the capability to easily add new ice materials (3) planetary properties, and the capability to easily add new planets or moons, and (4) the capability to analyze stratified ice units. The changes have been coded and developed by me.

2.1.2 3D Icesheet Modelling

Ice-sheet and Sea-Level System Model (ISSM; the hyphens are used to follow the branding of the product) is a 3D thermomechanical software solution that is developed by an international community of collaborators, and it is supported by NASA’s Jet Propulsion Laboratory (JPL). ISSM has capabilities to enable full 3D thermal and dynamical analysis of ice flow. ISSM was developed specifically to analyze and model water-based glaciers on earth. It, as a software package, includes about 2400 files, covering about 300,000 lines of code (see *https://issm.ess.uci.edu/doxygen/chtml/index.html*) and offers:

1. Anisotropic spatial mesh refinement, allowing to leverage higher resolution of spatial mesh in specific areas of interest while conserving computational resources by allowing to use lower resolution mesh in other areas,

2. Finite Element Modelling of analyzing and solving differential equations in unstructured and adaptive meshes,

3. Advanced ice dynamics models such as Higher-Order and Full Stokes, as well as more commonly used approaches of Shallow Ice Approximation (SIA) and Shallow Shelf Approximation (SSA),

4. Thermal balance as well as stress balance and associated calculations,

5. A suite of sensitivity analysis tools,

6. Inverse methods, which leverages data from observations to estimate unknown variables, and

7. The use of parallel computing technologies, with optional utilization of state-of-the-art clusters and supercomputers.

For further information see https://issm.jpl.nasa.gov, as well as relevant publications including Larour et al. (2012).

To model icesheets in 3D and to determine the differential stresses and temperatures across an ice deposit, ISSM sets up the icesheet model as a gridded mesh in 3D (Figure 1.9). The mesh consists of elements, with each corner of an element corresponding to a node. ISSM assigns the thermodynamical differential equations to each node in the model and uses Finite Element Method (FEM) to solve these equations. The results from the discretized differential equations will describe the flow of the modelled ice deposits. FEM incurs a higher computational cost relative to modelling methods. however, ISSM results provide more accurate ice flow predictions in comparison to 1D and 2D modelling tools (Larour et al., 2012). One limitation of this approach, however, is that ISSM treats an icesheet as a block of homogeneous water ice. Note that many of functionality offered by ISSM might also be offered by other tools.

ISSM was successfully used in targeted cases on Mars by Smith et al., (2022) to model CO_2 ice flow and in Arnold et al., (2022) to investigate flow within H2O glaciers. This work resulted in the expansion of ISSM to function in the Martian environment (through the introduction of appropriate temperature, gravity, geothermal flux, and other planet specific properties) and to use CO_2 ice rheological flow laws properly (through implementing the rheological parameters provided by Cross et al., (2020)). As introduced earlier, the rheology of CO_2 ice has been the subject of different laboratory experimentation, and these laboratory-based studies on the deformation of CO_2 ice, when done under conditions similar to those of Martian polar regions, generally demonstrated that the CO_2 ice tends to be up to 2 orders of magnitude weaker than H_2O ice (Cross et al., 2020).

To continue developing ISSM for extraterrestrial locations and exotic ices, we must consider existing limitations. ISSM considers the following foundational assumptions:

1. An icesheet represents a uniform mass of material, maintaining a consistent chemical composition throughout its expanse.

2. The density, latent heat, thermal conductivity and heat capacity of an icesheet leveraged static numbers regardless of the temperature regimes in which the icesheet existed.

To address these limitations, we started the work on ***M***ulti-unit ***I***ce ***D***eposits ***A***nalysis and ***S***imulation (MIDAS) as a set of software libraries to augment ISSM. Using MIDAS a researcher can model and simulate the formation of exotic ice types and configurations (e.g., N_2, CO_2 based glaciers, stratified glaciers) on a planetary body with alternating material types. In this dissertation,-MIDAS is being used to three-dimensionally model the formation of CO_2-H_2O (or other types of exotic-based ice units) layered icesheets that vary in rheology with respect to depth and temperature. MIDAS and ISSM accepts input from 1D models to test flowing ice scenarios. In short, MIDAS can handle stratified icesheets, allowing rheological contrasts at vertical mesh layers, which affect shear distribution and basal stress. In contrast, ISSM can only treat homogenous icesheets.

An additional functionality in MIDAS is the use of temperature-dependent material properties (such as density and thermal conductivity) instead of relying on constant values across broad temperature ranges (note that ISSM already used temperature dependent rheology). Since MIDAS uses ISSM to solve the differential equations dictating icesheet evolution, the same stress balance methodologies offered by ISSM are available to users, including Full Stokes (FS), Blatter–Pattyn Higher Order (HO), Shallow Shelf Approximation (SSA), or a combination of them across specified sections of a gridded mesh.

MIDAS also introduces other minor changes to ISSM, including routines to convert between Cartesian coordinates (metres) and geographic coordinates (degrees of latitude and longitude) on Mars and Pluto. Additional plotting functions for multi-unit ice sheets and cross-sections were also developed and used to generate several figures in this dissertation.

While such modifications might appear straightforward under terrestrial glaciological conditions, where temperature ranges are narrow and close to the melting point of H_2O ice, the situation is rather different for exotic ices. For CO_2, N_2, and other volatile ices, these material properties such as density, latent heat, thermal conductivity, and heat capacity vary significantly with temperature across ranges relevant to Martian and outer solar system environments (See the next Section).

2.1.3 A Note on Validating the Mesh Structure

For numerical stability and to validate the spatial resolution of a mesh, the Courant–Friedrichs–Lewy (CFL) criterion should be applied to a mesh. ISSM/MIDAS can use adaptive time stepping and adjust to the CFL criterion. However, this is a time consuming and resource intensive process; it is recommended that the time step as well as the spatial resolution is devised using this criterion prior to starting the modelling process.

For this, an evaluative simulation can be run to provide a high-level view of the velocity values for each time period. Then, the CFL criterion (i.e., $\Delta t < CFL \times (\Delta x / |u|)$, where Δx is the local element mesh size, $|u|$ the local modelled velocity magnitude, Δt the time step and CFL is the constant, generally considered to be 1) can be used for each time period. Mesh refinement can be iterated until all (or at least a good majority of) elements satisfy the CFL constraint under the largest expected velocities. This way one can ensure the thermal, mechanical, and mass-flux solutions remain stable, and temporally convergent. This also protects the results from formation of numerical artefacts. If a few time periods remain violating the CFL constraint, ISSM will try to overcome the issue using its own internal process.

2.1.4 MIDAS Development and Methods

Upgrade Guiding Principles

To extend the modelling of ISSM for a greater variety of applications, the following guiding principles were used:

1. Maintain the full set of functionalities offered by ISSM;

2. Generalize ISSM modelling capability for other planets and exotic ices; this is to provide the rheological laws for different ice compounds with various non-terrestrial environments (gravity, angular velocity);

3. Continue to leverage multiple cores (i.e., CPUs) of computer clusters to solve models; and

4. Expand tools and techniques offered by ISSM, only required for simulating transient icesheet models.

Upgrades Summary

Overall changes that MIDAS introduce can be considered as a wrapper around ISSM (Figure 2.1). The changes include new modules in the MATLAB codebase of ISSM, these are discreet library files that will require the updated (and MIDAS) enabled version of the backend to function. This approach enables MIDAS to leverage other functionality that ISSM offers, while as a wrapper, MIDAS manages the structure of the icesheet with multi-units of different material types. In short, changes provided are both in the front end (i.e., MATLAB) and backend of the ISSM toolset.

ISSM provides various front-end services: other than MATLAB, it exposes Python and Javascript based front services. However, when my work on MIDAS started ISSM, offered its most comprehensive set of services through MATLAB. Hence, I began my work on MATLAB. In future, MIDAS functionality can be ported into Python or Javascript as well.

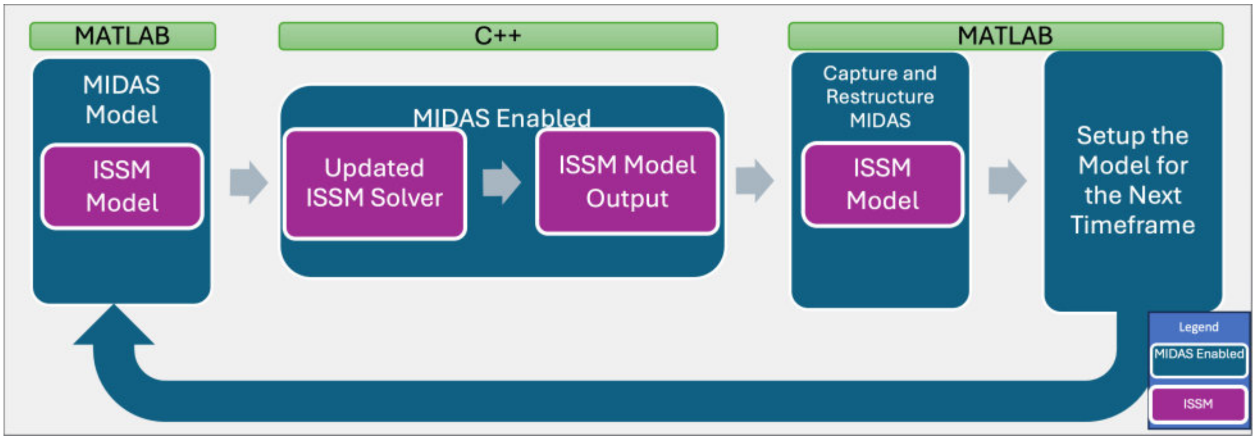

Figure 2.1 – MIDAS creates a wrapper around the ISSM by adding the multi-unit capability. This model is then sent to the solver which will recognize the augmented information and will solve the model appropriately. However, the overall process to generate the results has not changed, and the final result will have to be used as the starting point for the following time period.

Using MIDAS for Icesheet Modeling

MIDAS provides a structured workflow for setting up and running 3D thermomechanical icesheet models for stratified ice deposits with different material types in non-terrestrial environments. MIDAS uses a forked version of ISSM, that can be found here at *https://github.com/KBF-I/MIDAS/tree/Gen-1*. Installing and setting up MIDAS is the same as ISSM. However, the subfolder called MIDAS will have to be added to MATLAB path. While ISSM offers interfaces to MATLAB and Python, MIDAS only offers MATLAB interface. Having set up ISSM, and to use MIDAS, one can follow these steps in MATLAB.

1. Initializing a Model

To start a MIDAS simulation, initialize a new model using the modelmulti_Ice class:

```
model = modelmulti_Ice ();
```

This automatically configures model settings for multi-layered icesheets.

2. Defining Model Domain & Mesh

Defining the area domain and resolution will be the same as in ISSM. However, to properly initialize the modelling environment, use the following command. The currently acceptable bodies include EARTH, MARS, PLUTO, EUROPA, but the support can be extended to other planets by adding to the modelmulti_Ice library.

```
model = modelmulti_Ice.setPlanetMoonProperties('MARS');
```

At this point, we can continue with parameterization of the model, as it is done in ISSM.

3. Extruding the 3D Icesheet Model

Once a 2D mesh is generated, MIDAS transforms it into a 3D stratified model. This is done differently from ISSM that uses the “extrude ()” command:

```
model = extrudeModel (model, 1);
```

The second parameter indicates the extrusion approach. Value "1" indicates multi-unit, and value "2" indicates single unit extrusion. In ISSM, the number of vertical mesh layers used to build the 3D mesh is specified directly by the user. In MIDAS, however, the number of layers is determined by the thickness of the ice mass, within a range of values, since the icesheet may be composed of several distinct ice units. MIDAS defines the range such that the minimum number of layers per ice unit is always two (top and bottom mesh layers; see Figure 1.9 (2)), while the maximum of mesh layers in an ice unit is set by the user (or defaults to five if no value is provided – specifically for modelling MCID, five mesh layers demonstrated (through various tests performed) a good trade-off between performance and capturing the fine features on the slope of South Pole of Mars). During extrusion, MIDAS selects the appropriate number of layers from this range, based on the unit's average thickness. For every increment of average thickness (user-defined, with a default of 25 m – again a number selected purely for the use of MIDAS on the South Pole of Mars), the number of layers increases from the base value of two up to the maximum allowed. As the model evolves, the number of layers assigned to a unit can therefore change over time. Once the layer count is determined, each ice unit is extruded separately, using ISSM's logic to generate the full 3D multi-unit ice sheet. Note that predefined "default" values can easily be modified in settingsmulti_Ice.m file.

In short, MIDAS determines an appropriate number of layers based on the average thickness of a unit of ice and will assign the number of layers accordingly to the ice unit. As such, as the model evolves, the number of layers for a unit might change over time. The actual construction and handling of the vertical grid, however, are performed by ISSM. In ISSM each layer is represented as a fraction of the total ice thickness (σ-coordinate system), meaning that the vertical spacing (Δz) scales proportionally with the local ice thickness rather than being fixed in absolute distance. Consequently, thinner ice columns automatically have smaller absolute layer thicknesses, and thicker regions have proportionally larger ones.

4. Configuring Surface Mass Balance (SMB) & Climate Parameters

SMB inputs in ISSM (and therefore in MIDAS) define accumulation rates per node over time. These inputs can be set via parametrized input files. The SMB values can be static or vary through time and space, depending on the year of the model and the location of a node. These can be positive (i.e., accumulation) or negative (i.e., ablation) and be from any of CO_2, H_2O or N_2. MIDAS interpolates SMB values (in the x-y plane) if input data and surface coordinates do not align. It should be specified that it is also possible to change SMB according to its height if the SMB is assumed at a specific elevation (i.e. sublimation would be a different value at different elevations).

To apply SMB the addNewUnit function is used. This function will determine if the SMB of a new material type and a new unit need to be created, or if SMB should be applied to an existing ice unit.

```
md = md. multiIceMesh.addNewUnit(md, tempUnit, periodSMB);
```

where periodSMB is an array of SMBs; and tempUnit is a new unit of ice and is created and can be initialized using:

```
tempUnit=stratified_unit ();

tempUnit.Bed        = …           the elevation of the ice unit’s bed

tempUnit.Surface    = …           the elevation of the ice unit’s surface
```

tempUnit.IceType = …   *ice type such as CO_2*

tempUnit.ID   = …   *an identification number assigned to the unit*

Note that the bed and the surface are setup the same way that the bed and surface of the icesheet is setup in ISSM.

Surface temperatures can be defined for different time periods using preloaded climate data.

5. Material Properties

MIDAS assigns material properties at the element level to enable transition across ice layers. Unlike ISSM, which assumes static ice properties, MIDAS supports temperature-dependent density, latent heat, thermal conductivity and heat capacity for icesheets.

The matmulti_ice.m script defines these properties for N_2, CO_2, and H_2O ice by default. Researchers can modify or extend this file to include additional materials like CH_4, CO, or H_2O with dust/rock; or replace the equations that are currently used in the file.

MIDAS, through the matlmulti_ice class, exposes various methods to retrieve different material properties. For example, to access the properties for an element, or a range of elements we can use:

```
properties = matmulti_ice. matPropLst4ElmntRange (md, propertyCONST, iceType, elementID_s)
```

where md is the model, propertyConst is the name of the property (e.g., “density”), iceType is the type of ice (e.g., “CO_2”), and elementID_s is an element’s identification number, or a range of elements in form of [start_ID: end_ID]. The names of material properties are kept in mat_const.m and are values such as LatentHeat, ThermalConductivity, HeatCapacity, Rho_Ice, etc. MIDAS applies these properties automatically to elements during model setup, so there is no need for any action. Table 2.1

lists the modelling properties (including material properties) that need to be defined by the user versus the properties that are calculated and assigned by MIDAS; the equations, however, can be easily changed in the matmulti_Ice.m file. It should be mentioned that numerical stability requires that the chosen timestep satisfy Courant–Friedrichs–Lewy (CFL) constraints, meaning that information (e.g., advection of ice thickness or temperature) should not propagate across more than one mesh element per timestep (See section 2.1.3). In practice, this limits the maximum timestep that can be applied (i.e., longest modelling duration time period), especially in regions with fine mesh resolution or high ice velocities.

Property	*Property Type*
Geothermal Flux	To be defined by the user
Heat Capacity	Calculated and assigned by MIDAS. The equation is currently defined. But can be changed directly in the code.
Ice Density	Calculated and assigned by MIDAS. The equation is currently defined. But can be changed directly in the code.
Latent Heat	Calculated and assigned by MIDAS. The equation is currently defined. But can be changed directly in the code.
Melting Point	Calculated and assigned by MIDAS
Mesh Resolution	To be defined by the user, as an input parameter

Property	*Property Type*
Thermal Conductivity	Calculated and assigned by MIDAS. The equation is currently defined. But can be changed directly in the code.
TimeStep for Solving a Model	To be defined by the user, as an input parameter
Rheology Law - Glen's Exponent	Defined in MIDAS, currently defined. But can be changed directly in the code.
Rheology Law - A_{const}	Defined in MIDAS, currently defined. But can be changed directly in the code.
Rheology Law - Activation Energy (Q)	Defined in MIDAS, currently defined. But can be changed directly in the code.

Table 2.1 – List of material properties used by MIDAS.

6. Running Transient Simulations

MIDAS uses ISSM's adaptive time-stepping scheme to set solver intervals. The user defines the minimum and maximum allowed values. For MIDAS, the maximum recommended timestep is five years. The solver uses ISSM's adaptive time-stepping which adjusts the step size dynamically but will not exceed the user-specified maximum.

Tests comparing MIDAS and ISSM with a single material type show that timesteps longer than five years cause the results to diverge, while reducing the timestep below five years does not improve accuracy (Table 2.2). Thus, a five-year interval provides the best balance between accuracy and computational cost.

Comparative runs at 1-, 2-, 4-, and 5-year intervals confirm that basal temperature changes and surface ice-flow velocities remain close. This is specifically based on a test that was run for 64,000 years, with single material, and in both ISSM and MIDAS. Table 2.2 shows the ice flow rates through MIDAS when the solver was called for every 1, 2 and 5 years (i.e., calling the server 64,000; 35,000; and 16,000 times respectively). The difference between the maximum velocity for calling the solver every 1 year, to every 5 years for the last year, turns out to be: 2.0e^{-06} $[m. yr^{-1}]$. We compare these results against ISSM leveraging SMB updates with calling the solver at 1000-year time intervals. The maximum difference in ice velocity between models forced with annual SMB updates and those solved at annual or five-year intervals was only 0.000009 m yr^{-1}. In contrast, extending the interval beyond five years quickly increases discrepancies and leads to divergence.

Test Scenario	Maximum Velocity ($[m. yr^{-1}]$)
Solving the model for every 1 year	0.139549
Solving the model for every 2 years	0.139550
Solving the model for every 5 years	0.139551

Table 2.2 – Test model, and the resulting maximum ice flow velocities if the surface mass balance is adjusted every 1, 2 or 5 years. Test ran though MIDAS only.

It should also be noted that ISSM applies SMBs through its own internal logic, which allows efficient handling of thickness changes. MIDAS can leverage the same functionality. However, for stratified units, MIDAS applies the mass balance changes by directly modifying the thickness of ice units. For example, a CO_2 ice unit accumulating at 2 mm yr^{-1} will gain 10 mm in thickness per node when updated every five years. This is required because ISSM only applies the SMB to the surface of the ice unit (hence the name “surface” mass balance).

However, MIDAS is capable of applying changes to various ice units (e.g., increase of mass in the upper unit and simultaneously applying sublimation to lower ice units). ISSM SMB logic will not be able to impact the lower layers. As MIDAS is primarily developed for the analysis of stratified ice units, by default, it will handle mass balance using its own internal logic. User may override this by invoking the variable “useSMB2EndOfYear”. This variable will allow MIDAS to use the ISSM’s SMB for a certain duration, and possibly for the full duration of a transient simulation if required (e.g., for the Gale Crater simulation in Chapter 4). A detailed explanation of ISSM’s SMB implementation is outside of the scope of this work, and can be found in the ISSM technical manuals.

Like ISSM, MIDAS runs the simulation as follows:

```
model = solve (model, model_type);
```

Where model_type carries the same parameters as those defined in ISSM (e.g., Thermal and Transient which indicate thermal or transient models respectively). MIDAS automatically handles transient failures, ensuring model continuity.

7. Capturing & Analyzing Results

After solving the model, use captureResult to extract key outputs:

```
results = modelmulti_Ice.captureResult(model);
```

This function provides:

- Ice thickness evolution
- Flow velocity fields

- Surface/basal temperature changes

To plot the results, all the plotting functionality from ISSM can be used. Moreover, MIDAS exposes a new plotting function to plot a 3D meshed view of the icesheet with the ice units identified (Figure 1.9):

```
plotting. plotmultiUnit_mesh(model); % Visualize stratified icesheet
```

MIDAS also offers a predefined set of scripts which receive an excel file as input and leverages MIDAS functionality to define and analyze icesheets.

2.1.5 Modelling

MIDAS Quality Assurance

Before we start to leverage MIDAS for a multi-unit ice analysis, we should examine and test to confirm it will behave similar to ISSM, when there is only one type of material. To test the efficacy of MIDAS, we first use the approach that Smith et al. (2022) took to reproduce a more simplified version their simulation; then we demonstrate that if MIDAS is used under the same conditions, it will return the same results as Smith et al. (2022), who did not include bounding layers. In the next sub-section we set up this model and comparing the output of both.

For this test, we use the same modelling tool, approach, domain and parameters as used by Smith et al. in 2022. We, however, use a different mesh (keeping it the same for both tests). The mesh size is 5000 m fixed resolution; the duration of the simulation is 300,000 years. Then we replicate the same simulation through MIDAS (exactly the same input parameters). For these tests, we also employ fixed numbers for the material properties to keep MIDAS and

ISSM conditions as identical as possible. There was only one difference between MIDAS and ISSM (using the Smith et al. (2022) parameters) that was left in place. MIDAS determines the pressure on every node using the height of the ice mass above it and the density. For the comparison, we report the test results for the final year of the simulation (Figure 2.2) and compare the mean values over the course of the simulation; finally, we compare the evolution of the two modeled ice volumes (Figure 2.3). Based on those outputs, we find that the output from the MIDAS model to match the 2022 ISSM model very closely: MIDAS mean velocity starts to show minor differences starting the year 250,000 and the difference reaches about 0.1% slower velocity; mean temperature about 0.01% higher. From the next sub-section, we will start to discuss how MIDAS will be setup, and what the input parameters will be for using MIDAS on MCID with the inclusion of Bounding Layers.

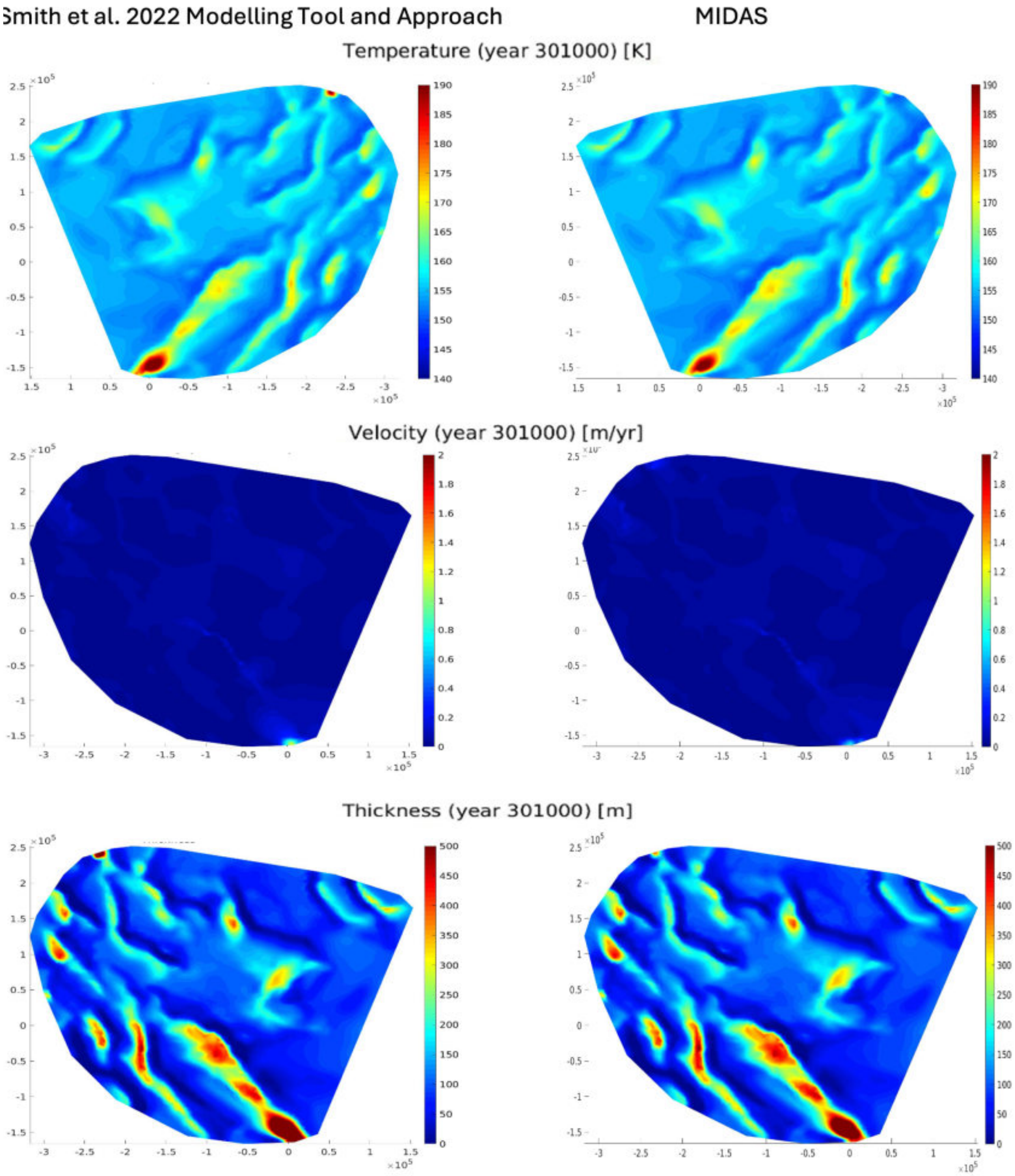

Figure 2.2 – Comparison between results

ISSM results (Smith et al., 2022), left, and MIDAS using the same parameters, right. Here the comparisons are for the basal temperature, surface velocity and the ice thickness during the final year (301000). See Figure 2.3 for further details.

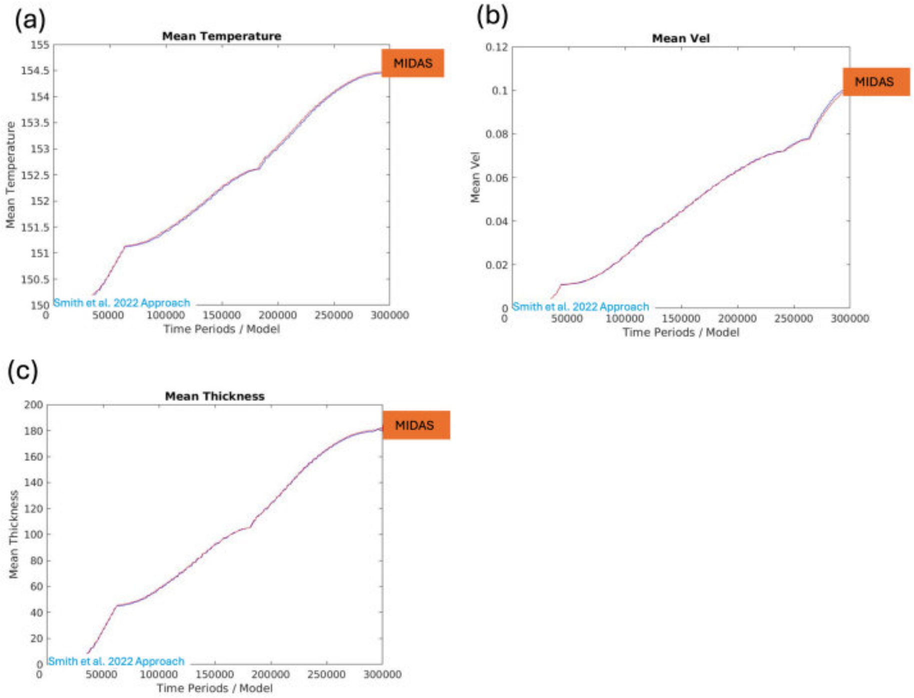

Figure 2.3 – Comparison between ISSM and MIDAS of the ice volume changes, temperature, velocity, and thicknesses for 301000 years.

(a) The results follow very closely, showing that MIDAS does not result in any loss of mass and maintains the conservation of mass. (b), (c) and (d) Plots are of the mean values for all the cells in the model. The blue line (rather hidden underneath the red curve) shows the ISSM results. The red curve shows the results from MIDAS. Only minor differences exist, demonstrating the efficacy of MIDAS in reproducing past results.

2.2 Models Start-up Parameters

A new model in MIDAS is created with series of default values that can easily be overwritten. See Table 2.3 for parameters defined in ***settingsmulti_Ice*** class (which extends ISSM ***issmsettings***), and Table 2.4 for parameters defined in the *planetProperties* class.

Parameter	Value	Comments
stressbalance_restol	2e-4	ISSM default value is 1e-4; see ISSM guidebook.
matlab_comparison_threshold	1e-8	To compare two numbers (A and B) and avoid dealing with rounding errors, MIDAS uses abs(A-B) <matlab_comparison_threshold to determine the two numbers are the same.
thickness_firstIceUnit_threshold	1	In meters, when starting a model, MIDAS will enforce a minimum thickness equal to this amount to the first ice unit. (i.e., the first ice unit will start with minimum of this thickness on every node and will not be reduced to less than this amount during transient runs.)
thickness_minThreshld	0	In meters, during transient simulations, MIDAS will not allow for an ice unit (other than the first ice unit) thickness to be reduced to less than this amount.
InitialResolution	100	In meters, the base mesh resolution. This can be increased to improve the mesh generation performance, especially if the final mesh is in the range of a few kilometers.
frictionCoeff	500	By using a high value of the friction coefficient, MIDAS assumes that the ice sheets are not sliding (i.e., the ice sheet is grounded). This parameter can be overwritten to a lower value, or the model can be instructed to use other friction laws. See ISSM guidebook detail on different friction laws supported in ISSM.
minNbrLayersInIceUnit	2	An ice unit mesh cannot have less than 2 mesh layers (one below, and one over the ice unit). However, this number can

Parameter	Value	Comments
		be increased to enforce MIDAS to build 3-d ice models using higher number as the minimum of the mesh layers.

Table 2.3- Default parameters defined in class ***settingsmulti_Ice*** *which extends* ***issmsettings*** *from ISSM.*

Parameter	Value	Comments
Planet	MARS	The planet where the ice model is defined for. This value is defined using the *setPlanetMoonProperties* (static) function of the *planetProperties* class.
Earth surface temperature	200 K	Defined in the minPlanetSurfaceTemperature (static) function of the *planetProperties* class.
Mars surface temperature	150 K	Same as above.
Pluto surface temperature	40 K	Same as above.

Table 2.4-Planet specific default values. By default, MIDAS assumes the ice sheet modelling is done for Mars.

MIDAS introduces specific properties for Mars, and Pluto, to augment the properties of Earth. These properties can be extended for other planets or in *planetProperties.m*.

3 Properties of Water, Carbon Dioxide, and Nitrogen Ices in Planetary Surface Environments

3.1 Introduction

3.1.1 Contributions of this Study

Numerous investigations have measured and identified properties of water and exotic ices in the planetary surface environments. These properties are measured at various pressures and temperatures; however, these disparate studies are sometimes difficult to find, confusing, or even contradictory. Here, I amass and present a catalogue of some temperature dependent equations on ice density, latent heat of fusion, constant values for latent heat of sublimation, specific heat capacity at constant pressure, thermal conductivity, and Arrhenius flow law parameters for water ice, carbon dioxide ice, and solid nitrogen. The equations are either directly cited from the sources or are fitted from data in past publications. I have identified the studies that are specifically done for the Planetary surface environments.

3.1.2 Background

In this section, I present how equations have been fitted to the data collected by various laboratory researches and works. In each plot, solid dots represent the data points, solid lines (where used in a plot) connect the data points, and dashed lines represent the curve best fitted to the data points. Fitted equations are included in the plot, as well as their corresponding coefficients of determination (R^2) which quantifies how well the fitted curve explains the variability of the data. The data sets used are also available. The focus of this section is mainly on the regimes where the pressure is lower than 5.5 MPa and has limited impact on the thermal properties of ice; as an example, the CO_2 ice in the south pole of Mars is likely to experience less than 5.5 MPa pressure (Cross et al., 2020). When certain equations are recommended for use, it is because the associated experiments were conducted under conditions comparable to those expected in non-terrestrial environments. For the definition of the material properties covered in this section, refer to Appendix 2.

3.2 Water, CO_2, and N_2 Ice Material Properties Look-up Tables

This section provides easy to access look up tables for the commonly usable material properties. The details around each equation will be further discussed in Section 3.3 and onwards. Also, there are some older equations cited in this section (for the sake of completeness) that have not been included in this table. For exotic ices we recommend using the equations presented in this section; these equations are the result of the newest laboratory test and field studies or have been specifically researched by their respective authors in the context of exotic ices.

3.2.1 Water Ice

Property	**Notes**	**Equation**	**References**
Density (ρ) $\left[\frac{kg}{m^3}\right]$	Region Ih 150 K to 190 K Pressure 0 to 5 MPa	$\rho = 929.2 \left[\frac{kg}{m^3}\right]$	SeaFreeze (Journaux et al., 2020)
	0 K to 273 K **See *footnote*** [±2] **for pressure dependent *A* and *B* variables**	$\rho = -3 * 10^{-4} * T^2 + A * T + B$	Fitted data from Feistel and Wagner (2006)

---

[2] ±The values of *A* and *B* are dependent on the pressure as follows (Feistel and Wagner, 2006):

Pressure (MPa)	*A*	*B*
0	0.0316	933.29
1.01325	0.0316	933.29
50	0.0301	937.64
100	0.0286	941.86
150	0.0266	945.94
200	0.0248	949.88

Property	Notes	Equation			References
Flow Law Parameters[3] (Parameters for ice type / temperature)		$A_{const}\left[\frac{1}{MPa^{n}.s}\right]$	$Q\left[\frac{J}{mol}\right]$	$n\ (dimentionless)$	
	Region Ih Less than 195 K	$1585 * 10^{-3}$	$39000\ \pm 5000$	$6.0\ \pm 0.4$	Durham et al., 1992
	Region Ih 95 K to 240 K	$10^{5.1\ \pm\ 0.03}$	$61000\ \pm 2000$	$4.0\ \pm 0.1$	Durham et al., 1992; Durham, Kirby, and Stern, 1997; Goldsby et al., 2001
	Region Ih	$10^{11.8\pm0.4}$	91000 ± 2000	$4.0\ \pm 0.6$	Durham et al., 1992;

---

[3] It should also be noted that while (as mentioned) more recent studies (e.g., Millstein et al., 2022) suggest higher Glen's exponents, the classical value of n = 3 has remained the standard (along with log10(Aconst)=4.5 MPa-3 s-1, and the activation energy of 60,000 [J/mol]) for over five decades because it provides an empirically validated approximation that reproduces large-scale icesheet behaviour reasonably well under many terrestrial conditions.

Property	Notes	Equation			References
	240 K to 258 K				Durham, Kirby, and Stern, 1997; Goldsby et al., 2001
	Ice II Less than 220 K	$10^{1.84 \pm 0.27}$	55000 ± 2000	5.3 ± 0.1	Durham et al., 1988; Durham, Kirby, and Stern, 1997
	Ice II More than 220 K	$10^{11.7 \pm 1.6}$	98000 ± 8000	5.2 ± 0.3	Durham et al., 1988; Durham, Kirby, and Stern, 1997
	Ice III Less than 230 K	$10^{13.3 \pm 1.5}$	103000 ± 8000	6.3 ± 0.4	Durham et al., 1988; Durham, Kirby, and Stern, 1997

Property	Notes	Equation			References
	Ice III More than 230 K	$10^{26.4\pm4.8}$	151000 ± 21000	5.3 ± 0.1	Durham et al., 1988; Durham, Kirby, and Stern, 1997
	Ice V	10^{23}	136000 ± 38000	6.0 ± 0.7	Durham et al., 1986; Durham, Kirby, and Stern, 1997
	Ice VI Less than 250 K	$10^{6.7}$	66000 ± 4000	4.5 ± 0.2	Durham et al., 1986; Durham, Kirby, and Stern, 1997
	Ice VI More than 250 K	$10^{6.7}$	110000 ± 20000	4.5	Durham et al., 1986; Durham, Kirby, and Stern, 1997

Property	**Notes**	**Equation**	**References**
Latent Heat of Fusion (L) $\left[\frac{J}{kg}\right]$	250 K to 273 K For water with impurities	$L = -7.929 * T^2 + 5094.31 * T - 466221.51$	Notz et al., 2005
	265 K to 273 K If there is no salinity	$L = -3.76812 * T^2 - 55.81 * T + 629992$	Ono, 1967
Latent Heat of Sublimation (L_v)	For Ih (i.e., hexagonal) Static number $\left[\frac{J}{kg}\right]$ (See 2.6)	$L_v = 25.9 * \ 10^5 \ \left[\frac{J}{kg}\right]$	Leliwa-Kopystyński et al., 2013

Property	**Notes**	**Equation**	**References**
	For Ih (i.e., hexagonal) $\left[\frac{J}{mol}\right]$ Less than 30 K	$L_v = 46782.5 + 35.8925 * T - 0.07414 * T^2 + 541.5 * e^{-\left(\frac{T}{123.75}\right)^2}$	Murphy and Koop, 2005
Specific Heat Capacity (C_p) $\left[\frac{J}{kg.K}\right]$	89.55 K to 273.15 K	$C_p = -22.86 * 10^{-3} * T^2 + 16.3163 * T - 720.5987$	Maass et al., 1925
	Region Ih 150 K to 189 K Pressure:0 to 5 MPa	$C_p = 6.8021 * T + 205.26$	Fitted data from SeaFreeze (Journaux et al., 2020)
	265 K to 273 K 0% salinity	$C_p = 7.53624 * T + 55.81$	Ono, 1967

Property	**Notes**	**Equation**	**References**
Thermal Conductivity $(K)\left[\frac{W}{m.K}\right]$	less than 40 K	$K = 5483.1 * T^{-1.662}$	Fitted data from Slack (1980)
	40 K to 273 K See Figure 3.7 for other equations in this temperature range	$K = 903.65 * T^{-1.072}$	Fitted data from Slack (1980)

Table 3.1 – Water ice properties

3.2.2 CO_2 Ice

Property	**Notes**	**Equation**	**References**
Density $(\rho)\left[\frac{kg}{m^3}\right]$	80 K to 195 K	$\rho = 1723.91 - (0.253) * T - (2.87 * 10^{-3}) * T^2$	Mangan et al., 2017

Property	**Notes**	**Equation**	**References**
Flow Law Parameters	150 K to 200 K We recommend the use of these parameters over other values presented in section 5.2.2.	$A_{const} = 10^{13\pm1.27} \left[\frac{1}{MPa^n.s}\right]$ $Q = 66900 \pm 4200 \ \left[\frac{J}{mol}\right]$ $n = 8 \pm 2.2$	Cross et al., 2020
Latent Heat of Fusion (L) $\left[\frac{J}{kg}\right]$	At melting point of 216.95 K	$L = 189{,}811 \ \left[\frac{J}{kg}\right]$	Maass et al., 1926
Latent Heat of Sublimation (L_v) $\left[\frac{J}{kg}\right]$	Static number (See 4.1.6)	$L_v = 7.58 * \ 10^5 \ \left[\frac{J}{kg}\right]$	Leliwa-Kopystyński et al., 2013

Property	**Notes**	**Equation**	**References**
Specific Heat Capacity (C_p) $\left[\frac{J}{kg.K}\right]$	15.52 K to 189.78 K	$C_p = -10^{-6} * \mathrm{T}^4 + 0.001 * \mathrm{T}^3 - 0.2381 * \mathrm{T}^2 + 28.253 * \mathrm{T} - 355.66$	Fitted from Giauque and Egan, 1937
	Less than 158 K	$C_p = 967 \left[\frac{J}{kg.K}\right]$	Maass et al., 1926
	158 K to 163 K	$C_p = 1188 \left[\frac{J}{kg.K}\right]$	Maass et al., 1926
	163 K to 217 K	$C_p = 1673.6 - 11.84072 * T + 0.0523 * T^2$	Maass et al., 1926
CO_2-Hydrate Specific Heat Capacity $\left[\frac{J}{kg.K}\right]$	5 K to 292 K	$C_{p100\%CO2} = 1.70 * T + 2098$	Ning et al., 2015; Mathews, Servio, and Rey 2020

Property	Notes	Equation	References
Thermal Conductivity (K) $\left[\frac{W}{m.K}\right]$	170 K to 210 K	$\log_{10} K = -5.39941 + 5.45894 * \log_{10} T - 1.41326 * (\log\rrbracket_{10} \llbracket T\ )^2$	Ross and Kargel, 1998; Konstantinov et al., 1988

Table 3.2 – CO_2 ice properties

3.2.3 Solid Nitrogen

Property	Notes	Equation	References
Density (ρ) $\left[\frac{kg}{m^3}\right]$	Less than 35.6 K	$\rho = -0.0334 * T^2 + 0.5547 * T + 1029.1$	Fitted data from Krupskii et al. (1975), and reported by Scott (1976)
	35.6 K to 60 K	$\rho = -0.0134 * T^2 - 0.6981 * T + 1039.1$	Fitted data from Krupskii et al. (1975) and reported by Scott (1976). Trowbridge et al. (2016) provide a different equation as cited in section 4.3.1.

Property	Notes	Equation	References
Flow Law Parameters	45 K to 56 K	$A_{const} = 0.00501 * \ e^{\left(9.378-\frac{422}{T}\right)} \ \frac{1}{MPa^{n}.s}$ $Q = 3500 \frac{J}{mol}$ $Glen's\ exponent\ (n) = 0.0155 * T + 1.4025$	Yamashita, Kato, and Arakawa, 2010; Moore et al., 2016
Latent Heat of Sublimation (L_v) $\left[\frac{J}{kg}\right]$	Static number (See 4.1.6)	$L_v = 2.00 * \ 10^5 \ \left[\frac{J}{kg}\right]$	Leliwa-Kopystyński et al., 2013
Specific Heat Capacity (C_p) $\left[\frac{J}{kg.K}\right]$	Less than 35.6 K	$C_p = 0.0688 * T^3 - 3.9291 * T^2 + 173.13 * T - 1046.1$	Giauque et al., 1933; Bagatskii et al., 1968; Scott, 1976
	35.6 K to 60 K	$C_p = 0.1957 * T^2 + 8.1019 * T + 2059.2$	

Property	**Notes**	**Equation**	**References**
Thermal Conductivity (K) $\left[\frac{W}{m.K}\right]$	Less than 4 K	$K = -1.8823 * T^3 + 13.846 * T^2 - 21.756 * T + 11.841$	Fitted from the data reported by Sagmiller and Hartwig (2020), based on the works of: Roder (1962); Manzhelii and Krupskii (1968) (via Manzhelii et al. (1999)); Koloskova et al. (1973); Manzhelii et al. (1975); Cook and Davey (1976); and Stachowiak et al. (1994).
	4 K to 60 K	$K = 213.27 * T^{-1.952}$	

6 *Table 3.3 – Solid nitrogen properties*

3.3 Water Ice

Different forms of H_2O ice are found at different temperature and pressure ranges, from amorphous to hexagonal crystalline and other crystalline structures/packing. These ice properties change depending on the pressure. To differentiate different types of ice, Roman numerals are generally used. Ice I includes two subsets generally identified as Ih and Ic. This distinction is based on the temperature at which the crystal structure of ice stabilizes and forms hexagonal structures. The plot below demonstrates the first 6 phases of water ice (Bertie et al., 1963; Engelhardt and Whalley, 1972; Durham et al., 1983; Minceva-Sukarova et al., 1984; Marti and Mauersberger, 1993; Durham et al., 1997; Durham et al., 1998; Chou et al., 1998; Klotz et al., 2005).

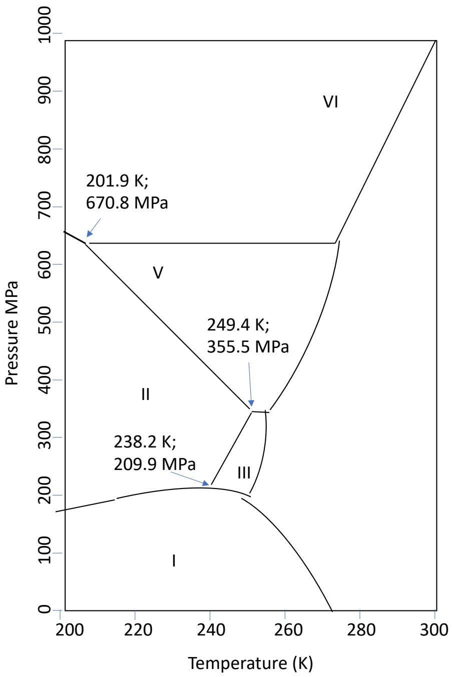

Figure 3.1 – Water ice phases diagram. Temperature and pressure values from SeaFreeze (Journaux et al., 2020)

3.3.1 Density

Density is a function of temperature as well as pressure. Here we present two approaches in measuring water ice density:

1) Water Ice Density Dependence on Temperature Using SeaFreeze: SeaFreeze (Journaux et al., 2020; and *https://github.com/Bjournaux/SeaFreeze*), provides thermodynamic property calculations for water and its ice phases, with phase stability predictions valid down to 130 K. Assuming the pressure of less than 5.5 MPa and a temperature range of 150 K to 190 K (region Ih), we arrive at the values presented in Table 3.4. SeaFreeze uses Gibbs free energy-based representations for various types of water ice (including those prepared for ices II, and above at high volume and low temperature) to determine the thermodynamical properties. Here, "stability prediction" refers to the model's ability to identify which ice phase is thermodynamically stable under a given combination of pressure and temperature, based on the lowest Gibbs free energy among all possible phases.

Parameter	Minimum	Maximum	Mean	Standard Deviation
$\rho\,[\frac{kg}{m^3}]$	927.166	931.067	929.223	1.0311

Table 3.4 – Water ice density for 150 to 190 Kelvin, region Ih

(SeaFreeze, Journaux et al., 2020)

Therefore, for H_2O ice, we could assume the constant (i.e., temperature independent density) of ***929.2*** $\left[\frac{kg}{m^3}\right]$ for the region Ih. It is worth noting that Röttger, et al. (2012) provided an expression (specifically for Ih ice) which was later used by the KRC thermophysical modelling

(Kieffer, 2013; and http://krc.mars.asu.edu/index.php?title=Material_Properties_and_Regolith_Layering)

2) Water Ice Density – Feistel and Wagner (2006): Using the data provided by Feistel and Wagner (2006), (temperature in Kelvin, pressure in MPa, region Ih and density in $\left[\frac{kg}{m^3}\right]$) we determine the equations of density (Figure 3.2).

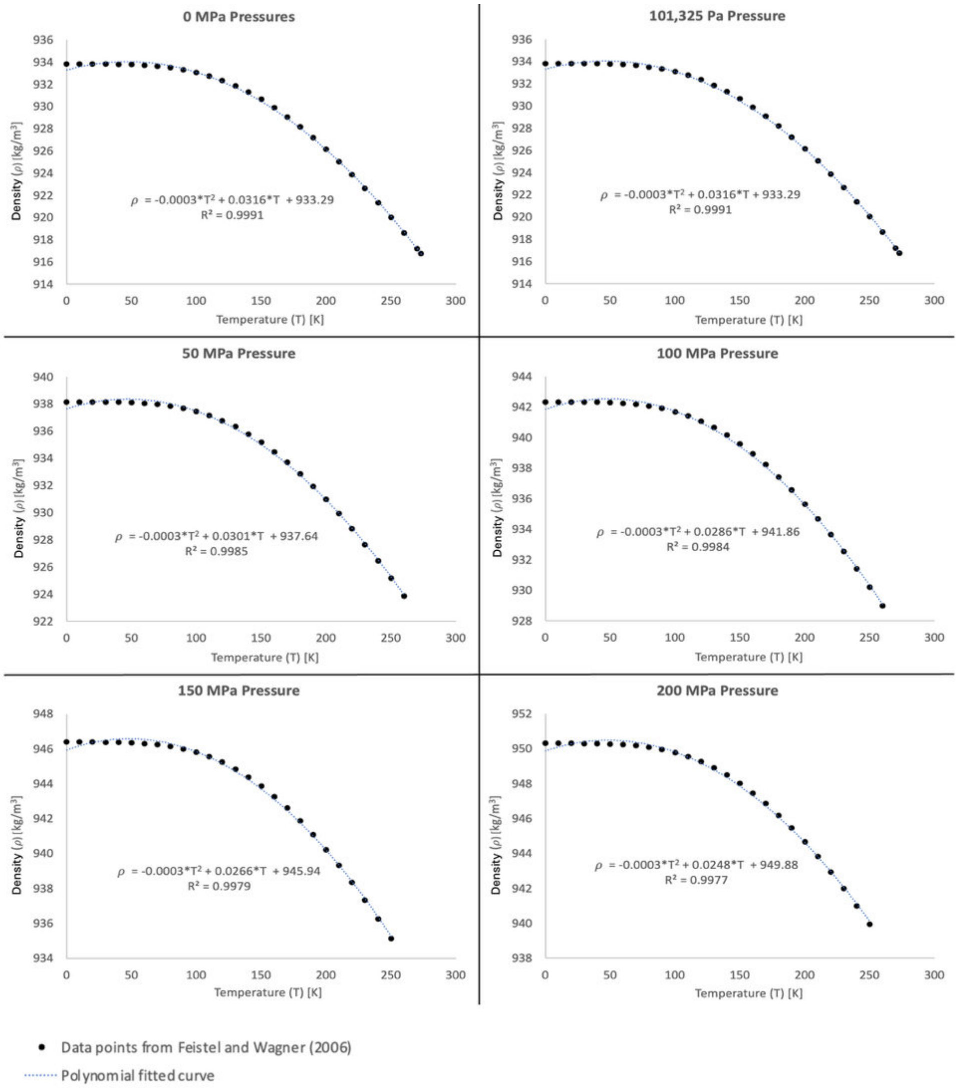

Figure 3.2 – Fitted data for the density of water ice kg.m^{-3} following Feistel and Wagner (2006)

Plots *in Figure 3.2 provide*:

$$\rho = -3 * 10^{-4} * T^2 + A * T + B \qquad \text{eq. 3.1}$$

The values of A and B are in the footnote in Section 3.1.1.

3.3.2 Flow Law Parameters

For H_2O, the activation energy is about 60 $[\frac{kJ}{mol}]$ (Goldsby and Kohlstedt, 2010), but it could be more sensitive to changes of temperature as explained and demonstrated by Durham et al. (2010). Millstein et al. (2022) tested the Glen's exponent at about 4.1± 0.4 and recommended this range. In their 2010 paper, Durham et al. provided a list of water ice flow law parameters in terrestrial settings (Alley, 1992; Budd and Jacka, 1989; Paterson, 1994; Petrenko and Whitworth, 1999; Schulson and Duval, 2009). However, it should be noted that the selection of an appropriate rheological set of parameters for modelling terrestrial and planetary icesheets remains an open question. Differences in experimental conditions, grain size, impurities, and temperature–stress regimes continue to produce variability in the reported parameters (A, Q, n), leading to ongoing laboratory tests and associated analysis in the literature. For the sake of completeness, in the table below, we have included the parameters collected in Durham et al., 1997. It should also be noted that while (as mentioned) more recent studies (e.g., Millstein et al., 2022) suggest higher Glen's exponents, the classical value of n = 3 has remained the standard (along with $\log_{10}(A_{const})=4.5$ MPa^{-3} s^{-1}, and the activation energy of 60,000 [J/mol]) for over five decades because it provides an empirically validated approximation that reproduces large-scale icesheet behaviour under many terrestrial conditions.

	$A_{const}\left[\frac{1}{MPa^{n}.s}\right]$ (Range)		$Q\ [\frac{J}{mol}]$ (Range)	n (Range)
Ice Ih, less than 195[a]	*No range. See Table* 3.6		34000 to 44000	5.6 to 6.4
Ice Ih, 195-245[b]	1.1749E+05	1.3490E+05	59000 to 63000	3.9 to 4.1
Ice Ih, 240-258[c]	2.5119E+11	1.5849E+12	89000 to 93000	3.4 to 4.6
Ice II, less than 220[c]	37.1535	128.825	53000 to 57000	5.2 to 5.4
Ice II, more than 220[c]	1.2589E+10	1.9953E+13	90000 to 116000	4.9 to 5.5
Ice III, less than 230[c]	6.3096E+11	6.3096E+14	95000 to 111000	5.9 to 6.7
Ice III, more than 230[c]	3.9811E+21	1.5849E+31	130000 to 172000	3.2 to 5.5
Ice V[d]	*No ranges available. See Table* 3.6		98000 to 174000	5.3 to 6.7
Ice VI, less than 250[d]			62000 to 70000	4.3 to 4.7
Ice VI, more than 250[d]			90000 to 130000	4.5

Note that the level of uncertainty for the scenarios where Aconst does not have a range has been included in the n and Q ranges (Durham, Kirby, and Stern, 1997)

[a] *Durham et al., 1997*

[b] *Durham et al., 1992; Durham, Kirby, and Stern, 1997*

[c] *Durham et al. 1988; Durham, Kirby, and Stern, 1997*

[d] *Durham et al. 1996; Durham, Kirby, and Stern, 1997*

$A_{const}\left[\frac{1}{MPa^{n}.s}\right]$ (Range)	$Q\,[\frac{J}{mol}]$ (Range)	n (Range)

Table 3.5 – Ranges of water ice flow law parameters for different temperature/pressure regimes

	$A_{const}\left[\frac{1}{MPa^{n}.s}\right]$	$Q\,[\frac{J}{mol}]$	n
Ice Ih, less than 195[a]	1.5849E–04	39000	6.0
Ice Ih, 195-245[b]	1.2589E+05	61000	4.0
Ice Ih, 240-258[c]	6.3096E+11	91000	4.0
Ice II, less than 220[c]	69.1831	55000	5.3
Ice II, more than 220[c]	5.0119E+11	98000	5.2
Ice III, less than 230[c]	1.9953E+13	103000	6.3
Ice III, more than 230[c]	2.5119E+26	151000	4.3
Ice V[d]	1.00E+23	136000	6.0
Ice VI, less than 250[d]	5.0119E+06	66000	4.5

	$A_{const}\left[\frac{1}{MPa^n.s}\right]$	$Q\left[\frac{J}{mol}\right]$	n
Ice VI, more than 250[d]	5.0119E+06	110000	4.5

[a] Durham et al., 1997

[b] Durham et al., 1992; Durham, Kirby, and Stern, 1997

[c] Durham et al. 1988; Durham, Kirby, and Stern, 1997

[d] Durham et al. 1996; Durham, Kirby, and Stern, 1997

Table 3.6 – Midpoints of water ice flow law parameters for different temperature/pressure regimes.

We plot the cited ice hardness (in logarithmic scale) vs. temperature for various water ices, CO_2 ice (Cross et al., 2020), solid N_2 (Yamashita, Kato, and Arakawa, 2010), and for comparison, CH_4 (Bolshutkin et al., 1968) have been added to this plot. See also Sections 3.4.2 and 3.5.2.

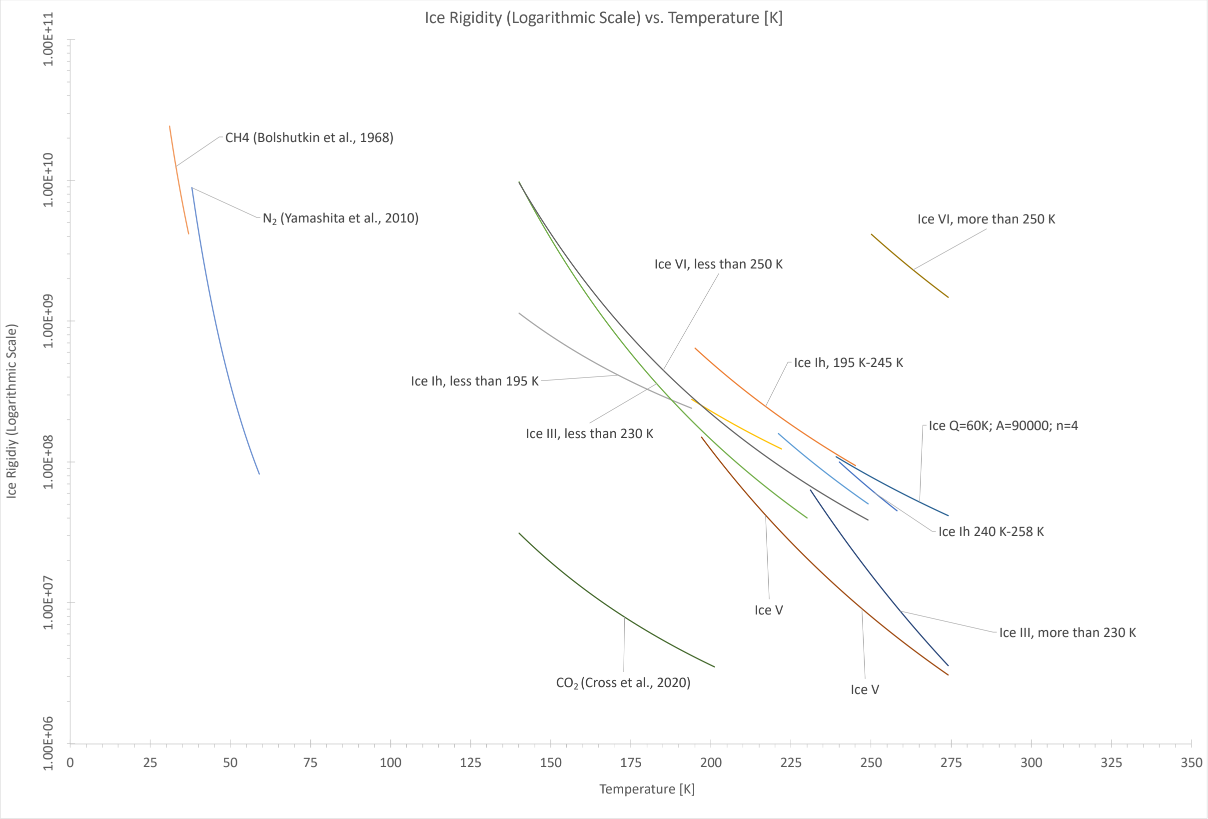

Figure 3.3 – Water ice rigidity

The plot shows the rigidity for different temperature/pressure regimes (sources in Table 3.6). CO2, N2, and CH4 rigidities have been added for comparison (sources included in the plot).

It is worth noting that the flow of ice will vary more greatly at pressures closer to ice material melting point (Duval, 1977; Adams et al., 2021).

3.3.3 Latent Heat of Fusion

Ono (1967) did a full set of laboratory tests while varying the percentage of salinity in water to determine the latent heat of fusion of ice and arrived at:

$$L_{TS} = 79.68 - 0.505 * T_c - 0.0273 * S + 4.3115 * \frac{S}{T_c} + 0.0008 * S * T_c - 0.0009 * {T_c}^2 \qquad eq.\ 3.2$$

Where T_c is the temperature in Celsius, S is the percentage of salinity, and L_{TS} is the latent heat of fusion in $\left[\frac{cal}{gr.C^{\circ}}\right]$.

If assuming no NaCl (i.e., $S = 0\%$), we can convert eq. 3.2 to $\left[\frac{J}{kg.K}\right]$ as:

$$L = -3.76812 * T^2 - 55.81 * T + 629992 \qquad \textit{eq. 3.3}$$

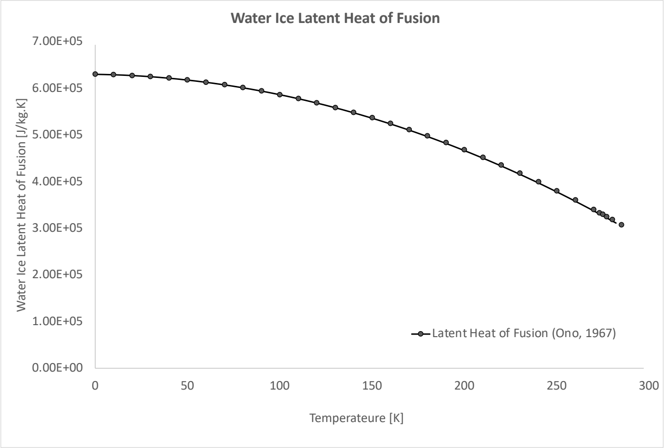

Figure 3.4 – Water ice, without salt, latent heat of fusion vs. temperature (Ono, 1967)

Notz (2005) provided the following equation for the latent heat of fusion for water ice that is formed from NaCl solutions.

$$L = 333700 + 762.7 * T_c - 7.929 * T_c^2 \qquad \textit{eq. 3.4}$$

Where L is the latent heat of fusion for water ice with impurities and T_c is the temperature in Celsius. To convert this equation to use temperature in Kelvin we can substitute T_c with $T(Kelvin) - 273.15$ and simplify to have:

$$L = -7.929 * T^2 + 5094.3127 * T - 466221.51 \qquad eq.\ 3.5$$

Equations above at the water ice melting point provide the textbook value of $3.34 * 10^5 \left[\frac{J}{kg.K}\right]$ (Young et al., 2019).

3.3.4 Specific Heat Capacity

There are various sources for the water ice specific heat capacity as a function of temperature. In this section, four different equations are presented.

1) Ono (1967) provides an equation to use the percentage of salinity in water to determine the specific heat capacity for ice. For the temperature range of 0 to 8 degrees Celsius Ono arrived at:

$$C_{pTS} = 0.505 + 0.0018 * T_c + 4.3115 * \frac{S}{T_c^2} - 0.0008 * S + 0.00002 * S * T_c \qquad eq.\ 3.6$$

Where T_c is the temperature in Celsius, S is the percentage of salinity, and C_{pTS} is the latent heat of fusion in $\left[\frac{cal}{gr.C^\circ}\right]$.

2) If assuming no NaCl (i.e., S=0), we can convert eq. 3.6 to $\left[\frac{J}{kg.K}\right]$ as follows:

$$C_p = 7.536 * T + 55.81 \qquad eq.\ 3.7$$

3) Using SeaFreeze (Journaux et al., 2020) we determine a range of specific heat capacity values, assuming the maximum pressure of 5.5 MPa, and temperature range of 150 to 190 K. This data (Figure 3.5) is used to write:

$$C_p = 6.8021 * T + 205.26 \qquad \textit{eq. 3.8}$$

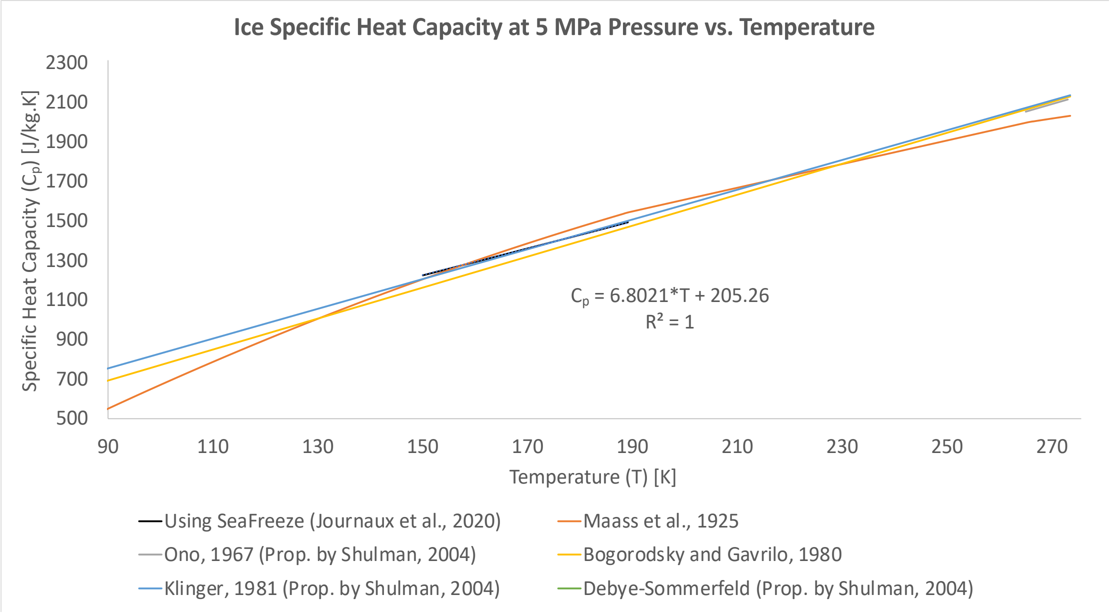

Figure 3.5 – Water ice specific heat capacities

The heat capacities are at constant pressure and from SeaFreeze (Journaux et al., 2020) for 5 MPa, and temperature range of 150 K to 190 K; along with plots from Maass et al. (1925), Ono (1967), as well as three equations proposed by Shulman (2004)

4) Maass (1926) showed for temperatures in the range of 89.55 to 273.15 Kelvin the specific heat capacity of ice can be expressed as:

$$C_p = -22.86 * 10^{-3} * T^2 + 16.3163 * T - 720.5987 \qquad \textit{eq. 3.9}$$

5) Shulman (2004) proposed the following three equations (later also used by Ferrari & Lucas (2016)). The equations are in $[\frac{J}{kg.K}]$. First one is from Bogorodsky and Gavrilo (1980):

$$C_p = 7.8 * T \qquad \textit{eq. 3.10}$$

The second equation is by Klinger (1981), also used by Prialnik (1992):

$$C_p = 7.49 * T \; + \; 90 \qquad \textit{eq. 3.11}$$

As Shulman explains eq. 3.11 contradicts with the Nernst heat theorem, and that both equations (eq. 3.10 and eq. 3.11) are valid for higher temperatures. Lastly, this paper cites the Debye-Sommerfeld equation. Different approximations of this equation are provided. Shulman cites eq. 3.12 as the most accurate approximation:

$$C_p = 7.73 * T * \left(1 - e^{-1.263*10^{-3}*T^2}\right) * \left(1 + e^{-3\sqrt{T}} * 8.47 * T^6 + 2.0825 * 10^{-4} * T^4 * e^{-4.97*10^{-2}*T}\right) \qquad \textit{eq. 3.12}$$

6) Other laboratory test and work includes the works of Barnes and Maass (1930); and Murphy and Koop (2005) who used the data from Giauque and Stout (1936) and for temperature of greater than 20 Kelvin arrived at eq. 3.13 which is in $[\frac{J}{mol.K}]$.

$$C_p = -2.0572 + 0.14644 * T \; + \; 0.06163 * T * e^{-\left(\frac{T}{125.1}\right)^2} \qquad \textit{eq. 3.13}$$

3.3.5 Thermal Conductivity

The thermal conductivity of water ice has been well researched and is reported to be dependent upon the environmental pressure and temperature (Slack, 1980). In this section we focus on pure water ice. For dirty ice, see the 2012 paper by Siegler et al. Slack (1980) proposed a factor to convert/correct the impact of the pressure and argued that due to the thermal expansion coefficient of water being high, the thermal conductivity (K) of water results in different values depending on whether the conditions are in constant volume or pressure. He merged laboratory test results from various sources (see Slack (1980) for the full sources of the data). Here, we focus mainly on low pressure (phase Ih, within ±10% of atmospheric pressure) as reported by Slack (1980) as in Table 3.7.

Temperature [K]	Thermal Conductivity $[\frac{W}{m.K}]$
10	120
15	60
20	38
40	16.1
80	8.1
100	6.5
120	5.4

Temperature [K]	Thermal Conductivity $[\frac{W}{m.K}]$
150	4.3
200	3.2
250	2.4
273.15	2.14

Table 3.7 – Thermal conductivity for water ice - Source Slack (1980)

We use this data to fit an equation that describes the thermal conductivity. To achieve the highest level of coverage of data points, we opt for two equations: one covering the temperature range of 10 K to 20 K, and another one covering the ranges of 20 K to 273.15 K.

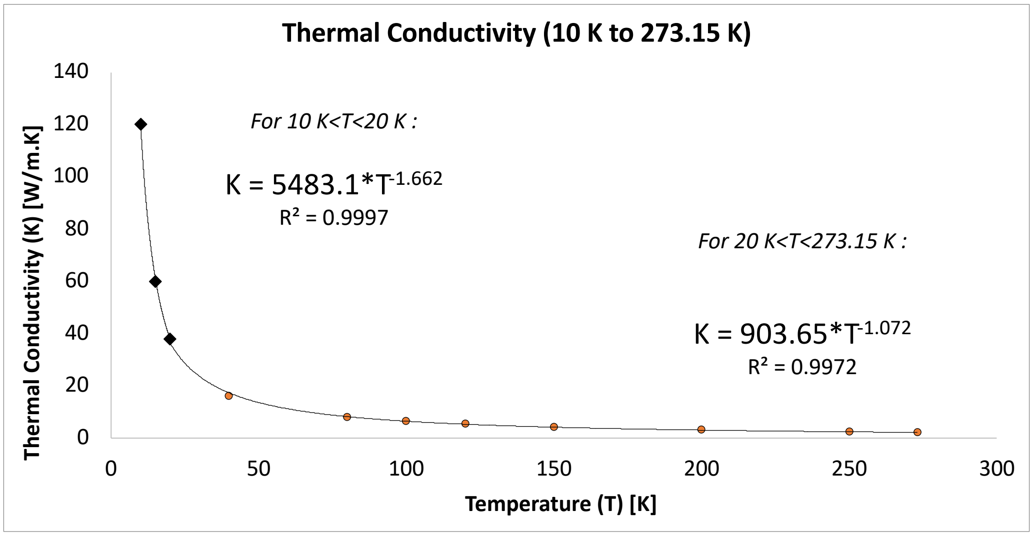

Figure 3.6 – Thermal conductivity equations

(Slack, 1980)

So, the equations will be:

$10\ K < T < 20\ K: K = 5483.1 * T^{-1.662}$ *eq. 3.14*

$20\ K < T < 273.15\ K: K = 903.65 * T^{-1.072}$ *eq. 3.15*

Bonales et al. (2017) fitted and cited thermal conductivity equations from a few researchers for 233 K to 273 K. These equations have been provided below and plotted in Figure 3.7.

- van Duser (1929): $K = 3.0605 - 3.553 * 10^{-3} * T$
- Lunardini (1981): $K = 5.7748 - 0.01349 * T$
- Waite et al. (2006): $K = 6.02433 - 0.01455 * T$
- Alexiades and Solomon (1992): $K = 5.9085 - 0.01365 * T$
- Choi and Okos (1956): $K = 1.0154 * 10^{-4} * T^2 - 0.06172 * T + 11.503$
- Ratcliffe (1962): $K = 2135 * T^{-1.235}$

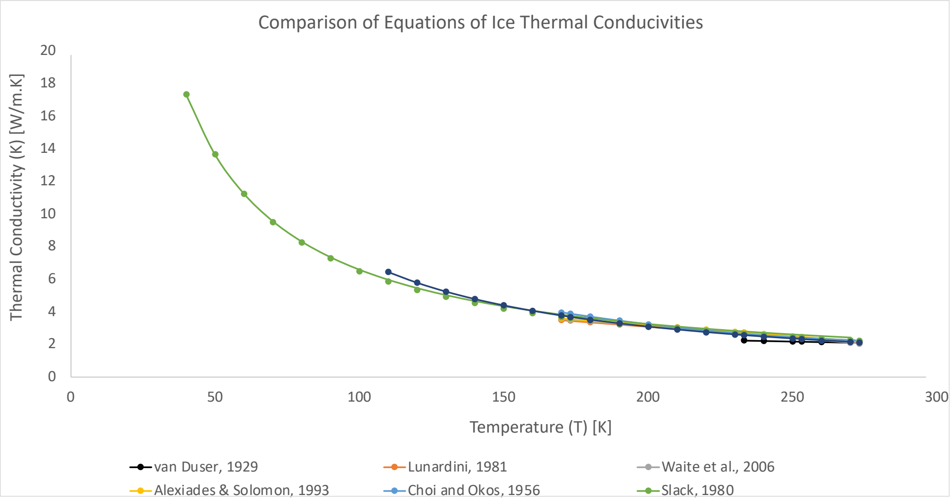

Figure 3.7 – Thermal conductivity of water ice

from various work fitted by Bonales et al., 2017.

There are further laboratory tests done in this field (Hobbs et al., 1974; Ferrari and Lucas, 2016; Siegler et al., 2012; etc.)

3.4 Carbon Dioxide Ice

3.4.1 Density

The density of CO_2 ice (i.e., dry ice) is a function of temperature, and the data for the temperature range of 80 to 195 degrees Kelvin can be described in $\left[\frac{kg}{m^3}\right]$ using the equation provided by Mangan et al. (2017):

$$\rho = 1723.91 - 0.253 * T - 2.87 * 10^{-3} * T^2$$ *eq. 3.16*

Other researchers have also defined equations; for example, Wang et al. (2018), provided an equation based on the work done by Maass and Barnes (1926). This equation is valid for the temperature range of 90 to 191.5 Kelvin, and measures the density of porous solid CO_2 in $\left[\frac{kg}{m^3}\right]$as follows:

$$\rho = -0.004 * T^2 + 0.1 * T + 1679.8$$ *eq. 3.17*

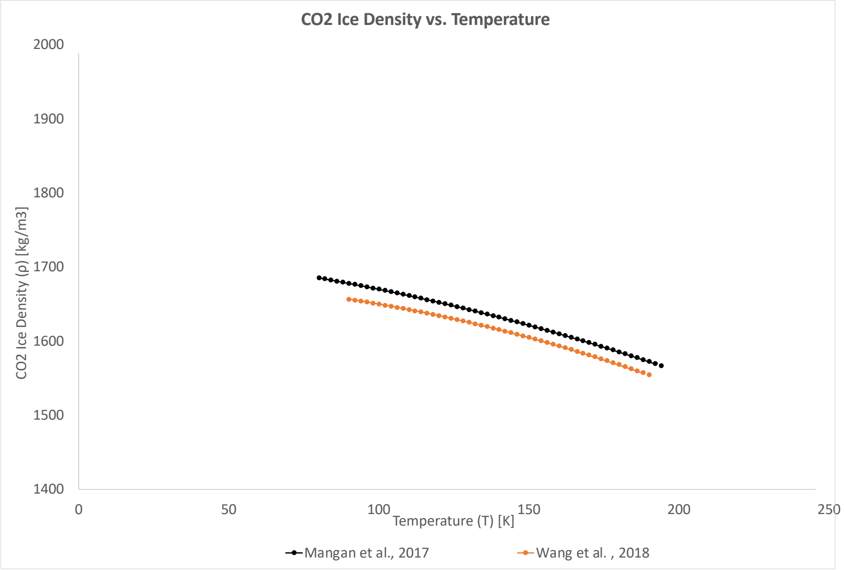

Figure 3.8 – CO_2 ice density

(sources in the plot)

3.4.2 Flow Law Parameters

Cross et al. (2020), updating the work of Durham et al. (1999) and Clark and Mullin (1976), but with lab-made CO_2 instead of commercial CO_2, demonstrated with laboratory experiments that CO_2 ice rheology reacts rapidly to stress with a high stress exponent. As the slope of the terrain where the CO_2 ice is located becomes steeper, the faster the CO_2 ice flows downhill. In their laboratory tests, which closely match the conditions found on the Martian surface, Cross et al. (2020), showed:

$$A_{const} = 10^{13.0} \frac{1}{MPa^8 . s}$$

$$Q = 66900 \frac{J}{mol}$$

$$Glen's\ exponent\ (n) = 8 \pm 2.2$$

Example: At *T*=100 K, B will be about $553.71 * \ 10^6 \left[Pa.s^{\frac{1}{8}}\right]$. Cross et al. (2020) provide other flow law parameters, through experimentations under conditions close to those on the Martian surface. While we recommend the use of the parameters determined and reported by Cross et al. (2020) for CO_2 based exotic ices (due to the closeness of the laboratory conditions to the Martian surface), for the sake of completeness, we are citing the other parameters from this publication in Table 3.8.

$A_{const}[MPa^{-n}S^{-1}]$	$Q\left[\frac{J}{mol}\right]$	n	***Reference***
$10^{13\pm1.27}$	66900 ± 4200	8 ± 2.2	Cross et al., 2020
$10^{11.1}$	59000	7	Nye et al., 2000 (reinterpreting Durham et al., 1999)
$10^{3.86}$	33000	5.6	Durham et al., 1999
$10^{10.5}$	51000	3.9	Clark and Mullin, 1976

Table 3.8 – Flow law parameters from different works (Cross et al., 2020)

3.4.3 Latent Heat of Fusion

Maass (1926) provides series of observed data points for the CO_2 ice latent heat of fusion and arrived at 189,811 $\left[\frac{J}{kg}\right]$ for the latent heat of fusion.

3.4.4 Specific Heat Capacity

Maass (1926), provided the measurements in $[°C]$ and $[\frac{cal}{gr.°C}]$ units which we can convert them to SI in Table 3.9.

Temperature Range [K]	Average Specific Heat $\left[\frac{J}{kg.K}\right]$
90.05 to 158.15	966.504
158.15 to 194.65	1188.256
194.65 to 216.92	1456.032
216.95 to 298.15	2050.16

Table 3.9 – Specific heat capacity

(Maass et al., 1926)

for the range of 163.15 K to 217.15 K, Maass et al. (1926) provide an equation that we convert to the SI units as follows:

$$C_p\left[\frac{J}{kg.K}\right] = 1673.6 - 11.84072 * T + 0.0523 * T^2 \qquad \textit{eq. 3.18}$$

As a separate approach, we use the measurements from the Giauque and Egan (1937) for 15.52 K to 189.68 K. This data has been fitted by Wang et al. (2018) to give:

$$C_p = -10^{-06} * T^4 + 0.001 * T^3 - 0.2371 * T^2 + 28.135 – T - 354.17. \qquad \textit{eq. 3.19}$$

However, we fitted the same data set into a slightly different equation here:

$$C_p = -10^{-06} * \mathrm{T}^4 + 0.001 * \mathrm{T}^3 - 0.2381 * \mathrm{T}^2 + 28.253 – \mathrm{T} - 355.66 \qquad \textit{eq. 3.20}$$

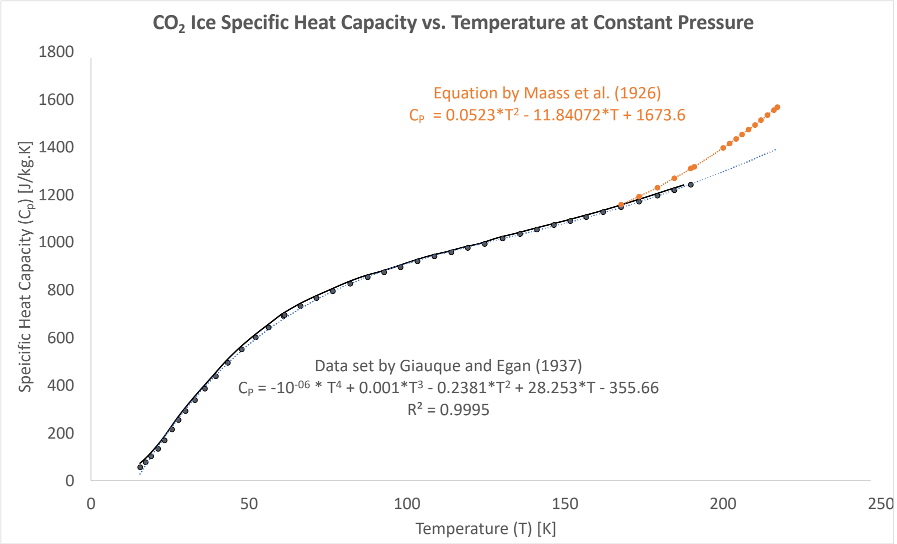

Figure 3.9 – Specific heat capacities of CO_2 ice for temperature ranges of 15.52 K to 217.15 K (Giauque and Egan, 1937; Maass et al., 1926)

3.4.5 Thermal Conductivity

Ross and Kargel (1998) summarize the various laboratory tests done around thermal conductivity of series of ices; one is CO_2. Based on the work of Konstantinov et al. (1988), in low pressure (isochoric) Ross and Kargel provide this equation for the temperature range of 170 K and 210K (Ross and Kargel, 1998[4])

$$log_{10} K = -5.39941 + 5.45894 * log_{10} T - 1.41326 * (log\rrbracket_{10}\llbracket T)^2 \qquad eq.\ 3.21$$

---

[4] See Table 1 in Ross and Kargel, 1998

Note that as Shieh et al. (2022) demonstrate the thermal conductivity of CO_2 ice at higher temperature and higher pressure would be much lower, for example the mean value of thermal conductivity of CO_2 ice at room temperature and at 0.3 to 0.5 GPa is about 0.28 $\left[\frac{W}{m.K}\right]$.

In their laboratory, tests and research done by Song et al. (2013), in the context of CO_2 frost formation and its thermal conductivity, discusses that the thermal conductivity of CO_2 between 150 K and 200 K might not change vastly. Song et al. (2013) report the following proposed equations for CO_2 frost thermal conductivity:

- Lee, Jhee, and Yang (2003): $K = 0.132 + 3.13 * 10^{-4} * \rho + 1.6 * 10^{-7} * \rho^2$
- Sanders (1974): $K = 1.202 * 10^{-3} * \rho^{0.963}$
- Yonko and Sepsy (1967): $K = 0.024248 + 0.00072311 * \rho + 0.000001183 * \rho^2$

ρ is the CO_2 ice density. If we assume the proposed equation by Mangan (2017) (see eq. 3.16) is valid in this context, it can be shown that thermal conductivity of CO_2 frost reduces by ~5% across 40 degrees Kelvin from 160 to 200.

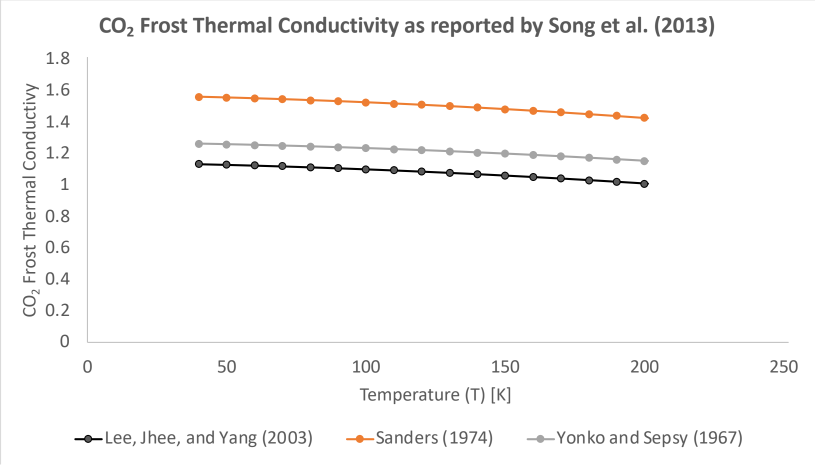

Figure 3.10 – A comparison of CO_2 frost (as a function of density) as reported by Song et al. (2013) (sources in the plot)

3.5 Solid Nitrogen

Umurhan et al. (2017) discuss that N_2 experiences two different crystal structures of hexagonal close-packed crystal (Scott, 1976; Fracassi et al., 1986) in its β phase, as well as primitive cubic crystals in the α phase (Scott, 1976). The transition point happens at 35.6 K (Fray and Schmitt, 2009). Here, we do not include the impact of the pressure; because the pressures where exotic ices exist (e.g., at the surface of Pluto or Triton) tend to be low enough to have limited or no effect.

3.5.1 Density

At low temperature, the density of N_2 ice remains relatively constant (Satorre et al., 2008). Satorre (2008) provides a plot that shows for solid nitrogen (below 23 K) the density varies from 950 to 970 $[\frac{kg}{m^3}]$. Trowbridge et al. (2016), using the data provided by Scott (1976) and the works of Krupskii et al. (1975), provide the below equation in $[\frac{kg}{m^3}]$:

$$\rho = 0.0134 * T^2 - 0.6981 * T + 1038.1 \qquad \textit{eq. 3.22}$$

However, considering the phase transition temperature of solid nitrogen at 35.6 K, using data from the same data set collected by Krupskii et al. (1975) and reported by Scott (1976), we propose two equations below for the different temperature ranges rather than the one used by Trowbridge et al. (2016); and since this data set covers more data points than the plot provided by Satorre et al. (2008), we propose the use of *eq. 3.23* and *eq. 3.24* for exotic environmental conditions.

For these equations, we have fitted the data from Krupskii et al. (1975), as reported by Scott (1976), instead of the data provided by Satorre et al. (2008). These equations have also been plotted in Figure *3.11*:

$$T < 35.6\text{ K}: \rho = -0.0334*T^2 + 0.5547*T + 1029.1 \qquad \textit{eq. 3.23}$$

$$35.6\text{ K} < T < 60\text{ K}: \rho = -0.0134 * T^2 - 0.6981 * T + 1039.1 \qquad \textit{eq. 3.24}$$

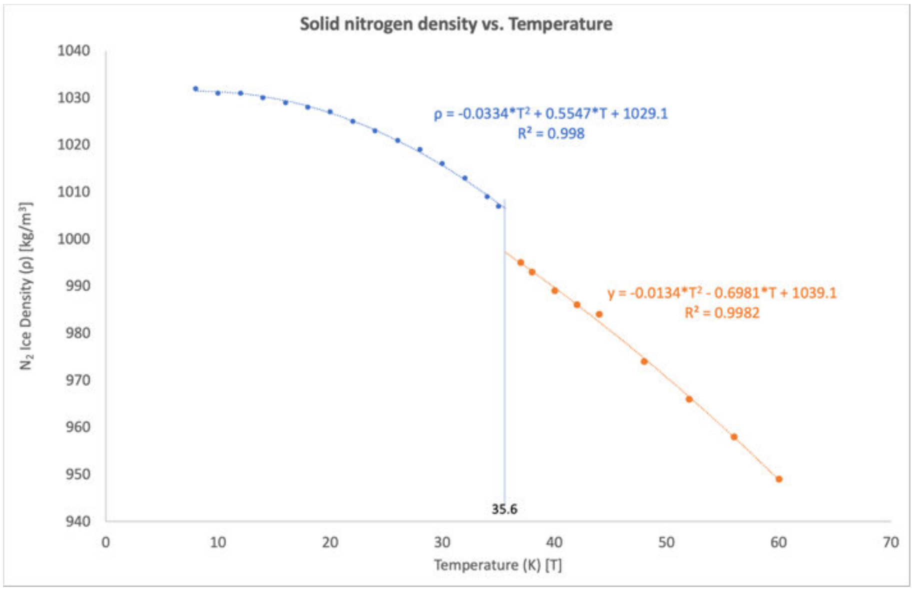

Figure 3.11 – Solid nitrogen density with equations representing two different phase using data from Krupskii et al., 1975, (reported by Scott (1976))

3.5.2 Flow Law Parameters

For solid nitrogen, we still use the Arrhenius Law. Eluszkiewicz et al. (1990) mention there is not much research available on solid nitrogen and argue that, since the crystal structure of solid nitrogen and solid methane is similar, the flow law parameters for methane can be used for solid nitrogen. Umurhan et al. (2017) reported that the crystal structure of nitrogen changes from cubic to hexagonal close-packed during its phase transformation. The solid methane crystal structure is cubic close-packed (Maynard-Casely et al., 2020), and the structure does not change during methane phase transformation (Mooy, 1931); therefore, for the temperature range below 35.6 K, the crystal structure of solid nitrogen resembles that of the solid methane. This supports the Eluszkiewicz's argument (albeit for the temperatures below 35.6 K. Figure 3.12 also shows that these parameters could only work for a limited temperature range). Eluszkiewicz et al. (1990) provide the following parameters for solid methane from Bolshutkin et al. (1968):

$$A_{const} = 10\frac{1}{MPa^3.s}$$

$$Q = 8400\frac{J}{mol}$$

$$Glen's\ exponent\ (n) = 3$$

Yamishita et al. (2010) demonstrated the results of series of tests under two temperatures of 45 and 56 K and reported the flow law parameters. Later, Moore et al. (2016) fitted the information to an Arrhenius form and arrived at the activation energy. Umurhan et al. (2017) summarized and reported the parameters as functions of temperature which we have summarized here and recommend for use for exotic ices.

$$A_{const} = 0.00501 * e^{\left(9.378-\frac{422}{T}\right)}\frac{1}{MPa^n.s}$$

$$Q = 3500\frac{J}{mol}$$

$$Glen's\ exponent\ (n) = 0.0155 * T + 1.4025$$

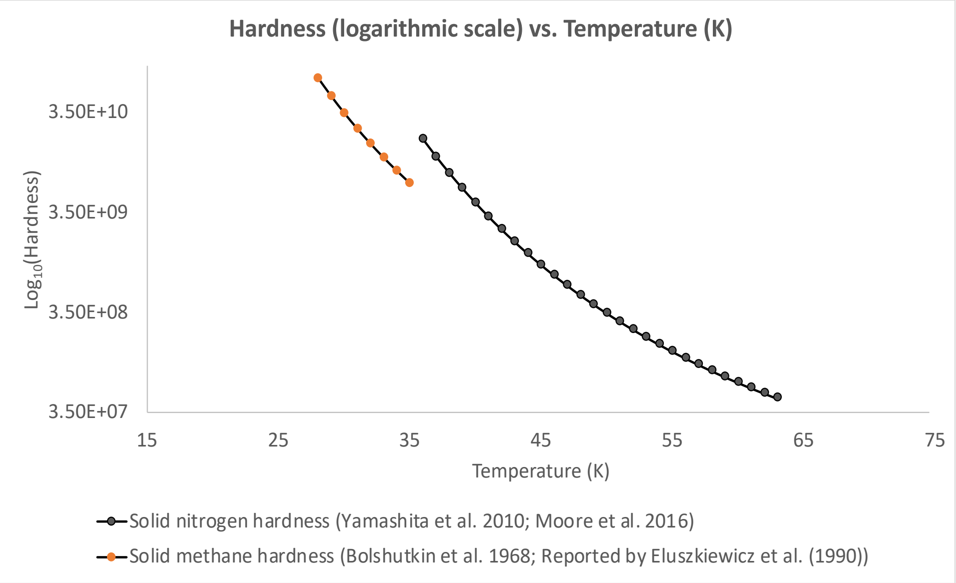

Figure 3.12 – Temperature vs. rigidity for solid nitrogen using two different models

3.5.3 Specific Heat Capacity

Scott (1976) provided a smoothed version of the data provided by Giauque et al. (1933) and Bagatskii et al., (1968). This data is provided in and fitted to eq. 3.25 and eq. 3.26.

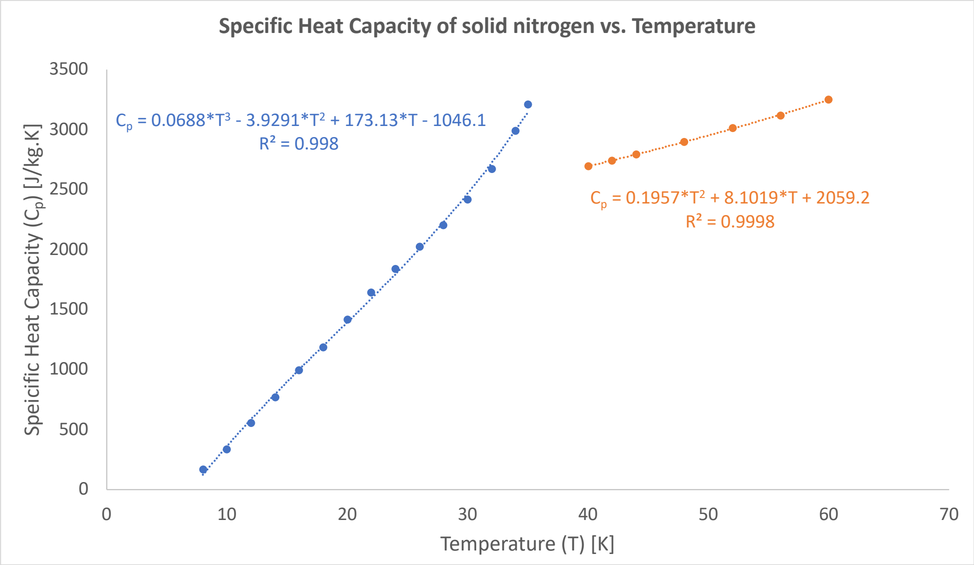

Figure 3.13 – Specific Heat Capacity of solid nitrogen vs. Temperature

$$T < 35.6\text{ K}: C_p = 0.0688*T^3 - 3.9291*T^2 + 173.13 - T - 1046.1 \qquad \textit{eq. 3.25}$$

$$35.6\text{ K} < T < 60\text{ K}: C_p = 0.1957*T^2 + 8.1019*T + 2059.2 \qquad \textit{eq. 3.26}$$

3.5.4 Thermal Conductivity

Sagmiller and Hartwig (2020) provide a full analysis of the works of different researchers who tried to determine the thermal conductivity of solid nitrogen. They summarized the works of Roder (1962), Manzhelii and Krupskii (1968) (via Manzhelii et al., 1999), Koloskova et al. (1973), Manzhelii et al. (1975), Cook and Davey (1976), and Stachowiak et al. (1994). We merged these works, ignoring parts of the data provided by Roder (1962) and Cook and Davey (1976) due to issues with the accuracy of their samples (see the respective papers as well as

Scott, 1975; Stachowiak et al., 1994; and Sagmiller and Hartwig, 2020). This merged data was fitted into two curves in Figure 3.14, and eq. 3.27 and eq. 3.28.

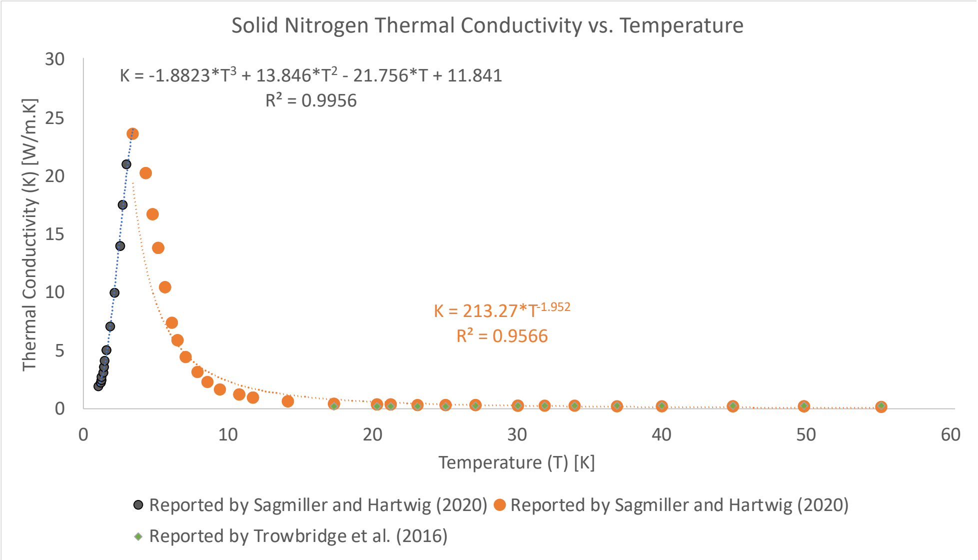

Figure 3.14 – Thermal conductivity of solid nitrogen

as summarized by Sagmiller and Hartwig (2020) as well as the equation provided by Trowbridge et al. (2016)

$$T < 4\ \mathrm{K}:\ K = -1.8823*T^3 + 13.846*T^2 - 21.756*T + 11.841 \qquad \textit{eq. 3.27}$$

$$4\ \mathrm{K} < T < 60\ \mathrm{K}:\ K = 213.27 * T^{-1.952} \qquad \textit{eq. 3.28}$$

Trowbridge et al., (2016), based on the work done by Scott (1976), provide the following equation for thermal conductivity of solid nitrogen as a function of temperature. As seen in Figure 3.14, this equation works best from about 15 K to 60 K:

$$K = 0.1802 * T^{0.1041} \qquad \textit{eq. 3.29}$$

It should be noted that the thermal conductivity of solid nitrogen at more than 20 K does not vary much with changes in temperature (Koloskova et al., 1973; Scott, 1975; Sagmiller and Hartwig, 2020).

4 Modelling 3D Flow of Potential Glaciers on Mt. Sharp (Aeolis Mons) in Gale Crater, Mars

4.1 Introduction

4.1.1 Contributions of this Study

In this chapter, I investigate the potential for ice to have shaped some of the surface features of Gediz Vallis, north of Mt. Sharp in Gale Crater on Mars. I study images of Mars taken from orbit and from the Curiosity Rover. For this, I modelled the behaviour of cold-based glaciers (to examine the flow direction, without simulating any possible erosion) for two initial scenarios that differ only in the ice accumulation rates: 1 mm and 10 mm per year for 30,000 years. The purpose of this work is only to determine whether ice would track and its flow directions would have be aligned with the features that have captured by Curiosity. This will be the first step. If ice flow directions did not align with the features, there would not be any benefits in modelling the potential glacial erosion. Since my model pertains to the Hesperian epoch, it is a better approach to slowly introduce different variables, and not include various uncertainties, at the same time, to the modelling process beyond the minimum required to determine the ice flow direction. Once the results confirm the flow directions, future studies can build on these findings and examine the potential resultant glacial erosion.

My results suggest that the hypothesized glaciers could have flowed in the direction that would support the formation of the key observed features, so they could have participated in shaping those key landscape features in Gediz Vallis.

4.1.2 Background

A suite of surface features on Mars is consistent with, or suggest, past ice accumulation. They include the North Polar Layered Deposits (Smith, 2022 and references within); Viscous Flow Features (VFFs) (Levy et al., 2014); the Latitude-Dependent Mantle (e.g., Kreslavsky and Head, 2002; Head et al., 2003; Dickson et al., 2015); and Tropical Mountain Glaciers (e.g., Shean et al., 2005; Head and Weiss 2014), which are viewed as low-latitude VFFs. The Polar Layered Deposits (PLDs) consist of alternating layers of ice and dust in the north and the south (e.g., Byrne, 2009; Smith, 2022). The south polar layered deposits (SPLDs) also include about 1% CO_2 ice (Smith et al., 2022), which form a stratigraphic sequence (Bierson et al., 2016; Putzig et al., 2018; Alwarda and Smith, 2021). The latitude-dependent mantle comprises ice masses upwards of tens of meters thick, with a high dust content; these probably formed during recent ice ages (Kreslavsky and Head, 2002; Head et al., 2003; Milkovich and Head, 2005; Smith et al., 2020). VFFs number in the tens of thousands and are primarily found between 30° and 60° in both hemispheres (Levy et al. 2014). Investigations of the spatial distribution, thickness, and dynamics of ice masses across different Martian latitudes can contribute to the understanding of the planet's climatic and geological evolution (Smith et al., 2020).

One area that has been subject to extensive study, feature analysis and modelling into Mars's past climate is Gale Crater. This site has been explored in detail by the Mars Science

Laboratory (MSL) Curiosity rover. Located at 5.4°S 137.8°E, near the equator (Figure 4.1 (a)) and on the dichotomy boundary of Mars (Figure 4.1 (b)), Gale Crater's diameter spans ~155 km (Figure 4.1 (c)). The age of the crater is estimated to be 3.6 to 3.8 billion years, placing its formation during the Late Noachian to Early Hesperian period (see Greeley and Guest, 1987; Thomson et al., 2011). Gale Crater features a central mound that rises roughly 5 km above the crater floor and notably above the rim of the crater: Aeolis Mons, also known as Mt. Sharp.

The sedimentary origin of Mt. Sharp remains a mystery. Published ideas about the formation of Mt. Sharp (as well as the formation of the geomorphic features present around the mountain) include aeolian activity, volcanism, lacustrine deposition, spring-related processes and mass wasting (e.g., Kite et al., 2013; Fairén et al., 2014; Day et al., 2016; Williams et al., 2022 and references therein). Evidence of aqueous activity and former lakes is abundant and extensive in the crater (e.g., Grotzinger et al., 2015; Palucis et al., 2016). Previous studies suggest at least three distinct lake stands could have occurred after the formation of Mt. Sharp. Each of these would have existed for over 1,000 years (Palucis et al., 2016). These lakes would have been initially sourced by regional fluvial systems, from locations such as Farah Vallis (northeast of Mt. Sharp), and later by more localized hydrological inputs (Palucis et al., 2014; Palucis et al., 2016 and references therein). Moreover, the Peace Vallis fan system (northwest of Mt. Sharp) may have been produced by sustained fluvial activity, and potentially from snowmelt, which would have transported sediments that formed the deposits observed at the Curiosity landing site (Palucis et al., 2014). There is also evidence of significant chemical alteration (Mangold et al., 2019), which includes the dissolution of minerals and formation of new minerals, due to aqueous interactions (Milliken et al., 2010; Chan and Netoff, 2017; Caravaca et al., 2021). This implies minerals interacted with liquid water over prolonged periods. Hughes et al. (2022) argue that canyon floors could reflect fluvial activity, landslides, and debris flows. The floor of Gale Crater (known as Aeolis Palus) also reflects past water activity through fluvial and deltaic sandstones and conglomerates (Stack et al., 2019; Williams et al., 2022). Moreover, it is notable that some studies have also suggested that massive, buried ice could currently be present to the east of Gale Crater (Fastook and Head, 2024; and Watters et al., 2024).

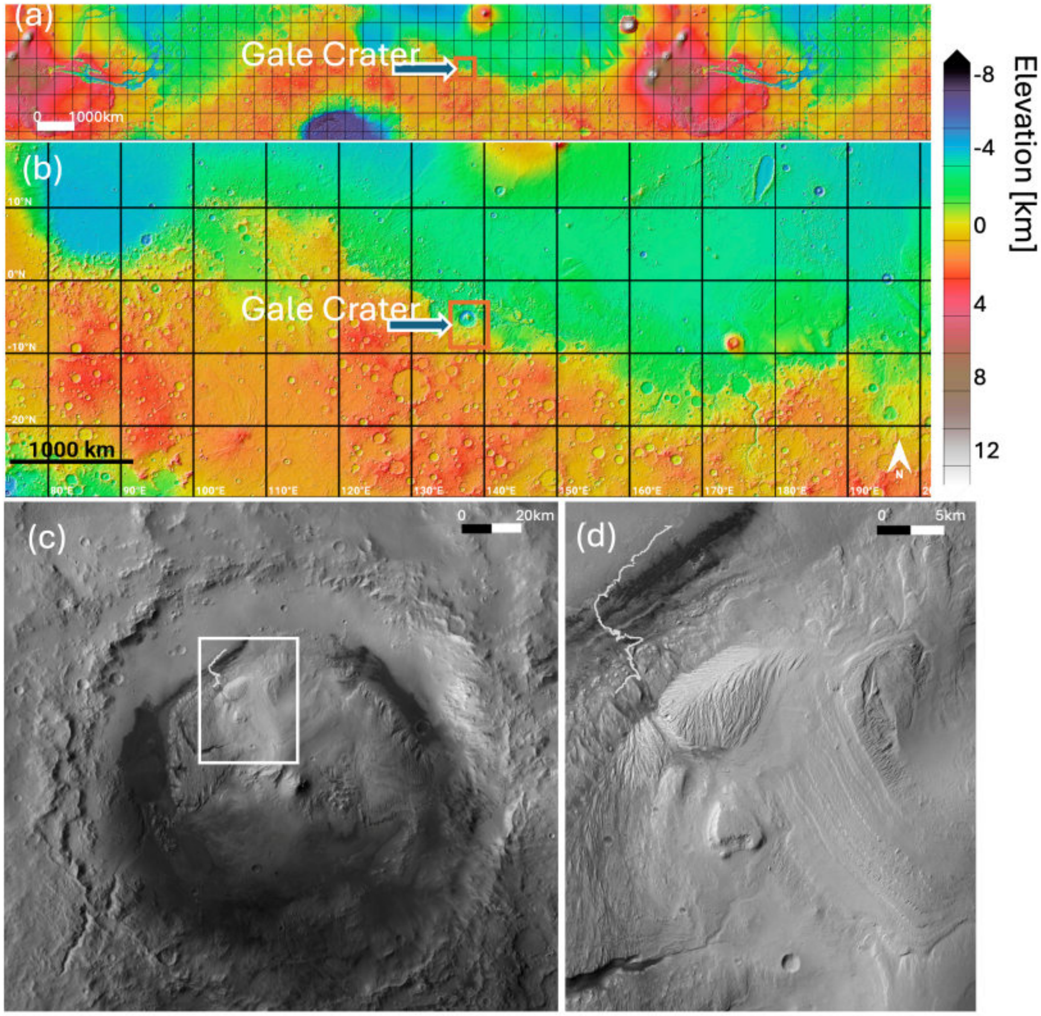

Figure 4.1 – Gale Crater Geographic Setting

(a) Mars Global Surveyor Mars Orbiter Laser Altimeter (MGS MOLA) Shaded Relief / Colourized Elevation showing the context and location of Gale Crater. (b) MGS MOLA Colourized Elevation

map showing Gale Crater with respect to the equator (i.e., zero degrees latitude). (a) and (b) were generated using JMARS (ASU, NASA/JPL) (c) Gale Crater with rectangle showing focus area for this study. (Source: Context Camera Mosaic) (d) The main area of focus of this study: Gediz Vallis and its potential ice accumulation area. The path of Curiosity up to sol 4609 (meaning 4609 Martian days after the Curiosity rover landed on Mars on August 6, 2012) is marked in white as it ascends into Gediz Vallis and beyond in (c) and (d) (Source: https://science.nasa.gov/mission/msl-curiosity/location-map/*; retrieved on July 28, 2025).*

Mars's present climate (i.e., dry and cold) differs significantly from its past climates. The variations in the planet's climate are influenced by its orbital parameters (various sources e.g., Forget et al., 2006; Madeleine et al., 2019), which have varied greatly over the past 4 billion years (Laskar et al., 2004). Martian climate changes are also governed by insolation variations; these are generally like terrestrial Milankovitch cycles (especially around ice-stable temperatures (Toon et al., 1980; Kite et al., 2012)), but with much larger spin-axis obliquity, as well as orbital eccentricity variations (Laskar and Robutel, 1993). Laskar et al. (2004) calculated these variations for tens of millions of years, and later work examined the significant impacts of the obliquity and eccentricity variations on the recent Martian climate (e.g., Levrard et al., 2007; Madeleine et al., 2009; Emmett et al., 2020), including insolation, atmospheric circulation, and thus the deposition of ice across Mars.

Laskar et al. (2004) reported probabilities between ~60% and ~90% for obliquities exceeding 60° in the past 1 and 3 Gyr, respectively (more recent than the formation of Gale Crater and probably during the time when liquid water could have been stable (e.g., Palucis et al., 2014; Palucis et al., 2016 and references therein)). Such large variations could allow periodic ice buildup at low latitudes (Madeleine et al., 2009), especially on high mountains (Forget et al., 2006). Madeleine et al. (2009) simulated accumulation of ice masses across the globe when Mars obliquity was 35º; within Gale Crater the rates exceeded 1 mm/yr. Notably, this obliquity would have occurred during the most recent 4 Myr (Laskar et al., 2004), potentially indicating recent ice accumulation on Mt. Sharp.

Considering the age of Gale Crater, as well as the long-term variability in orbital parameters, accumulation of considerable ice deposits within Gale Crater would have been likely in several points in the past. Given the current orbital values, water ice is currently unstable on the surface of Mars except for in polar regions; however, Mellon and Sizemore (2022) suggest that "ground ice would have been stable at all the landing sites for extended periods of tens of kyrs when the obliquity exceeded about 29º–33°". Those values were quite common until 5 Ma (see Figure 9 of Laskar et al. (2004) which shows the average of the Martian obliquity decreasing by ~10 degrees about 5 Ma); as such some ice could have persisted in Gale Crater for the portion of the obliquity cycle that exceeded 30° (i.e., about 30,000 years, as the full Martian obliquity cycle would take ~120,000 years (Laskar et al., 2004) and the largest values are ~1/4 of the total period), perhaps more than once during the most recent 5 Myr. Thus, Gale Crater could have experienced major environmental changes and possibly was mantled with thick ice as recently as 5 Myr ago, when the average obliquity was higher than its current value of ~25.19º. In short, we chose a 30,000-year modelling period because it corresponds to highest obliquity value of a Martian obliquity cycle. We suggest that this is the interval corresponds to the length of time surface ice would have been stable and able to accumulate at low latitudes.

Le Deit et al. (2013), following a study by Anderson and Bell (2010), proposed a glacial hypothesis for the evolution of some of the features within Gale Crater. This hypothesis suggests that ice accumulation occurred on Mt. Sharp, and that the associated glacial and periglacial processes could have led to the formation of diverse landforms. We will refer to this as the "glacial hypothesis" in this section. This hypothesis motivated various studies to investigate the potential existence of ice in the crater (Anderson and Bell, 2010; Le Deit et al., 2013; Fairén et al., 2014; Williams et al., 2022). Fairén et al. (2014) use high-resolution images from orbit to describe potential glacial, periglacial, and fluvial (including glacio-fluvial) landforms within the crater, as well as the potential existence of past ground ice and ice-related lakes high up on Mt. Sharp. Williams et al. (2022) presented ice flow modelling results to help describe rock glacier-like features on the northeastern slopes of Mt. Sharp. They modelled the shape of these forms to constrain their potential formation times and flow rates.

Mt. Sharp has easily identifiable features that can be attributed to wind scouring, mass wasting, surface runoff, groundwater, ice-related processes, or a combination thereof (e.g., Fairén et al., 2014; Hughes et al. 2022), but not all features are easily explained, thus the need to consider alternative mechanisms of erosion and transport for at least a few features.

In this manuscript, we present new geomorphic evidence and hypothesize that flowing ice formed several features in Gediz Vallis. Then, we test the hypothetical scenario with glacial modelling. In Sections 4.2 and 4.3, we look briefly into the geologic settings of Gediz Vallis to describe and examine some of the geomorphic features that have been captured by the Mars Science Laboratory rover, Curiosity that closely resemble glacial landforms on Earth. Sections 4.4 and 4.5 describe our modelling setup and results. Finally, in Sections 4.4, 4.6 and 4.7 we compare the modelled ice flow fields with the orientation of putative glacial landforms on Mt. Sharp and discuss our findings.

4.2 Geographic Setting

Our study area encompasses the northern part of the Gale Crater (white box in Figure 4.1(c)), with a focus on Gediz Vallis, a valley on the north side of Mt. Sharp. Gediz Vallis that is currently being explored by the Curiosity rover, which has provided and continues to provide a wealth of information about the stratigraphy, landforms and the environment. The 9 km-long Vallis (Figure 4.2) reaches 900 m in width and 140 m in depth. It has an average slope of about ~10° and is incised in sulfate-bearing bedrock (Hughes et al., 2022). A curious bedrock promontory named Mont Mercou, which is discussed below, is located slightly beyond and downhill of Gediz Vallis. Sand accumulation forms dunes and smaller bedforms along the walls and floor of Gediz Vallis (Anderson and Bell, 2010; Le Deit et al., 2013; Hughes et al., 2022). In this section we examine Gediz Vallis, seeking geological hints of glacial and preglacial activity in the past, briefly describing the Mars images and the geomorphic evidence used.

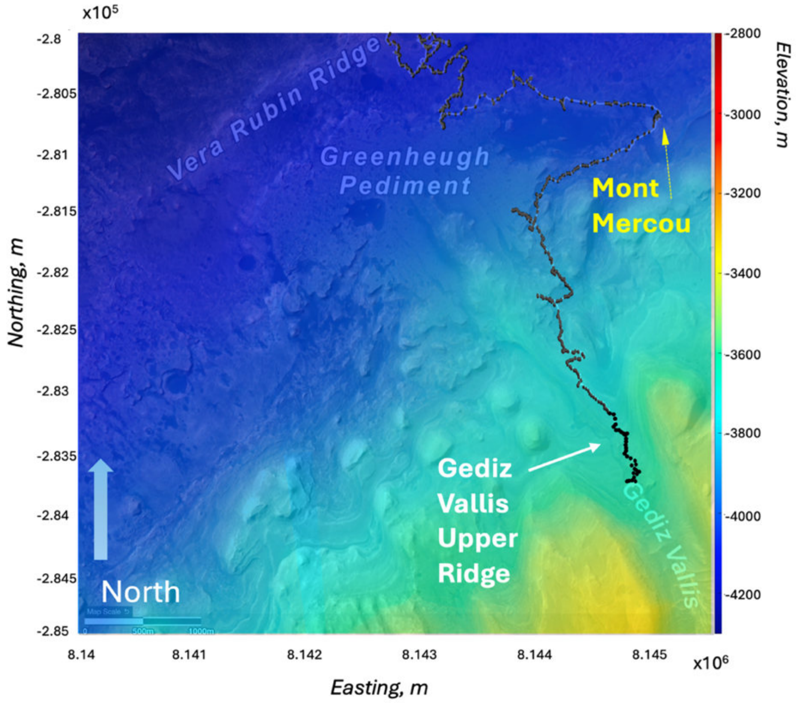

Figure 4.2 – Colourized topography showing Gediz Vallis and nearby major geomorphic features The path of the Curiosity rover above about -4200 m is shown up to sol 4042 only (marked in black) for image readability. The elevation data is primarily from HiRISE data (McEwen et al., 2007), supplemented with data from the Mars Orbiter Laser Altimeter (MOLA, Smith et al., 2001) for elevation referencing.

4.3 Data: Mars Images

The primary field information used in this manuscript are images captured from the Martian surface by the Curiosity rover's Mastcam stereo imaging system (Bell et al., 2017; Malin et al., 2017). Curiosity's imaging system consists of two separate cameras each with different focal lengths (Left: 34 mm, and Right: 100 mm) mounted side-by-side on the rover's Remote-Sensing Mast, about 2 m above the ground surface. The left camera is referred to as M34 or ML; the right camera is referred to as M100 or MR. Malin et al. (2017) provide detailed information on the cameras, and the associated hardware and software used to produce the colour images. Labels for the mosaics generally start with the sol number (Martian day of the Curiosity rover's mission, starting Aug 6, 2012), followed by the camera's focal length (ML or MR) and the observation's sequence number. Figure 4.3(b), for example, features a portion of the mosaic "sol04298_ML_106371" derived from Mastcam images acquired on sol 4298 using the 34 mm focal length camera images. They make up the Mastcam sequence "Mcam 106371" of 75 individual M34 images.

4.4 Geomorphic Evidence in Gediz Vallis

4.4.1 Potential Roches Moutonnées with Distinct Grooves

During the traverse of Gediz Vallis, the Curiosity rover encountered examples of asymmetric bedrock hills and small bedrock knolls that resemble terrestrial roches moutonnées (Figure 4.3(c)). Roches moutonnées (literally translated as 'sheep rocks,' or 'sheep back-shaped rocks) are asymmetrical (in form and texture) bedrock features, characteristic of glacial erosion. On Earth, the stoss side of these features (facing up-glacier) tends to be smooth due to abrasion and to slope gently up-glacier. On the opposite, lee sides (facing down-glacier) surfaces tend to be rougher and steeper as the lee sides are typically fractured surfaces, due to glacial quarrying (plucking) (Figure 4.3(d)).

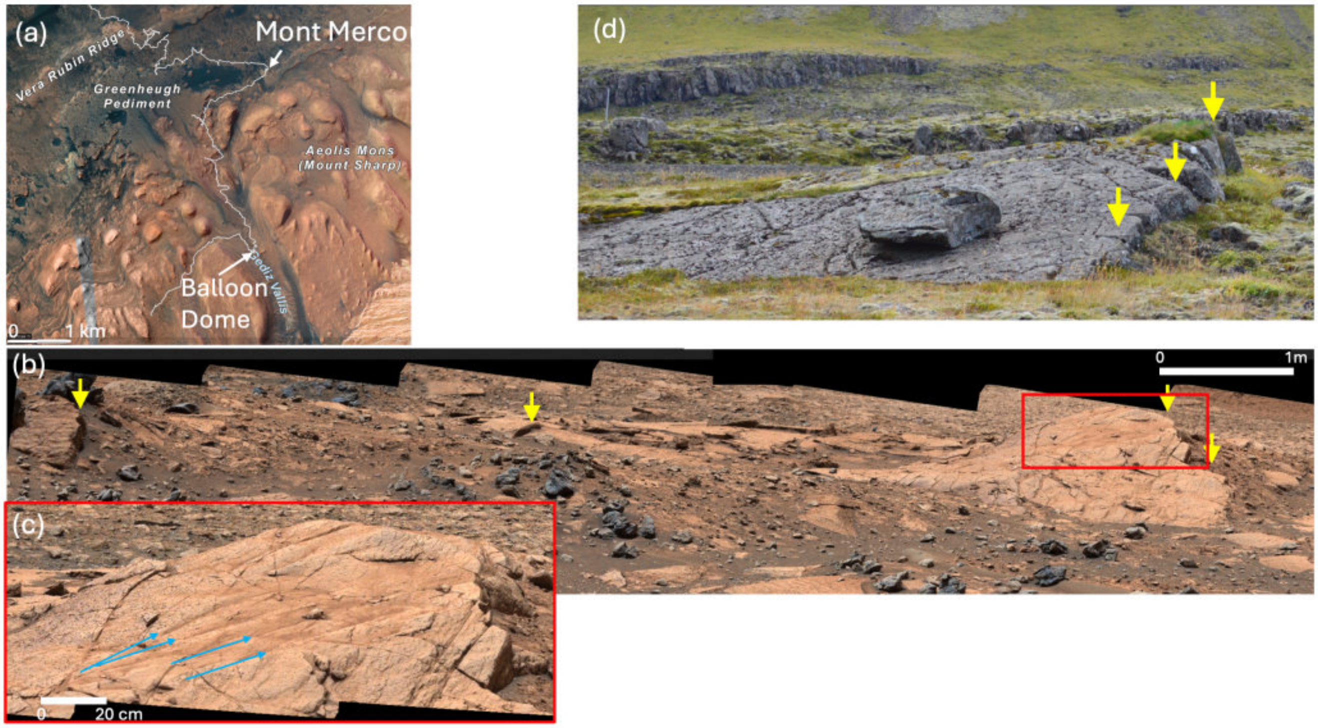

Figure 4.3 – Geomorphic features in Gale Crater suggestive of former glacial erosion.

(a) Map showing Curiosity's path. The location of (b) is marked as Balloon Dome at the tip of white arrow. Source: https://science.nasa.gov/mission/msl-curiosity/location-map/ (b) Mosaic sol04298_ML_106371, looking northwest. The terrain features a grooved bedrock knoll that closely resembles terrestrial roches moutonnées (d). The plucked areas are marked with yellow arrows. The red rectangle outlines Balloon Dome. (c) The zoomed-in view of Balloon Dome was acquired 4 days later (sol04302_ML_106393). Grooves climb from left to right, suggesting that hard rock asperities in forceful contact with the bedrock moved north (toward 20 deg azimuth) and that rock blocks on the right side of the knoll were removed (panels b and c credit NASA/JPL-Caltech & MSSS). (d) A small roche moutonnée in west Iceland, showing the contrast between the marks of abrasion on the stoss slope and plucking on the lee slope. Boulder on top is ~1 m wide. Ice flow was from left to right (adapted from Conway et al., 2018).

4.4.2 Mont Mercou

Mont Mercou (Figure 4.4) is a truncated ridge near the lower section of Gediz Vallis that closely resembles the archetypal product of glacial quarrying (Mont Mercou location with the valley is shown in Figure 4.2). Several features of Mont Mercou include:

1) Extensive fracture system on its upper surface, recently mapped in 3D by Schmauss et al. (2025): this could have been caused by plucking resulting from moving ice in areas where the bedrock was weaker.

2) The 6-meter-high “cliff”: this is a feature appearing abruptly relative to the surrounding area. This resembles the steep-lee sides of terrestrial roches moutonnées that tend to be formed through glacial plucking on Earth.

3) The absence of the dislodged blocks: The removal of bedrock block (or blocks) on the north side of Mont Mercou onto level terrain, and the absence of dislodged blocks today could be an indication of the blocks being plucked and transported away by the moving ice.

These features are consistent with the hypothesis that Mont Mercou was shaped during a period of glaciation through the interaction between the ice and the bedrock.

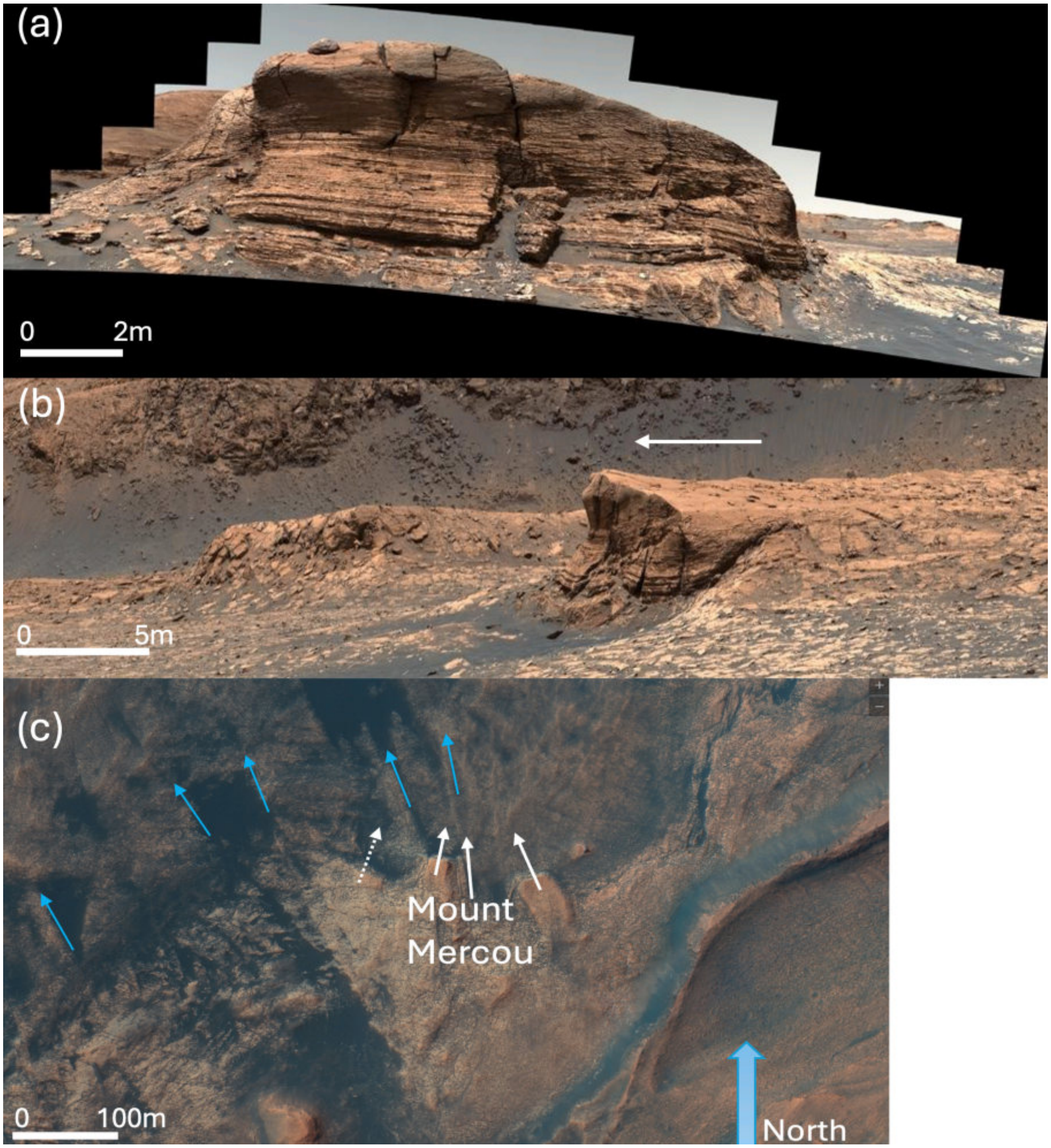

Figure 4.4 – (a) Mont Mercou, a 6-meter-high stands out in low relief terrain near Gediz Vallis (sol03051_MR_015933, looking south).

The asymmetric form of this feature, and the missing dislodged blocks on the north side, resemble the characteristics of roches moutonnées on Earth. (b) This view is looking ESE toward azimuth 120º (mosaic sol03040_ML_015879). The glacial hypothesis would require ice flow to have been from right to left (towards N-NE) as indicated by the white arrow. (c)

White arrows show inferred ice flow directions, assumed to be perpendicular to plucked ledge faces. Blue arrows parallel bedrock lineaments. (Source: https://science.nasa.gov/mission/msl-curiosity/location-map/*).*

4.4.3 Other Potential Geomorphic Examples and Evidence of Glacial Erosion

Other than the examples provided above, Curiosity has captured other evidence that could be interpreted as evidence of past glacial erosion within Gediz Vallis. Since much of these examples are open to various interpretations, including glacial erosion, we will not examine them in detail beyond a brief mention below:

- Grooves and ridges on generally smooth surfaces. Such potential expressions of glacial abrasion (i.e., striations) on "smooth polished" surface of geological features were observed on top of Mont Mercou, before they were first encountered by Curiosity. Similar smooth, gently undulating surfaces extend across several rock units stratigraphically above Mont Mercou. We hypothesize that these smooth surfaces probably reflect glacial abrasion because it tends to bevel bedrock surfaces; in contrast, aeolian abrasion tends to accentuate the lithological impact and difference in rock strength rather than smooth the surface. It should be noted that warm-based glaciers are generally required for effective glacial erosion. As the result of their basal sliding, striations, peeling, plucking, and other erosional processes occur that collectively produce abraded features and landforms we see in these images. These can be seen on sols 3117 and 3125 (Figure 4.5).

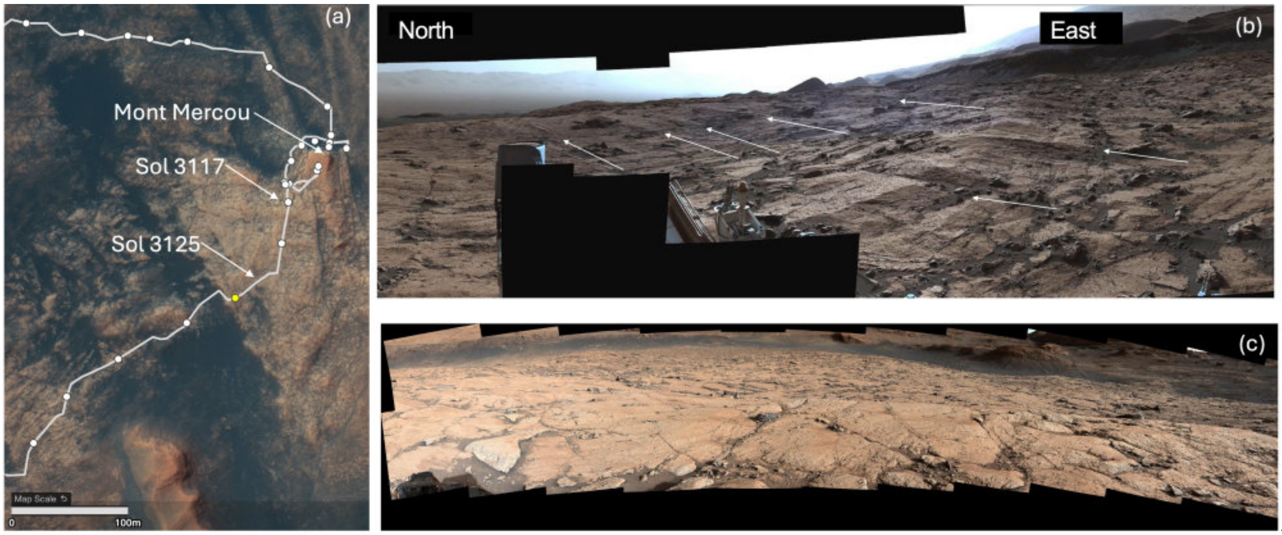

Figure 4.5 – Ridges and fluting on smooth surfaces can also be suggestive of glacial activity. As evident in these Mcam images acquired on sols 3117 and 3125 (a) Curiosity locations on sol 3117 and 3125 mosaics relative to Mont Mercou. (b) part of 360 degree-mosaic, sol03125_ML_100094: fluting and ridges on sedimentary rocks above Mont Mercou; these are consistent with former ice flow to the N-NE. (c) General smoothing of bedrock surface Sol03117_ML_100057.

- Truncated ridges and asymmetrical knolls that tend to be characteristic products of localized ice-bed interactions, where basal ice creep motion results in differential stress on the underlying bedrock, fractures the rock and subsequently entrains the debris. One key indicator of this process is stoss-lee asymmetry, which is characteristic of glacially eroded bedrock surfaces. As with roches moutonnées, stoss slopes tend to be smoothed by the overriding ice, whereas lee slopes tend to be steepened because of plucking where blocks of bedrock are plucked and then moved away by ice motion. Examples can be seen on sols, 3217 and 4140.

4.4.4 Glacial Hypothesis for forming these features

It seems to be difficult to explain how some of the mentioned bedrock surface features formed without considering the impact of glacial erosion. If the smooth and polished stoss sides (as seen in Figure 4.3, Figure 4.4 and Figure 4.5) are indeed results of glacial erosion, that would mean the valley, at some point (and episodically), experienced erosion by a warm-based, sliding glacier with sufficient basal debris to abrade the bedrock. Moreover, the glacial hypothesis provides explanation for some aspects of Mont Mercou's formation and morphology that might, otherwise, be difficult to explain. While there is substantial evidence in support of the influence of aeolian, fluvial and mass wasting processes in shaping Gediz Vallis, it is worthwhile to explore the possibility that ice flow also contributed either by eroding and shaping the valley and these features or in the case of thinner and slow-moving ice, by preserving the already formed features.

4.5 Modelling Method

4.5.1 Modelling Purpose and Scope

This study and our modelling efforts aim to address this question: If ice formed on Mt. Sharp, would it have flowed parallel to the inferred direction of flow over the asymmetric knolls and truncated ridges?

To test the glacial hypothesis, first, we will examine modeled flow directions for comparison with the geomorphic features. We will use low and high rates of ice accumulation to examine how they influence flow directions. We will also analyze the results to learn about catchment areas that could be formed for potential glacial meltwater. For this study we will consider pure water ice (no debris) and cold-based glaciers. Second, future modelling will consider warm-based ice and meltwater to further examine the impact and relevance of glacial erosion in the formation of Gediz Vallis. Our modelling represents a first-order test of ice flow patterns only. It will not consider glacial erosion explicitly (due to the assumption of negligible sliding). Similarly, it will also not incorporate basal meltwater. It is notable to mention that many of the observed features in the valley would require sliding, warm-based or debris-rich basal glacial flow.

4.5.2 Model Description

In conjunction with The University of California Irvine, The Jet Propulsion Laboratory (JPL) at NASA has developed a software application to model the flow of ice masses and their thermal characteristics on terrestrial settings (Larour et al., 2012). This open-source software is called the Ice Sheet and Sea Level System Model (ISSM). For this and past work, we extended the software to model ice accumulation, flow, and associated thermal properties in non-terrestrial settings, including the capability to simulate flowing carbon dioxide ice (Smith et al., 2022) and to incorporate temperature dependent material properties (other than rheology laws, which always have been temperature dependent) (Fard and Smith (2023) and references therein). ISSM uses the finite element method (FEM) to solve for stress and temperature distributions within ice masses in three dimensions (Larour et al., 2012). The FEM approach requires subdividing a large solid block of material into smaller, manageable "elements" connected at "nodes," and forming a "mesh" over the "domain." Then, the governing differential equations are solved numerically.

ISSM solves the full Stokes (FS) equations natively. This is the most computationally intensive approach. To reduce computational complexity with ISSM, several approximations can be applied, including the Blatter-Pattyn (BP) approximation (Blatter, 1995; Pattyn, 2003). The BP approximation belongs to a type of approximation method that are referred to as Higher Order (HO) approximations. Much like FS, BP leads to 3-dimensional solutions. To simplify the FS approach, BP assumes that the velocity in the vertical direction is much smaller than the velocities in the x-y plane, so that it can be ignored during the calculations without a major impact on the model results. BP is computationally intensive, but less so than FS. For these reasons, we use the BP approximation instead of FS, or other approximations that tend to make further simplifying assumptions such as Shallow Ice Approximation (which provides a depth-integrated shallow formulation with a prescribed vertically sheared velocity profile).

4.5.3 Numerical Mesh Development

To model ice mass growth, we first created a mesh over the domain of interest. As input to the mesh, we use the mosaicked topographic data available through HiRISE (McEwen et al., 2007) digital elevation models (DEMs) and data from the Mars Orbiter Laser Altimeter (MOLA, Smith et al., 2001) (Figure 4.6).

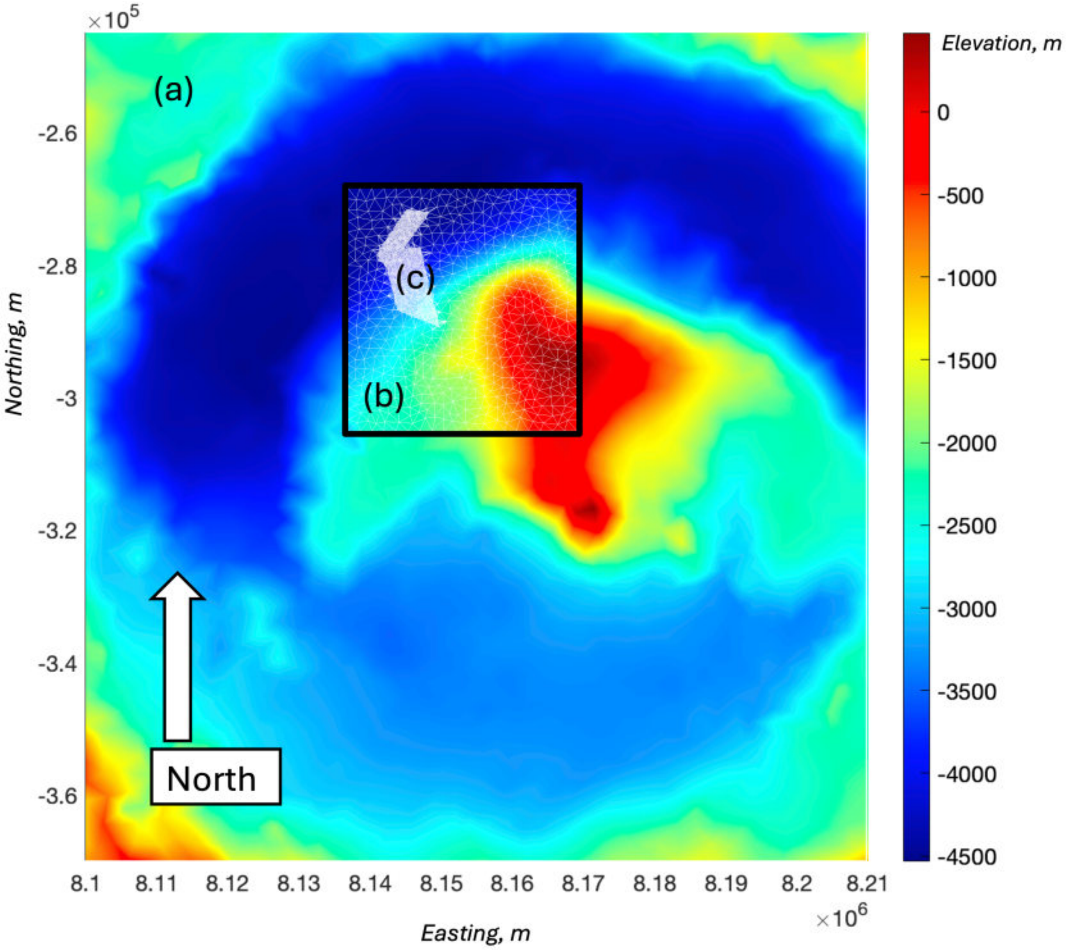

Figure 4.6 – Topographic map of Gale Crater and the modelling domain.

(a) Colourized topographic map of Gale Crater using MOLA 128 ppd data (Smith et al., 2001). (b) The modelling domain outlined in black rectangle where the mesh size decreases from 2000 m to 1700 m (i.e., spatially adaptive mesh) as the mesh elements approach the region of interest which is labeled as 'c'. (c) The mesh size is reduced to 150 m for the areas inside Gediz Vallis, so that relying on HiRISE Digital Elevation Models for topographic data, the mesh captures the main geometry of the Vallis.

For this study, we used a spatially adaptive mesh that allows the size of mesh elements to vary spatially. Each element is in shape of a triangle with sides varying from1700 m to 2000 m in the larger box and to 150 m inside the region of interest that encompasses the interior of

Gediz Vallis. For areas sufficiently distant from Gediz Vallis, the details of their geomorphology would have limited impact on the model result inside the Vallis, hence the lower the resolution of the mesh (Figure 4.6). In any given modelling year, during the simulation process, we divide the ice thickness into five virtual layers (in the vertical direction) of equal thickness to create a three-dimensional model of the ice mass dynamics, and to calculate and track the evolution of internal stresses, velocities and thickness profiles for each element in the 3D model over time. A quick check demonstrated that the direction of the flow vectors, beyond five virtual layers, were insensitive to the change of the count of the virtual layers, therefore five layers demonstrated the best trade-off between computational time and model's flow direction.

For the modelling purpose, we are assuming that no ice will flow into the modelling domain from outside of the marked black rectangle (i.e., inflow boundary conditions are set to zero). However, as ice flows and eventually reaches the boundaries of the modelling domain (e.g. well below the region of interest on the north side), it will only face atmospheric pressure (i.e., negligible resistance) and will flow outside of the domain. This assumption reflects the topography, which the northern section of the modelling domain lies in lower elevation region. In practice, horizontal velocity gradients normal to the boundary are set to zero. This will allow mass flux to continue naturally without constraining the flow direction or magnitude. While the ice near the boundary may keep some thickness, the model domain is defined large enough that any resulting outflow has a negligible effect on the upstream dynamics. This setup follows the standard open-boundary approach in ISSM and is suitable in this case, as it the main area of interest lies well within the interior of the modelling domain.

4.5.4 Model Input Parameters, Assumptions and Boundary Conditions

The input parameters are defined for two distinct modelling scenarios, each representing a slow and fast ice accumulation and flow, respectively. In the first scenario (SC1), ice accumulates at a rate of 1 mm/yr; in the second (SC2), ice accumulates at a rate of 10 mm/yr. These two accumulation rates are assumed to be uniform over the modelling domain (Figure 4.6(b)). They are chosen based on previous climate modelling simulations and studies (e.g., Madeleine et al., 2009; Forget et al., 2006) that suggest ice deposition rates in the range of 1-10 mm/yr near the Martian equator for moderate obliquity to peak obliquity conditions (~35°).

The choice of the modelling duration reflects the Martian obliquity cycle. The cycle in short includes periods when (1) surface temperatures were too high for water ice to remain stable, (2) orbital parameters favoured ice accumulation while ice also remained stable, (3) orbital parameters produced climate conditions to be too dry for deposition to occur, and finally (4) the period of high temperature again resulted in instability of ice. Parsons and Holt (2016) cite laboratory (from Chevrier et al., 2007) and theoretical studies (from Ingersoll (1970), Sears and Moore (2005), and Squyres (1989)) that under current atmospheric pressure on Mars, in the mid to low latitude regions, debris-free ice sheets could experience more than 5 mm/yr sublimation rate. As such, only one of the scenarios above (i.e., SC2) would produce favourable conditions for our simulations. Therefore, each scenario was modelled for 30,000 years, which corresponds only to the peak of an obliquity cycle, when ice would be stable enough to persist and atmospheric conditions would be moist enough to favour ice deposition.

(i.e., ice stability at low latitudes would be at its maximum). We therefore concluded that focusing only on the accumulation period would be sufficient for our study of the glacial hypothesis within Gediz Vallis. The output of each simulation was captured for every 1000 years. Both scenarios use the following assumptions and parameter values:

- Geothermal heat flux is 30 mW/m² (Grott et al., 2007) and uniform spatially.
- Annual surface average temperature is fixed at 230 K over the course of the simulation. This was selected as various studies, theoretical calculations and modelling efforts including General Circulation Models (GCMs) point to the mean annual Martian equatorial temperatures to vary from 220 to 240 K depending on the CO_2 density, albedo, dust and the orbital parameters (e.g., Forget et al., 2006; Wordsworth et al., 2013; Madeleine et al., 2019). Note that the temperature for nodes and elements below the surface is determined by the model's thermal calculations, and the surface temperature is the model's boundary condition. Besides thermal conductivity, geothermal flux, and heat capacity, this includes viscous dissipation based on the local stress and ice flow dynamics affecting each node of the mesh. As it will be shown later, the internal temperatures remain sub-melting in both scenarios, supporting the cold-based modelling assumption (see the next bullet point).
- The basal coefficient is set high. This assumption is to reflect the basal temperature being well below the pressure and solute dependent melting point, hence assuming a cold-based glaciation. This assumption, for the simulations presented herein, results in negligible sliding. Reducing the potential for basal sliding results in slower ice flow; however, the direction of ice flow should be only minimally affected by this assumption.

- The accumulated ice is assumed to be pure water ice. No rock or dust is included in the ice mass. Inclusion of rock debris in the ice affects the ice density and viscosity; its further analysis under the Martian conditions is outside of the current scope of this dissertation. Due to this assumption, we expect the modelled ice flow rates in this study (because of the assumption of pure water ice) to be higher than scenarios where there is rock present in the modelled ice.
- The model uses only net annual ice accumulation (no seasonal variability), a standard technique for studying glaciers over thousands of years.
- Gravitational acceleration on Mars is 3.71 m/s^2 (NASA fact sheet).
- The current topography serves as the surface on which ice accumulates.
- For the water ice rheology, these standard flow Glen's law parameters are used (Cuffey & Paterson (2010) and references therein):
    - $Glen's\ stress\ exponent\ (n) = 3$
    - $Ice\ Flow\ Factor\ (A_{const}) = 9 * 10^4$ [MPa^{-3} s^{-1}]
    - $Activation\ Energy\ (Q) = 60{,}000$ [J.mol^{-1}]
- The minimum ice thickness of any point across Gale Crater is 1 m; ISSM that does not allow for any point of a glacier to be thinner than 1 m. However, the results provided here are always for elements considerably thicker than 1 m.
- Once the model is solved for a 1000-year time period (i.e., transient modelling run), the output becomes the model input for the next period, ensuring temporal continuity.

4.6 Results

Although our simulations cover a larger domain than Gediz Vallis, for the purposes of numerical analysis and imaging, we focus on the high-resolution area shown in Figure 4.6(c). Furthermore, to provide model results relevant for the orientation of bedrock landforms potentially reflecting glacial erosion that were imaged by Curiosity, we concentrate on model output that bears on former ice flow direction along its route as much as possible, and focuses on the surface velocity (i.e., the vector sum of the surface velocity vectors (i.e., V_x, V_y, V_z)), and thickness evolution, we start from just south of the Vera Rubin Ridge and continue up to about the rover's location on sol 4300; then continue the path upward along the continuation of Gediz Vallis, following a path marked by yellow ellipses (Figure 4.7). For the part overlapping the Curiosity route, we follow exactly the rover's path where Curiosity imaged many geomorphic features at close range, allowing for close comparison between the ice flow direction calculated by our model and the observed landforms.

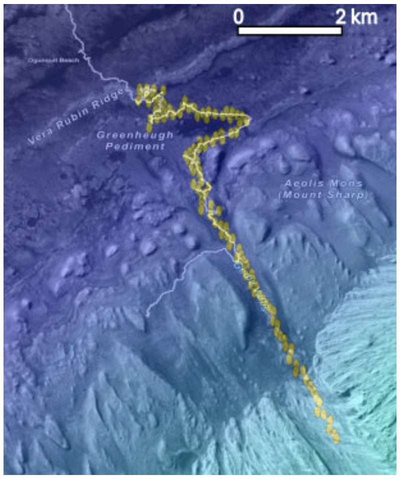

Figure 4.7 – Gediz Vallis area marked for analysis.

Here, we use the partial Curiosity route and extend it further southwest. This path is marked by larger yellow circles placed over the white line which represents Curiosity's route. The identified points are then used to analyze surface velocity, basal temperature, and ice thickness characterizing how these parameters change within the valley over the modelling period.

In both scenarios, the thickness, surface velocity, and basal temperature increase gradually and steadily. In SC1, each of these variables increases at a nearly uniform rate for the duration of the model (Figure 4.8). At the end of this simulation, the maximum velocity increases to 0.32 m/yr, while average velocities barely go over 0.16 m/yr. Maximum basal temperatures rise by less than 1 K over the full run to about 230.68 K.

The model with faster accumulation (i.e., SC2) yields non-linear thickening. For the first 17,000 years, all metrics grow linearly, similar to SC1, albeit with higher absolute values: maximum surface velocity peaks above 1.2 m/year, basal temperature reaches just above 232 K and ice thickness approaches about 190 meters. From this point, the behaviour of the two scenarios diverges. By the year 17,000, SC2 results in further ice accumulation north of Vera Rubin Ridge, which starts to act as a buttress, reducing the flux, which leads to increase of ice thickness inside the valley in the later time periods. After the year 20,000, as the ice builds up further north, the feedback becomes stronger, which results in further ice build-up within the valley (local ice accumulation), and slower ice flow within the valley. This table shows the reduction of the velocity increase rate (i.e., the slope of the plot in Figure 4.8). The continuous ice build-up in the northern part of the domain will eventually result in a slight decline in average velocity values after the year 25,000. From the year 17,000, the basal temperature will continue to increase. These changes correlate with the thickness growth rate reflecting the linear dependency of the temperature on the ice thickness.

The highest velocity observed is 1.3 m/year for SC2, at the end of the simulation. SC1 yields a maximum velocity of 0.32 m/year. Ice flow increases on steeper slopes (Figure 4.9) as expected because ice flow increases with the shear stress and, hence, the slope.

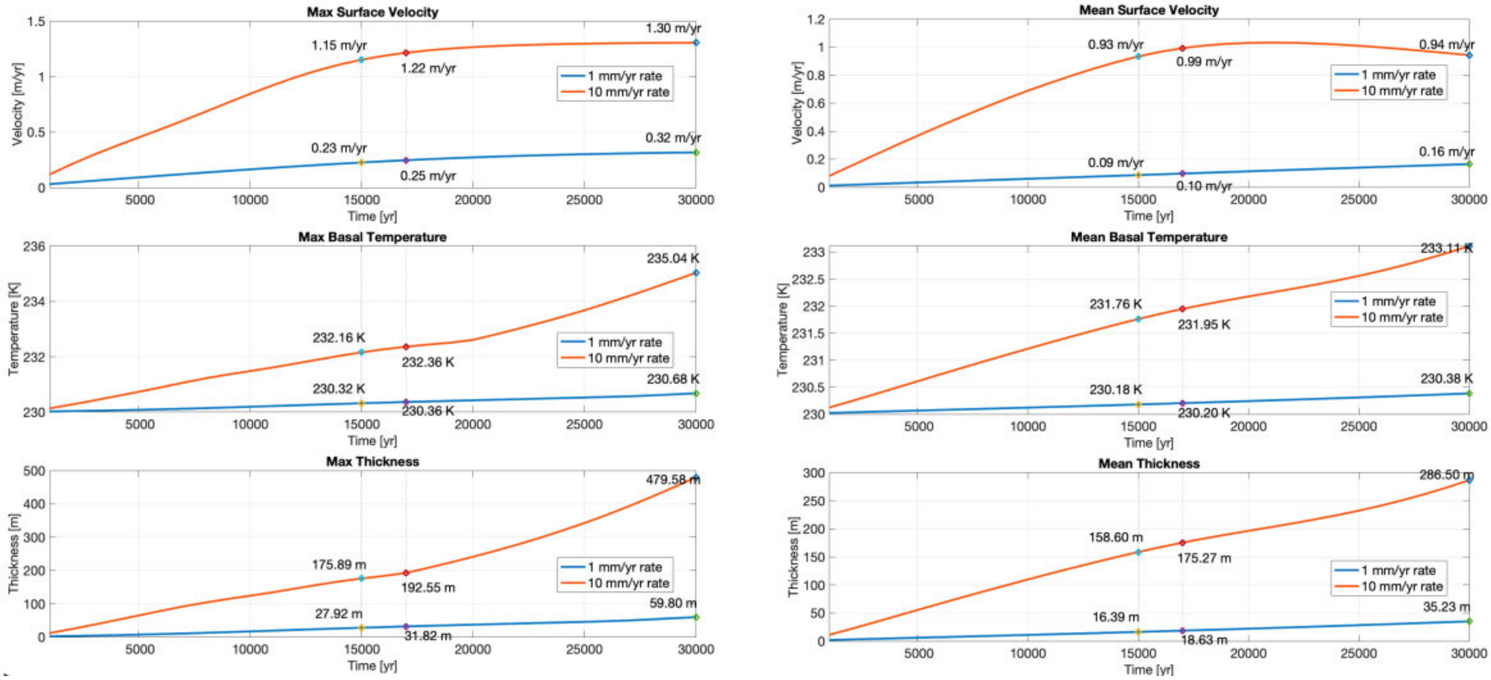

Figure 4.8 – Average and maximum ice thickness, surface velocities, and basal temperatures along the partial Curiosity path and continuing up Gediz Vallis (Figure 4.7), under the two different mass balance scenarios: the blue and red plots denote, respectively, the results for the slow (i.e., SC1, 1mm/year) and fast accumulation (i.e., SC2, 10mm/year). The values for the years 15,000, 17,000 and 30,000 for each plot are marked on the plots. For SC1 all of the variables increase linearly with time. SC2 shows a similar trend up to the year 17,000. The initial rapid ice accumulation accelerates flow, and then it reaches an inflection point around year 17,000 as ice accumulates north of the modelling domain, buttressing the flow and slowing the downslope flow of ice.

Figure 4.9 shows the speed distributions across the model along with the flow directions. This figure presents results for the physically plausible ice flow fields when the ice is moving as a glacier down-valley rather than down the slopes of Mt. Sharp. Then, we probe the model output in areas with landforms of interest. Under SC1, ice flows downslope towards north for the entire modelling period (Figure 4.9). This flow is aligned with the canyon and remains generally parallel for kilometers beyond the end of the Vallis – continually downslope towards the crater floor. The ice is fastest on the uphill steeper slopes, and surface velocities peak at 30,000 years, when ice is thickest. Except for extremely local flow in the first few thousand years, the ice maintains one general direction throughout the modelling process.

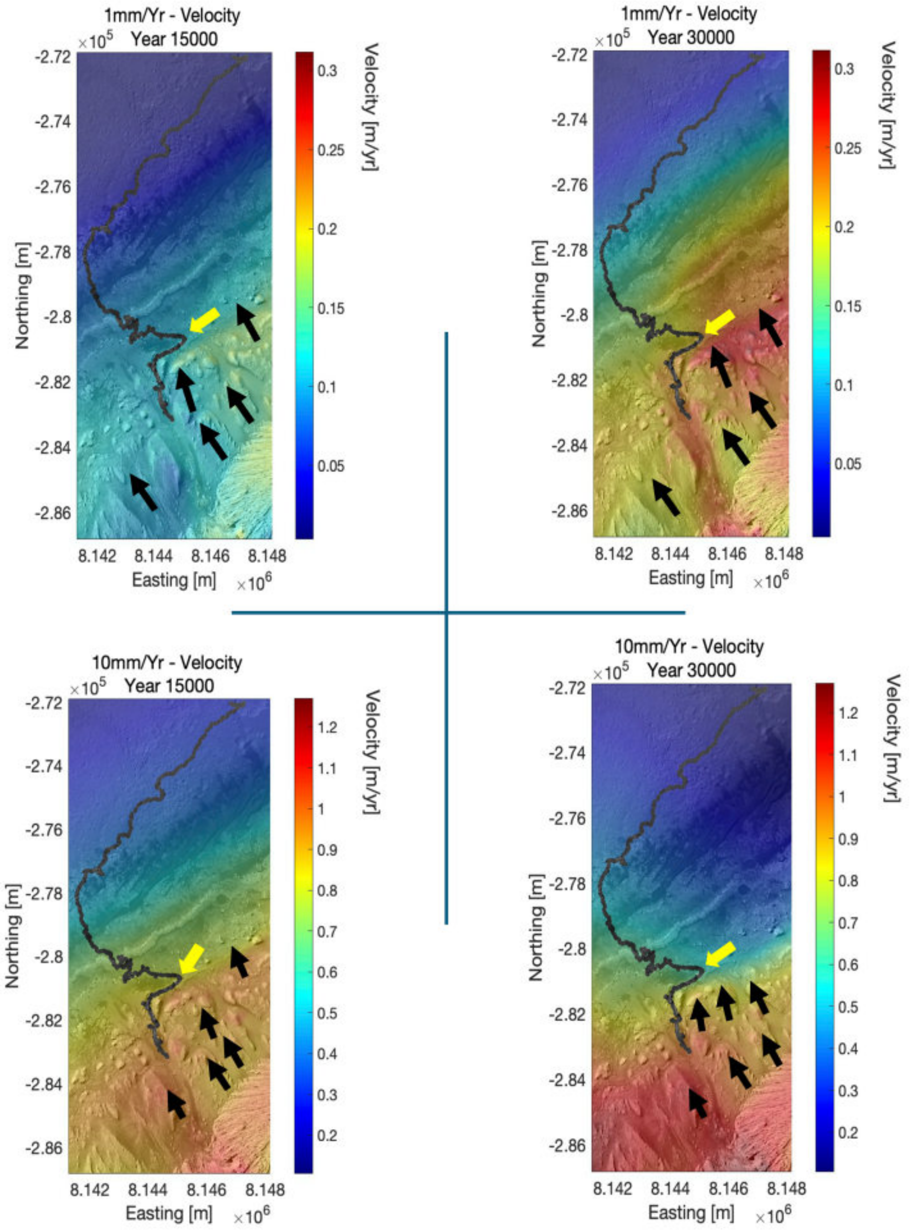

Figure 4.9 – Time evolution of surface speed within, and adjacent to and downslope of, Gediz Vallis for two specific years of 15,000 and 30,000, and two accumulation rates.

In this figure and Figure 4.10, the surface speed is overlaid in colour on CTX images. The plot colours show the magnitude of the velocity. The direction of the velocity vectors is shown with the black arrows. Curiosity's path is marked in grey. The yellow arrow points to the location of Mont Mercou. For both accumulation scenarios, the flow is aligned with valley *topography and directed downslope to the northwest. In SC2, the greater ice accumulation leads to faster flow until around the year 17,000 when sufficient ice has accumulated north of the Vera Rubin Ridge to buttress and impede the increase in the flow rate.*

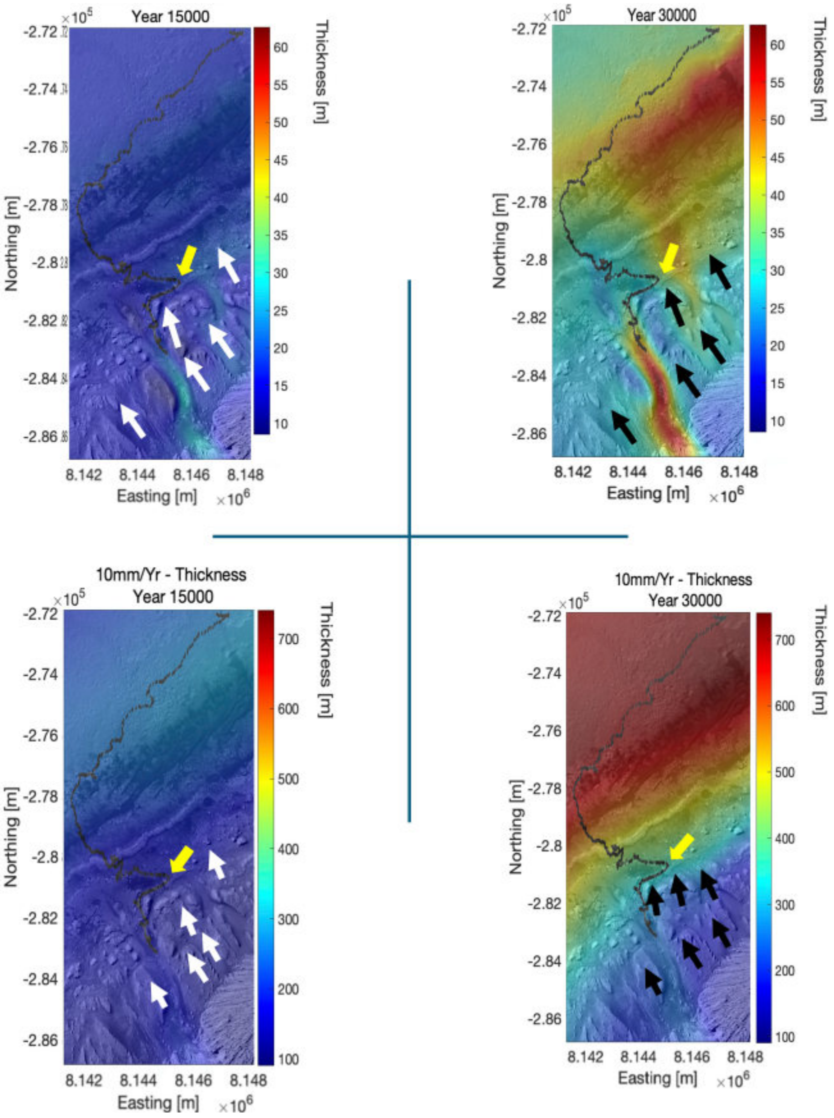

Figure 4.10 – Time evolution of ice thickness, colourized, across Gediz Vallis for the years 15,000 and 30,000 for both scenarios.

The black (for the year 30,000) and white (for the year 15,000) arrows indicate the ice flow direction. In SC1, ice thickens more gradually and uniformly. In SC2, initial rapid ice *accumulation in the north causes localized elevation of the ice surface as identified by the dark red colour.*

These plots demonstrate that once the flow is set up the flow directions remain similar under both scenarios, and throughout the modelling timeframe. Importantly, while testing our hypothesis, these patterns are consistent with the inferred ice flow direction, throughout the valley and especially around Mont Mercou (Figure 4.4(c)).

4.6.1 Comparison of the Different Modelling Formulations

The Gale Crater simulations rely on the Higher-Order (HO) approximation. This allows the flow to be defined by stress components interacting in 3-D. This cannot be modelled or captured by the Shallow Ice Approximation (SIA). Gediz Vallis includes steep, laterally constrained corridors, sharp bends, and buttressing features such as Vera Rubin Ridge—all of which generate significant longitudinal and transverse stress gradients. Even though the glacier is cold-based and sliding is negligible, the internal deformation field is still guided by horizontal stress couplings, particularly where ice flows through narrow topographic constrictions. SIA would simplify the stress balance into a vertical-shear system and force the glacier to respond only to local surface slope. This would simplify the mechanical influence of valley geometry and ridge buttressing. HO, by contrast, preserves the depth-integrated horizontal stresses needed to simulate down-valley flow alignment. In short, even without sliding, Gale's topographic complexity makes HO the minimum level of physical realism required to test the glacial hypothesis.

To demonstrate the differences between HO and SIA, I ran the same model shown here using the SIA formulation (for a comparison between SSA and HO approaches see Section 5.3.3).

Before presenting the details of the tests performed, I will note the major differences between the HO and SIA formulations. These two apply series of approximations to allow for the full stress balance equation (see Appendix 1) to be solved more efficiently. The full set of equations provide 4 unknowns and 4 equations: velocity in three directions of x, y and z; as well as the isostatic pressure. To simplify this, we use approximations:

(1) Shallow Ice Approximation (SIA):

This method assumes that the flow is dominated by vertical shear and the longitudinal stress gradients ($\partial\sigma_{xx}/\partial x$, $\partial\sigma_{\gamma\gamma}/\partial y$, $\partial\sigma_{x\gamma}/\partial y$) to be negligible and drops them from the formulation. It also assumes the driving stress balances basal drag is negligible; this means SIA assumes flow is driven purely by local gravity acting on the slope, resisted by friction at the base, without any stress interaction along or across the glacier. Flow is local, meaning velocity at a point depends only on local slope and thickness, and the stress from other columns of ice in the model will not impact the local stress. Another main assumption in SIA is that horizontal normal stresses (σ_{xx}, $\sigma_{\gamma\gamma}$) and shear stresses between horizontal directions ($\sigma_{x\gamma}$) are small compared to vertical shear stresses (σ_{xz}, $\sigma_{\gamma z}$). In short, mathematically, all horizontal stress gradient terms in the x- and y-momentum equations are neglected, and the only stress gradients that survive are the vertical derivatives of the shear stresses. The terms that are neglected in this approximation, become important when the surface slope is steep (as in Gediz Vallis), there is significant lateral drag from valley walls, or when flowlines converge/diverge. SIA, very specifically, can be considered for shallow icesheets (Hight/Length << 1).

In MIDAS, SIA can be used for diagnostic or simplified creep tests, not for layered or temperature-coupled simulations.

(2) Blatter–Pattyn Higher Order (BP-HO)

The Higher-Order approximation (Blatter, 1995; Pattyn, 2003) simplifies the stress balance equations by neglecting vertical stress gradients while retaining longitudinal and lateral stress components. It assumes the vertical velocity component is much smaller than the horizontal ones. Here, vertical shear is fully included, but vertical normal stress gradients are neglected.

SIA Tests

Below, I present the steps taken to run the model using SIA and the challenges encountered. For clarity, I refer to the original models as High_Res_HO_SC1 and High_Res_HO_SC2, for the high mesh resolution, the use of the Higher-Order formulation, and the scenarios. As a reminder, these models used a spatially adaptive mesh (i.e., 2000 m → 1700 m → 150 m), for a duration of 30,000 years (transient runs, for periods of 1000 years). I refer to this process and mesh resolution as "high-resolution,". To the uniform 1500 m mesh I refer to as "low-resolution." High_Res_HO_SC1 and High_Res_HO_SC2 ran in about 2 hours each. Unless explicitly stated otherwise in the tests below, I instructed the solver to record outputs every 1000 years to reduce computational cost.

1. First attempt: I started by only changing the formulation from HO to SIA in MIDAS, with all the other parameters the same as the main simulations, including the high-resolution mesh used (2000 m → 1700 m → 150 m). The first challenge I encountered was a high level of solver residue from the stiffness matrix. The finite-element formulation used in ISSM represents the stress-balance equations through a global n-by-n stiffness matrix (n being the number of degrees of freedom in the entire model). The stiffness matrix is the mathematical object that links nodal displacements to nodal forces in the model. In other words, it links the internal stresses, material properties, and strain rates across all elements. Solving it yields the velocity field for the momentum equations. During this model testing, however, the use of SIA resulted in high levels of solver residue, meaning the numerical solution did not adequately satisfy the stiffness-matrix equation. Large residues point to divergence and internal inconsistency in stress–velocity solution. When faced with high residuals, ISSM attempts to recover by restructuring and re-solving the matrix at each time step. This is very resource resource-intensive and time-consuming process, because the matrix will need to be re-setup, and then the solver tries to solve the matrix again. An example of high residue error is shown below. At this point, the solver is instructed that the minimum acceptable residue is 1e-06.

```
solver residue too high!: norm(KU-F)/norm(F)=0.364594 > 1e-06 (md.settings.solver_residue_threshold)
```

This message appeared repeatedly. For only 1000 years of modelling time, ISSM spent over an hour attempting to recover. Considering that HO completes the full 30,000-year simulation in ~2 hours, I terminated the process.

2. Second attempt: I disabled all MIDAS functionality and ran a “vanilla” ISSM SIA model. This modelling process ran for 13,000 years before the solver started to report that the basal ice had reached the melting point. I investigated the output and found that the transient run began with a basal temperature near 231 K at the beginning of the run, produced maximum velocities of 58 m/yr, and reached above 270 K at the end of the 1000 year run. These results were physically unrealistic. I terminated the run.

3. Third attempt: I switched to the uniform 1500 m low-resolution mesh and re-enabled full MIDAS functionality. I also changed the threshold for acceptable residue from the stiffness matrix to anything less than 0.1 (instead of 1e-06 which was the default value). This of course a very large acceptable residue from the stiffness matrix and would result in reduced reliability for the output, but allowed for completion of the modelling processes. These runs completed successfully, producing Low_Res_SIA_SC1 and Low_Res_SIA_SC2. To enable a fair comparison, I also ran HO with this low-resolution mesh, producing Low_Res_HO_SC1 and Low_Res_HO_SC2. As before, the two scenarios used SC1 = 1 mm/yr and SC2 = 10 mm/yr, and each run took roughly 30 minutes. I used the comparison path in Figure 4.7.

Here, first, I will review the results from low resolution HO runs. The results (Figure 4.11) show reduced velocity relative to the high-resolution results (Figure 4.8). Focusing on High_Res_HO_SC2 versus Low_Res_HO_SC2 (i.e., the 10 mm/yr scenario): the maximum velocity turned out to be ~5% lower; the slower flow yields ~18.7% thicker maximum ice, and the maximum basal temperature is ~0.36% lower. The overall trends between the low- and high-resolution runs remain the same, confirming consistency across modelling runs which supports the need for finer resolution within Gediz Vallis. I now proceed with the review of SIA simulations on the low-resolution mesh (i.e., uniform 1500 m resolution).

The SIA results were unexpected (Figure 4.11): ice flow rates remain constant throughout 30,000 years, and at a faster rate than the HO runs, producing lower thickness and correspondingly lower basal temperatures. Presumably, the constant high level of residue from the stiffness matrices, while was overcome by the solver, produced unreliable results.

To investigate these unexpected results, I performed two additional steps.

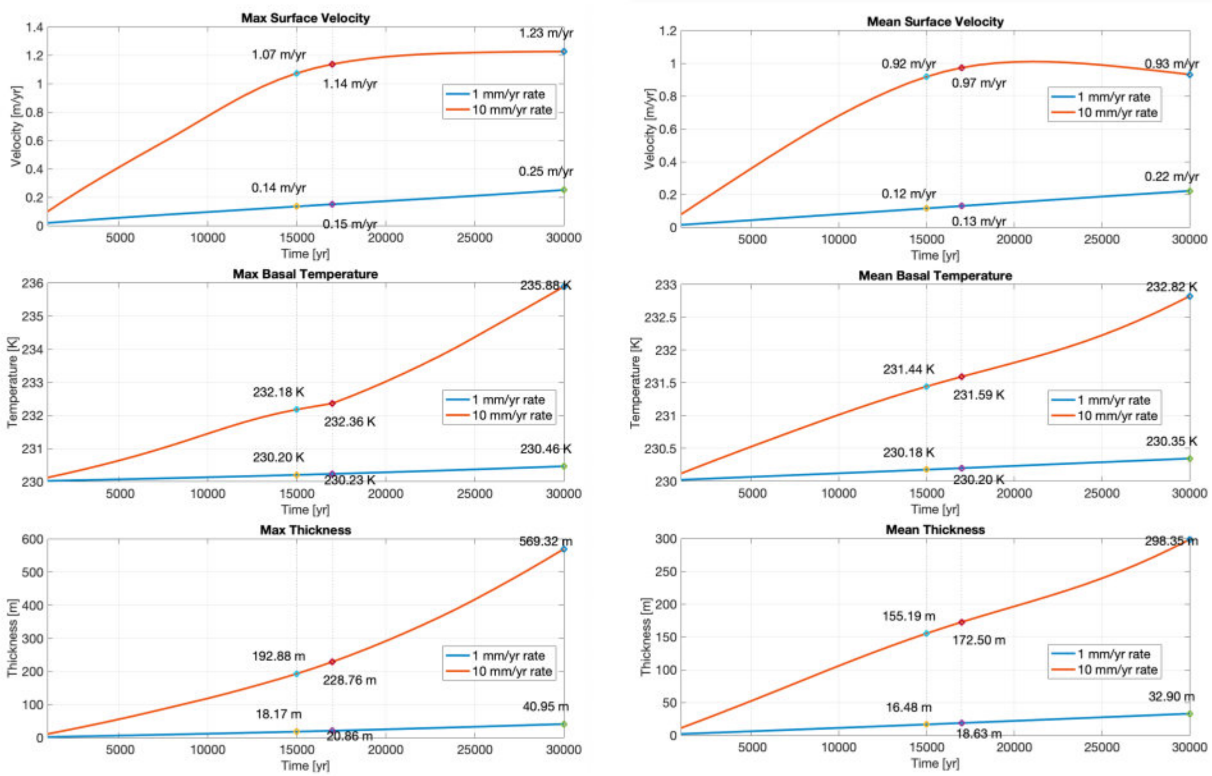

Figure 4.11 – The results of modelling Gale Crater – Gediz Vallis, HO with a uniform mesh at 1500 m through MIDAS.

Step 1: I ran the low-resolution domain using vanilla ISSM. Again, I encountered high residuals and repeated solver divergence. This indicated that the defaults values defined through MIDAS are better suited for modelling non-terrestrial ices. Figure 4.13 shows a screenshot of the encountered errors. After 13,000 years, I terminated the run.

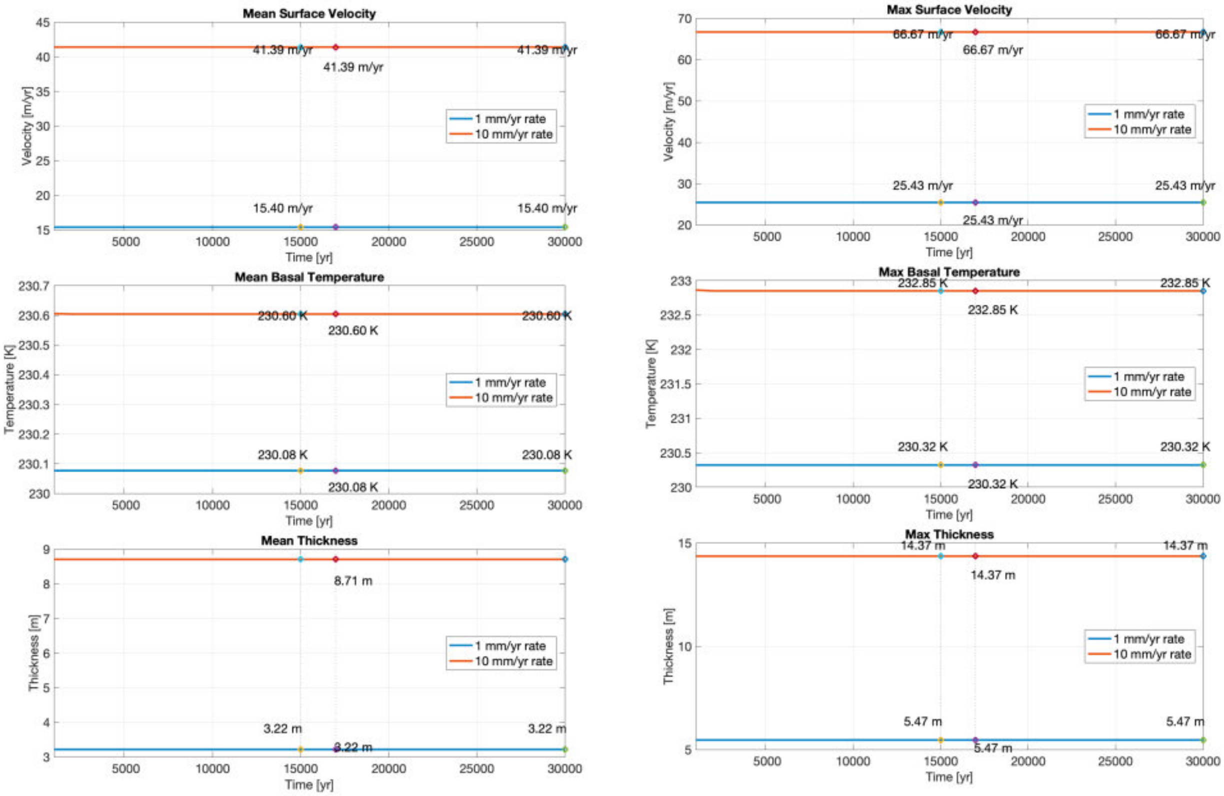

Figure 4.12 – The results of modelling Gale Crater – Gediz Vallis, SIA with a uniform mesh at 1500 m through MIDAS.

Step 2: I repeated the low-resolution SIA runs in MIDAS but instructed the solver to record results every 5 years; this way I could see if anything out of the ordinary would happen in time steps less than 1000 years. This produced an interesting results, showing wild fluctuations that I again attribute to the high level of the stiffness matrix residue (Figure 4.14).

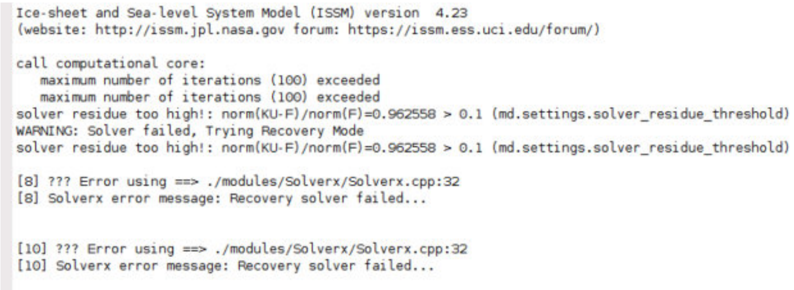

```
Ice-sheet and Sea-level System Model (ISSM) version  4.23
(website: http://issm.jpl.nasa.gov forum: https://issm.ess.uci.edu/forum/)

call computational core:
   maximum number of iterations (100) exceeded
   maximum number of iterations (100) exceeded
solver residue too high!: norm(KU-F)/norm(F)=0.962558 > 0.1 (md.settings.solver_residue_threshold)
WARNING: Solver failed, Trying Recovery Mode
solver residue too high!: norm(KU-F)/norm(F)=0.962558 > 0.1 (md.settings.solver_residue_threshold)

[8] ??? Error using ==> ./modules/Solverx/Solverx.cpp:32
[8] Solverx error message: Recovery solver failed...


[10] ??? Error using ==> ./modules/Solverx/Solverx.cpp:32
[10] Solverx error message: Recovery solver failed...
```

Figure 4.13 – Errors resulting from running Gale Crater simulation using SIA formulation

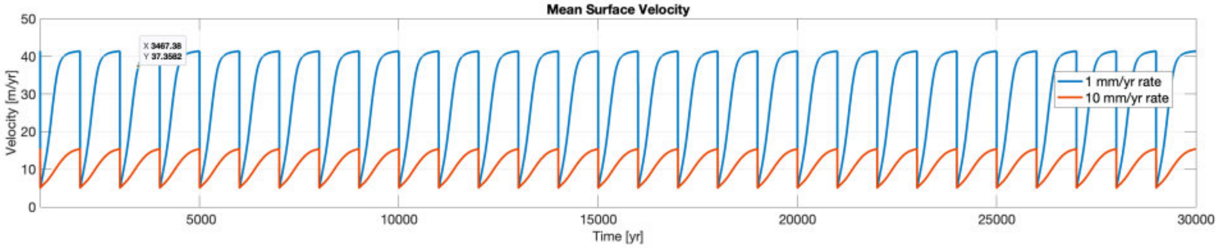

Figure 4.14 – Low_Res_SC1 and SC2 velocity results, when captured every 5 years. _

Testing Conclusion

Based on the results above, I conclude that due to the steep slope, and narrow structure of Gediz Vallis the longitudinal stretching components, and lateral drags, are not negligible. Moreover, Gediz Vallis surface (length: ~9km, width up to 900 m) and the maximum ice accumulation (~500 ice thickness) does not satisfy the H/L<<1 constraint. (H/L is about 0.06 and H/W is about 0.6). As such, for the Gale Crater the SIA is not an appropriate approximation method to be used. My conclusion is that HO formulation provides the best trade-off between accuracy and computational cost.

An Extra Step in Testing

As the last step in my testing, here I present the important of using temperature dependent material properties (except for the rheological properties which are always temperature dependent).

For this, I ran the High_Res_HO_SC1 and _SC2 with static property values (i.e., through vanilla ISSM). The results (Figure 4.15) show that the flow turns out to be slightly slower; and this results in lower maximum ice thickness, and in turn lower basal temperature. This is expected since lower temperature on Mars. At the start of the simulation the temperature produces specific values for heat capacity, thermal conductivity, density and latent heat of fusion will be determined specific to the location. These values will be different from the average static numbers that are generally used (Table 4.1). And the differences will contribute to an overall slower flow. Slower flow will result in a lower maximum ice thickness and cooler basal temperature.

Property	**Static Number (Larour et al., 2012)**	**Equations used / Value at T=230 K**	**Impact on the flow**
Ice Specific Heat Capacity	**2093 J kg^{-1} K^{-1}**	**-22.86*10^(-3)*T^2+16.3163*T-720.5987** **At 230 K → 1822.86 J kg^{-1} K^{-1}**	**Higher values increase the thermal sensitivity, and it increases the viscosity which results in slowing down the flow**
Ice Thermal Conductivity	**2.4 Wm^{-1} K^{-1}**	**903.65*(T^(-1.072))** **At 230 → 2.66 Wm^{-1} K^{-1}**	**Higher value results in higher faster diffusion of heat, and slowing down the flow**
Ice Density	**917 kg m^{-3}**	**-0.0003*T^2 + 0.0316*T + 933.29,** **At 230 → 924.69 kg m^{-3}**	**While higher density increases the stress, it increases the viscosity much more, and this results in slow down of the flow**
Ice Specific Latent Heat of Fusion	**334,000 J Kg^{-1}**	**-3.76812*T^2-55.81*T+629992** **At 230 K → 417822.15 J Kg^{-1}**	**Lowers the melting point, reduces the potential for sliding**

Table 4.1 – Impact of using static vs. variable material properties in the Gale Crater Simulation presented in this dissertation

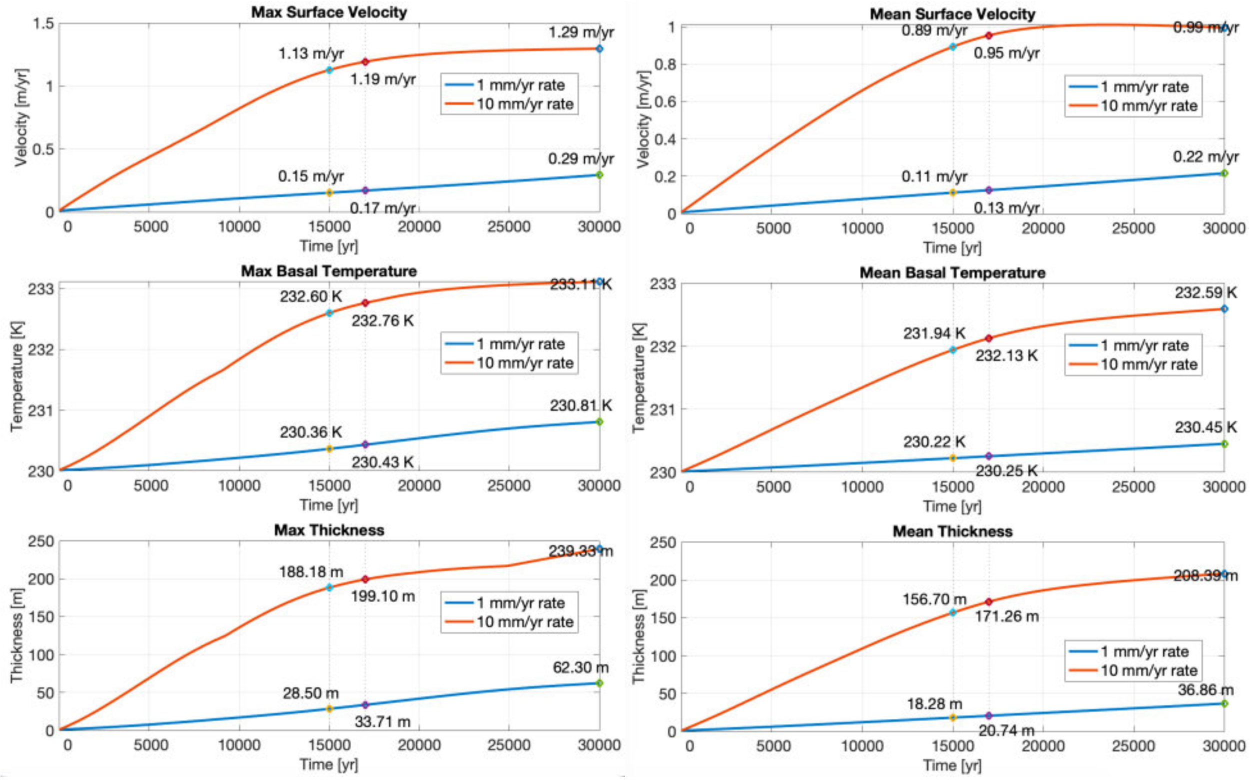

Figure 4.15 – Gale Crater Simulation when static numbers are used.

One Final Note

It should be noted that SIA can be implemented on a three-dimensional gridded mesh, which results in reductions of computational cost while, at the same time, producing robust large-scale results. When coupled with SSA in regions of basal sliding, this approach performs effectively in continental-scale icesheet modelling (Tarasov et al., 2025). Whether such a strategy can be reliably extended to stratified, multi-unit ice deposits like those examined in this study remains an open question and is identified as a point to be investigated further in future.

4.7 Discussion

The wealth of information collected and transmitted by Curiosity documents the impact of lacustrine, fluvial, deltaic, as well as aeolian and hillslope processes in Gediz Vallis

(Grotzinger et al., 2015; Stack et al., 2019). These processes alone, however, inadequately account for numerous bedrock features, especially the bedrock outcrops resembling roches moutonnées within Gediz Vallis.

In short, we seek to find support for or against the glacial hypothesis being able to explain the formation of Mont Mercou and the other enigmatic features observed in Gediz Vallis. To this end, we use modelling to provide a first-order test of glacial ice flow patterns and directions to examine if modelling results will yield glacial ice flow direction and magnitudes consistent with the landforms observed in Gediz Vallis. In this initial modelling, we focus on ice flow directions and rates, and do not explicitly consider glacier sliding, basal melt-water or basal debris, which are fundamental to glacial quarrying.

4.7.1 Uncertainties in the Results

While the Gale Crater models of Gediz Vallis potential cold based icesheets demonstrate internally consistent flow directions that align with the observed geomorphic indicators (see section 4.4), they also include uncertainties that should be considered when interpreting these results. These uncertainties arise from boundary conditions, mass and energy fluxes, rheological assumptions, and basal processes that cannot be fully constrained due to the limitations in the available data.

(1) Top Boundary Mass Flux: The uniform–rate ice deposition (1–10 mm yr^{-1}) rather than values derived from a climate model is a source of uncertainty. The purpose of these models is to test directional stability rather than to recover an exact accumulation history. Biases in the SMB directly influence ice thickness evolution and therefore the magnitude (but not the direction) of the predicted velocity field. The deposition rates should be temporally and spatially variable to account for a more realistic process. However, even when using variable rates, there is a high level of uncertainly inherent in the input values due to the limited data available.

(2) The Surface Temperature Boundary: This is fixed at 230 K, which is simplification due to lack of detailed knowledge of the spatial and diurnal thermal gradients. However, since the icesheets are cold-based, the impact on the vertical thermal gradient is considered to be limited.

(3) Rheology: The stress exponent for cold H_2O ice is typically constrained around $n \approx 3$, but laboratory works show a wider range of 2.5–4. H2O ice activation energy too, may, vary with impurity content and other environmental conditions. Increasing n increases the non-linear sensitivity of water ice to shear stress and would increase the contrast between fast- and slow-flowing zones within the same ice unit. The main objective of this modelling is to evaluate the direction of creep-dominated flow directions, and this uncertainty would impact the magnitude more than the flow direction.

(4) Basal Friction: This model contains none-sliding, cold-based glaciers and does not include sliding physics and therefore represents a lower-bound estimate of potential flow magnitudes.

(5) Geothermal Flux: Geothermal heat flux is assumed to be 30 mW m^{-2}. A higher value (e.g., 40–45 mW m^{-2}) would raise internal temperatures and reduce the water ice's viscosity. However, even under generous geothermal scenarios, temperatures remain below the pressure-melting threshold, and the cold-based assumption remains robust for the purpose of the current modelling exercise.

(6) Stress Balance Formulations: As shown in section 4.6.1, the type of stress balance approximation is used (i.e., BP-HO vs. Shallow Ice Approximation) will have a direct impact on the results. The choice for this modelling was to focus mainly on Higher Order, as explained in section 4.6.1. However, due to the sharper slope, Full Stokes formulation might be even more appropriate, albiet much more resource intensive.

4.7.2 Discussing the Results

To contextualize our current modelling, we note previous modelling efforts of Martian glacial-like ice flows under varying assumptions and conditions (see Parsons & Holt (2016), Williams et al. (2022), and Butcher et al. (2024)). These studies typically yield flow rates ranging from very slow creep to moderate glacial speeds, depending on assumed temperature, ice composition and debris content. Our simulations fall within the higher end of the results of past studies, as our models assume debris-free (and pure water) ice and a relatively elevated geothermal flux. SC1 results suggest that thin, cold-based glaciers would grow and flow with directions that are aligned with the formation of landforms and reflect the dominant past ice flow direction. Although our modelling does not explicitly include the basal sliding that is required for the quarrying and plucking, the direction of basal sliding is predominantly dictated by the general ice flow direction, which is precisely calculated.

The faster ice flow of SC2 yields a similar ice flow pattern that would likewise be consistent with landforms observed along Curiosity's path in Gediz Vallis region. These landforms include bedrock outcrops closely resembling roches moutonnées, with transverse cracks and abrupt lee-side terminations, as well as grooves and ridges on generally smooth surfaces. Such features that could be interpreted as potential expressions of glacial abrasion (i.e., striations) on “smooth polished” surfaces of geological features that were first noted from orbit, before they were imaged by Curiosity, near Mont Mercou. Similar smooth, gently undulating surfaces extend across several rock units stratigraphically above Mont Mercou. We hypothesize that these smooth surfaces reflect glacial abrasion because it tends to bevel bedrock surfaces. In contrast, while aeolian abrasion can smooth rock locally, rather than beveling bedrock surfaces, as is characteristic of glacial abrasion, wind-entrained sand and rock particles tend to accentuate the lithological control and differences in rock strength (Scheiber et al., 2020).

Both simulation scenarios (SC1 and SC2) yield significant ice flow in Gediz Vallis that ice would flow down Mt. Sharp in the direction that demonstrate alignment with the features captured by Curiosity, supporting the hypothesiz that these features could have been potentially produced by glacial erosion and that is directed primarily N-NE, parallel to the key potential glacial landforms, including Mont Mercou (Figure 4.4 and 4.5). North of Mont Mercou is not relevant to this discussion. Additional evidence supports the ice as the potential source of the cracks and roches moutonnées higher up-valley and south of Mont Mercou (Figure 4.10). It is inferred that the former ice flow was roughly towards north and note that this inferred flow direction is only approximate because glacial quarrying is sensitive to the orientation of pre-existing bedrock fractures (Hooyer et al. 2012).

At Mont Mercou, our model yields ice flow lines and vectors (Figure 4.10) running approximately northward, closely parallel to furrows on nearby bedrock exposures and the bedrock ridge culminating in Mont Mercou. Therefore, the orientation of Mont Mercou and adjacent bedrock features observed in HiRISE and Curiosity are consistent with the direction of glacial flow inferred from slip lines (Figure 4.4).

Lastly, one of the most enigmatic aspects of Gale Crater landforms is the lack of evident catchment areas for the relatively large and deep valleys including Gediz and Sakarya Vallis. Modelling can be used to propose plausible catchments of subglacial water. While our modelling has been focused on ice flow patterns, here we use modelled streamline patterns and topography to suggest a catchment area for Gediz Vallis (Figure 4.16).

For glacial catchment, we consider the surface velocity streamlines at the year 30,000 in SC2, and we compute the contributing area on the DEM grid. The result is a proposed catchment area of 120 km^2, which suggests, if melting occurred, large volumes of water at high elevations would have been available to help form this Vallis, and possibly others.

For sub-glacial water flow and drainage area, we follow Shreve (1972). Subglacial catchments are controlled by the basal hydraulic potential $\psi = z_b + \left(\frac{\rho_i}{\rho_w}\right) h$; where z_b is bed elevation; h is ice thickness ρ_i and ρ_w are the densities of ice and water. For the thin, ice system considered in our modelling relative to the elevation range, the ice thickness term is small; the subglacial hydraulic potential is, therefore, dominated by the bed topography. As a result, the subglacial catchment area for any potential meltwater in Gediz Vallis would be very close to the area of the glacial catchment, ~120 km^2.

Gale Crater possesses other valleys, including Sakarya Vallis, which is considerably larger than Gediz Vallis but lacks an obvious catchment that might have served as the source of water for fluvial incision required to form the valley. Our modelling could readily be used to consider potential subglacial catchment areas for Sakarya Vallis and other intriguing valleys in Gale Crater and beyond.

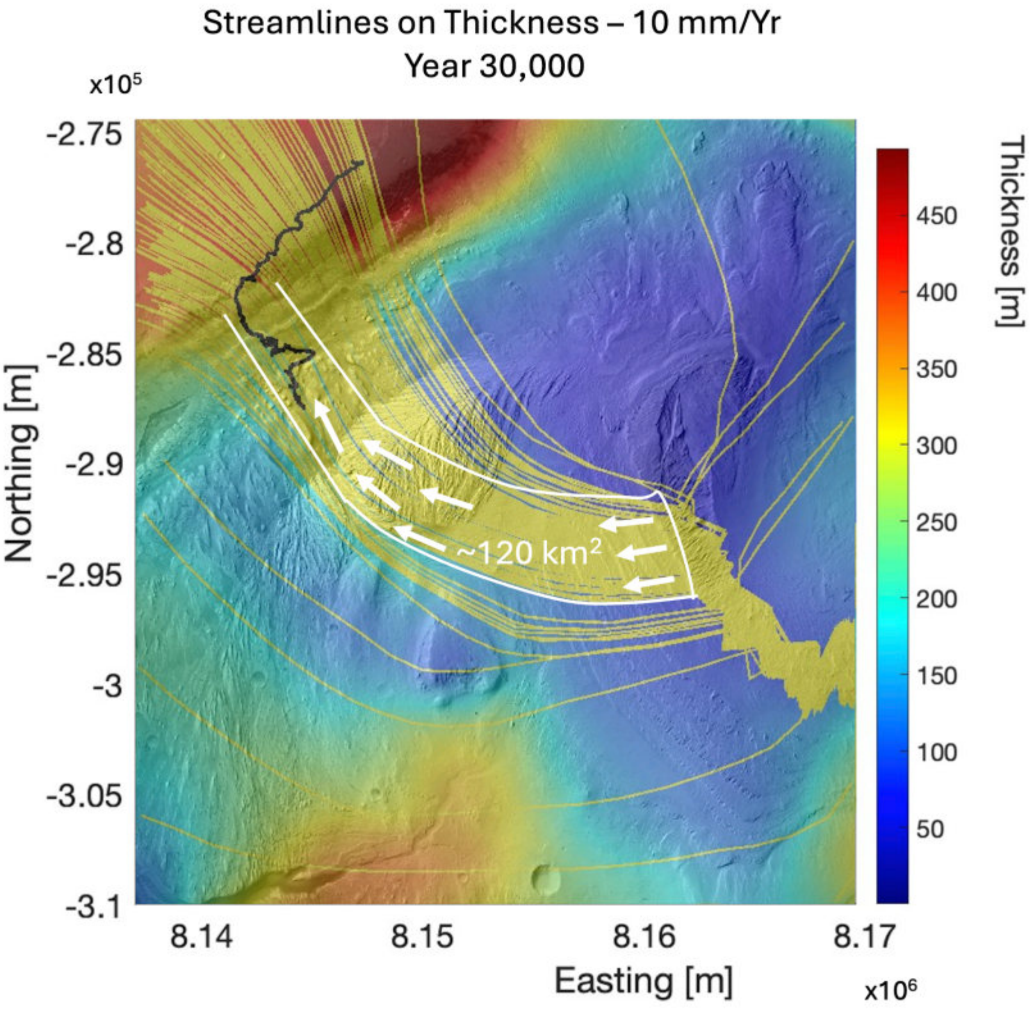

Figure 4.16 – Streamlines overlaid on ice thickness (SC2) at year 30,000.

SC2 was chosen for this image as the colour tones were more readable, but as noted earlier the flow patterns are the same in both scenarios. White arrows indicate ice flow direction. The outlined area marks the proposed catchment area for both ice and water. The high density of flow lines in Gediz Vallis reflects the higher mesh resolution there.

4.8 Caveats and Future Work

Model Assumptions: Our assumptions, for this initial work, are the simplest possible. We assume a spatially and temporally constant mass balance, no seasonal variability in temperature, and no dust and debris in the water ice. While the orientation of the observed landforms,-interpreted as products of glacial erosion, is consistent with modelled ice flow lines, this agreement should be viewed with caution because of the model's simplifying assumptions. However, the modelled ice flow directions are not sensitive to these simplifications, hence they can be compared with the orientation of potential glacial landforms. To improve the modelling, future work ought to include a range of surface temperature that permit basal melting and sliding, cyclic variations in surface temperature and mass balance guided by climate models (e.g., Madeleine et al., 2009; Forget et al., 2006) and from studies of ice masses on other tropical glaciers on Mars (Shean et al., 2005 and 2007).

Further analysis and modelling are warranted to shed light on the sliding, as affected by:

- the chemical composition of the bedrock (and solute-affected pressure melting temperature).
- the basal ice temperature, which depends on the assigned surface temperature, ice thickness, and heat transfer through the ice mass.

In addition, on occasion, basal temperatures may also be sensitive to episodes of surface melting, even under thick ice. Extensive field studies on the Greenland ice sheet have shown that water has a surprising ability to flow to the base of thick, cold ice masses through a network of conduits (aligned pores, cracks, etc.). Even only a few days of melting can accelerate basal motion and, presumably, erosion under cold, km-thick ice (Zwally et al.

2002). In the Martian context, Kite et al. (2013) noted that Gale Crater's mound is predicted to be a hemispheric maximum for snowmelt on Mars.

5 Modelling the Water-ice Bounding Layers in the Massive Ice CO2 Deposits, South Pole of Mars

5.1 Introduction

5.1.1 Contributions of this Study

As the temperature of the polar CO2 ice cap on Mars remains in equilibrium with the atmospheric temperature, the Martian atmosphere is very sensitive to the changes of the polar temperature, and these variations are governed by the insolation (Laskar et al., 2004). The distribution of solar insolation on Mars is governed primarily by variations in its orbital parameters, which are eccentricity, precession, and obliquity (Laskar et al., 2004). These variations result in the deposition of water and CO2 ices in the south pole of Mars in Massive CO2 Ice Deposits (MCID). To date no study has modelled the one-to-one correlation between the structure of MCIDs and the Martian orbital parameters (Buhler, 2023). In 2020, Buhler et al. estimated the CO2 ice deposition in MCID, and in 2022 Smith et al. modelled the resultant formation and volumetric distribution of CO2 ice deposits in MCID. Later in 2023, Buhler leveraged numerical modelling to estimate the south polar H2O deposition rates. This study aims to reduce the knowledge gap in this area by modelling the impact of the formation of H2O layers in the MCID.

5.1.2 Background

Studying the mechanics and workings of the solar system requires an understanding of bodies that exist within it, along with their histories, their evolution, and the climatic changes they have experienced. The climatic and geological histories of terrestrial as well as icy bodies influence the formation of ice on these bodies. Therefore, much like on Earth, studying ices on other planets in the solar system provides a view into understanding their histories. Examining the evolution of planetary bodies, through learning about the history of their atmospheres and surfaces, provides diagnostic constraints on their climatic and geologic evolution, and therefore a view into the workings and history of the solar system.

There is ample evidence that ice deposits on solar system bodies, other than Earth, include diverse (and often mixed) chemical compositions. Extraterrestrial glaciers, due to the low temperatures at which they formed, are likely to incorporate a wider range of compounds, particles, and materials. For example, on planets such as Mars or distant icy worlds like Pluto and Triton, the glaciers include compounds like carbon dioxide (CO_2), nitrogen (N_2), and methane (CH_4). Given climate cycles on those icy bodies, the exotic types of ice could even form as alternating units of icy materials within the same ice mass (Binzel et al., 2017). Each material has distinct physical and rheological properties that vary with temperature and pressure (Fard and Smith 2024); therefore, the terrestrial analogues will have limited applicability to help infer the glacial dynamics on other planets. Instead, understanding them requires dedicated approaches that account for differences in materials and their temperature dependence, as well as the unique boundary conditions (e.g., gravity, atmospheric composition, and insolation patterns) of each planet that will govern any modelling efforts for each.

On Mars, various locations, across different latitudes, have captured diverse cryospheric expressions that are the results of eons of climate evolution, including the episodic ice accumulation, flow, and ablation. The examples include the polar layered deposits (PLDs) in both poles, the latitude-dependent mantle, viscous flow features, and tropical mountain glaciers (e.g., Kreslavsky & Head, 2002; Head et al., 2003; Shean et al., 2005; Levy et al., 2014; Dickson et al., 2015; Smith et al., 2022). The South Polar Layered Deposits (SPLD) are covered by a thin (i.e., about a metre thick) layer of CO_2 ice that includes a seasonal CO_2 ice and a more resilient layer that remains all year round and is referred to as the South Polar Residual Cap (SPRC) (Kieffer, 1979; Fishbaugh and Head, 2001; Brown et al., 2010).

In 2011, data from the Shallow Radar (SHARAD) instrument aboard NASA's Mars Reconnaissance Orbiter revealed the Massive CO_2 Ice Deposits (MCID) beneath the SPRC through geophysical analysis and layer geometry that helped confirm the composition and thickness of these deposits; the dielectric properties and speed of light within these deposits are consistent with CO_2 ice (Phillips et al., 2011). Later, Bierson et al. (2016) demonstrated that the CO_2 ice thickness, in some locations, reaches up to 1,000 m and that the internal layering implied a climate cycle was stored in the deposits.

These identified deposits are primarily located in depressions. Many of these deposits are isolated and not connected. They are mostly under a layer of water ice (with dust) and then the SPRC, and collectively reach a mass of CO_2 that is close to the current mass of CO_2 present in the Martian atmosphere (Haberle et al., 2008; Guo et al., 2010; Putzig et al., 2018; Buhler & Piqueux, 2021). The SPRC, due to its composition, helps to maintain the surface temperature of these CO_2-dominated deposits at the condensation/sublimation point of ~150 K (Bierson et al., 2016; Buhler et al., 2020). The low temperature and the existence of the water-ice layer on their surface protected CO_2 deposits from sublimation for over 100,000 years (Bierson et al., 2016; Buhler et al., 2020). Crater counting puts the surface age of SPLD at tens of millions of years (e.g., Herkenhoff & Plaut, 2000); however, no craters have been identified above the SPRC or MCID.

Early studies on the rheology of CO_2 ice (Clark & Mullin, 1976; Durham et al., 1999; Nye, 2000) showed that CO_2 would not be viscous enough to support an entire ice cap over 10^7 years; even with the low temperature and low gravity the deposits would flow outward over time; something that is not observed (Nye, 2000). This positioned the possibility that potentially large and thick “layer” of water ice should be in place under the SPRC CO_2 ice to help stabilize SPLD to the shape we observe today (Byrne & Ingersoll, 2003).

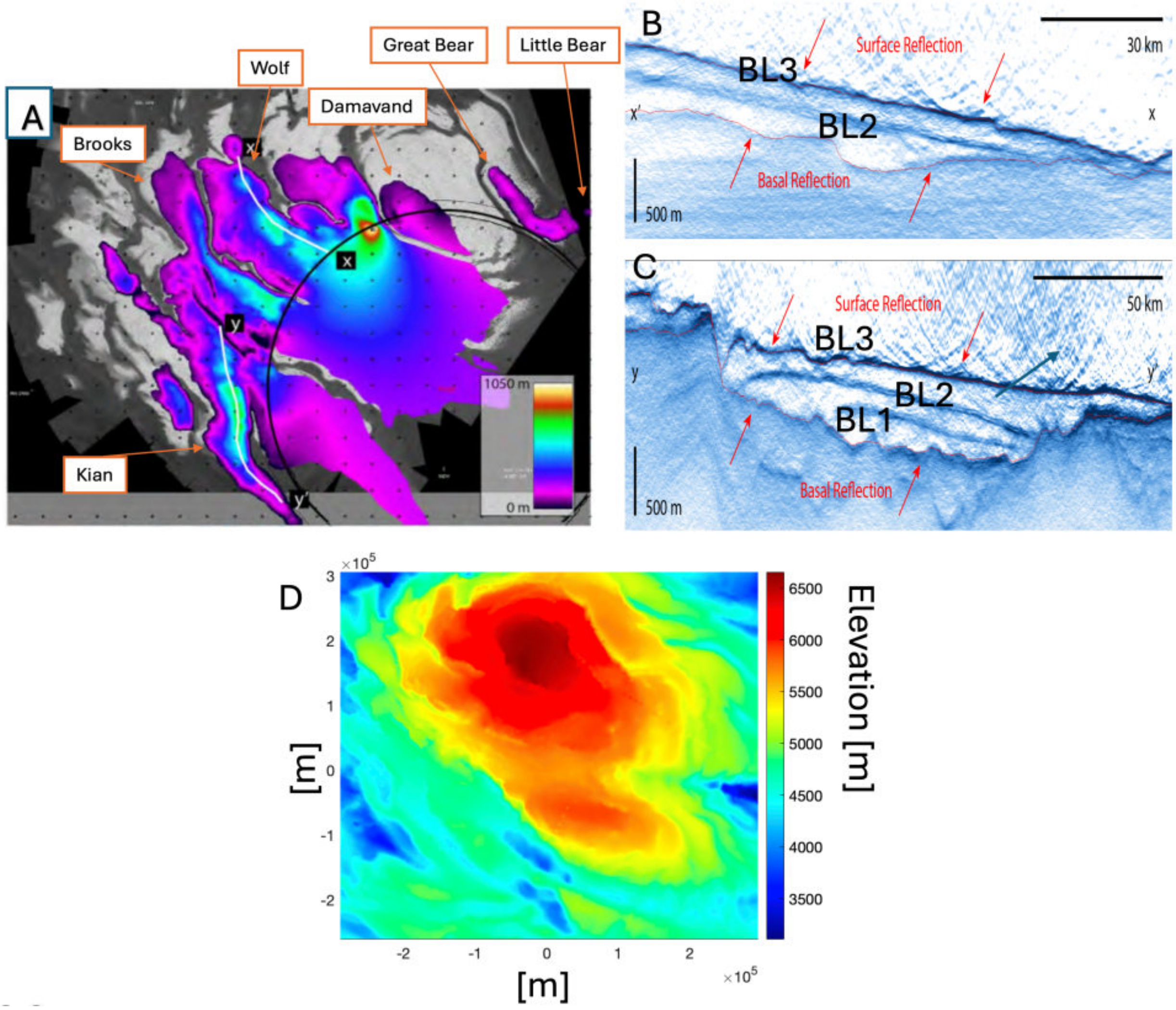

Figure 5.1 — Massive CO_2 Ice Deposits in the south polar region of Mars.

(A) CO_2 ice thickness over a Context Imager summer mosaic (Thomas et al., 2009). CO_2 ice thickness is mapped up to the southern latitude limit of the Mars Reconnaissance Orbiter (black circle), beyond which the ice is extrapolated to boundaries from geologic mapping. Unofficially named glaciers are marked with their names. (B) and (C) Radar profiles from a 3D radar data set (Foss et al., 2017; Putzig et al., 2018). H_2O bounding layers marked with BL1, BL2, BL3 (Alwarda & Smith, 2021), which correspond to the similar markings in Figure 5.8. Figure from (I. B. Smith et al., 2022). (D) South Polar surface topography of Mars plotted in Ice-sheet and Sea-Level System Model (ISSM) using data from the Mars Orbiter Laser Altimeter (D. E. Smith et al., 2001). The region closest to the pole (0,0) is interpolated because of the orbital inclination of Mars Orbiter Laser Altimeter (MOLA).

Like the terrestrial Milanković cycles, long-period oscillations in obliquity and eccentricity govern the Martian insolation (i.e., amount of solar radiation received on the planet surface) and therefore cause planetary climatic variations. However, the Martian orbital parameters experience much more chaotic and wider ranges than those of the terrestrial parameters (Laskar et al., 2004). One-dimensional deposition models show the impact of the low-obliquity intervals (and the associated reduction in the polar summer insolation) on atmospheric collapse and the resultant CO_2 accumulation at the South Pole. These models also demonstrate the impact of the higher-obliquity phases on increasing the rate of CO_2 sublimation, and the increase of CO_2 in the atmosphere (Manning et al., 2006; Manning et al., 2019; Bierson et al., 2016, Buhler et al., 2020, 2021, 2023). During deposition, scavenging of atmospheric H_2O by CO_2 snowfall (Piqueux et al., 2015; Alsaeed & Hayne, 2022) could support forming CO_2 units with interstitial water that later remains as a lag when CO_2 ablates (Buhler et al., 2020; Smith et al., 2022), as under typical Martian surface pressures of about 600 Pa, CO_2 sublimates at temperatures around 148 K (Piqueux et al., 2015).

As the obliquity of Mars repeats the cycles of peak and troughs every ~120,000 years (Laskar et al., 2004), it stands to reason that during periods of CO_2 sublimation would leave a water ice lag. When followed by another CO_2 deposition period, this would have resulted in the formation of multiple H_2O bounding layers (Bierson et al., 2016; Buhler et al., 2020) between CO_2 layers, which would have acted as time markers for each episode of the Martian atmospheric collapse. See figures 2 and 3 from the study done by Buhler et al. (2020), which demonstrate the formation of water-ice bounding layers.

CO_2 ice, if uniformly deposited across the SPLD, would have flowed in existing basins where the thickness of the mass would have caused the deposit to endure without complete sublimation during the high obliquity periods (Smith et al., 2022). On the other hand, for locations with thinner CO_2 ice (i.e., slopes where the ice flowed away), during longer sublimation periods, an entire unit of CO_2 could have completely sublimated, leaving a water ice lag above and resulting in the two bounding water ice units merging (Buhler et al. 2020; Alwarda and Smith 2021), potentially forming the SPLD recent accumulation of water ice identified by Smith et al., 2016; Whitten et al. 2018. One critical assumption that helps with explaining the formation of water-ice bounding layers is the hypothesis that CO_2 can sublimate beneath the H_2O layers, and communicate directly with the atmosphere, first presented by Buhler et al. (2020) and supported by Smith et al. (2022), who found evidence for crevasses in the H_2O bounding layers that would have exposed CO_2 ice.

This, thus, provides support that bounding layers could highlight the relationship between the orbital parameters and the formation of the features in SPLD, and multiple bounding layers in the MCID likely indicate multiple periods of atmospheric collapse (Figure 5.2) in Mars' past (Manning et al., 2019; Buhler et al., 2020). As such, studying the MCID can help with understanding the climatic history of Mars (and linking it to the orbital parameter changes), it also acts as a dynamic participant in Mars' CO_2 cycle as seen in Figure 5.2. Through their models, Buhler et al., (2020; 2021; 2023) demonstrated the correlation between the theoretical research done by Laskar et al. (2004) in determining the changes to the Martian orbital parameters and the timing of the formation of the MCID and its bounding layers. Laskar et al. (2004) showed that the Martian obliquity could have experienced values as high as ~45° or as low at ~15° in the past 20 Myr, which in comparison to Earth's obliquity demonstrates a much higher amplitude.

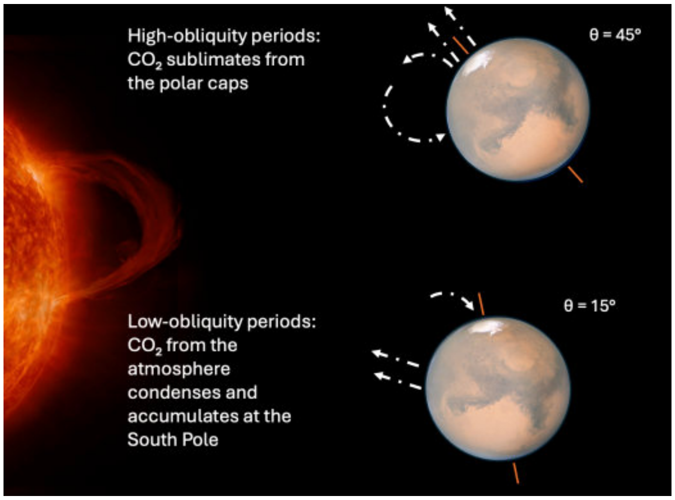

Figure 5.2 – The impact of the Martian obliquity changes to the transfer of the CO_2 to the surface and back to the atmosphere.

During low obliquity periods when the polar seasons are less pronounced, summer temperatures go down for long periods, CO_2 transfers to the surface. Over prolonged periods, this can develop into atmospheric collapse. During periods with higher obliquity, increased summertime insolation at the poles raises surface temperatures sufficiently to trigger CO_2 sublimation and therefore its transfer back to the atmosphere. Due to the Martian surface pressure and the temperature variations, CO_2 cannot exist in liquid form and sublimates directly back to the atmosphere (Piqueux et al., 2015).

Studies of the MCID typically rely on 1-D thermal equilibrium approaches that prescribe accumulation and ablation (e.g., Manning 2006; 2019; Buhler et al., 2020), but do not include the potential lateral redistribution by flow. In these scenarios, the lateral distribution of accumulation would slowly vary by latitude; hence those models are not sufficient in explaining the structure of the MCID as observed today (Figure 5.1). Such was the state of knowledge and the general modelling approach until 2022, when Smith et al. successfully modelled the formation of the MCID based on the modelled output of a uniform surface mass balance by Buhler (2019). They demonstrated that CO_2 glaciers in the MCID necessarily flowed as glaciers for the MCID to distribute and form the discontinuous deposits that are observable today. For their work, Smith et al. (2022) leveraged the CO_2 flow laws as identified in the laboratory work by Cross et al. (2020) and showed that the CO_2 ice flowed downslope into valleys, where the MCID currently resides (Figure 5.1).

While Smith et al. (2022) made this significant advancement, their work made one major simplifying assumption: it ignored the presence of water-ice bounding layers. Water ice is significantly more viscous at relevant temperatures and has different thermal properties; hence the modelled flow rate of the MCID from Smith et al. (2022) would not reflect the history of Mars. Our current study and modelling aim to address that gap by modelling and then analysing the formation and dynamics of the stratified (i.e., alternating CO_2 and H_2O units of ice) MCID at Mars' South Pole. For this, we rely on temperature-dependent rheology laws for CO_2 and H_2O as well as temperature-dependent densities and thermal conductivities (Fard and Smith, 2024) in a three-dimensional thermo-mechanical framework. In our approach, we explicitly model the formation and evolution of H_2O bounding layers within the CO_2 deposits via deposition–ablation cycles consistent with orbital forcing (using the work of Buhler et al. (2020)). Then, we will analyse how those layers could have influenced subsequent CO_2 glacial deformation and the heat transport across various vertical units. For our analysis we will focus on the following questions:

1. How do the contrasts between the H_2O ice and CO_2 ice viscosities guide the internal shear and, therefore, the flow of the overall deposits?

2. What are the thermal consequences of the water-ice bounding layers? How does the existence of these layers impact the vertical temperature gradient in the deposits, and does this affect the stabilization of the deposits?
3. What do these stratified mechanics mean for MCID preservation and mass balance, especially if the bounding layers slow CO_2 loss during low-obliquity phases?

For our work, we tie the H_2O ice bounding layer formation (sublimation lag) to obliquity changes to test whether the total count of modelled bounding layers match those observed, and to test whether the ice can reach the basins. We will continue the work of Smith et al. (2022) by using present-day observations (radar, topography, and thickness maps) and the laboratory-based flow laws for CO_2 (Cross et al., 2020).

5.2 Methods

5.2.1 3D Icesheet Modelling

Modelling is an effective method for studying and understanding the formation and behaviour of ice, particularly on other planets, where field measurements are currently impossible. Existing planetary ice models are typically either one-dimensional (1D) thermal equilibrium models or two-dimensional (2D) glacial models. Both 1D and 2D models, while they can help demonstrate the glacial flow and movement direction, are unable to properly distribute ice in three dimensions (3D) after deposition with respect to flow. In both cases, major assumptions are made that eliminate force and velocity components in one or two directions, reducing the fidelity in their results. In contrast, 3D Modelling, such as is available within the Ice-sheet and

Sea-Level System Model (ISSM), accounts for stress, thermal variations, and flow in all three dimensions, enabling a more realistic analysis of ice sheets and, consequently, more accurate predictions compared to 1D and 2D techniques.

ISSM is an open-source software solution that is developed by an international community of collaborators and supported by NASA's Jet Propulsion Laboratory (JPL). ISSM is a widely used modelling tool with capabilities to enable full 3D thermal and dynamical analysis of ice flow. ISSM was developed specifically to analyse and model water-based glaciers on Earth. ISSM offers:

1. Anisotropic mesh refinement, leveraging higher resolution of node density in specific areas of interest while conserving computational resources by using lower resolution mesh in other areas;

2. Finite Element Modelling (FEM) that solves differential equations in unstructured and adaptive meshes. FEM comes at a higher computational cost than other modelling methods;

3. Advanced ice dynamics models such as Blatter–Pattyn Higher-Order (HO) and Full Stokes (FS), as well as more commonly used (and 2D) approaches of Shallow Ice Approximation (SIA) and Shallow Shelf Approximation (SSA);

4. Thermal and stress balance and associated calculations;

5. A suite of sensitivity analyses tools;

6. Inverse methods, which leverage data from observations to estimate unknown variables; and

7. The use of parallel computing technologies, with optional utilization of state-of-the-art clusters and supercomputers.

For further information, see https://issm.jpl.nasa.gov, as well as relevant publications including Larour et al. (2012).

To model ice sheets in 3D and to determine the differential stresses and temperatures across an ice deposit, ISSM represents the icesheet model as a gridded mesh in 3D (Figure 1.9). The mesh is composed of triangular elements, with each corner of an element representing a node. ISSM assigns the thermodynamical differential equations to each node in the model and uses Finite Element Methods (FEM) to solve these equations. The FEM allows parameter values at each element of the mesh (and within each vertical layer in 3D) to vary. The solutions provide spatially resolved fields of velocity, stress, strain rate, and temperature. They are determined and applied for each grid cell locally before the stress, deformation, and velocity of the entire domain is solved. The solutions, therefore, describe the dynamics and flow of the modelled ice deposits.

For their modelling of CO_2 ice flow in the South Pole of Mars, Smith et al. (2022) upgraded ISSM to function on Mars and use CO_2 ice rheological flow laws properly (i.e., rheological parameters provided by Cross et al. (2020)). ISSM was successfully used in other targeted cases on Mars (e.g., Arnold et al., 2022, Fard et al., In Review).

In its standard form, ISSM considers a glacier to be a homogeneous mass. For this study, we extended ISSM to simulate stratified ice masses (i.e., ice masses with alternating units of distinct compositions and rheological properties). As the purpose of this augmented version of ISSM is to enable ***M***ulti-unit ***I***ce ***D***eposits ***A***nalysis and ***S***imulation, we refer to it as MIDAS.

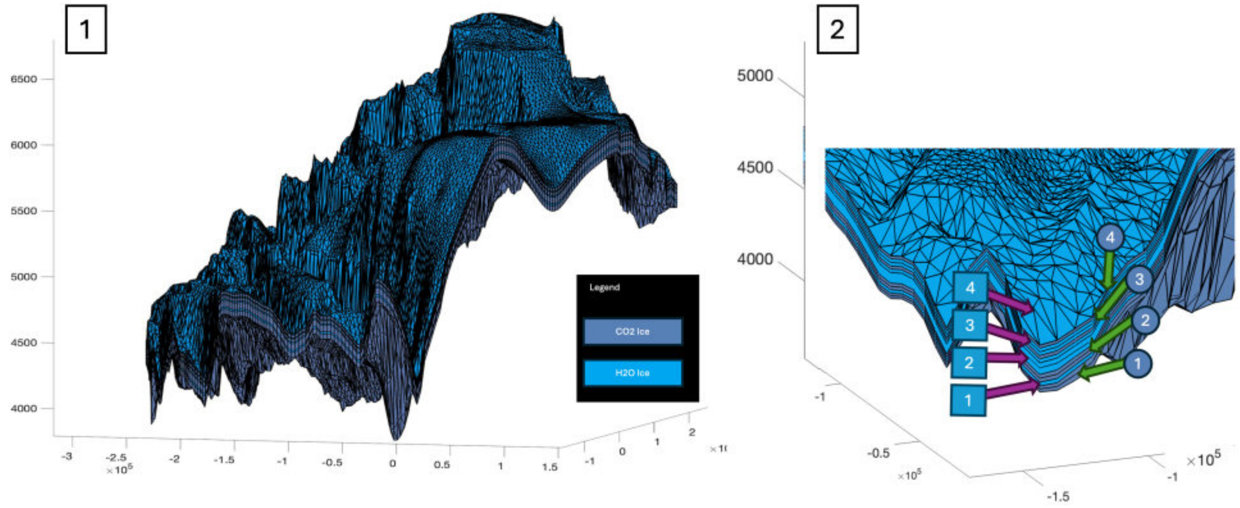

Figure 5.3 – Mesh Examples

(1) ISSM, originally designed to support a single ice mass, was upgraded to support multi-unit, multi-ice 3D models of ice deposit. This means that the CO_2 ice glaciers near the South Pole of Mars can be modelled with alternating layers of H_2O ice and CO_2 ice. This figure demonstrates the 3D gridded mesh of the South Pole of Mars as set up in MIDAS, with alternating layers of water and CO_2 ices. (2) A zoomed-in view to demonstrate the multiple units of ice managed by MIDAS. The numbers in circular icons point to CO_2 units, and numbers in squared icons show the H_2O units of ice. We will continue to use the same shades of colour referring to CO_2 (purple) and H_2O (blue) ice types in this paper.

5.2.2 Setting Up the Domain and Inputs from Climate Models

The input to our modelling work is surface mass balance (SMB) values from Buhler et al., 2020 for CO_2 depositions and Buhler (2023) for the lags left from the H_2O. Positive SMB indicates ice deposition or lag formation; negative SMB indicates sublimation. In their work, Smith et al. (2022) started from 600,000 years ago. They found that for the first 90,000 years of the simulation no bounding layer is formed and CO_2 deposits were near-zero thickness everywhere. To save computation time, we elected to use the output from Smith et al. (2022) after 90,000 years of their simulation as the starting point for our modelling. This way, we will set up our simulation to start from 510,000 years ago and to focus on the historical climate impact starting from that time (Buhler, 2023). Subsequently, we continue the simulation for the full 510,000 years which would bring the result to the present day. This allows us to model and examine the formation and impact of H_2O bounding layers (Figure 5.4).

For our modelling, which is very computationally expensive, we select a geographically reduced portion of the MCID to examine the growth of CO_2 units, the formation of its bounding layers and the impact of bounding layers on the overall flow and dynamics of the MCID. The selected portion (~30% of the full area of SPLD) was a compromise between model run duration and addressing our questions, so we chose an illustrative portion of the MCID that includes multiple basins and their catchments. Even with the downsized model, the simulation required several months to run.

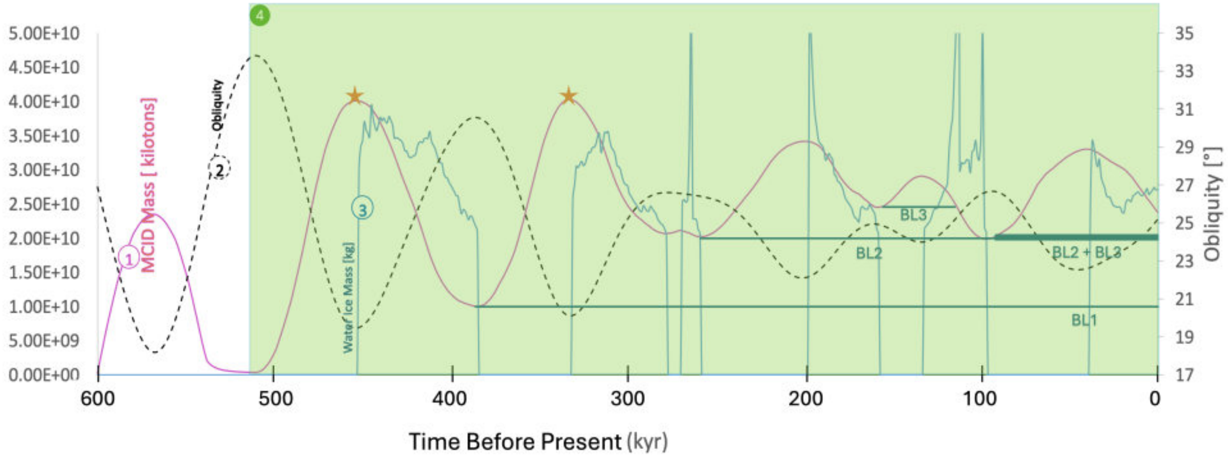

Figure 5.4 – Modelling surface mass balance (SMB) inputs over the time period in question.

Green box marked as 4. Starting from 510,000 years before present (near-zero MCID mass at that time). The curve marked as 1 demonstrates the accumulation of CO_2 *in MCID (in kilotons, left axis), reaching ~*4.4×10^{10} *kilotons at least two times (Smith et al., 2022). Curve 2 (black dashed line) illustrates the obliquity in degrees, varying between 15° and 35°. Curve 3 (water ice mass) depicts the mass of water ice accumulating over time (in kilograms) of all the water ice units combined. This is calculated based on the surface mass balance of water ice lag (Buhler, 2023), the area of modelling used by Smith et al. (2022) at about* 1.4763×10^{11} m^2*, and the density of ice Ih at about 934* $kg.m^{-3}$*. Three dark horizontal lines denoted as BL1-BL3 are the water-ice bounding layers that form as sublimation lag during negative* CO_2 *SMB. The two bounding layers start to form at about 452,000 and 330,000 years before present (yellow stars) respectively, when the* CO_2 *begins to sublimate. These two BLs reach their full thickness at 384,000 and 277,000 years before present, when* CO_2 *SMB switches to positive. The third BL forms around 160,000 years before present and eventually merges with BL2 about 100,000 years before present, when the* CO_2 *sublimated nearly fully, making the line thicker. This was predicted by Buhler et al. (2020) and observed by Alwarda and Smith (2021).*

Following the work of Smith et al. (2022), we used surface Digital Elevation Models (DEMs) from the Mars Orbiter Laser Altimeter (MOLA, Smith et al., 2001) aboard NASA's Mars Global Surveyor spacecraft and CO_2 base elevation from radar mapping using the Shallow Radar instrument onboard Mars Reconnaissance Orbiter (Alwarda and Smith 2021). These spacecraft and datasets do not extend to the south pole (they stop near 87° south), so we use the same extrapolation as Smith et al. (2022) to plot the topography of the South Pole, as in Figure 5.7. For our modelling, the first step is to remove the current MCID thickness; this will provide the basal topographic starting point (as in Figure 7(a)), which is the surface at the point when MCID started to form. This is done by subtracting the MCID depth as captured through radar from the current DEM (Putzig et al., 2018).

Several parameters used in MIDAS are temperature dependent (see Fard and Smith, 2024, and references within). Table 5.1 shows those used in MIDAS for this simulation.

	Thermal Conductivity	Heat Capacity	Density
CO_2	$10^{(-5.39941+5.45894*\log_{10}T-1.41326*(\log_{10}T)^2)}$	$-10^{(-6)}*T^4+0.001*T^3-0.2381*T^2+28.253*T-355.66$	$1723.91-0.253*T-(2.87*10^{-3})*T^2$
H_2O	$903.65*(T^{(-1.072)})$	$-22.86*10^{(-3)}*T^2+16.3163*T-720.5987$	$-0.0003*T^2+0.0316*T+933.29$

Table 5.1 - Temperature dependent material properties.

Other input parameters and assumptions for this simulation are as follows:

- Geothermal heat flux is 30 mW/m² and uniform spatially. We adopted the lowest geothermal heat flux value estimated by Grott et al. (2007) for the southern highlands scarps, as a conservative choice for our modelling. For comparison, Smith et al. (2022) covered a few different geothermal heat flux values, including 25 mW/m² for their simulation number 38 (SN#38) which we will refer to often as a comparison benchmark in this paper.

- Mesh Virtual Separation Layers: These are model separation layers between two rows of the gridded mesh (Figure 5.5). In effect, virtual layers divide an ice unit horizontally for more representative calculations. This simulation uses different numbers of virtual boundary layers depending on the height of each unit of ice (i.e., H_2O and CO_2 ice units) throughout the 510,000 years of modelling. We apply a minimum of 2, and maximum of 5 boundary virtual layers to each ice unit. As the thickness of each unit increases, so does the number of the virtual separation layers. This is done to ensure there is sufficient and effective vertical resolution maintained in each unit of ice.

- Rheological Laws:

- For CO_2 ice, Glen's exponent is considered to be 8, $\log_{10}(A_{const})=13$ MPa^{-8} s^{-1}, and the activation energy is 66,900 [J/mol] (Cross et al., 2020).

- For H_2O ice, Glen's exponent is 3, $\log_{10}(A_{const})=4.5$ MPa^{-3} s^{-1}, and the activation energy is 60,000 [J/mol] (Fard and Smith, 2024 and the references therein).

- Minimum Ice Thickness: Due to the inherent structure of ISSM, no node that is in contact with the ground can reach an ice thickness less than 1 m. As such, MIDAS enforces a minimum thickness of 1 m for the lowest ice unit (resting on the ground) at all nodes. Specific to this current simulation, the CO_2 ice thickness can only decrease through sublimation (or advection, usually on a slope). During the formation of MCID, sublimation of a CO_2 ice unit occurs during the formation of an H_2O ice lag deposit above it. Our tests showed a specific behaviour during the formation of the first H_2O ice unit, which occurs as the lowest CO_2 ice unit sublimates. During this process as the CO_2 ice thickness at a node reaches 1 m (and sublimation at that node is halted), the node immediately above it begins to accumulate more water ice than its adjacent nodes. To address this, MIDAS includes a check to ensure water ice accumulation at a node is proportional (and it is maintained as such) to that of its adjacent nodes, provided the underlying CO_2 ice at the node has reached the threshold of 1 m and is no longer undergoing sublimation.

- Surface Temperature: We kept the surface temperature for the duration of the simulation fixed at 150 K. The internal temperature, on the other hand, will be calculated by ISSM, and the internal model is governed by advective heat transport.

- Basal Friction: By assigning a very high friction coefficient (i.e., 500), we ensured there is negligible sliding at the base of the modelled MCID.

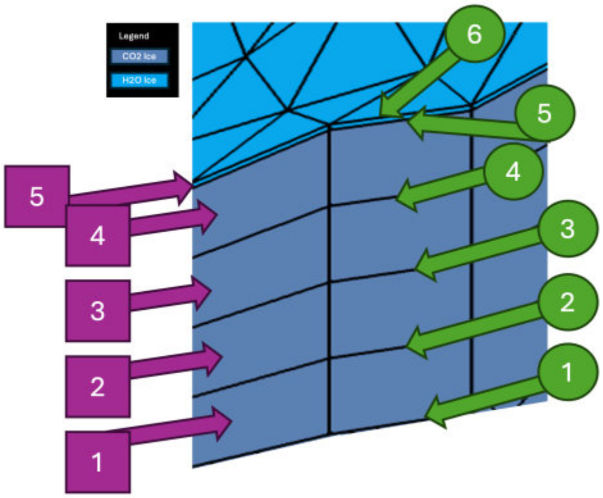

Figure 5.5 – Profile of a mesh.

The arrows identified with numbers in circles point to the virtual separation (mesh boundary between) mesh layers. Mesh Boundary 1 is the lowest and rests on the ground (or the previous ice unit). The arrows identified with numbers in square boxes point to the layers of elements in the mesh. This picture contains one unit of water ice (one layer) located over a unit of CO_2 ice that contains four virtual layers.

Changes to these parameters offer opportunities for future simulations. These include varying the geothermal flux, surface temperature and the rheology laws related parameters. Another opportunity includes varying the surface temperature as well as the deposition based on the elevation and node location, which they are all permissible in ISSM/MIDAS.

As mentioned, H_2O particles most probably were deposited as snow with CO_2 (Alsaeed & Hayne, 2022), and acted as sublimation lag, forming a bounding layer (Buhler 2019 and 2023; Smith et al., 2022). In this simulation, we make the simplifying assumption that the H_2O particles are deposited on the surface to form a new lag layer during the CO_2 sublimation process (Figure 5.6).

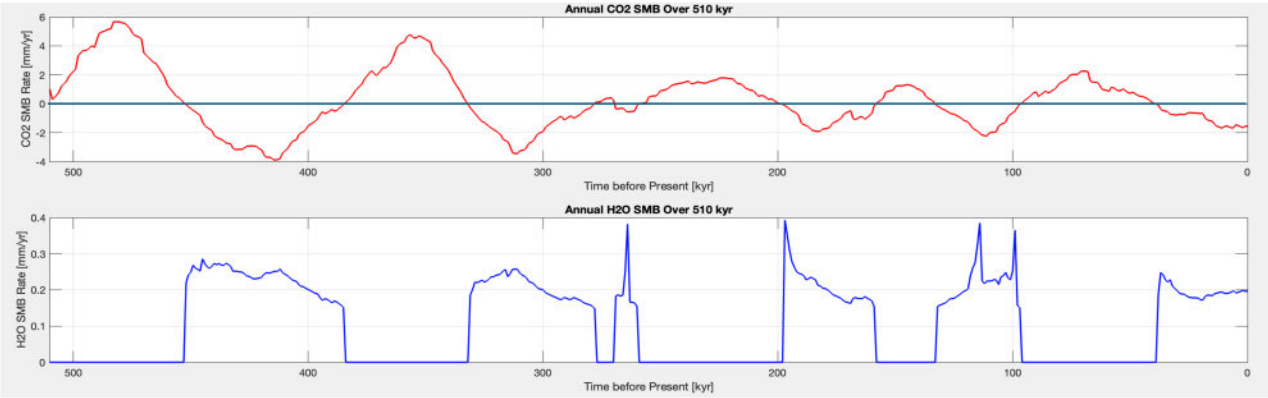

Figure 5.6 – Annual CO_2 and H_2O ice deposition over the past 510,000 years has been modelled (Buhler et al., 2020; Buhler, 2023).

H_2O deposits as a sublimation lag because it was formerly entrained in the CO_2 unit as the water was scavenged from the atmosphere during CO_2 deposition. Thus, the accumulation rate of the H_2O lag depends linearly on the CO_2 sublimation rate, during periods when the surface mass balance (SMB) of CO_2 is negative. During periods of CO_2 accumulation, to simplify the rheology of the material, we assume that no H_2O is present within the CO_2 ice unit mass outside of the BLs; this assumption works

because the volumetric contribution of H_2O particles is assumed to be too small (an order of magnitude smaller than the CO_2 component) to affect the thermal or viscous properties of the CO_2 ice unit.

5.2.3 Spatially Dynamic Mesh Structure

We initialize the model using the present surface and remove the modern MCID thickness where necessary to define basal topography (i.e., Figure 5.1 (D) minus Figure 5.1 (A) as in Figure 5.7), then we apply the CO2 distribution from the first 90,000 years from the Smith et al (2022) study to the surface. We can do this here because nearly all of the CO_2 had sublimated, and the bounding layers would have been in contact with the lower SPLD. This prepares the modelling domain for our process starting at 90,000 years applying deposition–ablation cycles derived from orbitally forced equilibrium CO_2 pressures (Buhler et al., 2020). Throughout, we retain community conventions for notation and units.

For the purpose of this simulation, we use nested domains to leverage the spatially adaptive gridded mesh functionality offered by ISSM. Each domain will have a different mesh resolution. Areas with finer spatial resolution can correspond to areas, for example, with higher surface velocity gradients or more sloped bedrock or surface elevation. The ISSM function that generates the spatially dynamic mesh takes the domain as an input; therefore, identifying the boundaries of domains is crucial for ensuring proper mesh structure. See ISSM documentation for further information about creating gridded mesh.

In our simulation, each mesh element is triangular in shape with the outer mesh resolution starting from 8000 m and reaching 7000 m where the inner mesh starts (area 1 in Figure 5.7d). The resolution of the nested mesh is 3900 metres (area 2 in Figure 5.7d). As the mesh is generated based on the surface geometry, the spatial resolution should be finest where the ice surface slope is the steepest. This results in a full two-dimensional, horizontal mesh with about 6,000 nodes and 11,800 horizontal elements. The number of nodes and elements in 3D, however, is variable depending on the number of mesh separation layers; the numbers vary from 30,000 nodes and 47,000 elements at the start of the simulation to about 66,000 nodes and 120,000 elements by the end of the simulation (with 11 mesh separation layers, as in Figure 5). The change in the number of elements will have a direct impact on the processing time.

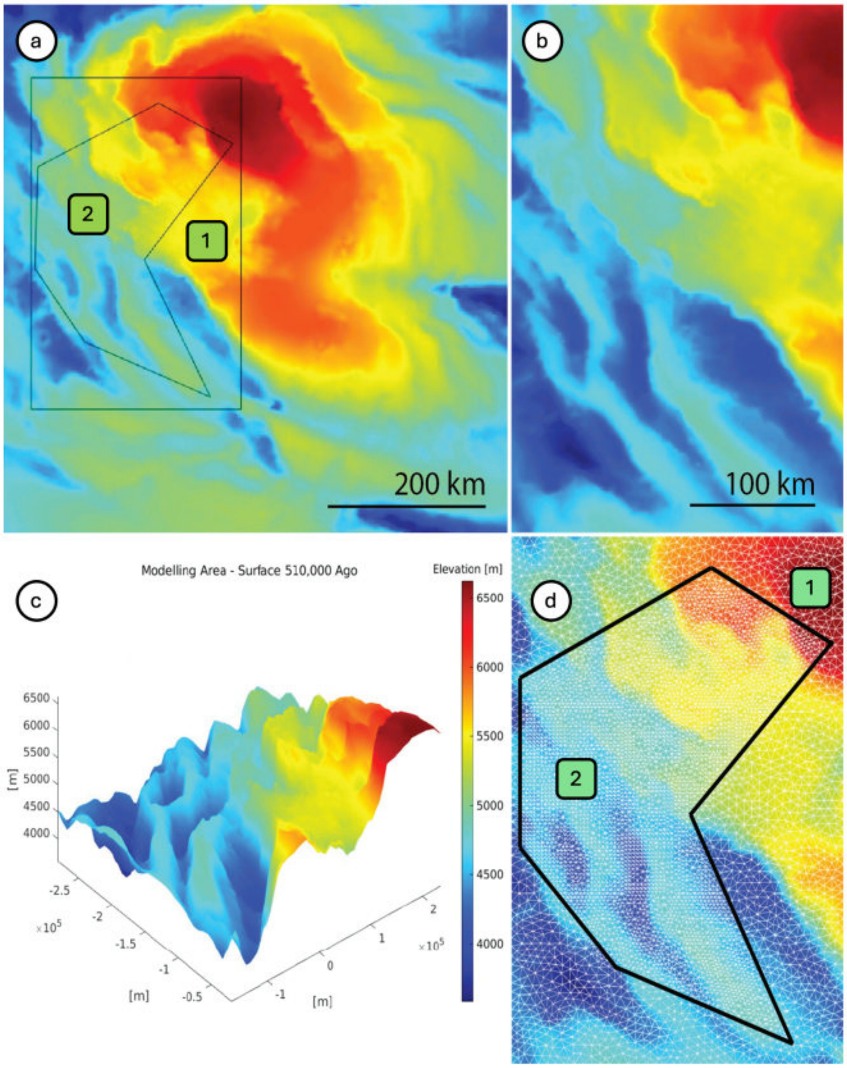

Figure 5.7 – Colourized Digital Elevation Models (DEMs) showing the domains and mesh resolution. (a) Context map of the SPLD showing the modelled domains. The current MCID has already been removed, leaving the SPLD surface as the deposition surface. The area of this plot is about 4.1x10^{11} m^2 (b) zoomed-in view corresponding to Domain 1 in figure 7a. This is the area where the simulation will focus on. The area of the simulation domain (i.e., area (1)) is about 1.07x10^{11} m^2. (c) A three-dimensional, perspective view of the simulation domain showing the basins. (d) The simulation will use a gridded mesh starting from 8000 m to 7000 m (area (1)) before merging with the inside mesh (area (2) where each side has a resolution of 3900 m). Domain (2) was selected to incorporate several of the most important MCID basins, avoid relying on interpolated data at the highest latitudes, and to match the external domain edge from Smith et al. (2022).

We use a hybrid-transient forward modelling approach. In order to accommodate the temporal evolution of multiple stratified units of ice, we have to recreate the mesh frequently, which requires pausing the transient model, recreating a mesh with the appropriate layers, and restarting a new transient model. For each restart, the output velocity components in x, y and z directions, temperature, pressure, stress and geometry of a model will become the input as boundary conditions to the subsequent time period modelled. Starting from 510,000 years before present, for the first 57,000 years of the simulation, there will only be CO_2 ice deposition, so MIDAS will treat the MCID as one block of homogenous ice forming over the ancient ice bed. Starting at the 58,000th year, CO_2 ice sublimates (i.e., negative SMB will be applied to the CO_2 block of ice), and water ice particles start to accumulate on the surface of MCID. This requires pausing the transient run to adjust the vertical mesh.

5.2.4 Stress Balance Formulations For MCID: SIA vs. HO

The choice of stress balance approximation is critical for accurately simulating the MCID. There are various approximations available (see Appendix 1) The Shallow Ice Approximation (SIA) assumes that flow is dominated by vertical shear and that longitudinal and lateral stress gradients are negligible. This assumption breaks down for the MCID for several reasons:

1. Complex 3-D Geometry: The MCID includes (at times interconnected) basins separated by ridges and slopes. Flow is not uniform or sheet-like; instead, it is guided by diverse spatial gradients that are dictated by the topography which requires lateral stress transmission. In many basins the ratio of ice thickness to the length of the icesheet, while small, is not negligible. The first condition for SIA (i.e., $H/L \ll 1$) is not satisfied.

2. High Viscosity Contrast Between CO_2 and H_2O Units: Alternating water-ice and CO_2 units generate sharp vertical gradients in viscosity and internal shear. These stratified layers need an approximation method that resolves depth-varying horizontal stresses (i.e., vertical gradient of horizontal stress components), and SIA in not able to do so as it ignores the longitudinal stretches and lateral drag on every layer of the mesh.

3. Large Glen Exponent ($n \approx 8$) for CO_2 Ice: For highly non-linear materials, even moderate longitudinal stress gradients is amplified due to the sheer thinning and high level sensitivity these materials have to stress. SIA would misrepresent these gradients entirely.

4. Cold-Based Conditions and Limited Basal Shear: Because the MCID is cold-based, deformation is concentrated within the body rather than the bed. This increases the

importance of longitudinal coupling between layers, this is, again, against the foundational assumptions of SIA.

5. Stratified Nature of MCID: The MCID is a set of stratified units of CO_2 ice and H_2O ice. SIA collapses the stress balance into an effectively two-dimensional formulation; it treats the vertical column as a single homogeneous material. In a stratified system, this would artificially merge layers of ice with different viscosity, conductivity, and activation energy into one blended rheological 2-D plain with artificial properties. In such model, as a result, SIA is unable to preserve the structure and contrasts of the materials which effectively define how the MCID behaves.

5.2.5 Model Validation

For validating the upgrades from ISSM to MIDAS, our first step is to compare against the ISSM results presented in Section 3.1 of Smith et al. (2022), from their 38th simulation (SN#38). For clarity, there are some major differences between parameters used for SN#38 and those used in this study. Apart from the temperature-dependent parameters that we develop for the first time, the existence of water-ice bounding layers in our study, and the geothermal heat flux values (see section 5.2.2), other defining factors are as follows:

1) Modelling framework differences: SN#38 solves the model by leveraging Shallow-Shelf Approximation (SSA). SSA is a depth-integrated, stress balance approach that assumes there is only negligible vertical shear (i.e., in xz and yz directions), which results in depth-uniform horizontal velocity. SSA is less computationally intensive. The current study leverages the Blatter–Pattyn (BP) Higher-Order (HO) formulation. This HO approach tends to capture and retain vertical shear as well as the across-flow stress gradients. This way the vertical velocity structure and lateral

shear are captured and retained. As a result, BP-HO might result in different thickness/temperature responses.

2) Domain and mesh sizes: SN#38 leverages a domain with an approximate area of 1.43x10^{11} m^2. We have selected a domain with an approximate area of (Figure *5.8*) 1.07x10^{11} m^2 which overlaps partially with SN#38's domain. The resolutions are also different. SN#38 resolution varies from 3500 m to 4000 m. The current simulation leverages an adaptive resolution from 8000 m to 7000 m for the outside domain and a fixed resolution of 3900 m for the inside domain. Vertically, SN#38 leverages 7 (a fixed number) of virtual mesh layers. The model in this study uses an adaptive number of vertical (i.e., variable) mesh layers that increase as new units of ice form and then decrease as CO_2 ice units disappear due to their sublimation.

3) Simulation Duration: SN#38 starts 600,000 years ago (at the start of the formation of MCID over the ancient ice). Extrapolating from the SN#38, our simulation uses the outputs from the first 90,000 years from SN#38 and then continues from 510,000 years ago to present day.

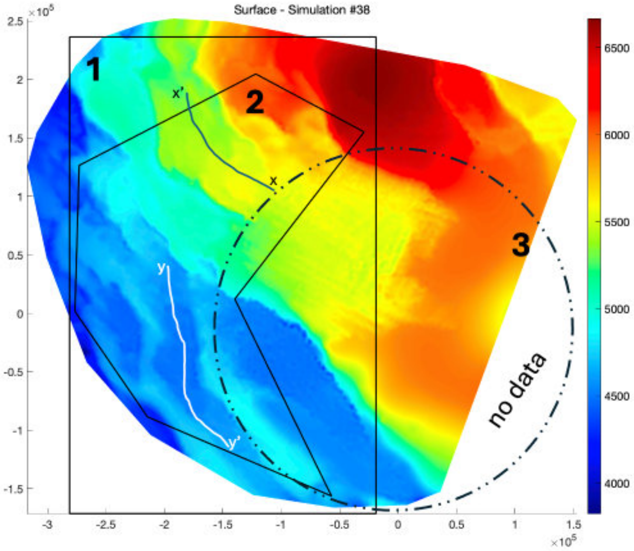

Figure 5.8 – SN#38 simulated surface.

The inner and outer domain boundaries used in our simulation have been overlayed over the SN#38 domain to provide a comparative view. Here, the "no data" zone is marked (i.e., area 3). This area is where the data has been interpolated using the surface from (Putri et al., 2019) as in Smith et al., (2022) minus the extrapolated MCID thickness (Smith et al., 2022). The x-x' and y-y' lines correspond to the radar profiles in Figure 5.1. *The rectangle box (area 1) and the plotted area inside it (area 2) correspond to the domain boundaries illustrated in Figure 5.7.*

5.2.6 Merging of CO_2 Ice Units

As units of ice undergo sublimation, it is possible for a unit of ice to completely disappear (especially as expected during the formation of MCID (Buhler et al., 2020; Smith et al., 2022; Buhler, 2023)). MIDAS monitors the thickness of ice in a unit and reacts accordingly. As an example, if the thickness of a CO_2 ice unit that is bounded between two water ice units, becomes less than 5 cm, MIDAS will remove that unit, and merge the two bounding water ice units. As a result, the overall MCID mesh will be restructured. The two merged water ice units will now be the new and active top ice unit, and sublimation will be applied to the CO_2 unit immediately below it.

5.3 Results

Similar to the work of Smith et al., (2022), this simulation demonstrates that the steeper the slopes, the faster the ice (CO_2, and H_2O) moves down the slope. To compare, we have included the results from their work (Figure 5.9) in this paper.

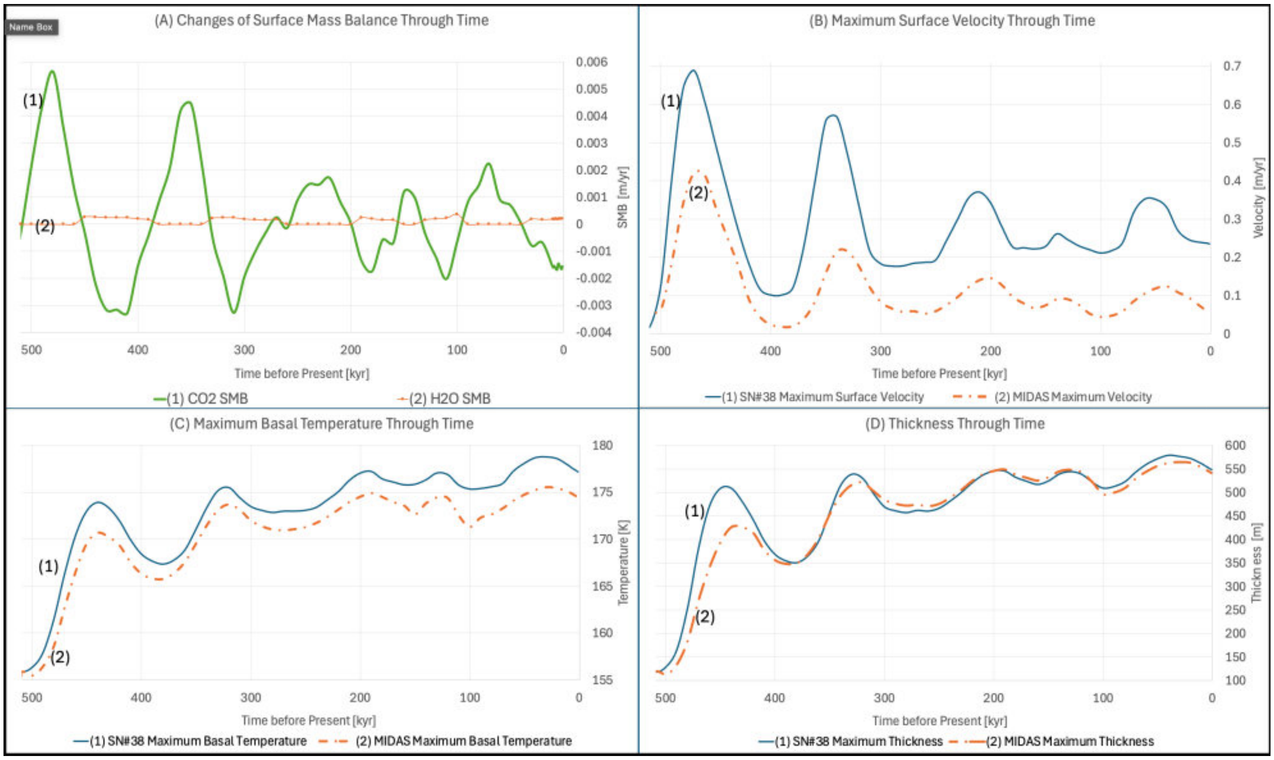

Figure 5.9 – Results from the Simulation Number 38 (i.e., SN#38) from Smith et al., (2022) that had no bounding layers (blue dashed lines), and used SSA vs. the results from this study which are marked as “MIDAS” (orange dashed lines), in panels B to D.

This study used the SN38 results at 510,000 years before present as input and then diverges. The horizontal axis shows time before present. For the purpose of this plot, we have extracted the data from SN#38 results pertaining only to the area that matches the domain of the current study (i.e., the rectangular region identified in Figure 5.8). (A) The changes to the surface mass balances in metre per year. The green solid line represents the CO_2 mass balance changes which are consistent across both sets of models. The solid orange line shows the water ice lag which is an input parameter used in the current study (Buhler et al., 2020; Buhler, 2023). (B) Maximum surface velocity through time. While following the same local minima and maxima as SN38, the MIDAS results demonstrate reduced velocities caused by the inclusion of BLs for two reasons. 1) the included H_2O is stiffer than CO_2 at the *same temperature and acts to slow the bulk ice, and 2) The temperatures are lower, which acts to stiffen the* CO_2 *ice. (C) Maximum basal temperature in the model. Because of the way the model calculates temperature, this varies linearly with maximum thickness (D). The orange curve is offset lower than the green dashed curve. This is primarily because of the difference in maximum thickness. A secondary reason is that* H_2O *BLs are better thermal conductors, which serves to increase heat throughput and reduce the basal temperature. (D) Thickness through time. The MIDAS maximum thickness is smaller than from SN38 because ice flows into the basins (where it collects) more slowly.*

Over the course of the entire simulation, while SN#38 experiences maximum surface velocity of about 0.70 m/year (in the area overlapping with the current study domain), the maximum surface velocity in MIDAS reaches 0.43 m/year, ~40% lower than the maximum surface velocity that SN#38 produces in the same area as that of used in the current study. This is to be expected as the water ice acts in two ways to slow the bulk flow. First, H_2O is stiffer, so the inclusion of BLs will act to retard the flow. Second, H_2O is a better thermal conductor, resulting in lower heat retention, that in turn increases the viscosity of the bulk ice mass.

Most of the basal temperature difference between SN#38 and MIDAS is caused by the difference in maximum thickness. Secondarily, the thermal conductivity of the included H_2O increases heat throughput, which has the effect of lowering the basal temperature in MIDAS. SN#38 basal temperature experiences a maximum of ~189 K (about 27,000 years before present); around the same time MIDAS results reach its maximum basal temperature at 175 K (Figure *5.9*).

Comparisons between the new results and those from SN#38 are collected in Figure *5.9* and reveal the following points:

1) The average temperature, thickness, and velocities across in this simulation are significantly lower than those in SN#38, typically 20-30% lower based on domain-averaged values.

2) Surface velocity maxima and minima in these results may have similar timing, but the peaks are more muted with the inclusion of the BLs.

This demonstrates the velocity-inhibiting impact of the water-ice bounding layers on the full ice column. However, as we will demonstrate below, localized comparisons (in slopes and basins), rather than global maximums, provide a more complex picture in which velocity magnitudes and basal temperature in MIDAS are, at times, lower, and at other times (due to thickening of CO_2 ice units) become higher.

5.3.1 Formation of water ice units

In our modelled MCID, the first water ice unit starts to form about 451,000 years before present (YBP, Figure *5.6*). The average thickness of the CO_2 ice unit is about 180 m at this point (Figure *5.10*). The formation of the water ice unit (along with the sublimation of the below CO_2 ice unit) continues for 66,000 years (until 385 KYBP). At 384 KYBP, a new CO_2 ice unit starts to form, reaching an average thickness of about 135 m after 53,000 years, at 331 KYBP. Then, during CO_2 sublimation, the second water ice unit will form. This process continues for another 293,000 years (to reach the final structure 38 KYBP), and includes formation of new layers, and merging of H_2O ice units due to sublimation. Figure *5.11* summarizes the full process.

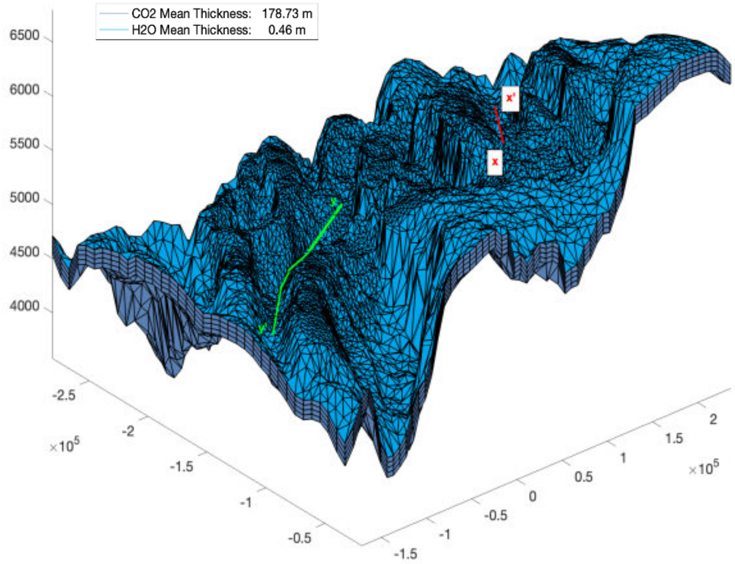

Figure 5.10 – A view of the MCID meshed domain at 451 kiloyears before present (KYBP), when the first water bounding layer begins to form.

The x-x' and y-y' markings correlate with Figure 5.1 *and Figure 5.8.*

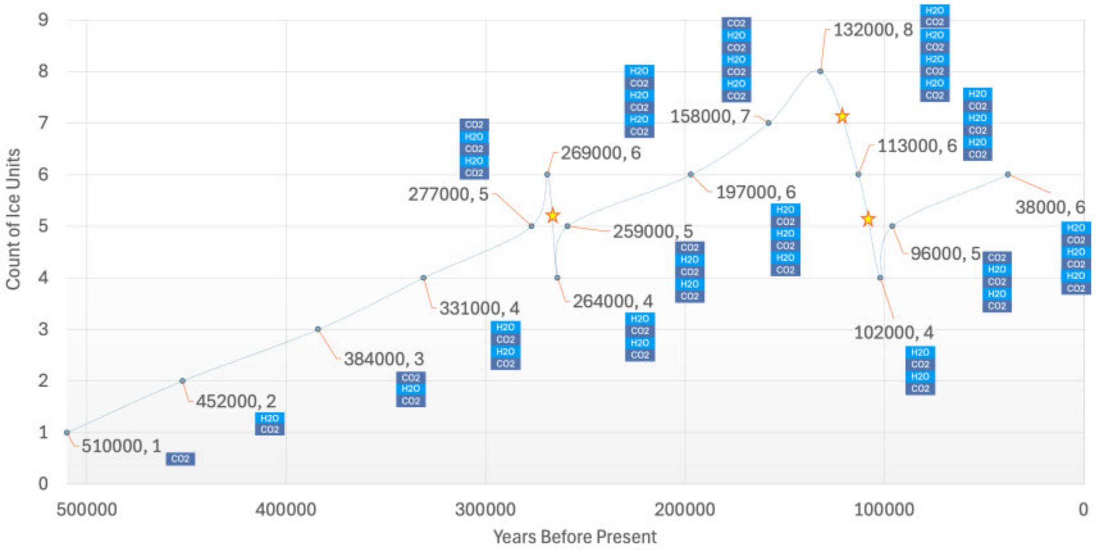

Figure 5.11 – Summary of MCID ice units' formation.

The labels on the plot give the year before present followed by the total number of ice units at the start of that year. For example, the second ice unit (i.e., a water ice unit) forms 452 kybp, so from that year 384 kybp there are two ice units in the model. The stars mark events where two H_2O ice units merge.

For instance, between 269 and 264 KYBP, sublimation of the highest CO_2 ice unit causes it to almost disappear and starting in year 264 the two H_2O ice bounding layers merge, reducing the total number of units from six to four. Each ice unit's composition is shown in the set of boxes placed next to each data point.

As demonstrated in Figure *5.11*, the model concludes with six ice units, three of which are water-ice bounding layers engulfing CO_2 ice units.

5.3.2 Unit Thickness and Flow Rates

In this section we present the cross section profiles of thickness (Figure 5.12), temperature (Figure 5.13), and "Δ velocity magnitude from the mean" (Figure 5.14) for the lines x-x' and y-y' (Figure *5.1*). Vertically, the magnitude of velocity does not vary discernably, so we define and plot $\Delta v = |v_i| - \langle |v| \rangle_n$, the deviation of each element's velocity magnitude from the vertical-column average, to highlight layer-to-layer contrasts.

For comparison we also present the cross-section profiles from SN#38, that show only one block of CO_2 ice. These profiles are from two different times: 452,000 years before present (which is when the first obliquity minima occurred, immediately before the first negative SMB of CO_2 and the first H_2O ice accumulated; Figure 5.4) and the concluding year of the simulation which correlates with present day. Considering that SN#38 and this study have different mesh resolutions, we selected the closest coordinates for extracting the profiles. See Appendix 3 for the longitude and latitude of the selected control points.

When compared to SN#38, the presence and placement of higher viscosity water-ice bounding layers alter the internal flow structure of the MCID. These layers act as mechanical barriers that locally suppress shear, reducing strain rate within the CO_2 ice (Figure 5.12). As a result of these lower deformation rates, internal frictional heating is reduced, which in turn produces a cooler thermal profile throughout an ice column. In the layered ices temperature decreases more gradually from the base toward the surface, and the overall flow rate is further inhibited by the lower internal temperatures in the next time periods (see Figure 5.13 and Figure 5.14). This effect is in combination with the thermal conductivity being overall higher in our simulation than in SN#38, as discussed earlier in this section.

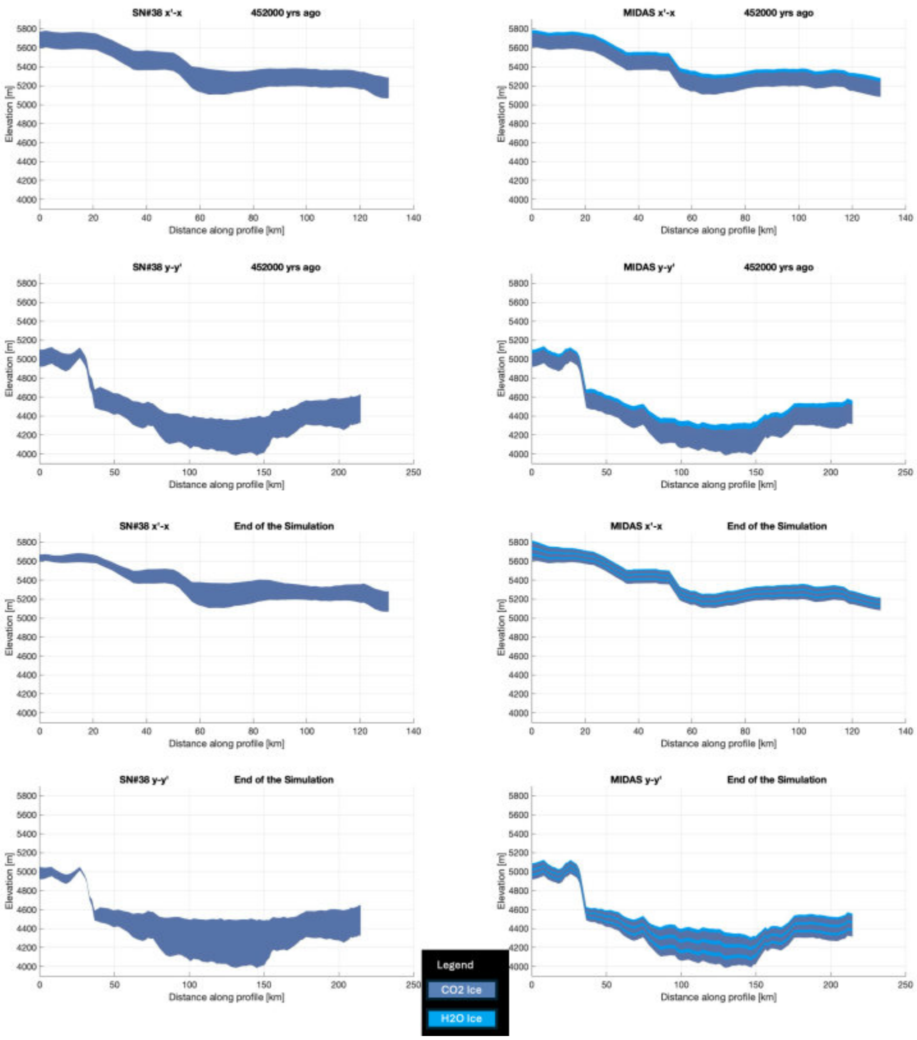

Figure 5.12 – The thickness profiles (including elevation) for x'-x and y-y' slices at 452 KYBP and present day.

Within the basins where the ice ponds, the MIDAS thickness for (both) is less than the thickness of ice in the SN#38. In contrast, on slopes, the MIDAS ice thickness is greater. Both of these results can be explained by reduced flow rates, as ice moves slower downhill, larger portions will remain at higher elevations.

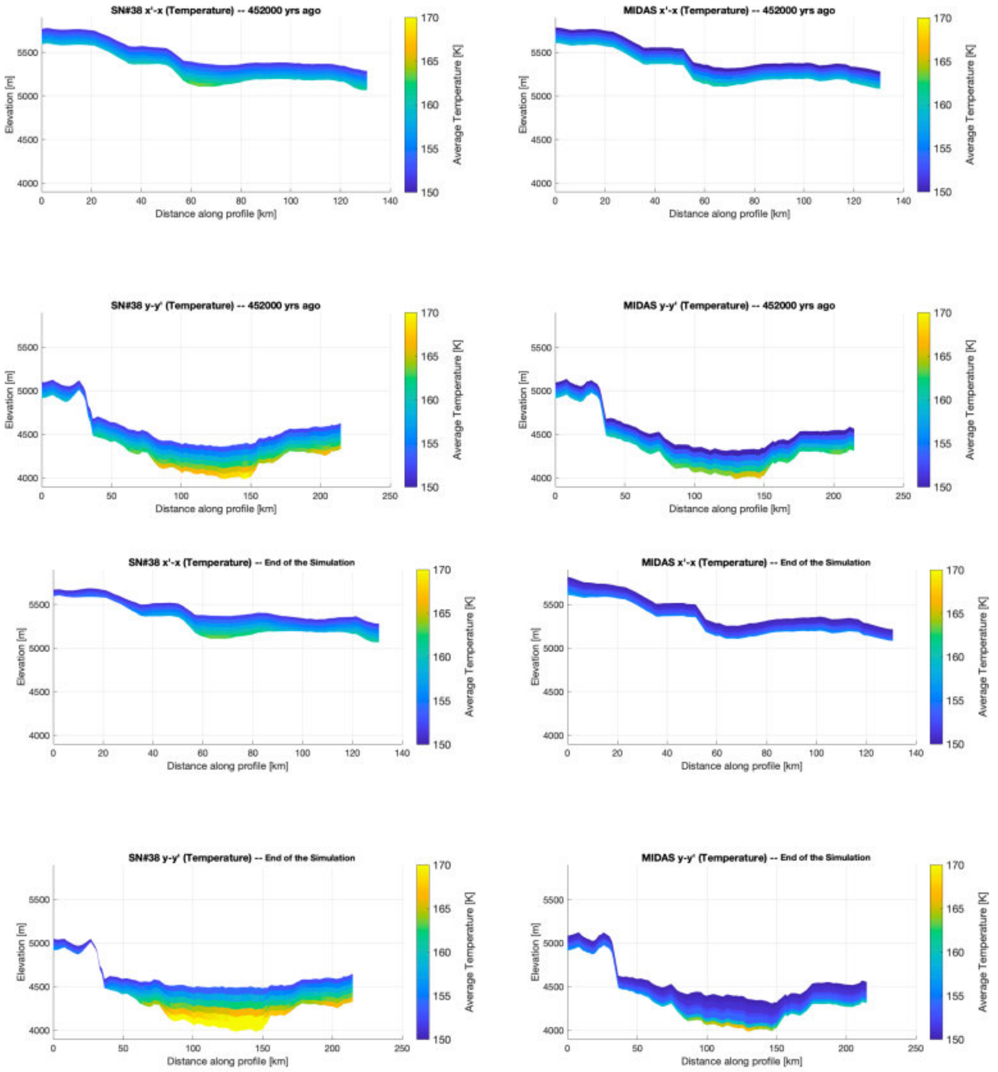

Figure 5.13 – Internal temperature profiles x'-x and y-y' of the two studies.

In each case, the MIDAS results have lower basal temperatures. There are three causes of this alteration: 1) temperatures are linearly dependent on ice thickness; 2) lower internal stress and strain reduce the heat generated through internal friction; 3) water ice bounding layers act as conductors of *heat, more efficiently transporting geothermal heat to the surface. Thus, the MIDAS results have a smaller thermal gradient between the surface and the base. Importantly, the highest basal temperatures remain well below the CO_2 sublimation temperature for the corresponding pressures (in the model, basal ice pressure reaches a maximum of ~3.26 MPa, which corresponds to a melting temperature of ~218 K).*

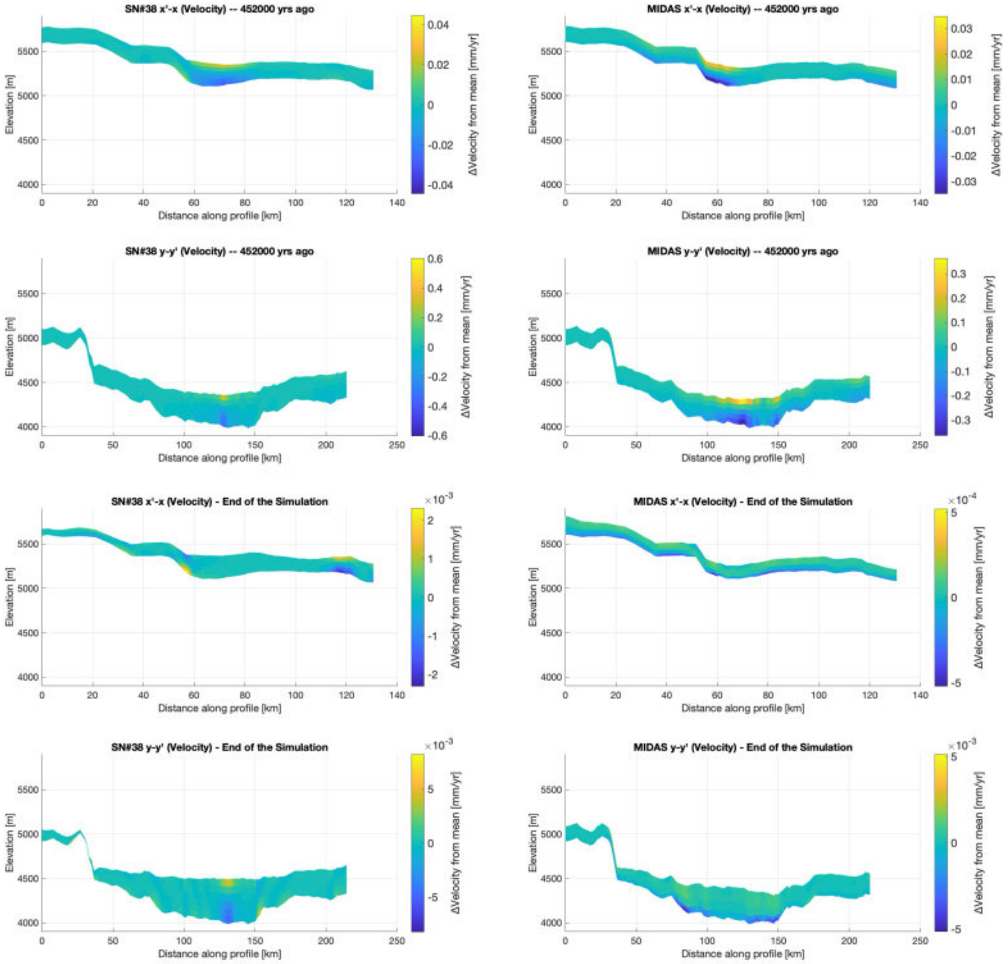

Figure 5.14 –Velocity Δ profiles at x-x’ and y-y’.

These panels show profile-relative velocity from the vertical profile mean, Δv, which is defined as velocity magnitude in each element minus the mean velocity magnitude of their corresponding vertical profile. Positive values (warm colours) present faster-than-vertical-profile-average; and negative values (cool colours) are slower elements. Because the vertical gradient in absolute velocity magnitude *is very small, the differences among mesh layers become rather hard to see in raw plots. As such, we elected to use columnar Δv to highlight layer-to-layer contrasts.*

For the velocities, we elected to show the difference between the speed of an element minus the column average of velocities (*Figure 5.14*). Note the differing colour scales between time slices. This is also done to keep the patterns in each plot readable (end-of-run anomalies are on the order of 10^{-3} mm yr^{-1}). At 452,000 years before present, for both scenarios, *Figure 5.14* shows that the flows tend to be rather uniform with only small anomalies. Where water-ice bounding layers are present, Δv skews negative (cool colours). This is consistent with the expectation that these layers should inhibit the flow by reducing the internal shear stress and deformation relative to surrounding CO_2 layers. Along x–x′, the MIDAS run shows slightly stronger positive anomalies over the mid-profile in comparison to SN#38; this too is consistent with the expectation that CO_2 flows faster locally before the water-ice bounding layer impact on inhibiting flow starts to show itself as CO_2 ice gets closer to the location of the H_2O ice layers. Along y–y′, the slope preserves a band of lower-than-average velocities. This suggests the impact of the slope on the strain (and therefore a reduction in the flow rate) and suggests strain concentration towards the basin floor. By the end of the simulation, Δv becomes very close to zero almost everywhere in both x-x' and y-y' and the flow becomes even more vertically uniform. This is again consistent with the expectation that the water-ice layers provide a mechanical impact as bounding layers, slowing down the overall flow of the glacier. This will result in guiding the distribution of the CO_2 units across the MCID as suggested by Figure 5.12. See Figure 5.13 for stress reduction impact of the water-ice bounding layers on the thermal profile of these slices.

5.3.3 Comprehensive Comparison: SN# 38 vs. the Current Study

An additional way to compare this study with SN#38 (Smith et al., 2022) is to focus on four control points on the slopes and basins along x–x′ and y–y′ cross sections. This comparison also serves as a baseline check against a different modelling approach: SN#38 uses SSA, however, this current study uses HO-BP. SSA, or the Shallow Shelf Approximation, assumes that vertical shear stresses are insignificant, and therefore, neglects series of stress-gradient terms in the full Stokes equations. This is done to simplify the momentum balance and improve computational efficiency. This approach can lead to less accurate approximations in settings where vertical shear or longitudinal stress gradients are important. We can see the differences between SN#38 and thic current study (which uses HO-BP) in Figure 5.15. For the first 58 000 years of the modelling period, and before any water-ice bounding layers develop, the results from MIDAS and SN#38 already show divergence. The primary reason, we hypothesize, is the different stress-balance formulations (HO in MIDAS versus SSA in SN#38). Additional contributing factors include differences in domain size and the fact that SN#38 begins at 600 KYBP.

In this study, the first 90,000 of SN#38 output is extracted and interpolated to obtain the ice-thickness at 510 KYBP, which is then used as the initial condition for this current study. This approach was used to reduce computational cost; however, it result in differences between the two models as the simulations progress.

This shows how the formulation differences also result in different modelling outputs. I call the points that are on higher elevation, the slope points (S1 and S2), and the points in the lower elevation the basin points (B1 and B2) (along x-x′ and y-y′ respectively). I locate the target coordinates on the south-polar DEM, and use the nearest mesh nodes in each model (See Appendix 3 for the longitude and latitude of the selected control points), and track two quantities through the full modelling window: (1) the column-average velocity vectors magnitudes (i.e., the mean of velocity magnitudes of the columnar nodes along the vertical layers of the mesh) and (2) the local ice-column thickness. That is, each curve represents the temporal evolution of a vertical column at that location (Figure 5.15). In general, the two velocity and thickness maxima occur near 450 and 325 KYBP. These points as well as the local maxima and minima points are aligned with the obliquity peaks and valleys (Figure 5.4). The localized impact of the water-ice bounding layers, as demonstrated by these plots, present a complex picture (Figure 5.15):

(a) S1 (Figure 5.15**(a)):**

The selected point lies about 30 km along the cross section. The slope where is S1 is located is ~0.4°. During the first 58,000 years (i.e., before the formation of the first H_2O bounding layer), both models produce nearly identical thickness and velocity magnitude curves. Minor offsets arise from the difference in stress-balance formulation (BP-HO in MIDAS vs SSA in SN#38). Once the first water-ice layer begins to form, MIDAS velocity magnitudes for S1 begin to decline by >25% in comparison to SN#38. However, the CO_2 ablation, which will continue until 385 KYBP, will reduce the ice overall thickness in S1 to ~50 m in SN#38 and ~70 m in MIDAS. For the next ~55,000 years, the S1 thickness is slightly higher (likely due to the inclusion of the newly formed water ice layer). We conclude that the locally higher velocity magnitudes in MIDAS results after 330 KYBP (compared to SN#38) are driven by the greater ice thickness upstream (Figure 5.12) which increases the driving stress in S1; as a result, CO_2 velocity magnitudes are increased, despite the presence of viscous H_2O layers. In other words, since CO_2 ice is more sensitive to stress than H_2O ice, the increased shear stress allows CO_2 to continue flowing downslope even while mechanically bounded. We consider this as a conclusion that greater thickness on slopes could locally offset the flow inhibiting effect of water ice bounding-layers.

(b) B1 (Figure 5.15**(b)):**

B1 is located in the flat surface of the basin in comparison to where S1 is located. MIDAS results support a process that, as ice flows downslope toward B1, it first accumulates over a nearly flat surface where, due to the flatness of the area, the shear stress becomes minimal. However, continued inflow from the upstream slope provides a continuous source of ice, resulting in the ice to eventually accumulate within the basin (at B1). Figure 5.15(b) shows that velocity magnitudes at B1within the basin track closely with those of S1 on the slope, indicating that the accumulation rate at B1 is highly dependent on the incoming ice flow.

(c) S2 (Figure 5.15**(c)):**

At about 5°, this slope is considerably steeper than S1 of the x′–x cross-section. Before the formation of the first H_2O bounding layer, both models behave nearly identically, aside from minor offsets caused by the difference in stress-balance formulations. SN#38 shows a small early-time anomaly in S2 that is absent in MIDAS.

After the first H_2O layer has fully formed, MIDAS S2 velocities are reduced in comparison to S2 velocities in SN#38. This is expected as a result of the higher level of effective viscosity possessed by the water ice bounding layers. As the simulation progresses, the increase in the thickness and count of the bounding layers inhibits the overall flow even further. By the end of the simulation, the velocity magnitude of S2 from MIDAS becomes half of those in SN#38.

The flow behaviour in S2 is characteristic of a strongly shear-dominated regime, where the presence of water-ice layers inhibits deformation and limits the amount of CO_2 ice available to move downslope. SN#38 exhibits generally higher velocities at S2 throughout because its CO_2 ice, unbounded by viscous H_2O layers, is more sensitive to stress and therefore deforms more readily. MIDAS results demonstrate flow velocity is reduced along the slope, and less ice accumulates in this section compared to SN#38. This results in delayed lateral mass redistribution and reduced ice accumulation along the slope, reflecting the rheological control of the bounding layers. This behaviour at S2 differs from the observed behaviour in S1. This is likely due to the relatively thicker ice present immediately upslope of S1, which serves as additional source of CO_2 ice for the flow. In S2, however, we observe surface ice before the slope starts, and a small depression on the flat surface preceding the slope which may act as a temporary ice accumulation area for CO_2 ice, further reducing the amount of ice available to flow downslope.

(d) B2 (Figure 5.15**(d)):**

In general, the pattern for B2 follows from S2, and the same logic applies here. We note that SN#38 shows a small early-time anomaly that is absent in MIDAS. Throughout the simulation the thickness and velocity on the slope and the basin of the y-y′ follow the same pattern.

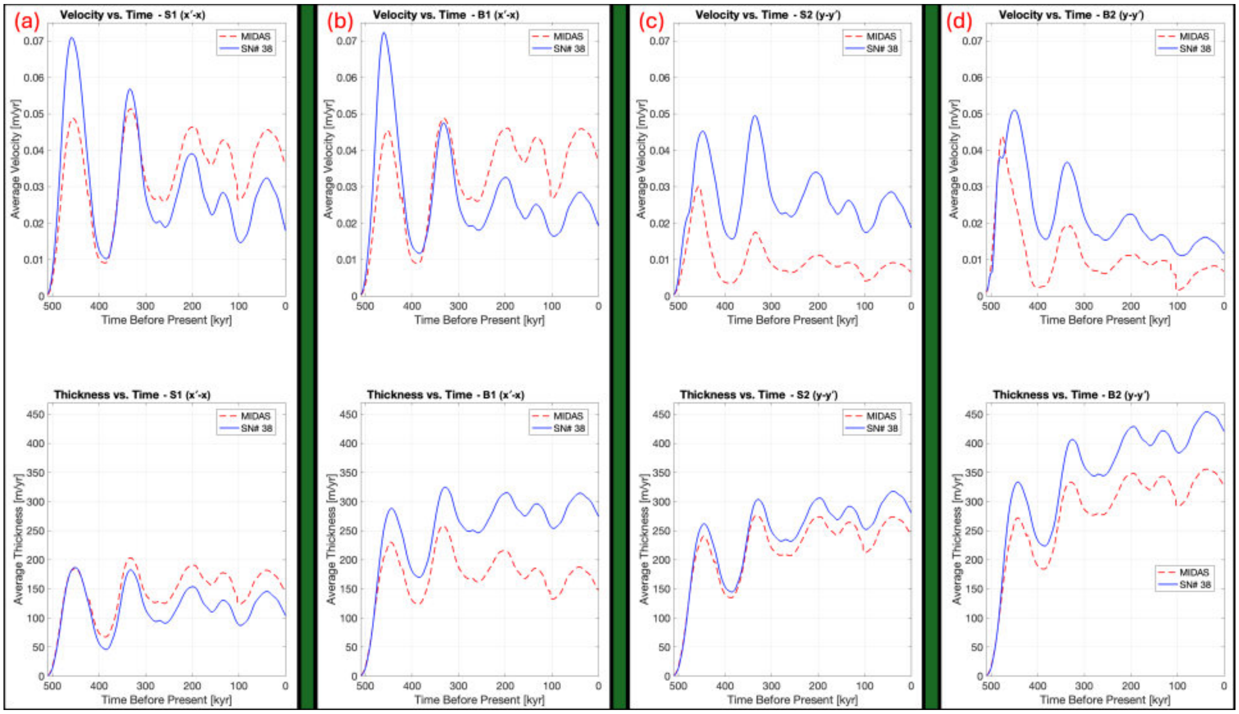

Figure 5.15 – Comparison of ice column-average velocity and ice column thickness through time at four control points from this study (MIDAS) and SN#38.

These points are on the slope and basins along the x-x' and y-y' paths (For the location of the points see Figure 5.16). Before the first water-ice layer forms, both models produce similar velocities and thickness. Any difference at this time arises due to the use of SSA vs BP-HO. After the formation of the first water-ice bounding layer, the x-x' cross section plots likely provide support for the notion that higher slope-side thickness could locally increase the driving shear stress which could offset the flow inhibiting effect of water ice bounding-layers; while MIDAS velocity magnitudes for the y-y' points are consistently lower as the water-ice layers inhibit flow.

5.3.4 Comparisons of MIDAS results and Radar data

Comparing the thickness profiles extracted from the 3D radar (Putzig et al., 2018) the model results with the radargram profiles of x-x’ and y-y’ (Figure 5.16) reveals two main sets of differences. First, the observations demonstrate a thicker ice profile with a smoother and more uniform surface. Second, the water-ice bounding layers in exhibit differences: x-x' radargram (Figure 5.16(B)) shows two closely separated layers, nearly merged (as in figure 4 of Alwarda and Smith, 2021). For the y-y' radargram, we see the same number of bounding layers; however, in the radar observation, the water-ice layers are discontinuous and slope poleward on the left side, which is not present in the model results. The differences are further discussed in the Discussion section.

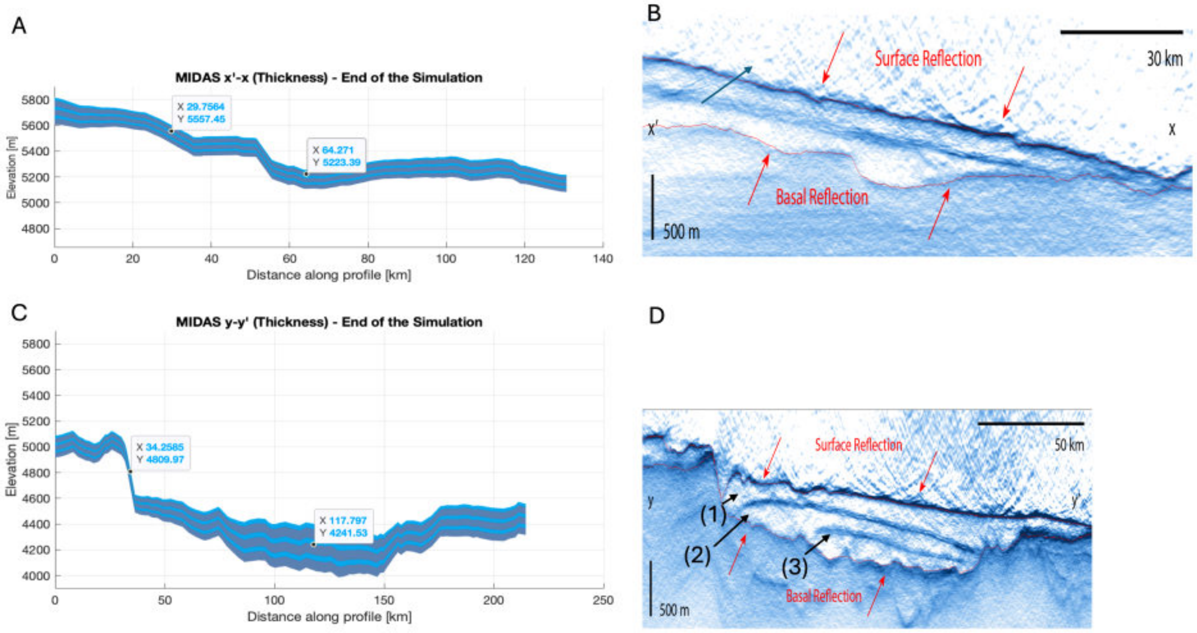

Figure 5.16 – Radar figures versus the simulation results.

Panels A and C are repeats from Figure 5.12, including the control points chosen for further localized analysis. X signifies the distance along the profile, and Y signifies the elevation of the point. For the ease of access, we call the first points from left on each plot the "slope point," and the second points the "basin points," as they are located on the slopes and the basins respectively. Panels B and D are radargrams of the respective CO_2 *reservoirs and repeats of Figure 1, brough here for ease of access and comparison. The surface and basal reflections are marked in red. The dark arrow in panel (B) marks a bounding layer that seems to be two nearly merged water-ice layers – like the interpretation of this glacier by Alwarda and Smith (2021) in their figure 4. Points (1), (2) and (3) in panel D show how* *the water-ice layers are sloped polewards and discontinuous, while they remain continuous in our model results.*

To examine the spatial and volumetric distribution of the results produced by MIDAS, we compare the final ice thickness output of this study with those from SN#38 and those observed through SHARAD. The figure is adapted directly from Smith et, al. (2022). As SHARAD provides no data for the high latitudes, these areas is marked by a circle in the plots (Figure *5.17*).

It is important to consider the differences in domain size mesh resolution between the models. Since this study's domain is a subset of the SPLD, much of the peripheral ice that contributes to the full MCID formation is not included in the current study's modelling. In addition, the mesh resolution of our current study is much coarser (8-7 km outside of the region of interest, and ~4 km within it), and this make it difficult to resolve smaller-scale features that are captured by the finer mesh in SN#38.

Despite these limitations, the overall volumetric distribution pattern of this current study closely follows the distribution pattern observed by SHARAD. One observation is the location marked by the red star, which SN#38 identified as an anomaly between their simulated thickness and the SHARAD data. and difference between their simulation and the SHARAD observation. MIDAS results did not produce that discrepancy in the distribution patterns.

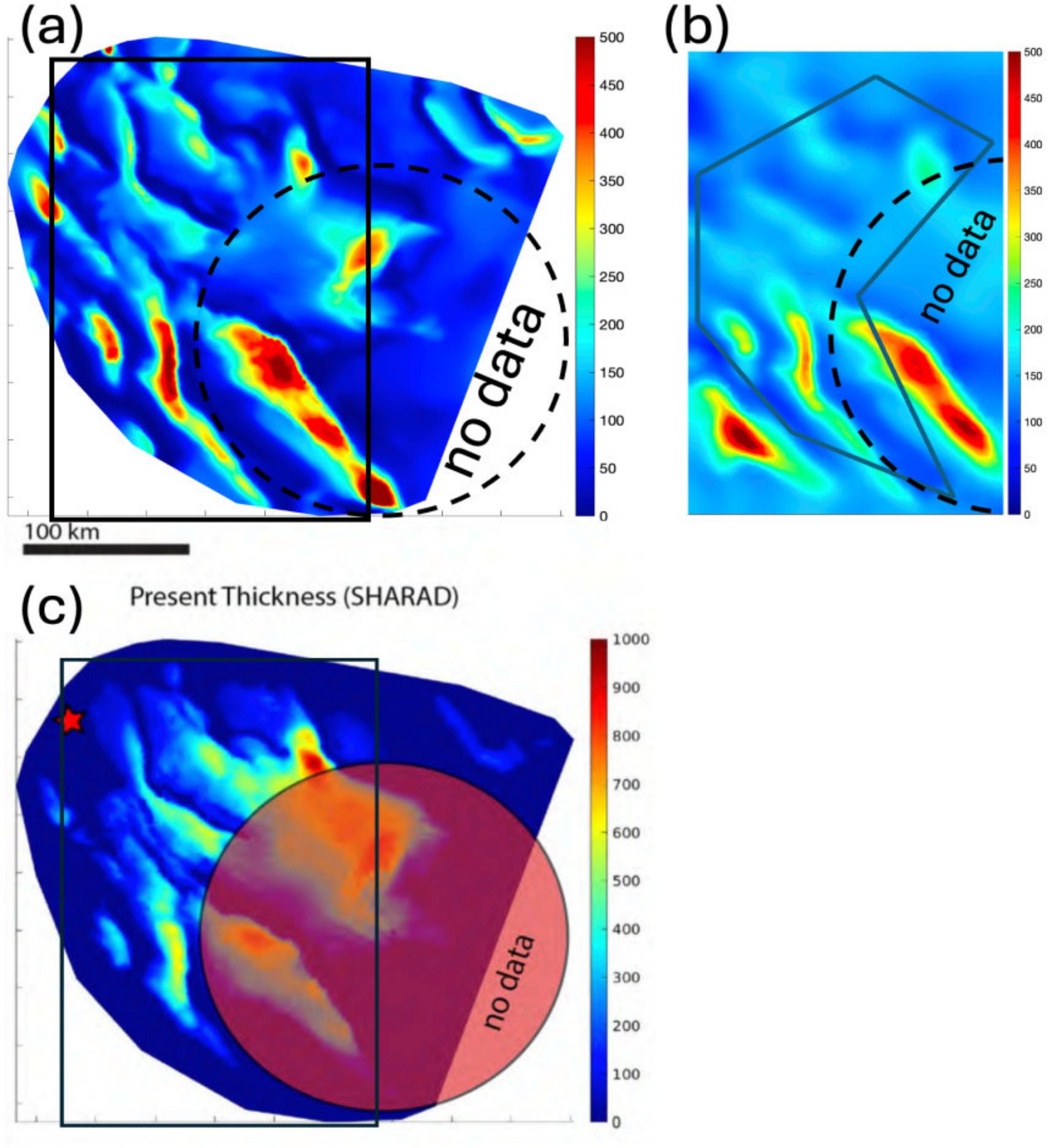

Figure 5.17 – Volumetric distribution at the end of the simulation.

The area marked with a star symbol is the location of the largest discrepancy between the SN#38 results and the SHARAD observed data. This current study domain is marked by the black rectangle, and the area with no SHARAD data is marked with a circle. (a) SN#38 thickness of CO_2 ice, with no water ice bounding layer and resolution of 3500 m. (b) Current study's domain with the higher-resolution region marked with a polygon. (c) The SHARAD-derived thickness map of the present day MCID, adapted directly from Smith et al. (2022). In comparison, high level patterns in the current study follows the *patterns observed by SHARAD, including the area marked by the star symbol that SN#38 results identified as an anomaly.*

5.4 Discussion

5.4.1 Uncertainties in the Results

Much like the modelling of Gediz Vallis, this model also relies on parameters that cause uncertainties in the results. Here, similar to section 4.7.1 some of the sources of uncertainty in the results are discussed:

(1) Top Boundary Mass Flux: The uniform–rate of ice deposition used in this simulation is derived from a 1-D obliquity modulated deposition model (Buhler, et al., 2020 and 2023). This approach is consistent with the previous MCID studies. However, it does not take the impact of altitude, and distance to the pole on the deposition rates into account. Moreover, the H_2O lag is considered as a separate deposition which is a simplification of the natural process of H_2O and CO_2 particles depositing together and at the same time. This neglects the rheological impact of mixing water ice with CO_2 ice, as well as the impact of CO_2 sublimation through diffusion on the rheology of the ice units.

(2) Rheology: While the uncertainty in n for H_2O ice remains, the uncertainty in n for CO_2 (8 with a range of plus and minus 2.2) will have a larger impact on the flow velocities. These, however, should have limited results in the direction of the flow. Moreover, the dual behaviour of CO_2 is another source of uncertainty. In shallow slopes, n for CO_2 is reduced to 1. In such scenario, CO_2' rheology will be sensitive to the grain size, and its effective viscosity becomes higher than that of water ice. This imposes two main issues: (1) it is uncertain in which locations in MCID this happens, and (2) it is unclear what the grain size in such locations will be.

(3) Basal Friction: This model contains none-sliding, cold-based glaciers and does not include sliding physics. However, due to the temperature regime at MCID, as well as the MCID basal pressure, the basal temperature should remain lower than the CO_2 melting point, and the MCID could possibly considered a set of cold-based glaciers.

(4) Geothermal Flux: Geothermal heat flux is assumed 30 mW m^{-2}. Due to the insulating property of CO_2, a variation in the flux value would change the internal thermal gradient of a unit of ice and impact the viscosity and the flow rate of the unit.

(5) Stress Balance Formulations: As shown in section 5.3.3 and 5.3.4, depending on what type of stress balance approximation is used (i.e., BP-HO vs. Shallow Ice Approximation) would have an impact on the results. Either one of these approaches contain approximations and series of assumptions which become sources of uncertainty themselves.

5.4.2 Discussing the Results

Similar to other terrestrial studies (e.g., Morlighem et al., 2016) our study used radar-based Digital Elevation Models (DEMs) to build a model with a basal topography that is aligned closely to observed features. We ran the simulation from 510,000 years before present, initializing from the SN#38 results at that year. We, then, select locations in the MCID to compare the current modelling results against radar profiles and past modelling. During low-obliquity time periods, atmospheric CO_2 deposits to the surface and forms new ice units. During this time, our model predicts movement of the CO_2 towards basins. Subsequently, the ice sublimates, leaving a water ice lag bounding layer. CO_2 ice continues to sublimate through the BLs over tens of thousands of years. Later, when obliquity lowers again, CO_2 once again is deposited over the BL

Broadly speaking, our modelled results that include water ice bounding layers agree with past modelling of CO_2 glaciers that have no bounding layers from Smith et al. (2022). In the simplest terms, the rate and direction of the ice flow will be guided down the valleys and canyons; the thickest deposits form within valleys and basins; and the thinnest deposits reside on steep slopes, where the ice departed. This provides a good match for radar observations for the 3D distribution of the MCID.

Our modelling relies on several assumptions. First, the obliquity cycles result in periodic, and uniform deposition of CO_2 ice across the modelling domain. We used time-bound variable surface mass balance (SMB) inputs from Buhler et al. (2020; 2023) that ignores the impact of elevation and latitude on the SMB.

Our other major set of assumptions center on how H_2O interacts with the CO_2 deposits. First, we assume that water ice co-deposits in the CO_2 matrix, usually when CO_2 snow scavenges H_2O particles from the atmosphere (Alsaeed & Hayne, 2022). This results in a mixture of CO_2 and H_2O ice particles that we assume behave thermally and rheologically as pure CO_2. Later, during periods of CO_2 sublimation, H_2O ice deposits will form on the surface as a lag (Buhler et al., 2020). Following that study, we assume is that CO_2 ice can sublimate from under a water-ice layer, either through vapor diffusion or direct contact at crevasses. For simplification, our model treats the water ice *lags* as a separate *deposition* of H_2O mass directly on top of the uppermost CO_2 layer.

The results reached the volumetric and spatial distributions that would be expected based on interpolations from the radar observations. Similar to Smith et al. (2022), our study provides testable predictions in terms of temperatures and rheological properties and makes use of simplifying assumptions and imposes a few limitations.

When compared to the results of Smith et al., (2022), our modelling demonstrates that the BLs and the stratified nature of the MCID have a thermo-mechanical impact on lowering the overall velocity, which slows the redistribution of ice units as they flow towards the basins. First, instead of flowing readily, the MIDAS results indicate that the water-ice bounding layers significantly retard the flow, such that deformation occurs only when the stress from increased ice thickness overcomes the resistive forces. Because MCID are cold-based glaciers (CO_2 ice melts at ~218 K under and 3.26 MPa which is the highest basal pressure value captured during our modelling) with negligible basal sliding, the glacial flow is primarily due to internal deformation, driven by changes in the strain rate that cause ice crystals to deform and move relative to one another. It is important to note that the literature does not provide a good coefficient of friction for CO_2-H_2O interfaces.

We note that water ice viscosity at 150 K is significantly higher than on Earth, and so the BLs tend to act as stiff layers that sandwich the softer CO_2 ice. CO_2 ice has a stress exponent of 8, as compared to 3 for water ice (Cross et al., 2020), so the slopes are the locations we expect with the greatest strain. This implies that CO_2 on slopes should flow much faster than water, all things being equal. Therefore, the bounding layers act as barriers and reduce the strain rate to the CO_2 ice immediately below a water-ice layer on slopes.

An important outcome of this study is to demonstrate that a retarding capping layer restricts the deformation and causes a slowdown of the overall flow. This is a behaviour similar to that of rock glaciers on Earth, where we see high-viscosity surficial lithic debris reducing the flow of underlying icesheet, slowing down the flow of rock glaciers in comparison to uncovered glaciers (Anderson & Anderson, 2025). Our modelling results show as much reduction as 50% in maximum velocity in some areas across the 3-dimensional model compared to SN#38 from Smith et al., (2022). It is worth noting that depending on the amount of the shear stress imposed on a block of flowing CO_2 ice (mostly thick ice on steeper slopes), the stress can offset the inhibiting impact of the water ice bounding layer.

Second, our work shows that the BLs modulate the thermal profile within the MCID, with the inclusion of water layers reducing the thermal gradient when compared to the less conductive CO_2 alone. This has the effect of reducing basal temperatures in comparison to SN#38, which in turn raises the viscosity of every unit.

As mentioned above, radar and topography observe the water-ice bounding layers slope down in points 1-3 in Figure 5.16D. These slopes are not modelled (i.e., Figure 5.16C). We believe that this occurs in nature but not in the model because MIDAS does not include other processes affecting the ice deposits, especially aeolian processes that drive the sublimation and redistribution that shape the MCID. To explain this, we refer to Smith et. al (2014) who leveraged observations (including near-surface clouds, surface features and subsurface layering) as well as mesoscale atmospheric simulations to create a process model that explains the observations. They demonstrated that basin infilling and evolution related to the spiral troughs are often in an aeolian-prominent regime (sublimation and redistribution rates from winds is greater than that from viscous deformation) so that differential sublimation can be a dominant process in some locations, especially at slope breaks. Thus, over long periods, glacial flow is the primary driver for ice distribution, and it is modified by sublimation at slope breaks, causing the discrepancy between our model and observations. Besides the pole-ward slopes, aeolian processes will also explain why the internal BLs intersect the basin instead of merging or following the basal topography as modeled in Figure 16C.

The radargrams show thicker ice profiles that exhibit an equilibrium in panels B and D of Figure 5.16. This contrasts with what the model predicts. We believe this could be due to two reasons: (1) Our modelling domain covers only a portion of the MCID; as such, ice flowing from outside the modelling domain has been excluded, and (2) the flow in this model is actually slower than in nature. Hence, less ice that has not yet reached equilibrium.

Another discrepancy is that radargram transect x′-x appears to show a single water-ice layer (Figure 15D). Based on interpretations from Alwarda and Smith (2021), this layer actually consists of two closely spaced layers, which would then agree in number with our modelling. We believe this difference is due to a possible merger between the water-ice bounding layers that has not been captured in the model results. One possible explanation was that perhaps that CO_2 unit was thinner to begin with, which allowed the BLs to merge as the CO_2 sublimated.

In general, our MIDAS simulations support the hypothesis of Bierson et al. (2016) that the presence of water-ice bounding layers would enhance the thermal stability of the CO_2 deposits by preventing total sublimation during peak obliquity periods; however, this is incomplete as some locations have water ice deposits but no CO_2 beneath them, and in other locations nature reveals that BLs have merged. As Buhler et al. (2020) predicted and Alwarda and Smith (2021) confirmed with observations, there must be some communication between the buried MCID and the atmosphere, through vapor diffusion or direct contact at crevasses, or the bounding layers would not merge. Following the results of Smith et al., (2022), we find that the MCID flow into basins, where they are large enough masses to endure the high obliquity cycles that thin the ice elsewhere. The total number of un-merged bounding layers then match the number of high obliquity excursions experienced since the first CO_2 deposited.

To explain the interpretation that the water ice bounding layers in our model are actually stronger than in nature, we revisit the crevasse hypothesis. Crevasses occur when the surface layer experiences stresses that are greater than the yield strength of the material. In the stratified MCID deposits, stiff water ice overlies relatively low viscosity carbon dioxide ice. This is a recipe for strains greater than the H_2O can accommodate, and brittle failure occurs (see supplemental information from Smith et al., 2022). After brittle failure of the surface layer, the retarding stresses on the CO_2 are reduced, which should allow faster flow. The new flow is faster than our model can predict because the H_2O remains unbroken in our model. Future work should then consider a reduced stiffness H_2O layer. This, coupled with employing a finer spatial mesh to better capture slopes (and therefore the resulting stress) and extending the domain to cover the entire MCID, would likely produce results that more closely match the observed features.

6 Conclusions and Summary

Studying the solar system's mechanics requires understanding solar system bodies, their histories, and climate changes. Ice deposits across the Solar System, known as exotic ice deposits, have unique physical properties and specific rheological laws. Thus, terrestrial ice knowledge, while useful, is insufficient for accurately modelling stratified or exotic ice on Mars and other bodies. As such, the approach and software provided in this dissertation contributes to both the scientific understanding of planetary ice dynamics and the technical advancement of icesheet modelling tools applicable in non-terrestrial conditions.

This dissertation introduces an approach to modelling ice deposits across the solar system with a focus on multi-unit ice deposits. MIDAS is the code name used for a set of software libraries I wrote to model stratified icesheets. To better showcase MIDAS, I reviewed two distinct case studies. These demonstrate the use of MIDAS to contribute to studies in two primary questions:

1) In Gale Crater, in the Martian mid-latitude area, if ice accumulated on Mt. Sharp (the crater's central mound), would it have flowed downslope to shape Gediz Vallis a nearby canyon? As Gale Crater is close to the Mars's equator, the involvement of glacial processes seems counterintuitive. However, Mars's orbital history suggests significant climatic fluctuations could support such phenomena, indicating profound environmental changes.

2) How do water ice bounding layers and surface crevasses affect and influence CO_2 ice flow (sublimation and stress relief) at Mars's south pole? Water ice layers, due to their greater viscosity, act like barriers, impeding flow until more CO_2 ice accumulates or crevasses form, easing constraints on the underlying CO_2.

The functionality of MIDAS enables one to simulate a diverse set of glacier types which includes CO_2 based glaciers on Mars. In this dissertation, I focus on Mars. However, the relevance of MIDAS extends beyond Mars to other planets in the solar system. Exotic ices, which are ices composed of CO_2, N_2, and CH_4 and other non-water-based components can be found across the outer Solar System. For example, on Pluto, nitrogen-based icesheets exist which also demonstrate convective flow (the convection can be interpreted as an indication that the nitrogen-based glaciers are actively experienced internal stress, flowing, deforming and shaping the planet's surface (McKinnon et al., 2016; Moore et al., 2016)).

Europa and Enceladus, moons of Jupiter and Saturn respectively, present future modelling opportunities too. These global subsurface oceans under the surface of these planets, however, could pose modelling challenges due to continuous tidal flexing. The resulting thermal gradients and dynamic stresses will have to be taken account in the modelling and MIDAS is well positioned to be extended to account for such forces.

In summary, this dissertation demonstrates the value of modelling and also in broadening our conceptual understanding of ice dynamics within planetary environments. It helps with interpreting some of the most enigmatic features observed on Mars, answering some of the associated outstanding questions.

6.1 Properties of Water, Carbon Dioxide, and Nitrogen Ices in Planetary Surface Environments

Recent modelling work research in the field of exotic ices (Smith et al. 2022; Umurhan et al., 2017; etc.) motivates the collection of various material properties of the building blocks of such ices in one place. In this section of my dissertation, there is a collection of some of the research previously done for density, flow law parameters, latent heat of fusion, specific heat capacity (in constant pressure), and thermal conductivity as functions of temperature of water, carbon dioxide, and nitrogen ices.

Using plots, and fitting the existing data sets, the best interpretation for each property was presented and recommended equations became available in easy to access tables.

6.2 Modelling 3D Flow of Potential Glaciers on Mt. Sharp (Aeolis Mons) in Gale Crater, Mars

A decade ago, Fairén et al. (2014), supported by studies such as Le Deit et al. (2013), hypothesized that ice accumulation on Mt. Sharp and related glacial and periglacial processes might have shaped Gediz Vallis and other landscape features. Although detailed colour images from the Curiosity rover's cameras provide insights, they alone cannot conclusively prove glacier presence. Features like striations, which indicate glacial erosion, might have been eroded by wind over time. Yet, when paired with orbital evidence, these signs of glacial erosion become more persuasive (Fairén et al. (2014); Le Deit et al. (2013)). My modelling work started as an attempt to examine this glacial hypothesis by comparing modelled ice-flow directions and the observed landscape features and morphology. This modelling work, along with the features analysis builds on recent studies into glacier-like formations on the northeast side of the central mound (Williams et al. (2022)).

The concept that glaciers might have sculpted Mt. Sharp in Gale Crater seems implausible given the current instability of ice near Mars's equator and the strong erosive force of Martian winds. However, Mars's orbital history, as detailed by Laskar et al. (2004), presents a different picture. The current Martian climate is dry and cold. The current planetary obliquity of about 25.19º is significantly different from the average of ~37.62º that extensive modelling and theoretical calculations show Mars has experienced over the past 4 billion years (Laskar et al., 2004). This deviation suggests that the planet has experienced major environmental changes because these obliquity variations would have had significant global environmental effects (Madeleine et al., 2009), potentially leading to net ice accumulation rates exceeding 1 mm per year near Gale Crater with an obliquity of 35º, which is considered to be a common value in Mars's recent past (Madeleine et al., 2009). This suggests that Gale Crater might have periodically hosted ice, possibly until the late Amazonian period (Laskar et al., 2004). The Amazonian period, one of Mars's three major geological epochs, started about 3 billion years ago and persists today. Despite the current instability of ice beyond polar regions, recent research by Mellon and Sizemore (2022) indicates that ground ice could have remained stable at all explored landing sites for extended periods when obliquity ranged from 29º to 33º, suggesting that ice in Gale could have lasted from the late Hesperian to several hundred thousand years ago.

In this section, I modelled ice in a domain encompassing Gedis Vallis to examine the hypothesis that glacial ice accumulated over portions of Mt. Sharp and played a significant role in shaping bedrock features and carving canyons in the crater.

This modelling was motivated by high-resolution observations from the Curiosity rover of geomorphic features in Gediz Vallis that closely resemble glacial landforms on Earth, including flutings on bedrock outcrops and roches moutonnées.

Collectively, modelled ice flow directions and analyses of Mars features imaged from the ground and from orbit are consistent with the hypothesis that ice accumulation, driven by periods of high obliquity, played a significant role in shaping Gediz Vallis and its bedrock landforms.

In short, the presence of glaciers in Gale Crater as recently as the late Amazonian period would have implications: it would influence our understanding of Martian climatic and geomorphic history, as well as the relationship between orbital parameters and equatorial environmental conditions and Martian surface processes. For instance, the potential spatial correlation between a large ice mass at the base of Gediz Vallis, and the Greenheugh Pediment motivates further inquiries into how glacial ice may have shaped the pediment's history and contributed to the formation of the Gediz Vallis ridge and the diamict covering its surface (Bryk et al., 2024 - LPSC).

6.3 Modelling the Water-ice Bounding Layers in the Massive Ice CO2 Deposits, South Pole of Mars

This second case study focuses on the Massive Carbon Dioxide Ice Deposits (MCID) at Mars' south pole to examine the significant impact of water ice bounding layers situated between layered units of CO_2 ice on the flow and stability of SPLD. This also supports the impact of the Martian obliquity cycles and orbital parameters on the evolution of Martian atmosphere and lastly provides correlation to estimate the potential changes in orbital parameters in recent Martial history.

As mentioned, glaciers with diverse chemical compositions, on various planets in the solar system, provide ways to study and understand the past atmospheric history of those planets, and subsequently learn more about their orbital parameters as well as their evolutions. The Massive CO_2 Ice Deposit (MCID) near the South Pole of Mars are such deposits. Smith et al. (2022) modelled the behaviour of flowing CO2 ice and explained the spatial distribution of ice as we observe today. However, this study was limited because it did not include the water-ice bounding Layers (BLs) that exist within these deposits.

The model presented in this dissertation incorporates the stratified nature of the MCID and allows the properties such as density and thermal conductivity to vary by temperature through upgrades made to the Ice-sheet and Sea-level System Model (ISSM). To achieve this, first, we modified ISSM to incorporate stratified ice deposits. Then, we simulate part of the MCID formation starting at 510,000 years before present to capture the formation of the MCID, including bounding layers.

The modelling results show that the assumption from Smith et al. (2022) the MCID was a uniform deposit of CO_2 led to higher predicted flow velocities (~20% greater than we model). Thus, by incorporating water-ice bounding layers, our work provides a more comprehensive representation of MCID dynamics, resulting in slower flow rates and lower basal temperatures. Lastly, our changes to ISSM, by including temperature-dependent material properties (other than simple rheology laws which are already covered by ISSM) further results in the use of more realistic input numbers, which in turn supports the current observations that CO_2 deposits are more dynamically stable than previously thought, particularly when protected by bounding layers. In short, water-ice bounding layers play crucial roles in inhibiting the CO_2 ice flow, insulating the CO_2 ice units, and modifying their internal temperature.

Future work will incorporate adaptive mesh refinement techniques to better resolve areas with steep gradients and investigate the effects of variable geothermal flux on ice flow. To address the basal assumptions, series of sensitivity analyses and leveraging inversion can help with finding acceptable friction coefficient. Expanding the domain to the entire South Pole of Mars will provide additional insights into the climatic cycles that shaped the MCID. Also, future work can investigate further the relationships between the formation of the bounding layers and the timing of the atmospheric collapses.

6.4 The Path Forward

In this dissertation, I discussed the motivations for augmenting ISSM and developing the MIDAS libraries. Now, the motivations and opportunities for further advancement remain strong. One value that MIDAS will bring to the scientific community is its ability to simulate the impact of the debris included in glaciers. Debris covered glaciers are present at various places on Mars as well as Earth. For modelling such glaciers specific rheological factors will need to be considered to be able to accurately model such glaciers and their flow dynamics (and the subsequent erosion). MIDAS is able to streamline the processes to modelling the glacial behaviour across debris-rich environments.

Debris will result in protecting water ice-based glaciers from ablation, which will result in slowing down the glacial flow. Rock glaciers become a specific case with “just enough” debris so the headwalls do not experience erosion (Anderson and Anderson, 2025). MIDAS’s ability to include various units in the same ice mass and accommodate for various types of rheology (even at the mesh element level) will be a support for such modelling efforts.

There are improvement opportunities in MIDAS, especially to improve computational performance, and scalability for large-scale simulations. The opportunities also exist to extend the current work on the MCID to model its entire set of CO_2 deposits and investigate the timing and mechanisms of Martian atmospheric collapses.

MIDAS has the potential to provide major contributions to terrestrial and non-terrestrial icesheet modelling.

Appendices

7 Appendix 1: Mathematics of Icesheet Dynamics

This section covers some of the foundational mathematics and physical concepts necessary for analyzing icesheet dynamics. For the use in this, the key notations, as well as their measurement units (The International System of Units, or SI) are listed in Table 7.1. The mathematics of Icesheet dynamics are well documented, and these are brought here for the sake of completeness, this section uses various sources including Greve and Blatter (2009), Cuffey and Paterson (2010), Morlighem (2011), Larour et al., (2012), and references therein.

Symbol	Definition
c	Heat capacity in $[J.K^{-1}]$
$\vec{f}$	Volume force
n	Glen's exponent
q	Heat flux in $[W.m^{-2}]$
u	Specific internal energy, defined as $c \cdot T$, measured in the joule
$\vec{v}$	Velocity vector
A	$[Pa^{-n}.a^{-1}]$, where n is the Glen exponent
B	Ice hardness or rigidity $\left[Pa.a^{\frac{1}{n}}\right]$, where n is the Glen exponent
K	Thermal Conductivity, in $[W.m^{-1}.K^{-1}]$
T	Temperature in $[K]$
σ	Cauchy stress tensor

Symbol	Definition
$tr(\sigma)$	Trace of the stress tensor
σ_v	Volumetric stresses
σ^T	Cauchy stress tensor, transposed
σ'	Deviatoric stress tensor
ϵ	Strain tensor
$\dot{\epsilon}$	Strain rate in $[s^{-1}]$
$\dot{\epsilon}_e$	Effective strain rate
η	Shear viscosity (also viscosity) in $[Pa.s]$
τ	Shear Stress
ρ	Density in $[kg.m^{-3}]$
Φ	Dissipation power
$\nabla\cdot$	Divergence of a vector

Table 7.1 – Mathematical and physical notations used in this dissertation

In the following sections some of the key concepts have been reviewed.

7.1 Definitions

7.1.1 Dissipation power

The *dissipation power* (Φ) is an intrinsic quantity that represents the conversion of mechanical energy (including both kinetic and strain energy) into heat (i.e., internal energy or u). The absolute value of this quantity is defined using the Cauchy stress tensor (section 7.1.5) and the strain rate tensor (section 7.1.6) as $tr(\sigma \cdot \dot{\epsilon})$; or it is defined using the shear viscosity (section 7.1.7) and the effective strain rate (section 7.1.6) as $4 \cdot \eta \cdot \dot{\epsilon}_e^2$. Φ can also be defined as the amount of heat that internal friction creates (Greve and Blatter, 2009).

7.1.2 Heat Flux

Heat flux (q), and in glaciology often specifically geothermal heat flux (Cuffey and Paterson, 2010) is the rate of thermal energy transfer per unit area and per unit time (Halliday, Resnick, and Walker, 2013). For conductive heat transfer, Fourier's law expresses how this flux depends on the temperature gradient, relating the two through the thermal conductivity (K): $\mathrm{q} = -\mathrm{K} \cdot \nabla \mathrm{T}$ (e.g., Greve and Blatter, 2009).

7.1.3 Incompressibility Assumption

ISSM assumes that ice is an incompressible material, meaning its density is taken to be constant under pressure (Larour et al., 2012). Under this assumption, the mass conservation equation simplifies to the divergence-free condition for velocity, $\nabla \cdot \vec{v} = 0$ (Greve and Blatter, 2009). While ice is treated as incompressible, its rheology is non-Newtonian and follows a power-law (i.e., Glen's law).

7.1.4 Stress, Shear Stress, and the Cauchy Stress Tensor

This section will touch on some basic and yet fundamental Concepts. *Stress* (measured in $[Pa]$ in the SI unit system) is the deforming force per unit area (Halliday, Resnick, and Walker, 2013 (P315)). The tensor representation of all stress elements at every point is called the *Cauchy Stress Tensor* (σ). The sum of its diagonal elements (i.e., the *trace* of the tensor) is denoted as

$tr(\sigma)$. This tensor transposed is σ^T. On the base of a glacier, *shear stress* (τ) causes shear deformation. Duval et, al. (1983) show that the amount of shear stress (and by association the resulted deformation) depends on the strain rate (Cuffey and Paterson, 2010). For clarity and consistency with the remainder of this dissertation, I will show the equations without the full tensor notations, while it is understood that the underlying quantities are tensors.

The matrix form of the Cauchy stress tensor:

$$\sigma = \begin{pmatrix} \sigma_{xx} & \sigma_{xy} & \sigma_{xz} \\ \sigma_{yx} & \sigma_{yy} & \sigma_{yz} \\ \sigma_{zx} & \sigma_{zy} & \sigma_{zz} \end{pmatrix} \qquad eq.\ 7.1$$

Cauchy stress tensor, transposed:

$$\sigma^T = \begin{pmatrix} \sigma_{xx} & \sigma_{yx} & \sigma_{zx} \\ \sigma_{xy} & \sigma_{yy} & \sigma_{zy} \\ \sigma_{xz} & \sigma_{yz} & \sigma_{zz} \end{pmatrix} \qquad eq.\ 7.2$$

Trace of the Cauchy stress tensor:

$$tr(\sigma) = \sigma_{xx} + \sigma_{yy} + \sigma_{zz} \qquad eq.\ 7.3$$

Normal stresses are: $\sigma_{xx}, \sigma_{yy}, \sigma_{zz}$.

Shear stresses are: $\sigma_{xy}, \sigma_{yx}, \sigma_{xz}, \sigma_{zx}, \sigma_{yz}, \sigma_{zy}$.

7.1.5 Deviatoric Stress

Since the normal stresses are defined as the diagonal elements of the Cauchy stress tensor, we can define the value of the isotropic stress through:

$$\sigma_v = \frac{tr(\sigma)}{3} \qquad eq.\ 7.4$$

σ_v is in fact the amount of pressure (i.e., p) that causes compression (see Hauret (2004) or Cuffey and Paterson (2010)).

$$abs(p) = \frac{1}{3} \cdot tr(\sigma) \qquad eq.\ 7.5$$

Since p is a downwards force its sign is generally considered to be negative.

We can find the deviation (σ') that the Cauchy stress tensor experiences as:

$$\sigma' = \sigma - \sigma_v.I \qquad eq.\ 7.6$$

$$\sigma = \sigma' + p.I \qquad eq.\ 7.7$$

Where I denotes the identity tensor of the same dimensions as that of σ. This new tensor (i.e., σ') is the stress tensor that causes the deformation in icesheets (i.e., an incompressible material). See Cuffey and Paterson (2010).

Using eq. 7.1 the deviatoric stress tensor can be defined to be:

$$\sigma' = \begin{pmatrix} \sigma_{xx} - \sigma_v & \sigma_{xy} & \sigma_{xz} \\ \sigma_{yx} & \sigma_{yy} - \sigma_v & \sigma_{yz} \\ \sigma_{zx} & \sigma_{zy} & \sigma_{zz} - \sigma_v \end{pmatrix} \qquad eq.\ 7.8$$

It can be seen that σ' is traceless tensor:

$$tr(\sigma') = 0 \qquad eq.\ 7.9$$

7.1.6 Strain and Strain Rate

Strain (ϵ) represents deformation per unit area and is a dimensionless quantity. The rate of deformation per unit of time is denoted as the strain rate ($\dot{\epsilon}$), which is measured in units of inverse time (e.g., seconds^{-1}). The strain rate tensor is defined similar to the stress tensor; the derivatives of the strain rate tensor elements will describe the strain rates. These rates can be expressed as:

$$\dot{\epsilon}_{ij} = \frac{1}{2}\left(\frac{\partial v_i}{\partial j} + \frac{\partial v_j}{\partial i}\right) \qquad eq.\ 7.10$$

Where v_i and v_j are the velocities in the directions of i or j (i.e., x, y, or z).

The *effective strain rate* ($\dot{\epsilon}_e$) is generally discussed in the context of ice-structures and helps with scaling up the laboratory gained results to field size scenarios (Matskevitch, 1997). By definition:

$$\dot{\epsilon}_e = \left[\frac{1}{2}\left(\dot{\epsilon}_{xx}^2 + \dot{\epsilon}_{yy}^2 + \dot{\epsilon}_{zz}^2\right) + \dot{\epsilon}_{xy}^2 + \dot{\epsilon}_{xz}^2 + \dot{\epsilon}_{yz}^2\right]^{\frac{1}{2}} \qquad eq.\ 7.11$$

Greve and Blatter (2009) simplify the definition:

$$\dot{\epsilon}_e = \sqrt{\frac{tr(\dot{\epsilon}^2)}{2}} \qquad eq.\ 7.12$$

7.1.7 Shear Viscosity

Shear viscosity or *viscosity* (η) for short, is the resistance that a substance shows while flowing (Halliday, Resnick, and Walker, 2013).

The inverse of viscosity defines the “fluidity” of a substance (here denoted as η^{-1}), and it can be described using the Arrhenius law (Greve and Blatter, 2009). The Arrhenius law demonstrates the relationship between the rigidity, grain size and the temperature of the deposit. This law is used to predict (or describe) the flow and distribution of ice across an area (for a catalogue of properties of the Arrhenius law under different conditions for CO_2, N_2 and H_2O (Fard and Smith, 2023)). Therefore, we can use the Arrhenius law to define the fluidity.

Consider the units in the rigidity equation and the Arrhenius law.

$$fluidity\ (\eta^{-1}) = 2.A.f(\sigma_e, n) \qquad eq.\ 7.13$$

$$A = A_{const}.e^{C} \text{ where } C = \frac{-Q}{T^{*}.R_g} \qquad eq.\ 7.14$$

$$f(\sigma_e, n) = \sigma_e^{n-1} \qquad eq.\ 7.15$$

Generally speaking, C is *temperature* and *pressure* dependent; however, by using the temperature that is measured relative to the melting point pressure (T^{*}), the pressure-dependant factors can be removed from C (Greve and Blatter, 2009).

n is the Glen’s exponent (which is dimensionless), $f(\sigma_e, n)$ is called the creep function, A (the rate factor, measured in the SI unit system as $[MPa^{-n}.s^{-1}]$) can be considered the frequency of collisions of molecules colliding. The Activation Energy (Q) is lowest amount of energy required for a chemical reaction to be initiated and is measured as $[J.mol^{-1}]$. R_g is the universal gas constant (i.e. 8.314 $[J.K^{-1}.mol^{-1}]$).

By using equations above, viscosity (η) is defined using the rheological properties (as functions of T^{*}) of a glacier (Greve and Blatter, 2009):

$$\eta = \frac{1}{2.A.\sigma_e^{n-1}} \qquad eq.\ 7.16$$

Hardness of ice ($B(T^*)$) is defined as $A(T^*)^{\frac{-1}{n}}$. Using the effective strain rate ($\dot{\epsilon}_e$), Greve and Blatter (2009) show that:

$$\eta = \frac{B.\dot{\epsilon}_e^{\frac{1-n}{n}}}{2} \qquad eq.\ 7.17$$

$B(T^*)$ is measured in $\left[Pa.s^{\frac{1}{n}}\right]$. For detailed discussion of shear viscosity see section 4.3.1 of Greve and Blatter, 2009.

7.1.8 Conservation Laws

ISSM uses the conservation of momentum, mass, and energy (Larour et al., 2012). In the context of ISSM as well as glaciology see Greve and Blatter (2009), Cuffey and Paterson (2010), Morlighem (2011), and Larour et al. (2012). A summary has been provided in Table 7.2.

Balance of	Equation	Comments
Mass	$\dot{\rho} + \rho \cdot \nabla \cdot \vec{v} = 0$	Assuming ice as an incompressible flow (i.e., no change to density as the result of pressure, or $\dot{\rho} = 0$) will result in $\nabla \cdot \vec{v} = 0$.
Angular momentum	$\sigma = \sigma^T$	The angular momentum balance can be shown by the symmetry of the Cauchy stress tensor (i.e., $\sigma_{ij} = \sigma_{ji}$)
Linear momentum	$\rho \cdot \frac{d\vec{v}}{dt} = \nabla \cdot \sigma + \vec{f}$	If the momentum is not calculated in an inertial system, $\vec{f}$ will need to include the inertial forces such as the Coriolis force.

Balance of	Equation	Comments
Internal energy	$\rho \cdot \frac{du}{dt} = \Phi - \nabla \cdot q + \rho.r$	With Φ being viscous dissipation, q being the heat flux, and r a specific radiative heat source term (Greve and Blatter, 2009). If radiative transfer contributes within the ice, it will be added to the energy balance as an additional volumetric source term. Also, $\frac{du}{dt}$ can be expressed as $c \cdot \frac{dT}{dt}$.
Continuity equation	$\frac{\partial v_x}{\partial x} + \frac{\partial v_y}{\partial y} + \frac{\partial v_z}{\partial z} = 0$	This is not a conservation law, but the component form of $\nabla \cdot \vec{v} = 0$ which accompanies various modelling approaches.

Table 7.2 – Summary of conservation laws as well as the continuity equation

7.2 Icesheet Dynamics

7.2.1 Full Stokes (FS)

The Stokes equation considers the gravitational, centrifugal and the Coriolis forces acting on an icesheet. The first two forces can be combined into the effective gravitational force ($\vec{f}$) as density times the gravitational constant or $\vec{f} = \rho\vec{g}$. The third force (or rather effect) is a function of the ice flow velocity ($\vec{v}$) and the angular velocity of the planet on which the icesheet is being modelled ($\vec{\omega}$). As the ratio of the Coriolis effect to pressure gradient on Earth can be shown to be negligible, the Coriolis term can be safely ignored as a force acting on the icesheet (Greve and Blatter, 2009). In short, the body force is gravity; Coriolis is negligible for glacier flow and is omitted. This is an inherent assumption in ISSM, carried over into MIDAS.

As mentioned (Section 7.1.3), for incompressible materials the mass balance is simplified to $\nabla.\vec{v} = 0$. Also, the deformation will only depend on the amount of stress that *deviates* from the isotropic state (Cuffey and Paterson (2010)); this *deviation* will only be applied to the diagonal elements of the stress tensor, and the average deviation from the normal stress will be represented by σ' (Section 7.1.5). The relationship between the deviatoric stress (σ'), which is traceless, and σ' is defined in eq. 7.6 and 7.7.

The deviatoric stress is also defined using the strain rate tensor ($\dot{\epsilon}$) as (see Greve and Blatter (2009)):

$$\sigma' = 2 \cdot \eta \cdot \dot{\epsilon} \qquad \textit{eq. 7.18}$$

The i_{th} of the divergence of σ' is (Greve and Blatter (2009)):

$$(\nabla . \sigma')_i = \partial_j (2. \eta . \dot{\epsilon}_{ij}) \qquad \textit{eq. 7.19}$$

In the special case of constant viscosity, this reduces to eq. 7.20 (where ($\nabla^2 v_i$) denotes the Laplacian of the velocity component):

$$(\nabla \cdot \sigma')_i = \eta \nabla^2 v_i \qquad \textit{eq. 7.20}$$

Apply the negative sign to eq. 7.5, and rewriting 7.7 as:

$$\sigma = \sigma' - p \cdot I \qquad \textit{eq. 7.21}$$

Taking the divergence of the equation above, and substituting the equations for σ' and p:

$$\nabla \cdot \sigma = -\nabla p + \nabla \cdot \sigma' \qquad \textit{eq. 7.22}$$

Using the conservation of linear momentum (i.e., $\rho \cdot \frac{d\vec{v}}{dt} = \nabla \cdot \sigma + \vec{f}$):

$$\rho \cdot \frac{d\vec{v}}{dt} = -\nabla p + \nabla \cdot \sigma' + \vec{f} \qquad \textit{eq. 7.23}$$

If we review the contributions of acceleration, inertia and the Coriolis force (Reist, 2005), even in the most extreme cases for terrestrial glaciers (which flow faster than glaciers on Mars), we will notice they are negligible (pressure gradient is at least 7 orders of magnitude higher than the Coriolis effect), therefore, the Full-Stokes equation (for an incompressible fluid) can be written as:

$$\rho\vec{g} - \nabla p + \nabla \cdot \sigma' = 0 \qquad \textit{eq. 7.24}$$

And we also know that the incompressibility will result in the trace of the strain rate tensor to be zero. Expanding the equation above will result in (and considering that $\rho\vec{g}$ only has a vertical non-zero component):

$$2\,\partial\frac{\left\{\eta\cdot\frac{\partial v_x}{\partial x}\right\}}{\partial x} + \frac{\partial\left\{\eta\cdot\left(\frac{\partial v_x}{\partial y}+\frac{\partial v_y}{\partial x}\right)\right\}}{\partial y} + \frac{\partial\left\{\eta\cdot\left(\frac{\partial v_x}{\partial z}+\frac{\partial v_z}{\partial x}\right)\right\}}{\partial z} = \frac{\partial p}{\partial x} \qquad \textit{eq. 7.25}$$

$$\frac{\partial\left\{\eta\cdot\left(\frac{\partial v_x}{\partial y}+\frac{\partial v_y}{\partial x}\right)\right\}}{\partial x} + 2\,\partial\frac{\left\{\eta\cdot\frac{\partial v_y}{\partial y}\right\}}{\partial y} + \frac{\partial\left\{\eta\cdot\left(\frac{\partial v_y}{\partial z}+\frac{\partial v_z}{\partial y}\right)\right\}}{\partial z} = \frac{\partial p}{\partial y} \qquad \textit{eq. 7.26}$$

$$\frac{\partial\left\{\eta\cdot\left(\frac{\partial v_x}{\partial z}+\frac{\partial v_z}{\partial x}\right)\right\}}{\partial x} + \frac{\partial\left\{\eta\cdot\left(\frac{\partial v_y}{\partial z}+\frac{\partial v_z}{\partial y}\right)\right\}}{\partial y} + 2\,\partial\frac{\left\{\eta\cdot\frac{\partial v_z}{\partial z}\right\}}{\partial z} = \frac{\partial p}{\partial z} + \rho\cdot g \qquad \textit{eq. 7.27}$$

And we also have the continuity equation:

$$\frac{\partial v_x}{\partial x} + \frac{\partial v_y}{\partial y} + \frac{\partial v_z}{\partial z} = 0 \qquad \textit{eq. 7.28}$$

These equations will be used to solve for v_x, v_y, v_z, and p (i.e., analyzing Stokes flow with 4 unknowns).

Using Full Stokes, ISSM solves the icesheet models with the associated differential equations and provides the velocities in three directions (i.e., *x*, *y* and *z*), as well as the pressure (See Figure 7.1).

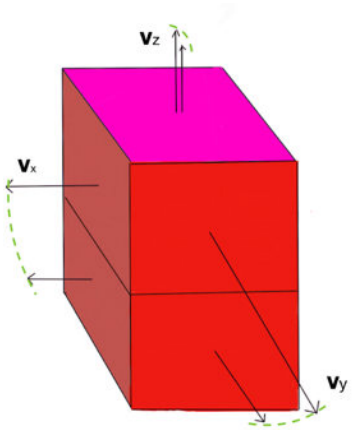

Figure 7.1 – Full Stokes

FS results in solving an icesheet model in 3 dimensions, and determining the velocities at different directions that will be different depending on different conditions governing every element in the mesh

7.2.2 Higher Order (HO)

1. The Blatter-Pattyn approximation (BP) (Blatter,1995; Pattyn, 2003) Higher Order (HO) or BP-HO, is a 3-dimensional approach to modelling ice shelves. The HO approximation neglects the horizontal derivatives of vertical velocity and assumes the bridging stresses (e.g., $\frac{\partial \sigma_{xz}}{\partial z}$ and $\frac{\partial \sigma_{yz}}{\partial z}$) is negligible. These assumptions are implemented in ISSM as follows:

2. $\frac{\partial \sigma_{xz}}{\partial x} \ll \frac{\partial \sigma_{zz}}{\partial z}$

3. $\frac{\partial \sigma_{yz}}{\partial y} \ll \frac{\partial \sigma_{zz}}{\partial z}$

4. $\frac{\partial v_z}{\partial x} \ll \frac{\partial v_x}{\partial z}$

5. $\frac{\partial v_z}{\partial y} \ll \frac{\partial v_y}{\partial z}$

The first two assumptions are due to the bridging effects (van der Veen and Whillans, 1989) being negligible. Further explanation is beyond the scope of this work.

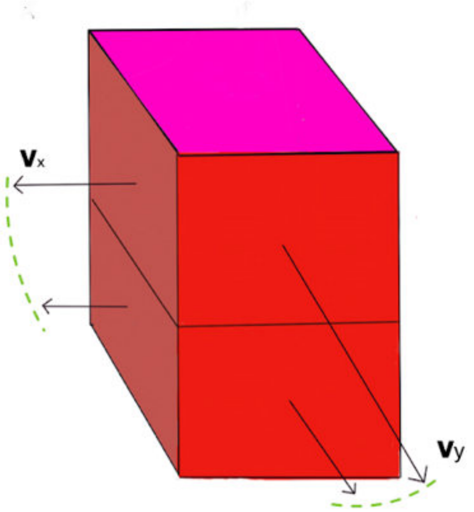

Figure 7.2 – Higher Order

In the Higher Order model, the differential equations only are solved for the velocities in the horizontal plane. This is a simplified version of the Full Stokes model, and the estimations made help with solving a model faster.

7.2.3 Shallow Shelf Approximation (SSA)

The Shallow Shelf Approximation or Shelfy Stream Approximation (Morland and Zainuddin, 1987; MacAyeal, 1989) is a two-dimensional approach that attempts to model floating icesheets (i.e., icesheets that are not grounded) in an efficient way. We start from the BP Higher Order approach and make further assumptions (i.e., $\dot{\epsilon}_{xz} = 0$; $\dot{\epsilon}_{yz}$=0; and neglecting the horizontal gradients of vertical velocity (due to being negligible in comparison to the vertical gradients of horizontal velocities) to solve the Full Stokes equations, as follows (Greve and Blatter, 2009; Larour et al. 2012).

In the SSA approach, once the horizontal velocities are determined, their depth averages will be assigned uniformly to the vertical nodes in different virtual elements in a 3-dimensional mesh, resulting in the velocities on all virtual layers being assumed to be the same. This poses specific challenges in using this approach in modelling the icesheets and glaciers: In ice shelves where there is basal shear, the ice experiences substantial variations in the vertical velocity, and the depth-average will become a less accurate representation of the velocity in the lower layers of the mesh. This becomes more prominent when this method is used for non-floating icesheets (i.e. non-ice shelves) (Larour et al., 2012).

The SSA works better for floating ice shelves, or in the case of fast-flowing ice streams, where most of the displacement is due to sliding.

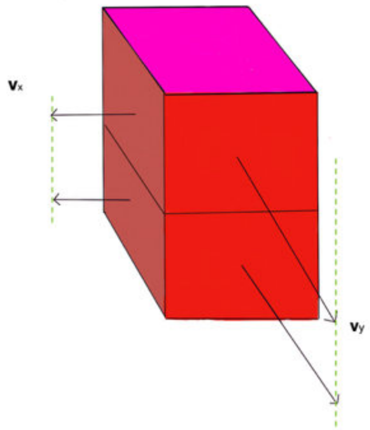

Figure 7.3 – Shallow-Shelf Approximation

The SSA is a two-dimensional model that solves for the depth-averaged velocity and therefore cannot be applied in areas where vertical variations in speed are not negligible like in the vicinity of grounding lines (where ice detaches from the bed).

7.2.4 Shallow Ice Approximation (SIA)

The Shallow Ice Approximation (SIA) method represents a two-dimensional approach to modelling icesheets, originally proposed by Hutter in 1983. This method focuses on the velocity in two horizontal directions (x and y), and also that all components of the stress tensor except for σ'_{xz}; σ'_{yz}. These assumptions will result in the pressure being linear with depth. SIA also assumes that the ice is grounded (not floating) and that the shear stress at the base of the glacier is balanced by the driving stress (Hutter, 1982; Larour et al., 2012).

In this model, the shear stresses in the x–z and y–z planes are dominant, whereas longitudinal and lateral stresses are neglected (Morlighem, 2011). These assumptions yield a set of computationally efficient equations. However, due to significant differences between vertical shear stress and lateral shear, this model is less suitable for modelling floating ice shelves, especially over short periods (Larour et al., 2012).

7.2.5 SIA, SSA, HO and FS in MIDAS

MIDAS is capable of analyzing icesheets composed of one or multiple units of ice. When using one type of material (e.g., water ice-based modelling of icesheets on Gale Crater), in scenarios where icesheets and glaciers are relatively shallow and grounded, such as the south pole of Mars (with only CO_2 ice), SIA can quickly provide insights into expected outcomes over longer periods, albeit less accurately than other methods.

Contrastingly, the SSA (Shallow-Shelf Approximation) method proves more effective for floating icesheets as it averages horizontal velocities across depth and uniformly assigns these velocities to vertical elements in virtual layers.

For icesheets with multiple units of ice, SIA and SSA cannot be used. The reason is that these two methods are both 2D. We cannot analyze a multi-unit icesheet’s rheology after the icesheet has been collapsed into 2D. And, as the vertical shear stresses are neglected in SSA, when applied to non-floating ice sheets, the influence of bedrock slope on the stress balance becomes negligible in this approach, especially when SSA is used for non-floating icesheets).

8 Appendix 2: Definition of Some Material Properties Used in This Dissertation

8.1 Arrhenius Law and the Flow Laws

Rheological properties of a material inform the material deformation. In case of a glacier, this helps describe the distribution of ice across an area. In its most fundamental form, rheology of a material defines the strain rate as a function of differential stress (Van Der Veen and Whillans, 1990; Durham et al., 2010). If ϵ is strain, and σ is the stress $[\frac{N}{m^2}]$, then the strain rate will be $\dot{\epsilon}$ [s^{-1}]. In icesheet modelling, strain and stress are tensor quantities. Glen's flow law relates the strain rate tensor $\dot{\epsilon}_{ij}$ to the deviatoric stress tensor (does not treat them as scalar quantities) τ_{ij}. The effective stress, τ_e, is defined through the second invariant of the deviatoric stress tensor (and to maintain the isotropy of the creep relation). This reduces the tensorial stress state to a scalar measure of stress magnitude that shows the deformation rate independent of coordinate system orientation. The scalar invariant form is what makes Glen's law consistent with isotropic, power-law creep behaviour in polycrystalline ice. For clarity and consistency with the remainder of this dissertation, I will show the equations without the full tensor notations, while it is understood that the underlying quantities are tensors. $\dot{\epsilon}$ in its simplest form can be defined as a function of stress as follows:

$$\dot{\epsilon} = A * f(\sigma, n) \qquad \textit{eq. 8.1}$$

The stress exponent (*n*) is a dimensionless number which is called the flow-rate exponent or the Glen's exponent. The property denoted as $A(T)$ $\left[\frac{1}{MPa^n.s}\right]$ is the temperature dependent rate factor and is defined as:

$$A(T) = A_{const} * e^{\frac{-Q}{T*R_g}} \qquad \textit{eq. 8.2}$$

A_{const} is a constant that is dependent on the grain size and liquid content of the material. The unit for A_{const} is the same as that of $A(T)$ (i.e., here the unit will be $[1/(MPa^n.s)]$). Q is the activation energy, or the lowest amount of energy required for a chemical reaction to be initiated and is measured in $[\frac{J}{mol}]$ in SI units. A_{const} and Q depend on the material type (e.g., CO_2 or H_2O). R_g is the universal gas constant (i.e., 8.3144598 $\left[\frac{J}{K.mol}\right]$) and T is the temperature measured in Kelvin. In its simplest form:

$$f(\sigma, n) = \sigma^n \qquad \textit{eq. 8.3}$$

For different conditions (such as the grain size, temperature or other environmental conditions impacting the flow), A_{const} and Q are adjusted accordingly. (Glen, 1955; Larour et al., 2012). Various sources discuss the flow laws in detail (e.g., see Cuffey and Paterson, 2010, and references therein).

As an example, for CO_2 and for the temperature range of 150-200 K Cross et al., (2020) provide:

$$A_{const} = 10^{13\pm1.27} \quad \left[\frac{1}{MPa^n.s}\right]$$

$$Q = 66900 \pm 4200 \quad \left[\frac{J}{mol}\right]$$

$n = 8 \pm 2.2$

For MIDAS, the above parameters were incorporated directly and then tested by running test simulations and validating against Smith et al. (2022) simulations.

8.1.1 Arrhenius Law and the Ice Rigidity

Using the Arrhenius law, we can define the ice rigidity or hardness *B* (Glen, 1955; Larour et al., 2012) as a function of temperature, activation energy, and the stress exponent in $\left[Pa.s^{\left(\frac{1}{n}\right)}\right]$ as follows:

$$B = A(T)^{\frac{-1}{n}} * 10^6 \qquad \textit{eq. 8.4}$$

And we can substitute *A(T)* with eq. 8.2 and write:

$$B(T) = \left(A_{const} * e^{\frac{-Q}{T*R_g}}\right)^{\frac{-1}{n}} * 10^6 \qquad \textit{eq. 8.5}$$

B is not stress dependent; however, the effective viscosity, which is determined using the rigidity, is stress dependent. The three equations of eq. 8.1, eq. 8.2 and eq. 8.3 can be used to define the strain rate. For the purpose of my dissertation, and with a focus on modelling, we can focus on the standard Glen-type flow law with temperature-dependent rate factor. This way we are not considering the grain size and prescribing a single dominant creep mechanism (as this is still an open question for water ice). Instead, any potential grain size influences would be collected in the effective rate factor A(T). As a result, we can write the equation below for large-scale icesheet modelling.

$$\dot{\epsilon} = A_{const} * e^{\frac{-Q}{T*R_g}} * \sigma^n \qquad eq.\ 8.6$$

Now, 8.6 can be used to define effective viscosity as:

$$\eta(\sigma) = (A_{const})^{-1} * e^{\frac{Q}{T*R_g}} * \sigma^{1-n} \qquad eq.\ 8.7$$

From eq. 8.5 and eq. 8.7 we can write:

$$\eta(\sigma) = B(T)^n * \sigma^{1-n} \qquad eq.\ 8.8$$

In other words, *B(T)* is the non-stress dependent part of viscosity (i.e., the material hardness).

8.2 Definition of Some Other Material Properties

For the purpose of this dissertation, other material properties will be referenced as well. As these concepts are fundamental, for the sake of completeness their definition have been collected in this appendix.

8.2.1 Density

Density is defined as the mass of an ice compound per unit of volume; it is measured as kilogram per cubic meter $\left[\frac{kg}{m^3}\right]$ (in SI units) and denoted with the Greek letter ρ. Due to the impact of environmental conditions, density is measured using the ratio of sufficiently small volume and the mass of that volume (Young et al., 2019; Halliday, Resnick, and Walker, 2021). Density is a function of temperature and pressure.

8.2.2 Exotic Ice

When considering ices in non-terrestrial settings, materials may include N_2, CO_2, CH_4, and others. Such deposits and glaciers are also subject to different gravitational forces and atmospheric pressures from the host planets and bodies. Because of this, we follow precedent in the literature and call these deposits “exotic ice” to be differentiated from water ice deposits on Earth.

8.2.3 Latent Heat of Fusion and Deposition

Latent heat of fusion, heat of fusion, or latent heat for short (denoted with L in this dissertation), is the amount of energy (i.e., heat) that a unit of mass of a solid substance needs to absorb in order to transform to its liquid state (or will release to solidify, in case of the latent heat of deposition) during an isothermal phase transition, and is measured in Joules per kilogram $\left[\frac{J}{kg}\right]$ (Young et al., 2019; Halliday, Resnick, and Walker, 2021).

8.2.4 Latent Heat of Sublimation

Latent Heat of sublimation or the enthalpy of sublimation (denoted with L_v in this dissertation) is the amount of energy (i.e., heat) that a unit of mass of a solid substance needs to absorb in order to transform to its gas state. Similar to latent heat of fusion, this is measured in Joules per kilogram $\left[\frac{J}{kg}\right]$. L_v can be measured using the Clausius-Clapeyron equation, as:

$$L_v = \left(\frac{dP_{sublimation}}{dT}\right)_{equilibrium} * T * \Delta V \qquad eq.\ 8.9$$

Where ΔV is the change in the volume from sold to gas (i.e., $\Delta V = V_{gas} - V_{solid}$). See Fray and Schmitt (2009) for further discussion. For the purpose of this dissertation, we focus mainly on the surface of glaciers, where the pressure remains constant; therefore, eq. 8.9 will result in constant numbers as reported in section 3 of this dissertation.

8.2.5 Specific Heat Capacity

Heat capacity (i.e., C) is the ratio of the energy that a substance absorbs to the resulting change in its temperature, and it is measured in Joules per Kelvin $\left[\frac{J}{K}\right]$ in SI units. Specific heat (i.e., c), measured in $\left[\frac{J}{kg.K}\right]$ in SI units, is heat capacity defined for the unit of mass:

$$C = m.c \qquad eq.\ 8.10$$

Specific heat can be expressed per mole (i.e., $6.02 * 10^{23}$ units) and measured in constant pressure (C_P) or constant volume (C_V). Specific heat capacity in constant pressure (C_p) is the amount of heat that a substance needs to absorb (or to lose) per unit mass to experience a unit temperature change, while the pressure on the substance remains unchanged. In SI, this is measured in $\left[\frac{J}{kg.K}\right]$ (Halliday, Resnick, and Walker, 2021). In this text, specific heat capacity refers to specific heat at constant pressure unless it is specified otherwise. As demonstrated by various research, the impact of environmental changes (i.e., the temperature) on the C_p of a substance or object could be complex (see Maass et al. (1926) for an example). Other units of measure, identical but modified for changing units, are as follows:

$$1\left[\frac{J}{kg.C^{\circ}}\right] = 1\left[\frac{J}{kg.K}\right]$$

$$1\left[\frac{cal}{kg.K}\right] = 4.1867\left[\frac{J}{kg.K}\right]$$

$$1\left[\frac{cal}{gr.K}\right] = 4186.8\left[\frac{J}{kg.K}\right]$$

The molar heat capacity is measured in $\left[\frac{J}{mol.K}\right]$ or $\left[\frac{cal}{mol.K}\right]$. As an example, for CO_2 with molar mass of 44:

$$1\left[\frac{cal}{mol.K}\right] = \frac{1}{44}\left[\frac{cal}{gr.K}\right]$$

Example: 0.231 $\left[\frac{cal}{gr.K}\right]$ (Maass et al., 1926) yields $44 * 0.231 = 10.17$ $\left[\frac{cal}{mol.K}\right]$, which is within the range provided by Giauque and Egan (1937). See section 4.2.4 for further information.

8.2.6 Thermal Conductivity

Thermal Conductivity (K; measured in Watts per meter per Kelvin $\left[\frac{W}{m.K}\right]$) is a parameter describing the rate of energy transfer of a material. For a substance, the higher this constant, the better the conduction of energy, and the higher its thermal transfer rate (Halliday, Resnick, and Walker, 2021).

Parts of the body of research conducted on the thermal conductivity of water ice, solid nitrogen, and CO_2 was covered in the earlier sections.

9 Appendix 3 – MCID Study

Table 9.1 shows the original coordinates of points along the path of the x-x' slice from Figure 5.1 that were selected to identify the slice. The other columns in the table show the selected points from SN#38 and this study domain meshes, and the respective distances. Table 9.2 provides the same information for the points selected along the y-y' path from Figure 5.1.The orders of x'-x and y-y' points are kept this way to follow the same pattern as in Figure 5.1 which is from a previous study done by Alwarda & Smith (2021). The cross-section profiles in the figures collected in this section follow the pattern and direction of Figure 5.1(B) and (C).

Original X Coordinate [m]	Original Y Coordinate [m]	Closest SN#38 X [m]	Closest SN#38 Y [m]	Distance of Original Coordinates to SN#38 [km]	Closest MIDAS X [m]	Closest MIDAS Y [m]	Distance of Original Coordinates to MIDAS [km]	SN#38–MIDAS Distance [km]
-184472.52	203945.01	-183978.53	205186.16	1.34	-186168.93	204090.36	1.70	2.45
-182856.72	201380.16	-184203.23	201959.51	1.47	-183950.61	198024.06	3.53	3.94
-178270.60	183575.93	-177369.84	185553.85	2.17	-177287.56	180933.98	2.82	4.62
-171235.52	166985.09	-170490.97	168427.27	1.62	-169159.90	167354.81	2.11	1.71
-160211.84	152621.01	-161213.24	152714.04	1.01	-161722.50	151657.23	1.79	1.17
-141112.41	143948.39	-141865.69	145037.34	1.32	-140440.31	143477.12	0.82	2.11
-122201.07	135527.64	-122769.84	136732.78	1.33	-121042.87	134977.49	1.28	2.46
-90788.82	133692.05	-92760.39	134186.84	2.03	-91875.72	134219.15	1.21	0.89

Table 9.1 -The original (X,Y) coordinates for points that make up x'-x slice from Figure 5.1.

Columns 3,4, 6 and 7 provide the coordinates of closest points from SN#38 and MIDAS constructed meshes respectively. Columns 5 and 8, in kilometers, provide the distance between the original points and the selected points from each modelling mesh. The last column provides how far each point from SN#38 and MIDAS modelling meshes are from each other. The first row corresponds to point x', and the last row corresponds to point x.

Original X Coordinate [m]	Original Y Coordinate [m]	Closest SN#38 X [m]	Closest SN#38 Y [m]	Distance of Original Coordinates to SN#38 [km]	Closest MIDAS X [m]	Closest MIDAS Y [m]	Distance of Original Coordinates to MIDAS [km]	SN#38–MIDAS Distance [km]
-185024.72	82959.41	-186421.45	83954.20	1.71	-184662.18	81570.66	1.44	2.96
-200152.09	32489.27	-201264.75	32778.41	1.15	-199729.66	33448.07	1.05	1.67
-185025.51	-12808.45	-184684.23	-13217.81	0.53	-184662.18	-11333.15	1.52	1.88
-184174.59	-37002.32	-183034.13	-36250.46	1.37	-184662.18	-38305.22	1.39	2.62
-177718.94	-62689.33	-177499.12	-61601.02	1.11	-179550.31	-63610.46	2.05	2.87
-160680.11	-86502.86	-160327.96	-87262.49	0.84	-161840.44	-85756.71	1.38	2.13
-139341.48	-113159.01	-139512.05	-111663.89	1.50	-138954.55	-113711.65	0.67	2.12

Table 9.2 - The original (X,Y) coordinates for points that make up y-y' slice from Figure 5.1. For the detail description of each column see Table 9.1 caption. The first row corresponds to point y, and the last row corresponds to point y'.

Table 9.4 also collects and presents the actual values for the surface velocity magnitudes, thickness, and basal temperature for these 4 control points and for 11 points in time corelating to major changes in the planet obliquity (Figure 9.1), for both modelling scenarios to provide quantitative means of comparing the impact of the water ice bounding layers.

Point Location	Original Coordinates (X, Y) [m]		SN#38 Closest Coordinates (X, Y) [m]		Original Points - SN#38 Points Distance [km]	MIDAS Closest Coordinates (X, Y) [m]		Original Points - MIDAS Points Distance [km]	MIDAS Points - SN#38 Points Distance [km]
x-x' Slope	-120494.55	135427.92	-121055.28	134127.74	1.41	-121042.87	134977.49	0.71	0.85
x-x' Basin	-152133.89	148952.00	-151727.16	150213.83	1.32	-151680.58	148481.42	0.65	1.73
y-y' Slope	-160746.09	-86410.64	-160327.96	-87262.49	0.95	-161840.44	-85756.71	1.27	2.13
y-y' Basin	-186191.09	-9318.03	-185286.37	-9805.50	1.03	-187675.68	-8370.70	1.76	2.79

Table 9.3 - Coordinates of the points used for Figure 5.16, and their representative points in SN#38 and MIDAS modelling meshes.

Columns 5, 8 and 9 show the distance between the actual points in the slices to chosen points in the SN#38 mesh, and the MIDAS mesh, and lastly the distance between the points on SN#38 and MIDAS meshes.

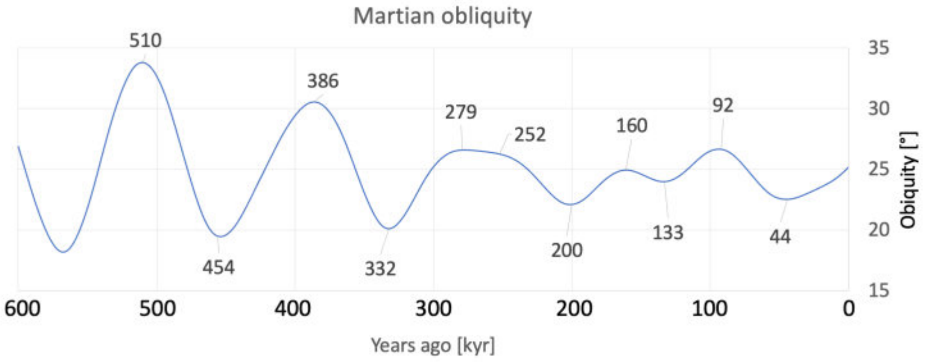

Figure 9.1 – This plot shows the years (in thousands of years since present), used for Table 9.4.

Yr ago [kyr]	**SN#38 x-x' path**	**MIDAS x-x' path**	**% Change**	**SN#38 y-y' path**	**MIDAS y-y' path**	**% Change**
	Slope Average Velocity [mm/yr]			Slope Average Velocity [mm/yr]		
510	0.64	0.39	-39.04%	0.41	1.02	151.13%
454	70.02	48.67	-30.49%	44.29	88.83	100.55%
386	10.29	9.14	-11.16%	15.67	5.93	-62.19%
332	56.69	51.30	-9.52%	49.03	47.55	-3.02%
279	20.13	26.23	30.32%	22.59	19.12	-15.39%
252	19.56	27.05	38.29%	22.22	24.58	10.61%
200	39.04	46.38	18.82%	33.78	46.05	36.32%
160	22.41	35.94	60.40%	22.60	25.98	14.99%
133	28.38	42.75	50.63%	26.19	31.34	19.68%
92	15.08	27.20	80.35%	17.73	24.63	38.87%
44	32.20	45.38	40.91%	84.30	45.02	-46.60%
	Slope Thickness [m]			Slope Thickness [m]		
510	1.00	1.28	28.03%	1.00	1.28	28.06%
454	186.17	184.03	-1.15%	251.40	207.71	-17.38%
386	45.86	67.47	47.11%	144.56	73.24	-49.34%
332	182.57	203.13	11.26%	302.63	240.65	-20.48%
279	93.90	126.51	34.73%	231.96	126.55	-45.44%
252	93.08	128.51	38.07%	234.60	122.82	-47.65%
200	153.57	190.10	23.79%	305.50	183.95	-39.79%
160	110.49	156.95	42.06%	268.80	187.57	-30.22%
133	130.30	177.52	36.24%	291.90	207.97	-28.75%
92	88.58	126.37	42.67%	253.91	123.62	-51.32%

Yr ago [kyr]	**SN#38 x-x' path**	**MIDAS x-x' path**	**% Change**	**SN#38 y-y' path**	**MIDAS y-y' path**	**% Change**
44	144.72	181.73	25.57%	60.71	181.35	198.71%
	Slope Average Temperature [K]			Slope Average Temperature [K]		
510	150.02	150.03	0.00%	150.02	150.06	0.02%
454	154.63	154.39	-0.16%	156.25	159.95	2.37%
386	151.15	151.00	-0.10%	153.61	152.50	-0.72%
332	154.55	155.41	0.56%	157.53	160.48	1.88%
279	152.35	150.15	-1.44%	155.80	150.43	-3.44%
252	152.32	151.87	-0.29%	155.84	154.45	-0.89%
200	153.83	154.40	0.37%	157.61	157.40	-0.14%
160	152.76	152.29	-0.31%	156.73	157.27	0.34%
133	153.25	153.05	-0.13%	157.28	158.23	0.60%
92	152.21	151.78	-0.28%	156.32	154.40	-1.23%
44	153.61	154.09	0.32%	151.49	157.16	3.74%
	Basin Average Velocity [mm/yr]			Basin Average Velocity [mm/yr]		
510	0.44	0.31	-28.86%	1.36	1.17	-13.86%
454	69.89	45.16	-35.39%	50.60	63.23	24.96%
386	11.77	8.98	-23.71%	15.72	5.99	-61.88%
332	47.52	48.34	1.71%	36.18	30.30	-16.27%
279	19.25	26.40	37.10%	17.00	18.24	7.30%
252	18.38	27.17	47.82%	15.43	19.44	25.95%
200	32.52	45.73	40.60%	22.49	34.98	55.52%
160	21.31	36.63	71.95%	15.62	19.06	22.02%
133	25.14	43.52	73.10%	16.80	22.45	33.61%

Yr ago [kyr]	**SN#38 x-x' path**	**MIDAS x-x' path**	**% Change**	**SN#38 y-y' path**	**MIDAS y-y' path**	**% Change**
92	16.58	27.80	67.61%	11.18	17.72	58.52%
44	28.30	45.62	61.22%	4.76	33.14	596.69%
	Basin Thickness [m]			Basin Thickness [m]		
510	1.00	1.28	28.05%	1.00	1.28	28.05%
454	274.65	217.06	-20.97%	314.73	175.29	-44.30%
386	169.75	123.79	-27.08%	223.69	95.92	-57.12%
332	323.79	257.83	-20.37%	402.46	204.42	-49.21%
279	248.79	167.33	-32.74%	344.03	148.84	-56.74%
252	248.80	164.03	-34.07%	347.52	142.59	-58.97%
200	314.68	215.14	-31.63%	427.42	204.86	-52.07%
160	275.27	167.90	-39.00%	396.12	163.92	-58.62%
133	296.30	184.90	-37.60%	421.74	185.38	-56.05%
92	255.52	134.63	-47.31%	385.73	146.68	-61.97%
44	313.49	187.22	-40.28%	446.71	204.72	-54.17%
	Basin Average Temperature [K]			Basin Average Temperature [K]		
510	150.02	150.03	0.00%	150.03	150.06	0.02%
454	156.78	155.23	-0.99%	157.75	158.49	0.47%
386	154.25	152.12	-1.38%	155.60	153.60	-1.28%
332	158.05	156.06	-1.26%	159.91	158.80	-0.69%
279	156.24	150.13	-3.91%	158.60	150.44	-5.15%
252	156.21	152.09	-2.64%	158.63	155.24	-2.13%
200	157.86	154.45	-2.16%	160.60	158.18	-1.51%
160	156.92	152.09	-3.08%	159.95	155.98	-2.48%

Yr ago [kyr]	**SN#38 x-x' path**	**MIDAS x-x' path**		**% Change**		**SN#38 y-y' path**	**MIDAS y-y' path**		**% Change**
133	157.41	152.83		-2.91%		160.47	157.00		-2.16%
92	156.38	151.67		-3.01%		159.58	155.31		-2.68%
44	157.82	153.96		-2.44%		161.11	158.04		-1.91%

Table 9.4 – The quantitative comparison of the modelling results.

This table, for 11 selected points in time (see Figure 5.17) shows the columnar average of velocity and temperature of the nodes in the modelling meshes as well as the thickness of the column of ice from SN#38 and our current modelling work. The values are provided for points selected on the slope and basin along the x-x' and y-y's paths (Figure 5.15). The percentage changes have been provided to show how the change in the modelling results is a function of time. While there are fluctuations, the results with water ice bounding layers tend to be lower. The values in this table correspond to Figure 5.16.

10 References

Adams, C. J., Iverson, N. R., Helanow, C., Zoet, L. K., & Bate, C. E. (2021). “Softening of temperate ice by interstitial water.” Frontiers in Earth Science, 9, 702761.

Alexiades, V. (1992). Mathematical Modeling Of Melting And Freezing Processes. CRC Press. https://books.google.com?id=WfJ13xBpBNYC.

Alsaeed, N. R., & Hayne, P. O. (2022). Transport of Water Into the Polar Regions of Mars Through Scavenging by CO 2 Snowfall. Journal of Geophysical Research: Planets, 127(11). https://doi.org/10.1029/2022JE007386

Alwarda, R., & Smith, I. B. (2021). Stratigraphy and Volumes of the Units Within the Massive Carbon Dioxide Ice Deposits of Mars. Journal of Geophysical Research: Planets, 126(5). https://doi.org/10.1029/2020JE006767

Anderson, R. & Bell, J. F. (2010). Geologic mapping and characterization of Gale Crater and implications for its potential as a Mars Science Laboratory landing site. MARS MARS. Mars, 5, 76-128. https://doi.org/10.1555/mars.2010.0004.

Anderson, R. S., & Anderson, S. P. (2025). Lingering beneath crumbling walls: The origin of Holocene rock glaciers. Geology.

Arnold, N. S., Butcher, F. E. G., Conway, S. J., Gallagher, C., & Balme, M. R. (2022). Surface topographic impact of subglacial water beneath the south polar ice cap of Mars. Nature Astronomy, 6(11), 1256–1262. https://doi.org/10.1038/s41550-022-01782-0

Bagatskii, M., Kucheryavy, V., Manzhelii, V., and Popov, V. (1968). “Thermal capacity of solid nitrogen.” Physica Status Solidi (b), 26(2), 453–460.

Barnes, W. H., and Maass, O. (1930). “specific heats and latent heat of fusion of ice.” Canadian Journal of Research 3 (3): 205–13. https://doi.org/10.1139/cjr30-056.

Behn, M. D., Goldsby, D. L., and Hirth, G. (2021). “The role of grain size evolution in the rheology of ice: implications for reconciling laboratory creep data and the Glen flow law.” The Cryosphere, 15, 4589–4605, https://doi.org/10.5194/tc-15-4589-2021, 2021.

Bell, J. F., III, Godber, A., McNair, S., Caplinger, M., Maki, J., Lemmon, M., et al. (2017). The Mars Science Laboratory Curiosity rover Mastcam instruments: Preflight and in-flight calibration, validation, and data archiving. Earth and Space Science, 4(7), 396–452. https://doi.org/10.1002/2016ea000219.

Bertie, J., Calvert, L., and Whalley, E. (1963). “Transformations of ice II, ice III, and ice V at atmospheric pressure.” The Journal of Chemical Physics, 38(4), 840–846.

Bierson, C. J., Phillips, R. J., Smith, I. B., Wood, S. E., Putzig, N. E., Nunes, D., & S. Byrne. (2016). Stratigraphy and evolution of the buried CO2 deposit in the Martian south polar cap. Geophysical Research Letters, 43(9), 4172–4179. https://doi.org/10.1002/2016GL068457.

Bills, B.G., 1999. Obliquity-oblateness feedback on Mars. J. Geophys. Res. 104, 30773–30797

Bogorodsky, V. V., & Gavrilo, V. P. (1980), "Ice, Physical properties, Modern methods for glaciology." Leningrad: Hydrometizdat, 384 (in Russian).

Bolshutkin, D. N., Borisova, L. I., and Leonteva, A. V. (1968). "Creep of crystalline methane." Sov. Phys. Solid State, 10, 1248-1249.

Bonales, L. J., Rodriguez, A. C., and Sanz., P. D. (2017). "Thermal Conductivity of Ice Prepared Under Different Conditions." International Journal of Food Properties 20 (December): 610–19. https://doi.org/10.1080/10942912.2017.1306551.

Brown, A. J., Calvin, W. M., McGuire, P. C., & Murchie, S. L. (2010). Compact Reconnaissance Imaging Spectrometer for Mars (CRISM) south polar mapping: First Mars year of observations. Journal of Geophysical Research: Planets, 115(E2).

Buhler, P. B. (2023). A 510,000-Year Record of Mars' Climate. Geophysical Research Letters, 50(5), e2022GL101752. https://doi.org/10.1029/2022GL101752

Buhler, P. B., & Piqueux, S. (2021). Obliquity-Driven CO2 Exchange Between Mars' Atmosphere, Regolith, and Polar Cap. Journal of Geophysical Research: Planets, 126(5). https://doi.org/10.1029/2020JE006759

Buhler, P. B., Ingersoll, A. P., Piqueux, S., Ehlmann, B. L., & Hayne, P. O. (2020). Coevolution of Mars's atmosphere and massive south polar CO2 ice deposit. Nature Astronomy, 4(4), 364–371. https://doi.org/10.1038/s41550-019-0976-8

Byrne, S., & Ingersoll, A. P. (2003). A sublimation model for Martian south polar ice features. Science, 299(5609), 1051–1053.

Byrne, S., 2009. The polar deposits of Mars. Annual Review of Earth and Planetary Sciences 37, 535–560.

Caravaca, G., Le Mouélic, S., Rapin, W., Dromart, G., Gasnault, O., Fau, A., ... & Lanza, N. L. (2021). Long-distance 3D reconstructions using photogrammetry with Curiosity's ChemCam remote micro-imager in Gale crater (Mars). Remote Sensing, 13(20), 4068.

Chan, M. A., & Netoff, D. I. (2017). A terrestrial weathering and wind abrasion analog for mound and moat morphology of Gale crater, Mars. Geophysical Research Letters, 44(9), 4000-4007.

Chevrier, V., D. Sears, J. Chittenden, L. Roe, R. Ulrich, K. Bryson, L. Billingsley, and J. Hanley (2007), Sublimation rate of ice under simulated Mars conditions and the effect of layers of mock regolith JSC Mars-1, Geophys. Res. Lett., 34, L02203, doi:10.1029/2006GL028401.

Choi, Y. (1986). "Effects of Temperature and Composition on the Thermal Properties of Foods." Transport Phenomena, 99–101. https://cir.nii.ac.jp/crid/1570291225046275200.

Chou, I.M., Blank, J. G., Goncharov, A. F., Mao, H., and Hemley, R. J. (1998). "In situ observations of a high-pressure phase of H2O ice." Science, 281(5378), 809–812.

Clark, B. R., & Mullin, R. P. (1976). "Martian glaciation and the flow of solid CO2." Icarus, 27(2), 215–228. https://doi.org/10.1016/0019-1035 (76)90005-1.

Conway, S. J., Butcher, F. E., de Haas, T., Deijns, A. A., Grindrod, P. M., & Davis, J. M. (2018). Glacial and gully erosion on Mars: A terrestrial perspective. Geomorphology, 318, 26-57.

Cook, T., and Davey, G. (1976). "The Density and Thermal Conductivity of Solid Nitrogen and Carbon Dioxide." Cryogenics 16 (6): 363–69. https://doi.org/10.1016/0011-2275(76)90217-4.

Correia, A.C.M., Laskar, J., Néron de Surgy, O., 2003. Long-term evolution of the spin of Venus I. Theory. Icarus 163, 1–23

Cross, A. J., Goldsby, D. L., Hager, T. F., & Smith, I. B. (2020). The Rheological Behavior of CO2 Ice: Application to Glacial Flow on Mars. Geophysical Research Letters, 47(22). https://doi.org/10.1029/2020GL090431

Cuffey, K. M., & Paterson, W. S. B. (2010). The Physics of Glaciers, 4th Edition. Amsterdam: Academic Press.

Day, M., & Kocurek, G. (2016). Observations of an Aeolian Landscape: From Surface to Orbit in Gale Crater. Icarus, 280, 37-71.

Dickson, J. L., Head, J. W., Goudge, T. A., & Barbieri, L. (2015). Recent climate cycles on Mars: Stratigraphic relationships between multiple generations of gullies and the latitude dependent mantle. Icarus, 252, 83-94.

Durham, W. B., Kirby, S. H., & Stern, L. A. (1999). Steady-state flow of solid CO2: Preliminary results. Geophysical Research Letters, 26(23), 3493–3496.

Durham, W. B., Kirby, S. H., and Stern, L. A. (1992). "Effects of dispersed particulates on the rheology of water ice at planetary conditions." Journal of Geophysical Research: Planets, 97(E12), 20883-20897.

Durham, W. B., Kirby, S. H., and Stern, L. A. (1997). “Creep of water ices at planetary conditions: A compilation.” Journal of Geophysical Research: Planets, 102(E7), 16293–16302. https://doi.org/10.1029/97JE00916.

Durham, W. B., Kirby, S. H., and Stern, L. A. (1998). Rheology of planetary ices. In Solar System Ices: Based on Reviews Presented at the International Symposium “Solar System Ices” held in Toulouse, France, on March 27–30, 1995 (pp. 63-78). Springer Netherlands.

Durham, W. B., Kirby, S. H., Heard, H. C., Stern, L. A., & Boro, C. O. (1988). Water ice phases II, III, and V: Plastic deformation and phase relationships. Journal of Geophysical Research: Solid Earth, 93(B9), 10191-10208.

Durham, W. B., Prieto-Ballesteros, O., Goldsby, D. L., and Kargel., J. S. (2010). “Rheological and Thermal Properties of Icy Materials.” Space Science Reviews 153 (1-4): 273–98. https://doi.org/10.1007/s11214-009-9619-1.

Durham, W., Heard, H., and Kirby, S. H. (1983). “Experimental deformation of polycrystalline H2O ice at high pressure and low temperature: Preliminary results.” Journal of Geophysical Research: Solid Earth, 88(S01), B377–B392.

Duval, P. (1977). “The role of the water content on the creep rate of polycrystalline ice.” Isotopes and impurities in snow and ice, 118, 29-33.

Eluszkiewicz, J., and Stevenson, D. J. (1990). “Rheology of solid methane and nitrogen: Applications to TRITON.” Geophysical Research Letters, 17(10), 1753–1756. https://doi.org/10.1029/GL017i010p01753.

Emmett, J.A., Murphy, J.R., Kahre, M.A., 2020. Obliquity dependence of the formation of the Martian polar layered deposits. Planetary and Space Science 193, 105047. https://doi.org/10.1016/j.pss.2020.105047.

Engelhardt, H., and Whalley, E. (1972). “Ice IV.” The Journal of Chemical Physics, 56(6), 2678–2684.

Fairén, A. G., Stokes, C. R., Davies, N. S., Schulze-Makuch, D., Rodríguez, J. A. P., Davila, A. F., ... & Squyres, S. W. (2014). A cold hydrological system in Gale crater, Mars. Planetary and Space Science, 93, 101-118.

Fard, K. B., & Smith, I. B. (2024). Properties of water, carbon dioxide, and nitrogen ices in planetary surface environments. Icarus, 115895. https://doi.org/10.1016/j.icarus.2023.115895.

Fastook, J. L., Head, J. W. (2024). Origin of ice in the Medusae Fossae Formation, equatorial Mars. Icarus, Volume 421, 2024, 116226, https://doi.org/10.1016/j.icarus.2024.116226.

Feistel, R., & Wagner, W. (2006). A new equation of state for H2O ice Ih. Journal of Physical and Chemical Reference Data, 35(2), 1021-1047.

Ferrari, C., & Lucas, A. (2016). "Low thermal inertias of icy planetary surfaces-Evidence for amorphous ice?." Astronomy & Astrophysics, 588, A133.

Fishbaugh, K. E., & Head III, J. W. (2001). Comparison of the north and south polar caps of Mars: New observations from MOLA data and discussion of some outstanding questions. Icarus, 154(1), 145–161.

Forget, F., Haberle, R. M., Montmessin, F., Levrard, B., & Head, J. W. (2006). Formation of Glaciers on Mars by Atmospheric Precipitation at High Obliquity. Science, 311(5759), 368-371.

Foss, F. J., Putzig, N. E., Campbell, B. A., & Phillips, R. J. (2017). 3D imaging of Mars' polar ice caps using orbital radar data. The Leading Edge, 36(1), 43–57.

Fray, N., & Schmitt, B. (2009). "Sublimation of ices of astrophysical interest: A bibliographic review." Planetary and Space Science, 57(14-15), 2053-2080.

Giauque, W. F., and Clayton, J. (1933). "The heat capacity and entropy of nitrogen. Heat of vaporization. Vapor pressures of solid and liquid. The Reaction 1/2 N2+ 1/2 O2= NO from spectroscopic data." Journal of the American Chemical Society, 55(12), 4875–4889.

Giauque, W. F., and Egan, C. J. (1937). "Carbon Dioxide. The Heat Capacity and Vapor Pressure of the Solid. The Heat of Sublimation. Thermodynamic and Spectroscopic Values of the Entropy." The Journal of Chemical Physics 5 (1): 45–54. https://doi.org/10.1063/1.1749929.

Giauque, W. F., and Stout, J. W. (1936). "The Entropy of Water and the Third Law of Thermodynamics. The Heat Capacity of Ice from 15 to 273° K." Journal of the American Chemical Society, 58(7), 1144-1150.

Goldsby, D. L., and Kohlstedt, D. L. (2001). "Superplastic deformation of ice: Experimental observations." Journal of Geophysical Research: Solid Earth, 106(B6), 11017–11030. https://doi.org/10.1029/2000JB900336.

Greeley, R., & Guest, J. E. (1987). Geologic map of the eastern equatorial region of Mars (No. 1802-B). US Geological Survey.

Grott, M., Hauber, E., Werner, S. C., Kronberg, P., & Neukum, G. (2007). Mechanical modelling of thrust faults in the Thaumasia region, Mars, and implications for the Noachian heat flux. Icarus, 186(2), 517-526.

Grotzinger, J. P., Sumner, D. Y., Kah, L. C., Stack, K., Gupta, S., Edgar, L., … & Vasavada, A. R. (2015). Deposition, Exhumation, and Paleoclimate of an Ancient Lake Deposit, Gale Crater, Mars. Science, 350(6257), aac7575.

Guo, X., Richardson, M. I., Soto, A., & Toigo, A. (2010). On the mystery of the perennial carbon dioxide cap at the south pole of Mars. Journal of Geophysical Research: Planets, 115(E4), 2009JE003382. https://doi.org/10.1029/2009JE003382

Haberle, R. M., Forget, F., Colaprete, A., Schaeffer, J., Boynton, W. V., Kelly, N. J., & Chamberlain, M. A. (2008). The effect of ground ice on the Martian seasonal CO2 cycle. Planetary and Space Science, 56(2), 251–255.

Haberle, R. M., Joshi, M. M., Murphy, J. R., Barnes, J. R., Schofield, J. T., Wilson, G., … & Zent, A. P. (2000). General Circulation Model Simulations of the Mars Pathfinder Atmospheric Structure Investigation/Meteorology Data. Journal of Geophysical Research: Planets, 105(E1), 1757-1777.

Hallet, B. (1996). Glacial quarrying: A simple theoretical model. Annals of Glaciology, 22, 1-8.

Halliday, D., Resnick, R. and Walker, J. (2021). “Fundamentals of Physics.” John Wiley and Sons.

Head, J. W., & Marchant, D. R. (2003). Cold-Based Mountain Glaciers on Mars: Western Arsia Mons. Geology, 31(7), 641-644.

Head, J. W., & Weiss, D. K. (2014). Preservation of ancient ice at Pavonis and Arsia Mons: Tropical mountain glacier deposits on Mars. Planetary and Space Science, 103, 331–338. https://doi.org/10.1016/j.pss.2014.09.004 .

Head, J. W., Mustard, J. F., Kreslavsky, M. A., Milliken, R. E., & Marchant, D. R. (2003). Recent ice ages on Mars. Nature, 426(6968), 797–802. https://doi.org/10.1038/nature02114

Herkenhoff, K. E., & Plaut, J. J. (2000). Surface ages and resurfacing rates of the polar layered deposits on Mars. Icarus, 144(2), 243–253.

Hobbs, P. V., Chang, S., & Locatelli, J. D. (1974). “The dimensions and aggregation of ice crystals in natural clouds.” Journal of geophysical Research, 79(15), 2199-2206.

Hooyer, T. S., Cohen, D., & Iverson, N. R. (2012). Control of glacial quarrying by bedrock joints. Geomorphology, 153, 91-101.

Hughes, M. N., Arvidson, R. E., Dietrich, W. E., Lamb, M. P., Catalano, J. G., Grotzinger, J. P., & Bryk, A. B. (2022). Canyon Wall and Floor Debris Deposits in Aeolis Mons, Mars. Journal of Geophysical Research: Planets, 127(2), e2021JE006848. https://doi.org/10.1029/2021JE006848.

Ingersoll, A. P. (1970), Mars: Occurrence of Liquid Water, Science, 168, 972–973, doi:10.1126/science.168.3934.972.

Iverson, N. R. (2012). A theory of glacial quarrying for landscape evolution models. Geology, 40(8), 679-682.

Journaux, B., Brown, J. M., Pakhomova, A., Collings, I.E., Petitgirard, S., Espinoza, P., Boffa, T., Ballaran, et al. (2020). “Holistic Approach for Studying Planetary Hydrospheres: Gibbs Representation of Ices Thermodynamics, Elasticity, and the Water Phase Diagram to 2,300 MPa.” Journal of Geophysical Research: Planets 125 (1). https://doi.org/10.1029/2019JE006176.

Kieffer, H. H. (1979). Mars south polar spring and summer temperatures: A residual CO2 frost. Journal of Geophysical Research: Solid Earth, 84(B14), 8263–8288.

Kieffer, H. H. (2013). “Thermal model for analysis of Mars infrared mapping.” Journal of Geophysical Research: Planets, 118(3), 451-470.

Kinoshita, H., 1977. Theory of the rotation of the rigid Earth. Celest. Mech. 15, 277–326

Kite, E. S., Halevy, I., Kahre, M. A., Wolff, M. J., & Manga, M. (2013). Seasonal melting and the formation of sedimentary rocks on Mars, with predictions for the Gale Crater mound. Icarus, 223(1), 181-210.

Kite, E. S., Lucas, A., & Fassett, C. I. (2012). Pacing Early Mars fluvial activity at Aeolis Dorsa: Implications for Mars Science Laboratory observations at Gale Crater and Aeolis Mons. arXiv preprint arXiv:1207.6726.

Klinger, J. (1980). “Influence of a phase transition of ice on the heat and mass balance of comets.” Science, 209(4453), 271-272.

Klinger, J. (1981). “Some consequences of a phase transition of water ice on the heat balance of comet nuclei.” Icarus, 47(3), 320-324.

Klotz, S., Strässle, T., Nelmes, R., Loveday, J., Hamel, G., Rousse, G., Canny, B., Chervin, J., and Saitta, A. (2005). “Nature of the polyamorphic transition in ice under pressure.” Physical Review Letters, 94(2), 025506.

Koloskova, L., Krupskii, I., Manzhelii, V., and Gorodilov, B. Y. (1973). “Thermal conductivity of solid nitrogen and carbon monoxide.” Sov. Phys. Solid State, 15(6), 1278–1279.

Konstantinov, V.A., Manzhelii, V.G., Smirnov, S.A. and Tolkachev, A.M. (1988) “Heat transfer in solid CO2 and N2O: dependence on temperature and volume, Sov. J. Low Temp.” Phys., 14, pp. 104-107.

Kreslavsky, M. A., & Head, J. W. (2002). Mars: Nature and evolution of young latitude-dependent water-ice-rich mantle. Geophysical Research Letters, 29(15). https://doi.org/10.1029/2002GL015392

Krupskii, I. N., Prokhvatilov, A.I, and Erenburg, A.I. “Fizika Nizkikh Temp. 1(1975) 359.” IN Krupskii, AI Prokhvatilov, and AI Erenburg. Low Temp. Phys, 1, 178.

Larour, E., Seroussi, H., Morlighem, M., & Rignot, E. (2012). Continental Scale, High Order, High Spatial Resolution, Ice Sheet Modelling Using the Ice Sheet System Model (ISSM). Journal of Geophysical Research: Earth Surface, 117(F1).

Larour, E., Seroussi, H., Morlighem, M., and Rignot., E. (2012). “Continental Scale, High Order, High Spatial Resolution, Ice Sheet Modeling Using the Ice Sheet System Model (ISSM).” Journal of Geophysical Research: Earth Surface 117 (1). https://doi.org/10.1029/2011JF002140.

Laskar, J., & Robutel, P. (1993). The Chaotic Obliquity of the Planets. Nature, 361(6413), 608-612.

Laskar, J., Correia, A. C. M., Gastineau, M., Joutel, F., Levrard, B., & Robutel, P. (2004). Long term evolution and chaotic diffusion of the insolation quantities of Mars. Icarus, 170(2), 343–364. https://doi.org/10.1016/j.icarus.2004.04.005

Le Deit, L., Hauber, E., Fueten, F., Pondrelli, M., Rossi, A. P., & Jaumann, R. (2013). Sequence of infilling events in Gale Crater, Mars: Results from morphology, stratigraphy, and mineralogy. Journal of Geophysical Research: Planets, 118(12), 2439-2473.

Lee, K. S., Lee, T. H., and Kim, W. S. (1994). "Heat and mass transfer of parallel plate heat exchanger under frosting condition." Korean Journal of Air-Conditioning and Refrigeration Engineering 6.2: 155-165.

Lee, Kwan-Soo, Jhee, Sung, and Yang, Dong-Keun (2003). “Prediction of the Frost Formation on a Cold Flat Surface.” International Journal of Heat and Mass Transfer 46 (20): 3789–96. https://doi.org/10.1016/S0017-9310(03)00195-9.

Leliwa-Kopystyński, J., Satorre, M. A., & Santonja, C. (2013). “Experimental studies of sublimation of highly volatile ices in relevance to the ices of the solar system.” Acta Geophysica, 61, 1304-1321.

Levrard, B., Forget, F., Montmessin, F., & Laskar, J. (2007). Recent formation and evolution of northern Martian polar layered deposits as inferred from a Global Climate Model. Journal of Geophysical Research: Planets, 112(E6).

Levy, J.S., Fassett, C.I., Head, J.W., Schwartz, C., Watters, J.L., 2014. Sequestered glacial ice contribution to the global Martian water budget: Geometric constraints on the volume of remnant, midlatitude debris-covered glaciers. J. Geophys. Res. Planets 119, 2014JE004685. https://doi.org/10.1002/2014JE004685.

Lunardini, V. J. (1981). “Heat Transfer in Cold Climates.” Van Nostrand Reinhold Company.

Maass, O., and Barnes, W. H. (1926). “Some thermal constants of solid and liquid carbon dioxide.” Proceedings of the Royal Society of London. Series A, Containing Papers of a Mathematical and Physical Character, 111(757), 224-244.

Maass, O., and Waldbauer, L. J. (1925). “The specific heats and latent heats of fusion of ice and of several organic compounds.” Journal of the American Chemical Society, 47(1), 1-9.

Madeleine, J. B., Forget, F., Millour, E., Montmessin, F., & Jouglet, D. (2009). Amazonian Glaciations on Mars: A Proposed Climate Scenario. Icarus, 203(2), 390-405.

Malin, M. C., Ravine, M. A., Caplinger, M. A., Tony Ghaemi, F., Schaffner, J. A., Maki, J. N., et al. (2017). The Mars Science Laboratory (MSL) Mast cameras and descent imager: Investigation and instrument descriptions. Earth and Space Science, 4(8), 506–539. https://doi.org/10.1002/2016EA000252.

Mangan, T. P., Salzmann, C. G., Plane, J. M. C., and Murray, B. J. (2017). “CO2 Ice Structure and Density Under Martian Atmospheric Conditions.” Icarus 294 (September): 201–8. https://doi.org/10.1016/j.icarus.2017.03.012.

Mangold, N., Dehouck, E., Fedo, C., Forni, O., Achilles, C., Bristow, T., ... & Wiens, R. C. (2019). Chemical alteration of fine-grained sedimentary rocks at Gale crater. Icarus, 321, 619-631.

Manning, C. V., Bierson, C., Putzig, N. E., & McKay, C. P. (2019). The formation and stability of buried polar CO2 deposits on Mars. Icarus, 317, 509–517. https://doi.org/10.1016/j.icarus.2018.07.021

Manning, C. V., McKay, C. P., & Zahnle, K. J. (2006). Thick and thin models of the evolution of carbon dioxide on Mars. Icarus, 180(1), 38–59.

Manzhelii, V. G., and Krupskii, I. N. (1968). “In Physics of condensed state” (Vol. 2, p. 3). Kharkov, USSR: Institute of Low Temperature Physics and Engineering. (In Russian).

Manzhelii, V. G., Kokshenev, V. B., Koloskova, L. A., and Krupskii, I. N. (1975). “Phonon-libron interaction and thermal conductivity in the simplest molecular crystals.” Soviet journal of low temperature physics, 1, 624–628.

Manzhelii, V. G., Prokhvatilov, A. I., Gavrilko, V. G., and Isakina, A. P. (1999). “Structure and Thermodynamic Properties of Cryocrystals: Handbook.” New York: Begell House.

Marti, J., and Mauersberger, K. (1993). “A survey and new measurements of ice vapor pressure at temperatures between 170 and 250K.” Geophysical Research Letters, 20(5), 363–366.

Mathews, S. L., Servio, P. D., and Rey, A. D. (2020). “Heat Capacity, Thermal Expansion Coefficient, and Grüneisen Parameter of CH4, CO2, and C2H6 Hydrates and Ice Ih via Density Functional Theory and Phonon Calculations.” Crystal Growth and Design 20 (9): 5947–55. https://doi.org/10.1021/acs.cgd.0c00630.

Maynard-Casely, H. E., Hester, J. R., and Brand, H. E. A. (2020). “Re-examining the crystal structure behaviour of nitrogen and methane.” IUCrJ, 7(5), 844–851. https://doi.org/10.1107/S2052252520007460.

Mellon, M. T., & Sizemore, H. G. (2022). The history of ground ice at Jezero Crater Mars and other past, present, and future landing sites. Icarus, 371, 114667.

Milkovich, S. M., & Head, J. W. (2005). North Polar Cap of Mars: Polar Layered Deposit Characterization and Identification of a Fundamental Climate Signal. Journal of Geophysical Research: Planets, 110(E5).

Milliken, R. E., Grotzinger, J. P., & Thomson, B. J. (2010). Paleoclimate of Mars as Captured by the Stratigraphy in Gale Crater. Geophysical Research Letters, 37(4).

Millstein, J.D., Minchew, B.M. and Pegler, S.S. (2022) "Ice viscosity is more sensitive to stress than commonly assumed." Commun Earth Environ 3, 57 (2022). https://doi.org/10.1038/s43247-022-00385-x.

Minceva-Sukarova, B., Sherman, W., and Wilkinson, G. (1984). "The Raman spectra of ice (Ih, II, III, V, VI and IX) as functions of pressure and temperature." Journal of Physics C: Solid State Physics, 17(32), 5833.

Moore, J. M., McKinnon, W. B., Spencer, J. R., Howard, A. D., Schenk, P. M., Beyer, R. A., Nimmo, F., Singer, K. N., Umurhan, O. M., White, O. L., Stern, S. A., Ennico, K., Olkin, C. B., Weaver, H. A., Young, L. A., Binzel, R. P., Buie, M. W., Buratti, B. J., Cheng, A. F., … Zirnstein, E. (2016). "The geology of Pluto and Charon through the eyes of New Horizons." Science, 351(6279), 1284–1293. https://doi.org/10.1126/science.aad7055.

Mooy, H. H. (1931). "Crystal Structure of Methane." Nature, 127(3210), 707–707. https://doi.org/10.1038/127707c0.

Morlighem, M., Bondzio, J., Seroussi, H., Rignot, E., Larour, E., Humbert, A., & Rebuffi, S. (2016). Modeling of Store Gletscher's calving dynamics, West Greenland, in response to ocean thermal forcing. Geophysical Research Letters, 43(6), 2659–2666. https://doi.org/10.1002/2016GL067695

Morlighem, M., Seroussi, H., Larour, É., Schlegel, N., Borstad, C., de Fleurian, B., Adhikari, S., and Bondzio, J. (2022). "Ice Sheet System Model 2022 User Guide." https://issm.jpl.nasa.gov/documentation/.

Mukherjee, G. D., and Boehler, R. (2007). "High-pressure melting curve of nitrogen and the liquid-liquid phase transition." Physical review letters, 99(22), 225701.

Murphy, D.M. and Koop, T. (2005), "Review of the vapour pressures of ice and supercooled water for atmospheric applications." Q.J.R. Meteorol. Soc., 131: 1539-1565. https://doi.org/10.1256/qj.04.94.

Néron de Surgy, O., Laskar, J., 1997. On the long term evolution of the spin of the Earth. Astron. Astrophys. 318, 975–989.

Ning, F. L., Glavatskiy, K., Ji, Z., Kjelstrup, S., and Vlugt, T. J. H. (2015). “Compressibility, Thermal Expansion Coefficient and Heat Capacity of CH4 and CO2 Hydrate Mixtures Using Molecular Dynamics Simulations.” Physical Chemistry Chemical Physics 17 (4): 2869–83. https://doi.org/10.1039/C4CP04212C.

Notz, D. (2005). “Thermodynamic and Fluid-Dynamical Processes in Sea Ice,” January.

Nye, J. (2000). The Instability of a South Polar Cap on Mars Composed of Carbon Dioxide. Icarus, 144(2), 449–455. https://doi.org/10.1006/icar.1999.6306

Ono, N., (1967). “Specific heat and heat of fusion of sea ice.” Physics of Snow and Ice: proceedings, 1(1), 599-610.

Pais, M.A., Le Mouël, J.L., Lambeck, K., Poirier, J.P., 1999. Late Precambrian paradoxical glaciation and obliquity of the Earth—a discussion of dynamical constraints. Earth Planet. Sci. Lett. 174, 155–171.

Palucis, M. C., Dietrich, W. E., Hayes, A. G., Williams, R. M. E., Gupta, S., Mangold, N., Newsom, H., Hardgrove, C., Calef, F. III, & Sumner, D. Y. (2014). The origin and evolution of the Peace Vallis fan system that drains to the Curiosity landing area, Gale Crater, Mars. Journal of Geophysical Research: Planets, 119, 705–728. https://doi.org/10.1002/2013JE004583.

Palucis, M. C., Dietrich, W. E., Williams, R. M. E., Hayes, A. G., Parker, T., Sumner, D. Y., Mangold, N., Lewis, K., & Newsom H. (2016). Sequence and relative timing of large lakes in Gale crater (Mars) after the formation of Mt. Sharp, Journal of Geophysical Research: Planets, 121, 472–496. https://doi.org/10.1002/ 2015JE004905.

Parsons, R., & Holt, J. (2016). Constraints on the formation and properties of a Martian lobate debris apron: Insights from high-resolution topography, SHARAD radar data, and a numerical ice flow model. Journal of Geophysical Research: Planets, 121(3), 432-453.

Phillips, R. J., Davis, B. J., Tanaka, K. L., Byrne, S., Mellon, M. T., Putzig, N. E., Haberle, R. M., Kahre, M. A., Campbell, B. A., Carter, L. M., Smith, I. B., Holt, J. W., Smrekar, S. E., Nunes, D. C., Plaut, J. J., Egan, A. F., Titus, T. N., & Seu, R. (2011). Massive CO2 ice deposits sequestered in the south polar layered deposits of Mars. Science, 332(6031), 838–841. https://doi.org/10.1126/science.1203091

Piqueux, S., Kleinböhl, A., Hayne, P. O., Kass, D. M., Schofield, J. T., & McCleese, D. J. (2015). Variability of the Martian seasonal CO2 cap extent over eight Mars Years. Icarus, 251, 164–180.

Prialnik, D. (1992). “Crystallization, sublimation, and gas release in the interior of a porous comet nucleus.” Astrophysical Journal, Part 1 (ISSN 0004-637X), vol. 388, March 20, 1992, p. 196-202. Research supported by NASA., 388, 196-202.

Putri, A. R. D., Sidiropoulos, P., Muller, J.-P., Walter, S. H. G., & Michael, G. G. (2019). A New South Polar Digital Terrain Model of Mars from the High-Resolution Stereo Camera (HRSC) onboard the ESA Mars Express. Planetary and Space Science, 174, 43–55. https://doi.org/10.1016/j.pss.2019.02.010

Putzig, N. E., Smith, I. B., Perry, M. R., Foss II, F. J., Campbell, B. A., Phillips, R. J., & Seu, R. (2018). Three-dimensional radar imaging of structures and craters in the Martian polar caps. Icarus, 308, 138-147.

Ratcliffe, E.H., (1962). “The Thermal Conductivity of Ice New Data on the Temperature Coefficient.” Philosophical Magazine 7, 1197–1203.

Rochester, M.G., 1976. The secular decrease of obliquity due to dissipative core–mantle coupling. Geophys. J. R. Astron. Soc. 46, 109–126.

Roder, H. (1962). “The thermal conductivity of solid nitrogen.” Cryogenics, 2(5), 302–304. https://doi.org/10.1016/0011-2275(62)90017-6.

Ross, Russell G., and Kargel, Jeffrey S. (1998). “Thermal Conductivity of Solar System Ices, with Special Reference to Martian Polar Caps.” In Solar System Ices, edited by B. Schmitt, C. De Bergh, and M. Festou, 227:33–62. Dordrecht: Springer Netherlands. https://doi.org/10.1007/978-94-011-5252-5_2.

Röttger, K., Endriss, A., Ihringer, J., Doyle, S., & Kuhs, W. F. (2012). “Lattice constants and thermal expansion of H2O and D2O Ice Ih between 10 and 265 K. Addendum.” Acta Crystallographica Section B: Structural Science, 68(1), 91-91.

Rubincam, D.P., 1990. Mars: change in axial tilt due to climate? Science 248, 720–721.

Rubincam, D.P., 1993. The obliquity of Mars and “climate friction.” J. Geophys. Res. 98, 10827–10832

Sagmiller, D., and Hartwig, J. (2020). “Survey of cryogenic nitrogen thermomechanical property data relevant to outer solar system bodies.” Earth and Space Science, 7, e2019EA000640. https://doi.org/10.1029/2019EA000640.

Sanders, C.T. (1974). “Frost formation: the influence of frost formation and defrosting on the performance of air coolers.” Ph.D. thesis. Technische Hogeschool, Delft, The Netherlands.

Satorre, M. Á., M. Domingo, C. Millán, R. Luna, R. Vilaplana, and C. Santonja. 2008. “Density of, and Ices at Different Temperatures of Deposition.” Planetary and Space Science 56 (13): 1748–52. https://doi.org/10.1016/j.pss.2008.07.015.

Sears, D. W. G., and S. R. Moore (2005), On laboratory simulation and the evaporation rate of water on Mars, Geophys. Res. Lett., 32, L16202, doi:10.1029/2005GL023443.

Schieber, J., Minitti, M. E., Sullivan, R., Edgett, K. S., Malin, M. C., Parker, T., & Calef, F. (2020). Engraved on the rocks—Aeolian abrasion of Martian mudstone exposures and their relationship to modern wind patterns in Gale Crater, Mars. The Depositional Record, 6(3), 625-647.

Schmauss, S., Le Mouélic, S., Mangold, N., Caravaca, G., Seignovert, B., & Cavalié, L. (2025). Photogrammetric processing of MSL images: a case study at the Mont Mercou outcrop in Gale crater on Mars. 56th Lunar and Planetary Science Conference, Lunar and Planetary Institute, Mar 2025, The Woodlands (Texas), United States. pp.2074. ⟨hal-04929382⟩. https://hal.science/hal-04929382.

Scott, T. A. (1976). "Solid and Liquid Nitrogen." Physics Reports 27 (3): 89–157. https://doi.org/10.1016/0370-1573(76)90032-6.

Shean, D. E., Head, J. W., & Marchant, D. R. (2005). Origin and evolution of a cold-based tropical mountain glacier on Mars: The Pavonis Mons fan-shaped deposit. Journal of Geophysical Research: Planets, 110(E5), 2004JE002360. https://doi.org/10.1029/2004JE002360.

Shean, D. E., Head, J. W., Fastook, J. L., & Marchant, D. R. (2007). Recent glaciation at high elevations on Arsia Mons, Mars: Implications for the formation and evolution of large tropical mountain glaciers. Journal of Geophysical Research: Planets, 112(E3), 2006JE002761. https://doi.org/10.1029/2006JE002761.

Shieh, Sean R., Hsieh, Wen-Pin , Tsao, Yi-Chih, Crisostomo, Christian, and Hsu, H. (2022). "Low Thermal Conductivity of Carbon Dioxide at High Pressure: Implications for Icy Planetary Interiors." Journal of Geophysical Research: Planets 127 (3). https://doi.org/10.1029/2022JE007180.

Shreve, R. L. (1972). Movement of water in glaciers. Journal of Glaciology, 11(62), 205-214.

Shulman, L. M. (2004). "The heat capacity of water ice in interstellar or interplanetary conditions." Astronomy & Astrophysics, 416(1), 187-190.

Siegler, M., Aharonson, O., Carey, E., Choukroun, M., Hudson, T., Schorghofer, N., and Xu, S. (2012), "Measurements of thermal properties of icy Mars regolith analogs." Geophys. Res., 117, E03001, doi:10.1029/2011JE003938.

Slack, Glen A. (1980). "Thermal Conductivity of Ice." Physical Review B 22 (6): 3065–71. https://doi.org/10.1103/PhysRevB.22.3065.

Smith, D. E., Zuber, M. T., Frey, H. V., Garvin, J. B., Head, J. W., Muhleman, D. O., ... & Sun, X. (2001). Mars Orbiter Laser Altimeter: Experiment summary after the first year of global mapping of Mars. Journal of Geophysical Research: Planets, 106(E10), 23689-23722.

Smith, D. E., Zuber, M. T., Frey, H. V., Garvin, J. B., Head, J. W., Muhleman, D. O., Pettengill, G. H., Phillips, R. J., Solomon, S. C., & Zwally, H. J. (2001). Mars Orbiter Laser Altimeter: Experiment summary after the first year of global mapping of Mars. Journal of Geophysical Research: Planets, 106(E10), 23689–23722.

Smith, I. B. (2022). A retrospective on Mars polar ice and climate. In Oxford research encyclopedia of planetary science. https://doi.org/10.1093/acrefore/9780190647926.013.242.

Smith, I. B., Schlegel, N.-J., Larour, E., Isola, I., Buhler, P. B., Putzig, N. E., and Greve, R. (2022). "Carbon Dioxide Ice Glaciers at the South Pole of Mars." Journal of Geophysical Research: Planets 127 (4): e2022JE007193. https://doi.org/10.1029/2022JE007193.

Smith, I.B., Hayne, P.O., Byrne, S., Becerra, P., Kahre, M., Calvin, W., Hvidberg, C., Milkovich, S., Buhler, P., Landis, M., Horgan, B., Kleinböhl, A., Perry, M.R., Obbard, R., Stern, J., Piqueux, S., Thomas, N., Zacny, K., Carter, L., Edgar, L., Emmett, J., Navarro, T., Hanley, J., Koutnik, M., Putzig, N., Henderson, B.L., Holt, J.W., Ehlmann, B., Parra, S., Lalich, D., Hansen, C., Hecht, M., Banfield, D., Herkenhoff, K., Paige, D.A., Skidmore, M., Staehle, R.L., Siegler, M., 2020. The Holy Grail: A road map for unlocking the climate record stored within Mars' polar layered deposits. Planetary and Space Science 184, 104841. https://doi.org/10.1016/j.pss.2020.104841.

Song, Chun-Feng, Kitamura, Yutaka, Li, Shu-Hong, and Jiang, Wei-Zhong. (2013). "Analysis of CO2 Frost Formation Properties in Cryogenic Capture Process." International Journal of Greenhouse Gas Control 13 (March): 26–33. https://doi.org/10.1016/j.ijggc.2012.12.011.

Squyres, S. (1989), Urey prize lecture: Water on Mars, Icarus, 79, 229–288.

Stachowiak, P., Sumarokov, V. V., Mucha, J., and Jeżowski, A. (1994). "Thermal conductivity of solid nitrogen." Physical Review B, 50(1), 543–546. https://doi.org/10.1103/PhysRevB.50.543.

Stack, K.M.; Grotzinger, J.P.; Lamb, M.P.; Gupta, S.; Rubin, D.M.; Kah, L.C.; Edgar, L.A.; Fey, D.M.; Hurowitz, J.A.; McBride, M. (2019). Evidence for plunging river plume deposits in the Pahrump Hills member of the Murray formation, Gale crater, Mars. Sedimentology 66, 1768–1802.

Sumarokov, V. V., Stachowiak, P., and Jeżowski. A. (2003). "Low-Temperature Thermal Conductivity of Solid Carbon Dioxide." Low Temperature Physics 29 (5): 449–50. https://doi.org/10.1063/1.1542510.

Tarasov, L., Lecavalier, B. S., Hank, K., & Pollard, D. (2025). The glacial systems model (GSM) Version 24G. Geoscientific Model Development Discussions, 2025, 1-55.

Thomas, P. C., James, P. B., Calvin, W. M., Haberle, R., & Malin, M. C. (2009). Residual south polar cap of Mars: Stratigraphy, history, and implications of recent changes. Icarus, 203(2), 352–375. https://doi.org/10.1016/j.icarus.2009.05.014

Thomson, B. J., Bridges, N. T., Milliken, R., Baldridge, A., Hook, S. J., Crowley, J. K., ... & Weitz, C. M. (2011). Constraints on the origin and evolution of the layered mound in Gale Crater, Mars using Mars Reconnaissance Orbiter data. Icarus, 214(2), 413-432.

Toon, O. B., Pollack, J. B., Ward, W., Burns, J. A., & Bilski, K. (1980). The astronomical theory of climatic change on Mars. Icarus, 44(3), 552-607.

Trowbridge, A. J., Melosh, H. J., Steckloff, J. K., and Freed, A. M. (2016). “Vigorous Convection as the Explanation for Pluto’s Polygonal Terrain.” Nature 534 (7605): 79–81. https://doi.org/10.1038/nature18016.

Umurhan, O. M., Howard, A. D., Moore, J. M., Earle, A. M., White, O. L., Schenk, P. M., Binzel, R. P., Stern, S. A., Beyer, R. A., Nimmo, F., McKinnon, W. B., Ennico, K., Olkin, C. B., Weaver, H. A., and Young, L. A. (2017). “Modeling glacial flow on and onto Pluto’s Sputnik Planitia.” Icarus, 287, 301–319. https://doi.org/10.1016/j.icarus.2017.01.017.

Van Der Veen, C. J., and Whillans, I. M. (1990). “Flow Laws For Glacier Ice: Comparison Of Numerical Predictions And Field Measurements.” Journal of Glaciology 36 (124): 324–39. https://doi.org/10.3189/002214390793701372.

Van Duser, M. S. (1929). “Thermal Conductivity of Non-Metallic Solids.” In International Tables of Numerical Data: Physics, Chemistry and Technology; Ed., Washburn, E.W. 216 pp. McGraw Hill.

Waite, William F., Gilbert, Lauren Y., Winters, William J. and Mason, David H. (2006). “Estimating Thermal Diffusivity and Specific Heat from Needle Probe Thermal Conductivity Data.” Review of Scientific Instruments 77 (4): 044904. https://doi.org/10.1063/1.2194481.

Wang, Y. N., Pfotenhauer, J. M., Zhi, X. Q., Qiu, L. M. and Li, J. F. (2018). “Transient Model of Carbon Dioxide Desublimation from Nitrogen-Carbon Dioxide Gas Mixture.” International Journal of Heat and Mass Transfer 127 (December): 339–47. https://doi.org/10.1016/j.ijheatmasstransfer.2018.07.068.

Ward, W.R., 1973. Large-scale variations in the obliquity of Mars. Science 181, 260–262.

Ward, W.R., 1974. Climatic variations on Mars: I. Astronomical theory of insolation. J. Geophys. Res. 79, 3375–3386.

Watters, T. R., Campbell, B. A., Leuschen, C. J., Morgan, G. A., Cicchetti, A., Orosei, R., & Plaut, J. J. (2024). Evidence of ice-rich layered deposits in the Medusae Fossae Formation of Mars. Geophysical Research Letters, 51(2), e2023GL105490.

Williams, J. M., Scuderi, L. A., & Newsom, H. E. (2022). Numerical Analysis of Putative Rock Glaciers on Mt. Sharp, Gale Crater, Mars. Remote Sensing, 14(8), 1887.

Wordsworth, R., Forget, F., Millour, E., Head, J. W., Madeleine, J. B., & Charnay, B. (2013). Global modelling of the early martian climate under a denser CO2 atmosphere: Water cycle and ice evolution. Icarus, 222(1), 1-19.

Yamashita, Yasuyuki, Kato, Manabu, and Arakawa, Masahiko. (2010). “Experimental Study on the Rheological Properties of Polycrystalline Solid Nitrogen and Methane: Implications for Tectonic Processes on Triton.” Icarus 207 (2): 972–77. https://doi.org/10.1016/j.icarus.2009.11.032.

Yonko, J.D., Sepsy, C.F. (1967). “An investigation of the thermal conductivity of frost while forming on a flat horizontal plate.” ASHRAE Transactions 73, 567–579.

Young, D. A., Zha, C.-S., Boehler, R., Yen, J., Nicol, M., Zinn, A. S., Schiferl, D., Kinkead, S., Hanson, R. C., and Pinnick, D. A. (1987). “Diatomic Melting Curves to Very High Pressure.” Physical Review B 35 (10): 5353–56. https://doi.org/10.1103/PhysRevB.35.5353.

Young, H. D., and Freedman, R. A. (2019). “University Physics with Modern Physics Technology Update.” Pearson Education.

Zwally, H. J., Abdalati, W., Herring, T., Larson, K., Saba, J., & Steffen, K. (2002). Surface melt-induced acceleration of Greenland ice-sheet flow. Science, 297(5579), 218-222.